IRE Transactions

on ANTENNAS and PROPAGATION

Volume AP-9 JANUARY, 1961 Number 1

Published Bimonthly

RADIO ASTRONOMY ISSUE

In This Issue

PUBLISHED BY THE

ofessional Group on Antennas and Propagation

IRE TRANSACTIONS® PGAP IS A PUBLICATION DEVOTED TO EXPERIMENTAL AND THEORETICAL PAPERS ON RADIO ANTENNAS, ON GUIDED OR UNGUIDED PROPAGATION OF RADIO WAVES, AND ON ALLIED FIELDS OF RADIO PHYSICS SUCH AS RADIO ASTRONOMY

MANUSCRIPTS should be submitted to Sidney A. Bowhill, *Editor*, 222 Electrical Engineering, Pennsylvania State University, University Park, Pa. Manuscripts should be original typewritten copy, double-spaced, plus one carbon copy and two sets of copies of illustrations. Original illustrations will be called for if the paper is accepted. References should appear as footnotes and include author's name, title, journal, volume, initial and final page numbers, and date.

CONTRIBUTIONS, which should average 15 double-spaced typewritten pages in length, are subjected to review by the Associate Editors and their readers. Each paper must have a summary of less than 200 words.

COMMUNICATIONS should not exceed five double-spaced typewritten pages in length, together with not more than three illustrations. Accepted at the Editor's discretion, they appear in the first available issue.

NEWS ITEMS concerning PGAP members and group activities should be sent to the News Editor, R. C. Hansen, Space Technology Laboratories, P.O. Box 95001, Los Angeles 45, Calif.

ORIGINAL ILLUSTRATIONS should be submitted as follows: All line drawings (graphs, charts, block diagrams, cutaways, etc.) should be inked uniformly and ready for reproduction. If commercially printed grids are used in graph drawings, author should be sure printer's ink is of a color that will reproduce. Photographs should be glossy prints. Call-outs or labels should be marked on a registered tissue overlay, not on the illustration itself. No illustration should be larger than 8 x 10 inches.

Copies can be purchased from **the INSTITUTE OF RADIO ENGINEERS, 1 East 79th St., New York 21, N.Y.** Individual copies of this issue, and all available back issues, except Vols. AP-5, No. 1; AP-6, No. 1; AP-7 Special Supplement, may be purchased at the following prices: IRE members (one copy) $2.25, libraries and colleges $3.25, all others $4.50. Yearly subscription rate: non-members $17.00; colleges and public libraries $12.75. IRE TRANSACTIONS ON ANTENNAS AND PROPAGATION. Printed in U.S.A. Printed by George Banta Co., Inc., Curtis Reed Plaza, Menasha, Wisconsin.

Second-class postage paid at MENASHA, WISCONSIN, and additional mailing offices under the act of August 24, 1912. Acceptance for mailing at a special rate of postage is provided for in the act of February 28, 1925, embodied in Paragraph 4, Section 412, P. L. & R., authorized October 26, 1927.

Cover—The pencil beam interferometer antenna at the Radioscience Laboratory of Stanford University is described by Dr. Ronald N. Bracewell, its originator, in this issue.

IRE Transactions on Antennas and Propagation

Volume AP-9 JANUARY, 1961 Number 1
Published Bimonthly

TABLE OF CONTENTS

Radio Astronomy and Radio Science

LLOYD V. BERKNER, PRESIDENT, IRE

WHILE radio astronomy has added a new dimension to the sciences of astronomy and astrophysics, its rigid instrumental requirements have plowed the hinterland of radio science. When widespread space communications arrive in the next few years, the instrumental methods of space radio relay will be the direct derivatives of radio astronomy. For the extremes of sensitivity, stability, integration capabilities and noise suppression have been basic requirements of radio astronomy for two decades. Likewise, antenna and feed characteristics in radio astronomy represent the limits of progress in radio optics at any time. To achieve these goals, instrumental development has been supported by the most advanced theoretical development of radiometers and antennas carried out in the physics sciences. And, in turn, these developments have provided to all radio science and technology a wellspring of fundamental knowledge that is applicable in almost every advanced endeavor in radio technology.

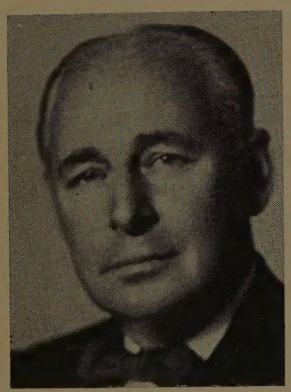

L. V. BERKNER

In the field of astrophysics, the contributions of radio astronomy have been explosive. Its observational data point the finger directly to the processes of star formation and destruction, toward the basic processes of galactic evolution, and toward phenomena at the observational limits of the universe. Involving neutral hydrogen and ionized matter in magnetic fields in space, the hyperfine 21-cm radiation and the polarized radiations in regions of nebulosity provide scientific opportunities that could only be exploited in the radio spectrum. Radio astronomy has shown us the center of our galaxy in surprising detail, when before it was hidden from view by the intervening concentrations of dust in the plane of the Milky Way.

While optical astronomy deals primarily with stars and their aggregations into galaxies and galactic groups, together with some spectacular dust clouds of minor import, radio astronomy deals with the other half of the universe—the masses of neutral hydrogen in various phases of concentration and condensation in the galactic areas and into new stars. It views the movement of this material into and out of the galactic center. It follows with special interest the disintegration products of the supernovae with their enrichment of the interstellar gas with heavy elements, explosions whose gases expand under strong magnetic control giving rise to marked wave polarization. Radio astronomy views special extragalactic phenomena which points the optical telescope to extraordinary events among the millions of galaxies. In this, its capability sometimes transcends the limits of optical observations. It may yet completely resolve the nearer galaxies such as the Andromeda into the special phenomena that, taken together, may characterize a typical galaxy more precisely. But, above all, radio astronomy has given a new insight to solar processes, especially the important active regions that give rise to chromospheric eruptions and solar cosmic rays. It views the Sun as a typical astrophysical subject. Together with special observations, radio astronomy is revolutionizing our comprehension of solar and terrestrial relations.

To achieve these successes, instrumental development has pushed outward the limits of radio science step by step. Since the historic observations of Jansky and Reber, of Southworth and Hey, of Purcell, Ewen, van der Hulst and Pawsey, sensitivities have climbed from power fluxes of 10^{-23} to 10^{-24}, 10^{-25}, 10^{-26} and even 10^{-27} watts/cm^2/cps, and the end is not in sight. The low-noise input has given way to the parametric amplifier and to the maser with its input characteristics approaching noise levels at absolute zero of temperature. Methods of

input switching of a wide variety provide stability levels that promise measurement of antenna temperature differences of 10^{-3} degrees. The old limit of 62 per cent feed efficiency seems about to tumble with improved Fresnel coverage to perhaps 85 per cent or better with corresponding improvement of mainlobe-to-sidelobe ratio. Antennas are working to repeatable precisions of seconds of arc for reasonable scan distances, bringing them toward the precision of optical instruments. Precise measurements of polarization at high sensitivity and stability have been brought within reach in the microwave ranges. Absolute measurements of radiation flux are setting new standards for precision in the microwave regions and with optimum horns promise to standardize sky sources to a repeatable few per cent so that variable sources can be studied. With high stability, integration methods provide useful measurements up to 50 db below noise, so that only 40 kw gives useful echoes from the Sun, nearly 1.5×10^8 km away, and integration is feasible over long intervals.

These and many other instrumental advances have been stimulated by the never-ending demands of radio astronomy toward new capabilities, toward new experimental opportunities. But their realization has advanced radio science as a whole to new capabilities. Radio astronomy has "put-on-the-shelf" a whole variety of advanced radio techniques which have been quickly exploited in radar, space technology, and advanced communications. It represents, perhaps, the prime example of the cross stimulus of a science and a technology in producing enormous advance to both. And we must not forget that this new dimension to astronomy was born from the curiosity and perspicacity of a radio scientist whose instruments and techniques brought him into contact with this new and now not so mysterious radiation that permeates the universe.

contributions

Some Characteristics of the Ohio State University 360-Foot Radio Telescope*

J. D. KRAUS†, FELLOW, IRE, R. T. NASH†, ASSOCIATE MEMBER, IRE, AND H. C. KO†, SENIOR MEMBER, IRE

Summary—**Design considerations and performance characteristics of The Ohio State University 360-foot radio telescope are discusssed. The telescope is well suited for precision position and intensity measurements at frequencies from 30 to 2000 Mc. The beamwidths expected at 2000 Mc are about 11 by 30 minutes of arc. Factors involved in determining the antenna temperature are considered, and an estimate is made of the expected temperature.**

Introduction

A COMPLETELY steerable parabolic dish is the most versatile radio telescope. Unfortunately, the cost of this type increases exponentially with aperture. If one is willing to confine his observations to regions close to the meridian, the antenna design can be greatly simplified and a telescope of larger aperture constructed for the same cost. For sky mapping, such a restriction is no handicap since observations can be made most precisely along the meridian. Furthermore, in mapping the entire sky, the region under observation at the moment is of little importance. These were some of the factors which led to the development of the 360-foot Ohio State University standing-parabola tiltable-flat-reflector radio telescope now nearing completion near Delaware, Ohio. The telescope is a meridian transit instrument designed to provide a large aperture per unit cost. It is especially well suited for precision position and intensity measurements of localized radio sources and of the sky background radiation over a very wide frequency range.

Description

The Ohio State radio telescope has 3 main components: 1) standing parabola, 2) tiltable flat reflector and 3) horizontal ground plane. The general arrangement is shown by the sketch of Fig. 1, which also gives the dimensions of the components. The basic telescope design calls for a horizontal length of both parabola and flat reflector of 720 feet of which only the central part, shown by the solid lines, is being constructed as the first phase. Several papers have described the original concept and some of the earlier considerations leading to the design.[1–3]

The telescope is situated about four miles from Delaware, Ohio, on a site provided by Ohio Wesleyan Uni-

* Received by the PGAP, September 20, 1960.

† Radio Observatory, Dept. of Elec. Engrg., Ohio State University, Columbus, Ohio.

[1] J. D. Kraus, "Radio telescopes," *Scientific American*, vol. 192, pp. 36–43; March, 1955.

[2] J. D. Kraus, "Radio telescope antennas of large aperture," PROC. IRE, vol. 46, pp. 92–97; January, 1958.

[3] J. D. Kraus, "The Ohio State University 360-foot radio telescope," *Nature*, vol. 184, 669–672; August 29, 1959.

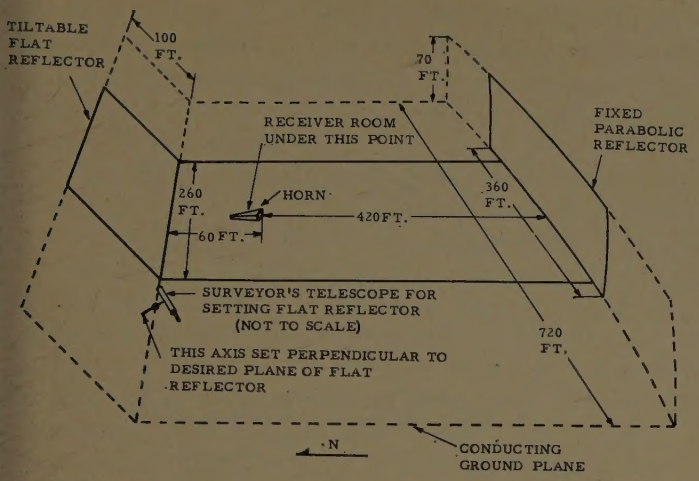

Fig. 1—Sketch of Ohio State University radio telescope with dimensions. The unit now nearing completion is shown by the solid lines.

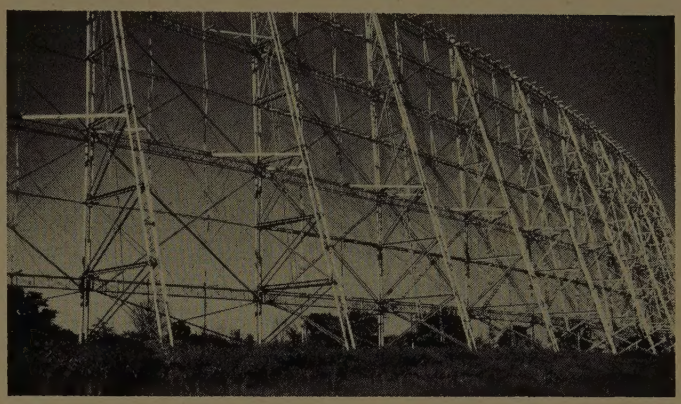

Fig. 2—360-foot standing parabola from southwest.

Fig. 3—North side of tiltable flat reflector showing 7 hoisting units.

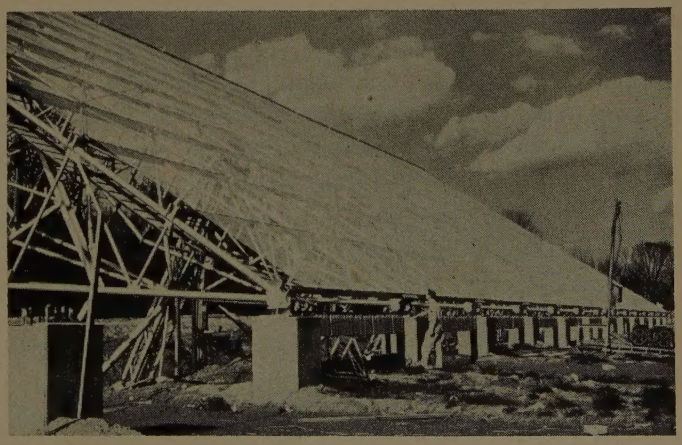

Fig. 4—South side of tiltable flat reflector.

versity. The radio observatory location is known as the Ohio State—Ohio Wesleyan Radio Observatory. The total cost of the telescope is expected to be about $375,000. To date, the National Science Foundation has provided about $330,000 and The Ohio State University about $20,000.

Construction on the telescope began in 1956 with work on the 360×70 foot parabolic reflector. It was completed in 1958 and work was begun late that year on the flat reflector. This unit, which is 260 feet long by 100 feet in slant height, was completed early in 1960. Work on the horizontal ground plane has been in progress during the summer of 1960, and it is expected that the telescope may be ready for mapping observations by early 1961. The standing parabola, as seen from the back (or south) side, is shown in Fig. 2, and rear and front views of the tiltable flat reflector are presented in Figs. 3 and 4.

The parabola is a section of a paraboloid of revolution with axis coincident with the ground plane and passing through the prime focus. The focal distance is 420 feet. The aperture area is 25,200 square feet or about 0.6 acre. This area is equal to that of a circular aperture antenna nearly 180 feet in diameter. The reflecting surface of the parabola consists of vertical copper-clad steel wires 0.081 inch in diameter, spaced 1 inch between centers over the central 180 feet and 3 inches between centers over the 90 feet to either side.

The flat reflector is constructed of seven movable units, each 20 feet wide (east-west) by 100 feet in slant height. These units are located with a 40-foot spacing between centers. Beams 20 feet long with hinges on each end bridge the space between units. The reflecting surface consists of 0.081-inch-diameter copper-clad steel wires spaced 1 inch between centers. Although each movable unit of the flat reflector is itself rigid, the flat reflector as a whole is nonrigid since the hinged connecting beams permit each unit to be moved a couple of degrees independently of the adjacent units. The flat reflector is ad-

justed for observations at a given declination by successively bringing each unit to the proper angle while monitoring the upper edge of the reflector with a surveyor's type telescope situated on the axis of rotation to the west of the base of the reflector (see Fig. 1). Each unit is elevated by a 3-horsepower electric winch and is secured by a fast-acting pneumatically operated brake and lock. Tests indicate that the top edge of the flat reflector can be readily adjusted and held to a precision of a few millimeters. The winch controls are within easy reach of an operator monitoring the flat reflector with the surveyor's telescope, and all are housed in a small building with a large viewing port west of the base of the flat reflector.

The horizontal ground plane extending between the parabola and the flat reflector will consist of a thin conducting coating (either aluminum sheet or conducting paint) on a flat concrete surface. This ground plane is some three acres in extent and acts as an electrical image plane and guiding surface for the waves traveling between the reflectors and between the parabola and prime focus. The wave polarization is vertical.

An important advantage of the ground plane is that the height of the feed antenna aperture is one-quarter the value required without ground plane. This means that the telescope may be operated at longer wavelengths with the ground plane for a given amount of aperture blocking. This may be explained with the aid of Fig. 5. Let the feed aperture height needed to properly illuminate the parabola without ground plane be equal to h, as in Fig. 5(a). As suggested in the figure, the feed antenna in this case may be a horn tilted so that its axis coincides approximately with the midpoint of the parabola. Now consider that a conducting ground plane is installed. The horn may then be tilted horizontally, as in Fig. 5(b), but only the upper half is needed since the ground plane acts as an electrical image surface. However, the beam produced by the upper half is now too narrow by a factor of 2, and consequently, the feed horn aperture height may be reduced to $h/4$ for proper illumination of the parabola.

Owing to the large horizontal dimension of the standing parabola, the required horizontal dimension of the feed aperture is also small. As a result, the aperture blocking of a single feed antenna is very small, amounting in a typical case to one-tenth of one per cent of the parabola aperture. It follows that a multiple feed can be employed without objectionable blocking to provide simultaneous operation over a wide range of frequencies.

Another important function of the ground plane is to reduce the antenna temperature by preventing ground radiation of approximately 290°K from entering the feed horn. The subject of antenna temperature is discussed further in the next section.

Directly under the prime focus point on the horizontal ground a 16 by 32 foot room is located for installation of the receiver front ends or entire receiving systems. Access to this room is by a tunnel which opens behind the

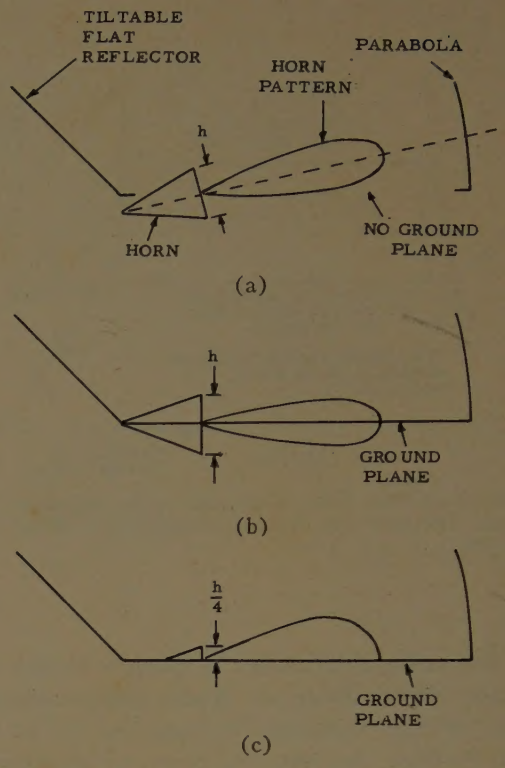

Fig. 5—Sketches showing feed horn dimensions required with and without ground plane.

tiltable flat reflector. Since preamplifiers can be placed on the ceiling of this room within inches of the feed horn terminals, transmission line or waveguide loss is negligible. Also, there are no weight restrictions on the equipment placed at the prime focus.

Since the feed horns are secured to a concrete pavement, they are relatively fixed in position. This rigidity feature, coupled with the fixed parabola and accurately adjustable flat reflector, should make it possible to observe the positions of radio sources with good repeatability and precision.

Performance

Pending completion of the antenna, complete data on the actual performance are not yet available. However, early in 1960, prior to the start of construction of the ground plane, the parabola and flat reflector were complete, and some preliminary observations were made at 950 Mc using a feed antenna as in Fig. 5(a). Extensive observations were made of Cassiopeia A over a range of declinations in order to determine the main and minor lobe structure in some detail. The measured half-power beamwidths at 950 Mc were about $\frac{1}{3}°$ in right ascension by 1° in declination. At this frequency and at all frequencies above about 500 Mc, only the central 180 feet of the parabola with 1-inch wire spacing are employed. At lower frequencies the effective horizontal dimension of the antenna is 260 feet. It is anticipated that the antenna will produce usable patterns over a frequency

range of at least 30 to 2000 Mc (10 meters to 15 cm). Based on the above-mentioned tests and measurements of a scale model of the antenna,[2,3] the expected beamwidths of the radio telescope over this frequency range are as listed in Table I.

From the preliminary performance data on the radio telescope, it is already obvious that if the wire surface on the parabola and tiltable flat reflector were replaced by conductors of larger size, the high frequency limit of the antenna could probably be increased to at least 5000 Mc. Such a modification would result in a beam about 4 minutes by 10 minutes of arc in half-power width. If, in addition, the antenna were increased in horizontal dimension to 720 feet as contemplated at some future date, the beam at 5000 Mc (6 cm) would be about 1 minute by 10 minutes of arc in half-power width. This beam has an area of 10 square minues of arc or about 0.003 square degree. With a beam of such high resolution, it is theoretically possible to resolve over 10,000,000 sources in the sky although, ad discussed in the next paragraph, detection limitations would make the number that could be observed less by about two orders of magnitude.

The anticipated number of sources which may be observed is indicated by Fig. 6. Two antenna sizes are considered; one where the effective horizontal reflector dimension is 180 feet, as at present, and another where the dimension is 720 feet as contemplated eventually. For both sizes the telescope is resolution limited at frequencies below about 300 Mc, while it is detection limited at frequencies above.[2] In the detection limited range two lines are shown. One is a solid line for conventional receivers (labeled "standard") where it is assumed that the receiver noise figure increases as the square root of the frequency, and the other is a dashed line for receivers with solid-state preamplifiers (labeled "low-noise") where the noise figure is assumed to be independent of frequency.[4] In all cases it is assumed that the sources are of the nonthermal type with a spectral index of 2/3. Accordingto Fig. 6, the present Ohio State radio telescope should be ideally capable of observing at least 3000 radio sources while an enlarged antenna of 720 feet would be capable of observing almost an order of magnitude more. As has been pointed out,[2] the number of sources observable in practice will be less; such figures are nevertheless useful in estimating the capabilities of the instrument. Since thermal type sources are not considered in Fig. 6, the trend in total number may not decrease as rapidly as indicated.

In order to achieve an increase in the number of observable sources at higher frequencies, as indicated by the difference between the dashed and solid lines in Fig. 6, it is necessary that the antenna temperature be

[4] The number of sources which can be detected (N_d) is given by $N_d = KA_{em}^{3/2}\lambda$ for the "standard" case (see footnote 2) and by $N_d = KA_{em}^{3/2}\lambda^{1/4}$ for the "low-noise" case.

TABLE I

Frequency (Mc)	Half-Power Beamwidths	
	Right Ascension	Declination
30	8°	35°
50	5°	20°
100	2.5°	10°
500	0.7°	2.0°
1000	0.35°	1.0°
2000	0.18°	0.5°

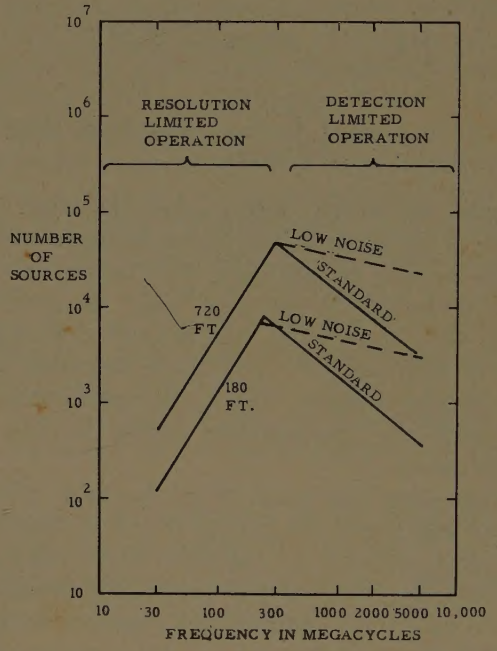

Fig. 6—Number of sources observable with the Ohio State University radio telescope as a function of frequency.

reasonably low. This follows from a consideration of the expression for the total noise temperature T_t of a receiving system. Thus, T_t is given by

$$T_t = T_A + (N - 1)T_0, \tag{1}$$

where

N = noise figure of receiver (dimensionless),
T_A = antenna temperature (°K),
T_0 = ambient receiver temperature ($\simeq$290°K).

If the noise figure is large, the second term effectively determines the total or system temperature T_t. However, in low noise receivers N may be small enough that the antenna temperature T_A largely determines T_t.

The antenna temperature can be computed from the antenna power pattern and a knowledge of the effective noise temperature of the sky and ground surrounding the antenna, and may be expressed by

$$T_A = \frac{1}{\Omega_A}\iint_{4\pi} T(\theta, \Phi)f(\theta, \Phi)d\Omega, \tag{2}$$

where

Ω_A = antenna beam area

$[=\int\int_{4\pi} f(\theta,\Phi)\ d\Omega]$,

$f(\theta, \Phi)$ = normalized antenna power pattern ($\leqq 1$),

$T(\theta, \Phi)$ = noise temperature distribution over sky and ground surrounding antenna.

Eq. (2) may be rewritten in terms of the contribution to the temperature from the main beam and from the minor lobes. Thus,

$$T_A = \frac{1}{\Omega_A}\left[\int\int_{\text{main beam}} T(\theta, \Phi)f(\theta, \Phi)d\Omega + \int\int_{\text{minor lobes}} T(\theta, \Phi)f(\theta, \Phi)d\Omega\right]. \quad (3)$$

In radio astronomy observations the main beam is directed at the sky. At the higher frequencies the sky tends to have a temperature well below that of the ground. Although the antenna "sees" the ground only through the minor lobes, the ground temperature is relatively high and the solid angle subtends approximately one hemisphere. Hence, the contribution of the second term may predominate unless the minor lobes are very small.

In most telescopes much of the backside minor-lobe structure which sees the ground is due to direct pickup by the feed antenna. In the Ohio State telescope the presence of the conducting ground plane should reduce the effective ground temperature observed by the feed horn. It is expected that most of the antenna temperature at the higher frequencies will be due to radiation from neighboring trees which leaks through the wire grid of the parabola and flat reflector. Even so, it is estimated that the antenna temperature at 1500 Mc with the present wire grid reflecting surface will be in the vicinity of 35°K. This is small enough to make the installation of a solid-state preamplifier worthwhile. If the wire grid were replaced by a solid surface, the antenna temperature should drop to only a few degrees when the main beam is directed at the coldest parts of the sky.

Observational Program

One of the most pressing needs in radio astronomy is that of more detailed and accurate spectra of localized radio sources and the sky background radiation. Since The Ohio State telescope is suited for operation over a wide frequency range, plans are in progress to install a multichannel receiver for use in a routine sky-mapping program. The receiver would record simultaneously on eight different frequencies spaced through the 50- to 2000-Mc range. After a survey at these frequencies, all channels would be changed a few per cent and a new survey made. By repeating this process, say 5 times, spectra with 40 points may be obtained for all of the objects and regions surveyed. The success of such a program will depend heavily on the accuracy of the calibrations used and careful consideration must be given to this and other factors. Besides obtaining spectra, it should also be possible to obtain relatively precise position data with the telescope since, as mentioned above, the surfaces are either fixed or can be accurately set. Since the prime focus is at ground level with no limitations on the weight placed there, the antenna is well adapted for the installation of low-noise preamplifiers of the maser type which should be of value at the higher frequencies.

The University of Illinois Radio Telescope*

G. W. SWENSON, JR.†, SENIOR MEMBER, IRE, AND Y. T. LO†, MEMBER, IRE

Summary—**The University of Illinois radio telescope is a reflector in the shape of a parabolic cylinder whose aperture is 400 feet×600 feet. A 425-foot-long phase-adjustable array of receiving antennas lies along the focal line and produces a pencil beam one-third degree in width, steerable in the meridian plane up to 30 degrees in either direction from the zenith. The array was designed by means of a novel procedure using both variable spacing and variable excitation to produce a prescribed beamwidth. The reflector is built of earth, utilizing a natural ravine. The purpose of the instrument is to compile a catalog of faint extragalactic radio sources.**

Introduction

THE principal mission of the University of Illinois radio telescope is to detect the largest possible number of extragalactic radio sources and to determine their intensities and positions on the celestial sphere. Such a catalog is of interest in cosmological studies;[1] large enough numbers of sources are required so that the relation between numbers and intensities can be determined with assurrance.

A number of catalogs have been compiled by radio astronomers.[2–5] A large degree of discordance exists among the various lists, suggesting that a thoroughly reliable list is one which has been agreed upon by at least two different observers using different instruments, preferably of different design. Furthermore, the existing surveys do not contain sufficient numbers of sources to satisfy cosmological requirements. Thus, another effort to compile an extensive catalog of sources appears to be justified. The design of the Illinois instrument, therefore, is to be optimized as far as possible for this purpose.

Design Philosophy

For a given size of antenna the operating frequency, and therefore the beamwidth, of a pencil-beam radio telescope is determined as a compromise between resolving power and sensitivity.[6] If the frequency is too high, the resolving power is high, but the sensitivity is reduced because of poorer noise figures and shorter available integration times. In addition, the typical spectrum of a radio source drops off rapidly with increasing frequency. If the frequency is too low the sensitivity is improved by better noise figures and longer integration times, and the typical source is stronger; however, the beamwidth is greater and the chance of confusion among sources is correspondingly higher. It is generally agreed that, on the average, one source per ten (or so) beam areas is the maximum source density that can be distinguished with acceptably small chance of confusion.

Low-noise receiving equipment using solid-state techniques reduces the dependence of noise figure upon frequency. Use of such a device would result in a higher optimum frequency for detecting a maximum number of sources with a given antenna size. Other considerations also enter, however. Effective use of an extremely low-noise receiver implies extremely low feed-system losses; this may be inconsistent with economical design of an extremely large antenna. Also, it may not be feasible to construct a large, low-cost antenna to the stringent dimensional tolerances required at a very high frequency.

After careful consideration of the above factors, it was decided that an instrument equivalent in size to a 400-foot diameter parabolic reflector, operating at a frequency near 600 Mc, represented the best compromise.

For a survey-type instrument it is sufficient that the beam be steerable in declination only. The earth's rotation scans the beam in right ascension and sets a limit on the permissible integration time as determined by the beamwidth. All instruments primarily intended for cataloging are of this type. In the present case it was desired to build an instrument of a different type from the Mills' Cross[2] used so successfully elsewhere, and, in particular, one which showed promise of having inherently lower sidelobe levels. A rectangular array with the chosen dimensions in wavelengths would require not less than 100,000 driven elements, a seemingly impractical number. At the same time it was considered necessary to forego any mechanical motion of the antenna in the interests of economy. A fixed paraboloid of revolution can be scanned only by a few beamwidths without excessive distortion of the beam shape. A fixed parabolic-cylindrical reflector whose focal line is in the meridian plane, with an array of phase-adjustable receiving elements along the focal line, provides the necessary steering in declination with a reasonable number of driven elements. This scheme was adopted.

Structural Details

Earth is the cheapest available building material with the necessary stability and permanence, and therefore

* Received by the PGAP, August 26, 1960.

† University of Illinois, Urbana, Ill.

[1] G. C. McVittie, "A radio astronomy project at the University of Illinois," IRE TRANS. ON MILITARY ELECTRONICS, vol. MIL-4, p. 14; January, 1960.

[2] B. Y. Mills, O. B. Slee, and E. R. Hill, "A catalog of radio sources between declinations of +10° and −20°," *Aust. J. Phys.*, vol. 11, pp. 360–387; 1958.

[3] J. G. Bolton, G. J. Stanley, and O. B. Slee, "Galactic radiation at radio frequencies," *Aust. J. Phys.*, vol. 7 (1), pp. 110–129; March, 1954.

[4] J. R. Shakeshaft, *et al.*, "A survey of radio sources between declinations −38° and +83°," *Mem. R.A.S.* (*Royal Astronomical Soc.*), vol. 47, pp. 106–154; 1955.

[5] D. O. Edge, *et al.*, "A survey of radio sources at a frequency of 159 Mc/s," *Mem. R.A.S.*, vol. LXVIII, pp. 37–60; 1959.

[6] J. L. Pawsey, "Performance Parameters of Radio Telescopes for Observation of Extremely Distant Objects," *C.S.I.R.O.* (Australia), Rept. No. R.P.L. 122; 1957.

was chosen for the support structure. One method studied was that of constructing a precise reflector of wire mesh suspended on posts above a roughly graded earth surface. This construction was discarded as being more expensive and considerably less permanent than a precisely graded and adequately protected earth surface bearing a reflecting screen. In either case, such an earth structure involves the excavation of at least 150,000 cubic yards of earth and poses a difficult drainage problem as well. An obvious and often-discussed solution is to make use of a natural depression in the earth; in the present instance this method provides a substantial saving in earth-moving and a ready-made drainage system, as well. A suitable site was found near the banks of the Wabash River at the Indiana-Illinois border. The chosen stream is a tributary of the Vermilion River about five miles southeast of Danville, Illinois, in a sparsely populated neighborhood. A small stream has cut through glacial till, clay, and sand to a thick layer of soft, blue shale, leaving a steep-sided gully of approximately the correct proportions. A balanced cut-and-fill operation, involving about 50,000 cubic yards of earth, was necessary to achieve the desired contours. Particular attention was given to the constitution and compaction of all filled portions, with the result that the material is very dense and hard and promises to retain its shape indefinitely.

The natural stream was straightened out and made to flow through a concrete channel along the center line of the reflector. Water collected by the reflector drains naturally into this channel. A number of springs in the sides of the ravine have been excavated and drain into the center channel by underground tiles or aggregate-filled waterways. Ordinarily, it is expected that the channel will be filled to a depth of about six inches. Storage capacity for occasional flash floods has been provided by installation of an earth dam upstream from the reflector. The entire reflector has a two per cent slope to the south (downstream) to assist drainage.

The focal length of the parabola was chosen in such a way as to minimize the amount of earth to be moved, subject to the requirement that the axis of the instrument be exactly north-south. The resulting value was 153 feet. The length of the reflector was chosen as 600 feet, and the length of the focal-line antenna array was chosen as 425 feet. This determines that the beam cross section will be circular when pointing 30 degrees from the zenith and very slightly elliptical when pointing at the zenith; furthermore, for zenith angles up to 30 degrees, all rays reaching the focal-line array must be reflected from the prepared reflector surface.

The focal-line array is supported beneath a wooden truss 425 feet long, 10 feet high, and 4 feet wide, the truss being supported, in turn, by four wooden towers 153 feet high. The towers are self-supporting in the north-south plane and are guyed in the east-west plane. Wooden towers were chosen after a mathematical study of the amount of electromagnetic energy scattered by simplified-model towers of both wood and steel. The wooden structure appeared to be superior by a rather small margin. It is believed that properly treated wooden members will require less maintenance than steel. In addition, considerably less guying was necessary in the wooden design than in the equivalent in steel. An unsuccessful attempt was made to find nonconducting guy materials with the necessary mechanical properties. Failing in this, it was decided to risk the unknown effects of guy wires rather than to accept the degree of aperture-blocking dictated by the use of self-supporting towers. The towers and trusses are of laminated, glued fir, impregnated with preservative material. It was found that a great many of the bolts in the towers were necessarily about one wavelength long; these were made for the most part of plastic-impregnated wood. The antenna is shown in Fig. 1.

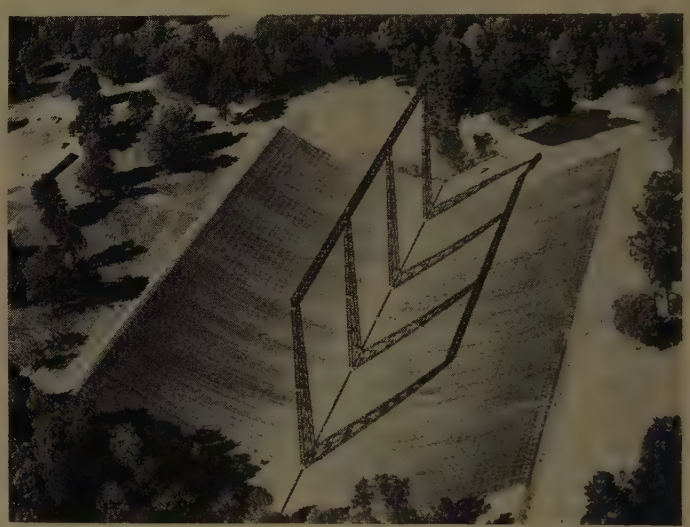

Fig. 1—The University of Illinois radio telescope.

General Design of the Feed System

For a uniformly spaced linear array of discrete elements, there exists a maximum spacing between elements in order to avoid the appearance of a secondary major beam in the usable range. In the present case a minimum of about 400 elements would be needed, each with its own precisely adjustable phase-shifter. This arrangement appears to be unnecessarily expensive. Instead, a system of circular polarization has been adopted. The advantage of such a system is that any source of circular polarization has an inherent facility for phase shifting,[7,8] for it is well known that any desired time-phase variation can be achieved simply by

[7] W. Sichak and D. J. Levine, "Microwave high-speed continuous phase shifter," Proc. IRE, vol. 43, pp. 1661–1663; November, 1955.
[8] R. E. Miller, A. T. Waterman, Jr., G. K. Durfey, and W. H. Huntley, Jr., "A rapid scanning phased array for propagation measurements," 1958 IRE WESCON Convention Record, vol. 2, pt. 1, pp. 184-196.

mechanical rotation of the source. However, it is clear that the success of such a system depends to a large extent upon achieving a low axial ratio in the radiated field.

Suppose that a given source has an axial ratio X; then the relative magnitudes of two circularly polarized components in opposite sense will be in a ratio

$$q = \frac{X+1}{X-1}. \qquad (1)$$

For convenience in later discussion, let us assume that the dominant component is right-handed (RH); then to achieve a certain phase shift $\alpha°$ it is necessary to rotate the antenna by $\alpha°$. However, such a rotation will result in a phase shift of $-\alpha°$ for the other component, namely the left-handed (LH) one. Then if one scans the RH beam to θ_0 from the zenith by progressively rotating the elements, an LH beam with a magnitude $1/q$ relative to the RH beam will be formed at $-\theta_0$. Since in the present application the source is randomly polarized, the received energy from these two beams becomes indistinguishable. This is, in effect, another source of minor-lobe error which is not experienced in linearly polarized systems.

Randomization of Phases

The problem described above may be resolved by designing two antennas from the same array in the following manner: for the RH one, it should be a very efficient antenna in the sense of high directivity, and for the LH one, a very poor antenna in the sense that the contributions from all elements are not collimated in any preferred direction in space. The available parameters are the phases of the elements. For the nth element, the net phase of the RH component is equal to that introduced by the transmission line ϕ_n plus that due to rotation α_n, while that of the LH component is equal to $(\phi_n - \alpha_n)$. Since their phase angles are different, it is possible to set the sequence $(\phi_n+\alpha_n)$ equal to an arithmetic progression while assigning the sequence $(\phi_n-\alpha_n)$ any desired values. One simple solution is to let $\alpha_n=-\phi_n$; then for the RH component all elements are in phase, while for the LH component they are $2\phi_n$ as shown in Fig. 2(a). Now if, in scanning, all elements are rotated progressively such that the nth element turns through $n\delta$, the LH phase sequence becomes $\{(2\phi_n-n\delta)\}$. Although in principle there is a best set of $\{\phi_n\}$ such that the LH contributions are collimated to the least degree for all scan angles, it appears extremely difficult to obtain such an optimum solution.

Nevertheless, the above discussion suggests a simple solution, that of randomizing the set of LH component phases $\{2\phi_n\}$. If $2\phi_n$ is the polar angle of a point chosen at random on a unit circle with an "equally likely" probability, then $(2\phi_n-n\delta)$ remains unchanged statistically. Thus the LH component magnitude can be estimated by the theory of random walks.

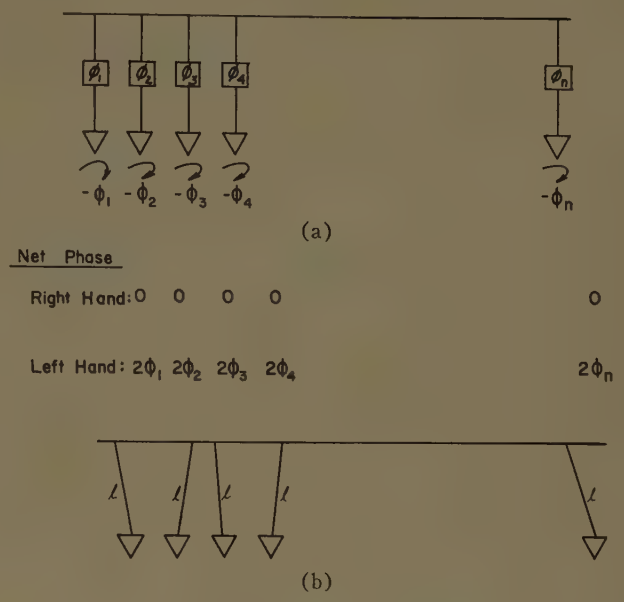

Fig. 2—Feed scheme for the antenna elements.

Let the array of $2N$ effective elements be weighted according to a cosine-square function; then the nth element contribution is given by

$$V_n = \cos^2 \frac{\pi(n+1/2)}{2(N+1/2)} e^{j\theta_n}, \qquad (2)$$

where θ_n is a random number uniformly distributed between 0 and 2π. Let

$$R_L = \left| \sum_{n=-N-1}^{N} V_n \right|, \qquad (3)$$

then R_L follows a Rayleigh distribution

$$p(R_L) = \frac{R_L}{\sigma^2} \exp\left(-\frac{R_L^2}{2\sigma^2}\right) \qquad (4)$$

where the variance $\sigma \approx 3N/4$. The mean value of R_L is given by

$$\overline{R}_L = \int_0^\infty R_L p(R_L) dR_L = 1.088\sqrt{n}; \qquad (5)$$

but for the RH component, the beam maximum is given by

$$R_R = q \sum_{n=-N-1}^{N} a_n \approx Nq. \qquad (6)$$

Therefore, the level of the LH beam on the average is given by

$$P_L = 20 \log \overline{R}_L/R_L \approx -20 (\log \sqrt{n} + \log q). \qquad (7)$$

For $2N=300$, $x=1.2$, the cumulative probability of getting P_L below a certain level is shown in Table I. It is seen that 99 per cent of the chances are that the LH beam will be below -32.5 db. To safeguard against

TABLE I

P_L less than	Cumulative probability
−42.6 db	55 per cent
−36.6 db	88 per cent
−32.5 db	99 per cent

bad luck, 300 random values of $\{2\phi_n\}$ have been generated and the actual peaks of the LH pattern computed with a high speed computer. It is found that they are all below −30 db.

In practice the randomization of ϕ_n should be achieved by tapping off the main transmission line at random with the branch line to each element kept constant as shown in Fig. 2(b). This method is preferred to that in which the branch line is made with random length because, with the latter method, spurious lobes and deterioration of the pattern will result unless the antenna element is matched to the branch-line impedance almost perfectly over all the scan angles.[9]

An antenna element which possesses the low axial ratio required by the above discussion is the equiangular spiral antenna on a conical surface developed by Dyson.[10] The construction and pattern of this antenna are shown in Fig. 3. This antenna has an extremely wide bandwith and a small axial ratio of about 1.07 over a conical region of a 40 degree half angle.

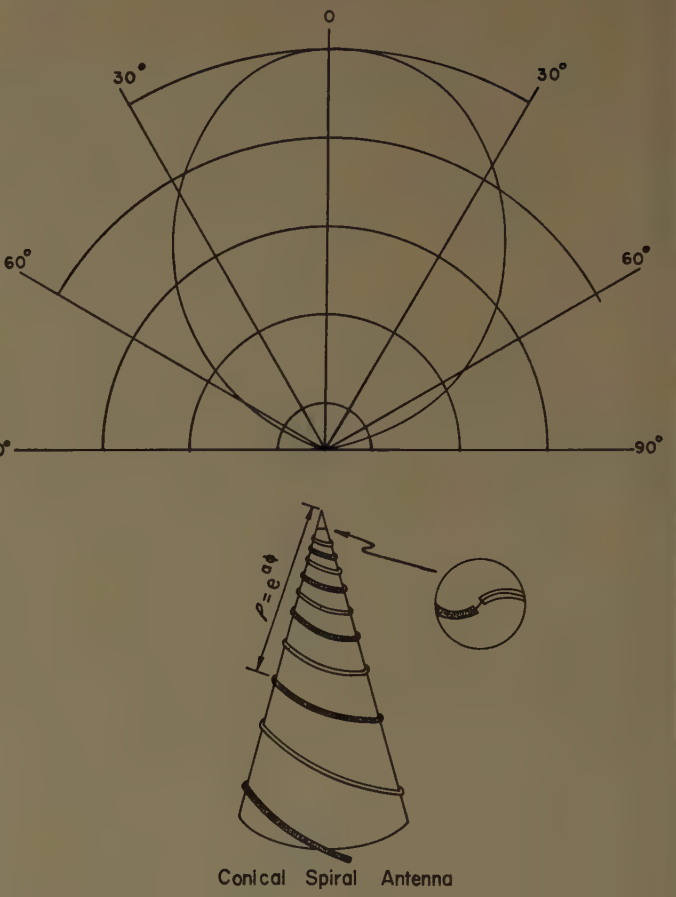

Fig. 3—Radiation pattern and structure of antenna element.

Nonuniform Spacings

As stated previously, the minimum number of elements required for a ±30-degree scan is about 400, so that the spacing between elements will be less than $2\lambda/3$. This restriction is merely a consequence of uniform spacing. For an array of N isotropic elements the pattern is given by

$$P(u) = \sum_{n=1}^{N} A_n e^{j\beta d_n u} \tag{8}$$

where

A_n = the current of the nth element,
d_n = the spacing between the nth element and the first, with $d_1 = 0$,
$u = \sin\theta$, θ being the angular position of observation point with respect to the normal to the line of array, and
$\beta = 2\pi/\lambda$.

In order to prevent the contributions of all terms from being added in phase at some angle θ other than 0°, it is necessary that $d_n < nd$, d being a constant. From this point of view, a uniformly spaced array seems to be the least attractive arrangement. From another point of view, for a uniform array the $(N-1)$ parameters, namely the set $(d_n - d_{n-1})$, have been arbitrarily set equal; in other words, the whole set is reduced to a single parameter.

Although uniformly spaced arrays have been almost exclusively used (perhaps because they are mathematically manageable), it is doubtful that very large uniform arrays are justified even for reasons of economy. During the course of this design effort, nonuniform spacing has been considered in an attempt to understand what advantages could be gained with these additional degrees of freedom.

It appears that the nonuniformly spaced array has received little attention;[11,12] further, this problem does not seem to yield to a simple, compact, mathematical analysis. First, consider a uniformly spaced array with a cosine-square taper as shown in Fig. 4. The pattern function is given by

$$P(u) = \sum_{n=-N-1}^{N} \cos^2 \frac{\pi(n+1/2)}{2(N+1/2)} e^{j\beta n d u}, \tag{9}$$

[9] L. A. Kurtz and R. S. Elliott, "Systematic error caused by the scanning of antenna arrays: phase shifters in the branch lines," IRE Trans. on Antennas and Propagation, vol. AP-4; October, 1956.

[10] J. D. Dyson, "The unidirectional equiangular spiral antenna," IRE Trans. on Antennas and Propagation, vol. AP-4, pp. 329–335; October, 1959.

[11] H. Unz, "Linear arrays with arbitrarily distributed elements," IRE Trans. on Antennas and Propagation, vol. AP-8, pp. 222–223; March, 1960.

[12] D. D. King, R. F. Packard, and R. K. Thomas, "Unequally spaced, broad-band antenna arrays," IRE Trans. on Antennas and Propagation, vol. AP-8, pp. 380–384; July, 1960.

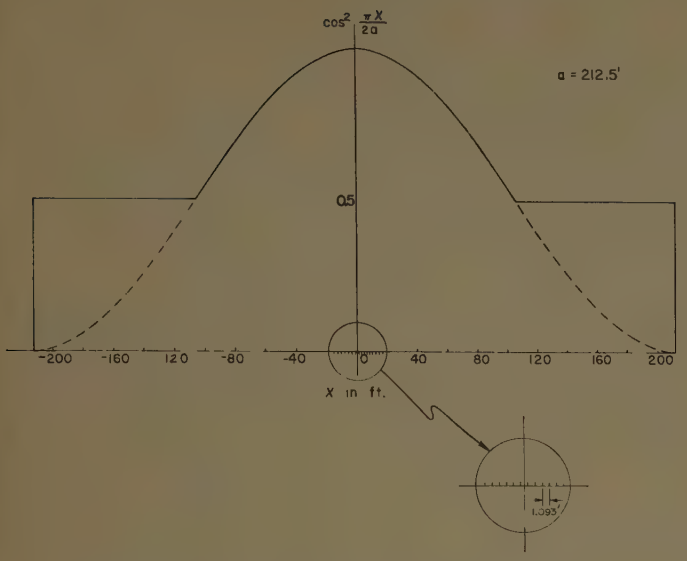

Fig. 4—Current magnitude weighting functions.

where the range of u depends upon the scan angle θ_0, namely, from $\sin\theta_0 - 1$ to $\sin\theta_0 + 1$. For the present problem it is sufficient to examine the range $u = 0$ to 1.5. It may be seen from (9) that in the direction of the main-beam maximum about 82 per cent of the total field is contributed by the central half of the array (194 elements), while only 18 per cent is due to the outer 194 elements. The outer half of the array is not mainly used to supply energy (or receive energy in the present application); instead, its function is to balance out the large minor lobes caused by the nearly uniform illumination over the central portion. This is an alternative statement of the well-known fact that the minor-lobe level depends primarily on the taper of the illumination over the aperture.

An effort was made to aproximate the desired cosine-squared illumination function by using variable spacing, the resulting radiation patterns being computed by the high-speed digital computer ILLIAC. The spacing weighting function shown in Fig. 5,

$$y(x) = \frac{a}{\pi}\sin\frac{\pi x}{a} + x,$$

is derived by integrating the original cosine-squared illumination function with the boundary conditions $y(0) = 0$ and $y(a) = a$. By projecting on this curve equally spaced points of set $\{y_n\}$ with $y_n - y_{n-1} = 2\lambda/3$, a set of unequally spaced points $\{x_n\}$ is obtained. Since $y'(a/2) = 1$ the interelement spacing

$$(x_n - x_{n-1}) \lesssim 2\lambda/3 \qquad \text{for } n \lesssim N/2$$

where $2\lambda/3 = 1.083$ feet as indicated in Fig. 4. However, it is known that the radiation pattern will not change significantly as the interelement spacing increases until it is close to $2\lambda/3$. It is therefore plausible to replace

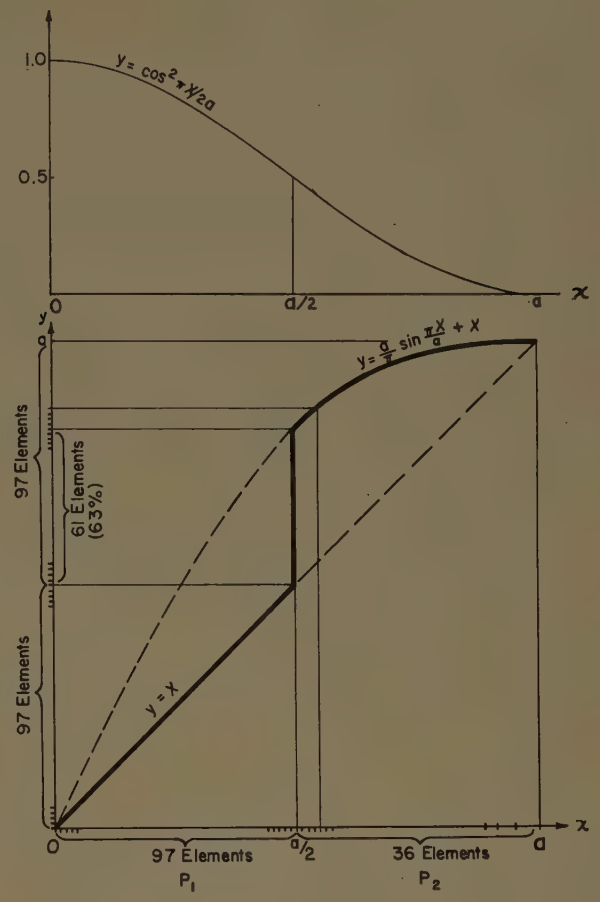

Fig. 5—Element spacing weighting function.

the portion of the curve $y(x)$ for $0 < x < a/2$ by a straight line $y = x$ as shown (Fig. 5). Thus, the spacing weighting function is given by

$$y = \begin{cases} x, & 0 \le x < a/2 \text{ (subarray } P_1) \\ \dfrac{a}{\pi}\sin\dfrac{\pi x}{a} + x, & a/2 < x \le a \quad \text{(subarray } P_2). \end{cases} \tag{10}$$

The number of elements corresponding to the discontinuity at $x = a/2$ represents those eliminated by this procedure; they amount to 61 pairs of elements or 63 per cent of the original P_2 subarray, or $\frac{1}{3}$ of the total $2N$ elements. The interelement spacing in P_2 ranges from $2\lambda/3$ to about 19λ, or an average of 1.85λ for this portion.

Since the spacings of the subarray P_2 have been weighted, it seems logical to keep their magnitudes uniform for the sake of simplicity. The magnitude is determined as one-half by the requirement that the new P_2 of 36 pairs of elements will contribute the same[13] in the main beam as the uniformly spaced P_2. Thus the

[13] It can be shown that in the neighborhood of the main beam the behavior of $P_2(u)$, whether it is uniformly spaced or nonuniformly spaced [although $P_2(u)$ is not predictable for large u's], remains more or less the same. Therefore, in order to replace one by the other, their total contributions should be made equal. This is also evidenced by the result in Fig. 6.

new magnitude weighting function is shown by the solid line in Fig. 4.

The radiation patterns of these new subarrays P_1 and P_2, as well as their sum P, have been computed and plotted in Fig. 6. It should be noted that the signs of P_1 and P_2 have been attached to each of their lobes. It is interesting to see that the first beamwidth of $P_1(0)$ between nulls is about three times that of $P_2(\theta)$. Since $P_1(0)$ and $P_2(0)$ are in phase, the first minor lobe of $P_1(\theta)$ is nearly balanced out by the third lobe of $P_2(\theta)$. It is expected that a similar result would be obtained if the original uniformly-spaced subarray P_2 is used. The same figure also shows the pattern $P_0(\theta)$ of the uniformly spaced array originally assumed by (9). The similarity of $P(\theta)$ to $P_0(\theta)$ is apparent.

Unfortunately, as one expects, the cancellation of the minor lobes between P_1 and P_2 does not hold through the entire range of u. Nevertheless, it seems rather remarkable to find that the cancellation is quite good for a substantial number of minor lobes (about the first 30 or 40 lobes). As u increases, they begin to fall out of coincidence and the average minor-lobe level increases slowly as shown in Fig. 7.

It may be noted that as u increases, the sidelobe level of P_1 decreases in a predictable manner (since $P_1(u)$ can be summed in closed form) such that, even though P_1 and P_2 are no longer coincident beyond a certain range of u, the magnitude of $P_1(u)$ becomes too small to be of any importance. In fact, the sidelobe level for large values of u is almost solely determined by that of $P_2(u)$ until u reaches the approximate value at which the secondary major beam of $P_1(u)$ occurs.

Since this particular array has about 206 minor lobes for $u=0$ to 1, for convenience of presentation only their levels and approximate locations have been plotted against u. In addition, those lobes between -35 and -40 db and those below -40 db are grouped together at their approximate locations with the number of lobes indicated. It may be noted that the average spacing now is about 1λ. If they were uniformly spaced, a secondary major beam would appear at $u=1$. Also shown in this figure is the pattern of a single element (the same as that in Fig. 3, but in different coordinates). It is seen that the high sidelobes of $P(u)$ at large value of u will be suppressed by the directivity of the individual elements. With the beam pointing at 0°, the minor-lobe level is -31 db; at 30° (the worst case), it is about -28 db.

Fig. 8 shows similar results for $u=1$ to 1.5. In this range the minor lobes are raised to -20 to -30 db. The high level near $u=1.5$ is actually due to P_1, for its inter-element spacing is equal to $2\lambda/3$. This situation can be rectified by using slightly smaller spacing. At the right edge of each of these figures is shown the distribution of minor lobes according to levels.

It should be mentioned that the above results are devived not from the set of $\{x_n\}$ as given by (10), but from a slightly modified version of this set. They differ

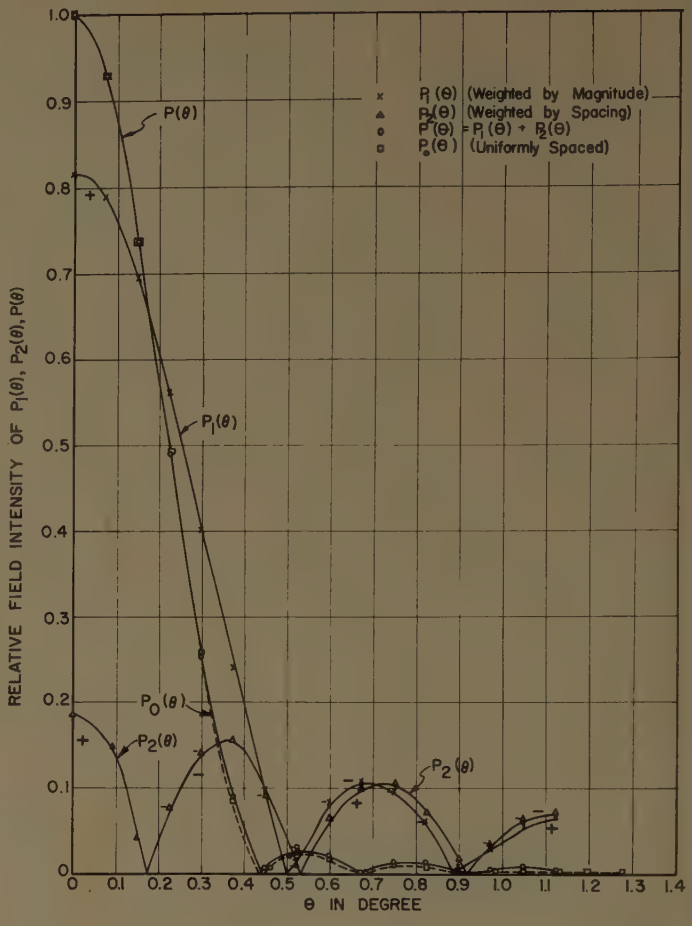

Fig. 6—Field intensity patterns of a completely uniformly spaced array P_0, subarrays P, P_1 and P_2 and the array P_1 and P_2.

only in that a few elements have been moved in an effort to reduce the maximum minor-lobe level. It is found that the improvement is not very significant, and that both results are quite similar. Because of the difficulty of providing rigorous analytical support for this method of design, an optimization procedure has been programmed for the ILLIAC, so that all elements can be moved in succession until a lower maximum minor-lobe level is reached. It can be shown that the movement of the elements has little effect on gain and on the shape of the main beam. After several cycles of this procedure, it is found that the improvement achieved is only in the order of -1 db or so. It is believed, therefore, that, even though the set $\{x_n\}$ as given by (10) is not optimum in the sense that the maximum sidelobe level is minimized, it is very close to one of the optimum solutions.[14]

Although the pattern of half of the P_2 subarray (with 36 elements only) has not been obtained, its approximate behavior can be inferred from that of the P_2 subarray (with 36 pairs of elements) which is shown in Fig. 6. The result indicates that for $u=0$ to 1 all sidelobes

[14] According to our definition and procedure for optimization, the solution may not be unique.

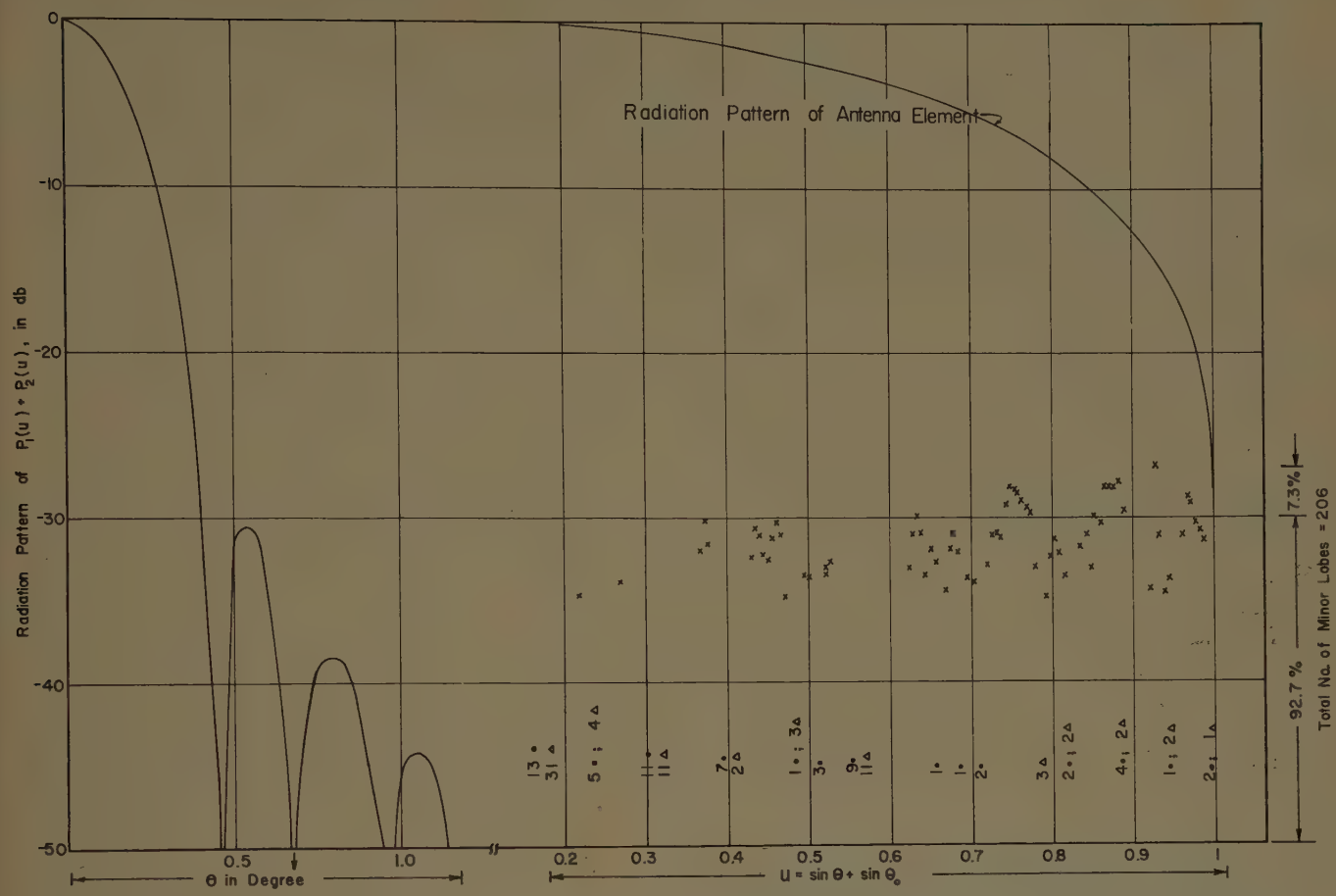

Fig. 7—Radiation pattern of the nonuniform array P_1 and P_2 for $u=0$ to $u=1$. ●—between −35 and −40 db; Δ—under 40 db.

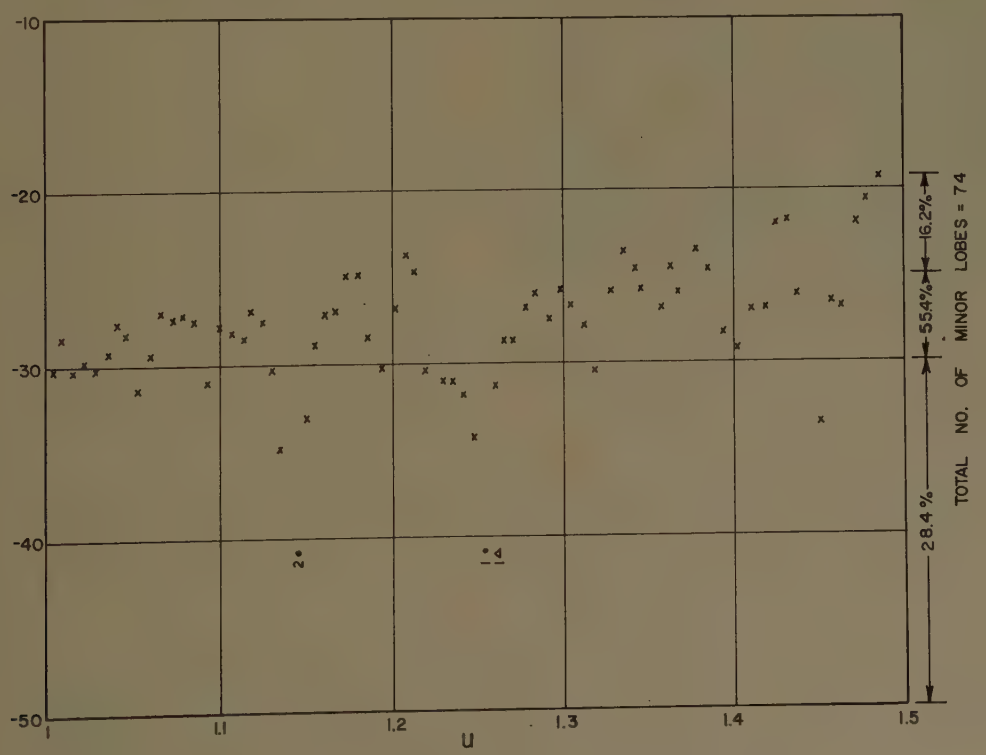

Fig. 8—Radiation pattern of the nonuniform array P_1 and P_2 for $u=1$ to $u=1.5$. ●—between −35 and −40 db; Δ—under −40 db.

are below -12 db and for $u=1$ to 1.5 they are below 10 db, in spite of their wide average spacing, 1.85λ. If they were spaced uniformly at this value, secondary major beams would occur at $u=0.54$, 1.08, 1.62.

To summarize, a nonuniformly spaced array seems to have the following properties and advantages:

1) Secondary major beams are eliminated.
2) The average minor-lobe level increases slowly as u increases, and decreases as N increases. These effects seem to be typical of most unequally spaced arrays. Since most elements have a certain directivity, the appearance of large sidelobes at high angles does not pose a serious problem. Furthermore, the lobe at large angles are in general very wide in beamwidth. This tends to reduce their contribution to a form of uniform background response.
3) The deterioration of main beam shape and gain due to the variation of spacing is of secondary effect unless all the spacings become too great or the total number of elements for a given aperture becomes too small.
4) The range of illumination weighting can be greatly reduced. For example, our particular array, if weighted only in magnitude, requires a range of 83.6 db; however, it requires only a 6-db range if partially weighted by spacing.
5) For a uniformly spaced and uniformly illuminated array, regardless of size, the first minor lobe is always at the -13.2-db level. By spacing the elements nonuniformly it is possible to reduce the first few lobes to a lower level.
6) A nonuniformly spaced array requires a smaller number of elements, or, for the same number of elements, either a larger scan angle is possible or a wider frequency range can be covered. In fact, nonuniform spacing is probably the only efficient method of obtaining a wide-band radiation pattern factor for a discrete array.

Finally, it should be mentioned that as the array dimensions increase and as the number of elements (actually the aperture) increases, the advantage of nonuniform spacing becomes much greater. As an example, for an array of 10^6 elements, 90 per cent of the elements probably can be eliminated without much sacrifice in performance. By reducing the number of elements, it is possible to lower not only the cost of the antenna and its accessories but that of operation and maintenance as well.

The radiation pattern in the E-W plane has also been computed, based upon the illumination produced by a conical spiral (Fig. 3). The beamwidth in this plane is about 0.3 degree with sidelobe level of -27.5 db, in quite close agreement with those in the N-S plane.

Summary of Radio Telescope Parameters

Reflector dimensions: 600 feet (N-S) $\times$400 feet (E-W) $\times$60 feet deep.
Focal length: 153 feet.
Feed array: 425 feet long, 276 elements.
Design frequency: 611 Mc.
Half-power beamwidth: 19 minutes of arc.
Feed elements: equiangular conical spirals.
Phase adjustment: manual rotation of antenna elements.
Polarization: circular.

Operating Procedure

It is proposed that the radio telescope be employed regularly on a survey of discrete sources between the declinations of $+10$ degrees and $+70$ degrees. Typically, the feed array will be phased manually to the desired declination during daylight hours and a drift curve recorded during the following night in order to avoid solar interference. Allowing for overlap between successive scans and possible reruns of scans necessitated by interference, it is anticipated that five years will be necessary to complete the survey.

Acknowledgment

The funds for design and construction of the instrument were granted by the Office of Naval Research under contract Nonr 1834(22). Funds for land, buildings, and utilities were granted by the Research Board of the University of Illinois, Urbana. Many colleagues participated in the engineering studies. The authors are particularly indebted to Professors G. C. McVittie, G. A. Deschamps, J. D. Dyson, and R. A. Davidson for contributions to the electrical design, and to Hanson, Collins, and Rice, consulting engineers, for the design of the structures. The general design was strongly influenced by discussions with J. L. Pawsey, B. Y. Mills, M. Ryle, M. Laffineur, and R. H. Brown. Most of the computer programming was done by S. Ray.

The Design and Capabilities of an Ionospheric Radar Probe*

W. E. GORDON†, SENIOR MEMBER, IRE, AND L. M. LaLONDE†

Summary—**Staff members of the Cornell University Center for Radiophysics and Space Research have designed an ionospheric radar probe to be located near Arecibo, Puerto Rico. The radar will have the following general specifications:**

1) **Antenna reflector, 1000-foot-diameter spherical bowl, illuminated by a 430-Mc dual-polarized feed.**
2) **Transmitter of 2.5 Mw peak, 150 kw average power, or 100 kw CW power.**
3) **Dual-channel receiver, capable of measuring total power, polarization and received spectrum.**

The radar will initially be used to measure the variation of electron density with height, the fluctuations of electron density at fixed heights and electron temperatures and magnetic field strengths at various heights. Ionospheric drifts may also be measured.

The radar will also be able to obtain echoes from planets, information of the moon's surface and possibly echoes from the sun. Hydromagnetic shocks may also be detected and a study of cislunar ionization can be made.

The passive system with the large antenna may be used as an instrument in radio astronomy to observe radio emission from planets and from true stars, and to make a survey of radio sources. With additional facilities, many radio astronomy measurements can be made taking advantage of the large antenna aperture and resulting high resolving power.

I. Introduction

STAFF members of the Cornell University Center for Radiophysics and Space Research have designed a radar to probe the ionosphere. The radar is the basic instrument of a radio observatory being constructed near Arecibo, Puerto Rico. The specifications for the radar were determined by the desire to observe and measure characteristics of the ionosphere using radio wave scattering by free electrons [1]–[7]. The antenna required for this purpose is a 1000-foot-diameter spherical dish using a suitably corrected feed.[1]

A summary of the radar specifications is given in Section II. The expected capabilities of the instrument in probing the ionosphere are described in Section III. A radar that is designed with the specifications given in Section II for the purpose of studying the ionosphere can make many other measurements in the solar system. These are included in Section IV. The uses of the radio telescope formed from the radar's antenna and a sensitive receiver or by the addition of antenna feeds and receivers at other frequencies are indicated in Sections V and VI.

* Received by the PGAP, September 15, 1960. The work described in this paper was sponsored by the Advanced Res. Projects Agency under Contract AF19 (604)-6158 with Electronics Res. Directorate of the Air Force Cambridge Research Center.

† Center for Radiophysics and Space Res., Cornell University, Ithaca, N. Y.

[1] The Antenna Laboratory of the Air Force Cambridge Research Center has contributed to the field of spherical antennas for over ten years. The basic fundamentals appear in: R. C. Spencer, C. J. Sletten, and J. E. Walsh, "Correction of spherical aberration by a phased line source," *Proc. NEC*, vol. 5, pp. 320–333; 1950.

The original design was a proposal from Cornell University based on studies by Professors W. E. Gordon, H. G. Booker, and B. Nichols of the School of Electrical Engineering and Professor W. McGuire of the School of Civil Engineering.

II. Summary of Specifications

The reflector will be a 1000-foot-diameter aperture of a spherical bowl with radius of curvature 870 feet and a surface tolerance of +0.1 foot.

The feed support will be a rotating azimuth truss supported on a triangular platform suspended from three towers by prestressed cables (Fig. 1). A movable carriage on the truss plus the rotation of the truss will provide sky coverage within 20° of the zenith. A reference point on the supported end of the line feed is to be positioned and held within a six-inch cube. The pointing and deflection of the line feed combined must not permit a departure of the unsupported end of the feed from the desired radial position of more than five inches.

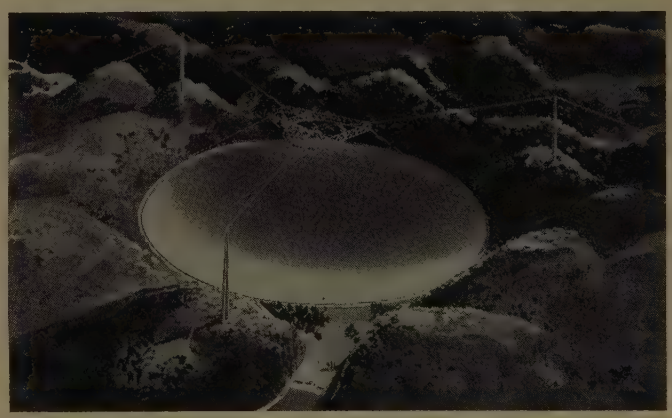

Fig. 1—Artist's conception of the ionospheric radar probe being built near Arecibo, Puerto Rico.

The feed will be dual-polarized at a frequency of 430 Mc, capable of fully illuminating the aperture. This will yield a beamwidth of $\frac{1}{6}$°, a gain of 60 db, sidelobes more than 17 db below main lobe, and polarization crosstalk below 30 db. The bandwidth will be at least 1 Mc, with power handling in one channel of 2.5 Mw peak. The weight will be less than five tons, and the feed will be rigid enough to operate in 30-mile winds and to survive 140-mile winds.

The transmitter will have a peak power output at 430-Mc frequency of 2.5 Mw, and an average power of 150 kw, with pulse-to-pulse stability of 0.2 db; or 100 kw CW power. The frequency stability of the primary source is 2,5 parts in 10^9 over periods from one second

to one hour. The frequency deviation of the RF output from the source frequency will be less than 3 cps. Pulse lengths of 2 to 10,000 μsec will be available with a repetition rate of 1 to 1000 pps. Provision will be made for coherent pulses, pulse shapes square or "Gaussian" and external modulation.

The duplexer will have a recovery time of 150 μsec, receiver isolation of 65 db, and an insertion loss in the receive direction of 0.3 db.

The receiver will be dual-channel at a frequency of 430 Mc, with a noise figure of less than 2 db. RF-IF conversion will be effected at the feed. The 30-Mc IF will pass through 1100 feet of cable to the operations building, where IF amplifiers, bandwidth adjustment, detection, and data recording/processing equipment will be located. The gain stability of the equipment will be 0.2 db. The oscillator frequencies will be derived from the primary source in the transmitter. Data recording will include a range-gated total power receiver for electron density measurements, spectrum analysis for temperature measurements and polarization indication for magnetic field measurements.

III. Ionospheric Measurements

A. The Upper Ionosphere

The first use of the radar will be to observe the nature of the echoes obtained with a beam directed at the zenith. Echoes will be obtained from the bottom of the *D* region up to the high *F* region of the ionosphere. The maximum height from which echoes will be obtainable will depend upon the pulse length, bandwidth, and the integration time used. In and above the *F* region, the strength of the echoes will give the variation of the electron density with height [1], [2]. Continuous observations over a period of time will give the profile of electron density as a function of time of day, season of year, and degree of solar activity.

Measurement of electron density by this method requires either absolute calibration of the radar, for example by means of a spherical satellite, or a local measurement of the maximum electron density in the *F* region by means of a conventional ionospheric sounder. A sounder is available at Ramey Air Force Base, 30 miles west of the Arecibo radar.

Observations will also be made of the frequency spectrum of the returns as a function of height. In the main part of the *F* region, this is expected to take the form of a narrow peak superimposed upon a weaker and broader maximum. There is little doubt that the narrow peak will be observed and that its width will give the thermal velocity of the positive ions. From this, it will be possible to deduce the temperature and the Debye distance as a function of height.

At great heights where the wavelength is of the order of the Debye distance, the spectrum is expected to take a more complicated form. At extremely great heights, the spectrum may take the form of three lines, the outer lines being separated from the central line by the plasma frequency. It is doubtful whether the two outer lines will be observable. If they are, however, their frequencies will give a direct measure of the electron density and their width will be a measure of the electron temperature.

The probable effect of the earth's magnetic field upon the returns from the high ionosphere is unclear. A search will be made for sidebands with a separation equal to the gyromagnetic frequency. An experiment should be carried out to see how the returns depend upon the angle between the axis of the beam and the direction of the earth's magnetic field. If these results provide a means of measuring the strength of the earth's magnetic field, this will then be measured as a function of height and time.

The polarization of the returns as a function of the height from which the return is observed should be examined for Faraday rotation. It is quite likely that, in this way, information will be available concerning the variation of the strength of the earth's magnetic field with height.

B. The Lower Ionosphere

With the beam vertical, measurements can be made of the strength of returns from the *D* and *E* regions of the ionosphere. These returns will include echoes from meteoric ionization. By making studies as a function of time of day and with the beam at various angles to the vertical, it should be possible to subtract out the returns from undiffused meteor trails. The remainder of the echo can then be interpreted as due to fluctuations of electron density. The spectrum of the returns can be observed and the Doppler spread can be interpreted in terms of the fluid mechanical velocities involved. Such observations probably refer to the small scale in the spectrum of fluid mechanical irregularities present in the lower ionosphere. It would be desirable to make observations in such a way that an appreciable portion of the spectrum of fluid mechanical irregularities is observed. This involves observing back scattering either as a function of scattering angle at a fixed frequency, or as a function of frequency at a fixed scattering angle. At 430 Mc the fixed frequency method observations would have to be made with receiving antennas at sites other than Arecibo.

C. Ionospheric Drifts

By maintaining the axis of the beam at a fixed angle to the vertical and scanning in azimuth, ionospheric drift should produce a sinusoidal variation of Doppler shift. From this the magnitude and direction of the horizontal drift of the irregularities responsible for the returns can be deduced. With the beam at an angle of 17° off the zenith, a horizontal drift of 10 meters per second would produce a maximum Doppler shift of 10 cps at 430 Mc.

IV. Capabilities in the Solar System

A. Planetary Observations

The power of the Arecibo radar at 430 Mc will be some 43 db above that of the Millstone radar with which echoes from Venus have already been observed [7]. There will be no difficulty therefore in obtaining echoes; 5 msec pulses could be used, transmitted with a repetition time of approximately 80 msec for periods of several minutes, but less than the radar transit time. The received signals would be recorded in digital form on tape and subsequently analyzed with an electronic computer.

In addition to obtaining echoes from Venus, it will be possible to obtain a fine range discrimination, dividing the planet into 10 or more range rings. The scattered power in each of these rings can then be measured separately for one angular position of the planet. Unless the surface of Venus is of great uniformity (if, for example, it were covered entirely with ocean), such a measurement will show the presently unknown rotation speed of Venus and the degree of roughness in the various discriminable range zones. Much information can be gathered concerning the nature of the planet's surface. If, for example, such an experiment were carried out with a planet like the earth, it would be possible to discover that a certain fraction of the area, approximately one half, consisted of a much smoother type of surface than the remainder. It would even be possible to observe the variation in the scattering properties of the sea that result from different degrees of storm disturbances on the surface, and through this variability infer the existence of a sea. The existence of solid ground inclined at different angles to the horizontal could be inferred, and the major mountain ranges could be detected.

Similar roughness measurements will be possible for Mars. In that case, it will be possible to observe the correlation between the visible features and the scattering properties. In particular, it will be valuable to know whether the large average inclinations to the horizontal, which are commonly associated with vegetation, occur on Mars and whether they are perhaps associated with the dark areas suspected of being vegetation.

For Jupiter, an approximate knowledge of the reflection coefficient at 430 Mc would serve to define more closely than is possible at present the main features of the Jovian atmosphere and surface. The Arecibo radar performance will suffice to give these data, unless the albedo of the planet is abnormally low.

Ranges to Mars and Venus will be measurable to very high accuracy. Velocity measurements can be made to high accuracy by means of the Doppler shift. These will contribute not only to precise definition of the scale of the solar system, but also to precise knowledge of the planetary orbits. The advance of the perihelion of the inner planet can be checked to great precision when range as well as angle is available, and this is of great consequence as a test of the general theory of relativity and other theories of gravitation.

Many other detailed radar studies of the planets will become possible, but planning studies beyond the observations described will depend, to a considerable extent, on the findings of the first phase of the work.

B. Lunar Observations

The object of obtaining radar reflections from the moon is to discover the reflecting properties and roughness of the lunar surface as measured at the radar wavelength of 70 cm. It will be possible to investigate the different types of lunar ground and to obtain detailed correlation between radar roughness and optical appearance. This is desirable both for eventual lunar exploration and for theories of the formation of the moon.

At 430 Mc, the Arecibo radar will be so powerful that range discrimination can be used limited only by the shortest pulse length that the transmitter will generate. With a beamwidth of $\frac{1}{6}°$ and a range discrimination of perhaps 1 km, it will be possible to measure in detail the correlation between the roughness of the ground and the optical appearance of the moon. The areas of the lunar surface that contribute at any instant to the echoes are in general in the shape of part of a ring. It should be possible to recognize the contribution of optically prominent features such as the more recent craters, for they are likely, in some cases, to make an overwhelming contribution to the particular patch in which they are included. A great deal, therefore, can be learned about the roughness on approximately the scale of greatest interest in planning transport on the moon.

If the gain of the Arecibo radar can be accurately calibrated, for example by the use of a spherical satellite, then the reflection coefficient of the surface material of the moon at 430 Mc can be measured more accurately perhaps than it is at present. This would help to determine some, though not all, of the electrical properties of the lunar surface.

C. Solar Observations

At 430 Mc, the absorption in the solar atmosphere before reflection occurs is very large, making it difficult to estimate the radar performance to be expected. The reflecting surfaces in general will be smooth and scattering will occur only from regions where the surfaces are normal to the direction of observations; that is, from "glints." In disturbed regions on the sun, such glints may, however, be plentiful, much as the glints in which the sun is reflected over a rough sea. If, in such regions of the sun, there are high gradients of electron density so that the attenuation is not too high, observable reflections may occur. The magnitude, angular extent and, especially, the time variation in the Doppler shifts associated with such reflections would contribute greatly to our present knowledge of the solar atmosphere.

The reflection of a 430-Mc wave from the sun is pre-

dicted by Cohen [8] to occur from levels sufficiently high so that severe absorption does not take place. In the presence of a magnetic field of the order of 140 gauss, he predicts an echo some 3 db greater than from Venus at closest approach, assuming similar reflectivities for the two bodies. The Arecibo radar will have sufficient power to see such a signal against the high background noise of the solar cloud.

D. Hydromagnetic Disturbances and Shock Waves

The manner in which the Arecibo radar might be able to detect the passage of a hydromagnetic wave or shock is by recording the increase of electron density averaged over the volume determined by the beamwidth and pulse length. This volume is of the order of one cubic kilometer at a height of 100 km. It is clear therefore, that the radar is most likely to see disturbances on a scale of the order of 1 km or larger.

The radar can be regarded as a pressure-sensitive microphone whose sensitive volume is any of the slabs defined by the beamwidth and the pulse length. The sensitivity diminishes with distance and with decreasing electron density. Maximum sensitivity to a fractional change of electron density will lie between 100 and 300 km and will amount to about one part in 300.

It should be noted that, while waves and shocks in the upper ionosphere are likely to be hydromagnetic in character and to concern only the ionized constituents of the atmosphere, in the lower ionosphere, waves and shocks are more likely to be of the type encountered in conventional fluid dynamics.

The present-day interpretation of magnetic storm phenomena implies rapidly-changing electron densities by amounts of the order of a few per cent for big storms. The Arecibo radar should, therefore, have no difficulty in detecting these phenomena. It will be important to correlate these ionospheric observations with magnetometer observations made at ground level. It is expected, however, that use of the magnetic observatory at San Juan will be adequate for this purpose. The interpretation of a number of known types of fluctuations on ground level magnetometers may be simplified by ionospheric observations made by the Arecibo radar.

The natural background of disturbances due to rapid hydromagnetic waves is not well known. It is clear that magnetic disturbances that have been recorded up to a frequency of $\frac{1}{10}$ cps are associated with such waves in the upper ionosphere, but no work exists at present that indicates the magnitude and localization of the density changes that are involved.

An experimental determination of the background level from natural causes of the density fluctuations at each height will be essential to give estimates of the measurable effects resulting from explosive disturbances at various altitudes and distances. It will also be possible then to give an estimate of the distance over which the shock wave from a high-velocity object, such as a missile, will give a sufficiently marked change in the electron density.

Hydromagnetic shock waves propagating in the space of the solar system may have fronts as narrow as 1000 km or so. If, across such a front, the electron density changes abruptly from a low value to one of the order of 10^3 or 10^4 per cubic centimeter, then this should lead to detectable effects with the Arecibo radar in some geometric circumstances. Such shock waves are of great consequence in the dynamics of the plasma of the solar system, and every effort should be made to detect them. In this connection, one is reminded of the long-delay radio echoes which appear to have been observed on occasion in the past and for which no explanation exists as yet [9]–[11].

E. Cislunar Ionization

Radar echoes from the moon suffer Faraday rotation of the plane of polarization. A good deal of this rotation is associated with the earth's ionosphere. In the light of the observations already suggested, particularly those made in Section III *A*, the effect of the earth's ionosphere should be known up to a considerable height. By subtracting the effects of the known ionosphere from the observed Faraday rotation on lunar echoes, it should be possible to make deductions about the remaining ionization out to the moon's orbit.

V. Radio Astronomical Capabilities with Initial Facilities

A. Radio Emission from Planets

Emission from the planets at sufficiently high frequencies consists of thermal radiation. Thermal radiation has already been detected from Venus, Mars, and Saturn [12], [13]. Bursts of radiation have been detected from Jupiter [14], and there is clear evidence that there is a nonthermal component in the radiation from the planet.

The temperature derived from thermal radio measurements agree reasonably well with the infrared values except for Venus, where the radio temperatures are substantially higher. These radio measurements are very important for the study of the Venusian atmosphere, and they should be extended as much as possible. The Arecibo dish should be able to observe Venus at 430 Mc and this will greatly extend the known spectrum of Venus.

B. Radio Emission from True Stars

The popular term "radio star" is a misnomer, for the sun is the only true star that has ever been seen in the radio spectrum. The Arecibo dish, however, will provide so much sensitivity that a search for radio emission from stars will be worthwhile. Assuming that the minimum sensitivity for the Arecibo dish is 10^{-27} watts at 100 Mc, and since the flux from the quiet sun at 100 Mc is 5×10^{-21} watts, the quiet sun would be marginally detectable if it were 450 times farther away. The nearest

star, however, is 10^6 times farther away. We expect therefore, that any signals received will be nonthermal in origin; probably they will be like Type II solar bursts.

C. Survey of Radio Sources

There is some disagreement between surveys of radio sources in England and in Australia. The latitude of the Arecibo site is such that a survey conducted at Arecibo would overlap both the English and the Australian surveys and could thus play an important role in resolving the discrepancies.

VI. Radio Astronomical Capabilities with Additional Facilities

It would be of great interest to perform most of the experiments and observations already listed at some different frequency, such as 40 Mc. Additional receiving equipment would also permit the performance of the following interesting experiments.

A. Study of Spectrum and Polarization of Solar Bursts in the Frequency Band 10–20 Mc

Study of solar bursts in the frequency band 10–20 Mc would give important information on the outer corona, but the use of these frequencies is now difficult because of interference caused by oblique scattering from the ionosphere. The narrow beam of the Arecibo system could give it a significant advantage over an interferometer in rejecting this type of interference.

B. Measurements of the Spectrum and Polarization of Bursts from Jupiter in the Frequency Band 15–25 Mc

In connection with the study of bursts from Jupiter, a measurement of spectrum and polarization should be made in the frequency band 15–25 Mc. Approximately this frequency band should be used, since it is known that the spectrum decreases rapidly with frequency from 18–22 Mc.

C. Two-Wavelength Comparison of Radio Sources

It is not known, at present, how many different classes of sources are involved in the multitude of radio sources detected thus far. An analysis of the radio spectrum seems a good way to obtain information on this. The argument here is that it is improbable that radio noise generation on enormously different scales and with different physical circumstances would result in similar spectra. It is expected that a two-wavelength comparison would suffice to show up different classes if they exist. This experiment would involve the construction of a smaller, accurately-scaled antenna. It is suggested that the frequencies 430 Mc and 108 Mc be used.

D. Interferometric Observations

Use of an interferometer would permit an investigation of the lunar surface on an extremely small scale. It would be possible to combine the two dishes of the previous experiment to form an interferometer. However, the interferometer does not necessarily have to be located at Arecibo.

E. Observations Associated with Deep Space Probes

A satellite would be in the narrow beam of the Arecibo radar for an extremely short period of time. The rates of change of angular position of a deep space probe would be much smaller, so that the Arecibo radar should be able to perform a function similar to that of the Jodrell Bank dish in connection with Pioneer V.

F. Scattering from Field-Aligned Irregularities

Many observations have been made under both auroral and nonauroral conditions of scattering from the ionosphere which appears to come from irregularities aligned along the earth's magnetic field [15]. Among such observations are those of forward scatter in the southwestern United States at 200 Mc [16]. The physics of the irregularities involved is not yet understood, and additional observations of this phenomenon would be very worthwhile. Since the beam of the Arecibo radar cannot be directed normal to the magnetic field, receiving equipment would have to be set up at locations that satisfy the requirement of specular reflection with respect to the magnetic lines of force.

G. Hydrogen-Line Observations

If at least a part of the big dish turns out to be good enough for use at the hydrogen-line frequency of 1420 Mc, a substantial program of observations at that frequency could be made.

H. Light of the Night Sky

The comparatively inexpensive equipment needed for measuring the light of the night sky should be installed at Arecibo for purposes of correlation with other ionospheric observations.

VII. Acknowledgment

The following organizations have contributed to the design and are participating in the construction of the radar.

Center for Radiophysics and Space Research, Cornell University.

Electronics Research Directorate, Air Force Cambridge Research Laboratory.

Joint Venture of Von Seb Inc.; Developmental Engineering Corporation; Severud-Elstad-Krueger Associates; Praeger-Kavanagh (design and field supervision during construction of antenna reflector and feed support).

Technical Research Group (antenna feed).

Levinthal Electronic Products, Inc. (transmitter).

U. S. Corps of Engineers (buildings, roads, utilities).

Many individuals, both in the organizations listed above and in other organizations, have contributed to the design and are contributing to the construction. The list is too long for inclusion here.

The material in this paper was developed by staff members of the Center for Radiophysics and Space Research (H. G. Booker, M. H. Cohen, J. P. Cox, T. Gold, W. E. Gordon, L. M. LaLonde, B. Nichols, E. L. Resler, Jr., and E. E. Salpeter). The task of the authors has been largely editorial.

Bibliography

[1] W. E. Gordon, "Incoherent scattering of radio waves by free electrons with applications to space exploration by radar," Proc. IRE, vol. 46, pp. 1824–1829; November, 1958.
[2] K. L. Bowles, "Observations of vertical incidence scatter from the ionosphere at 41 Mc/s," *Phys. Rev. Lett.*, vol. 1, pp. 454–455; December, 1958.
[3] J. P. Dougherty and D. T. Farley, "A theory of incoherent scattering of radio waves by a plasma," to be published *Proc. Roy. Soc. (London)*.
[4] T. Laaspere, "On the effect of a magnetic field on the spectrum of incoherent scattering," to be published in *J. Geophys. Res.*
[5] E. E. Salpeter, "Scattering of radio waves by electrons above the ionosphere," *J. Geophys. Res.*, vol. 65, pp. 1851–1852; June 1960.
[6] J. A. Fejer, "Scattering of radio waves by an ionized gas in thermal equilibrium," *Can. J. Phys.*, vol. 38, pp. 1114–1133; August, 1960.
[7] R. Price, P. E. Green, Jr., T. J. Goblick, Jr., R. H. Kingston, L. G. Kraft, Jr., G. H. Pettengill, R. Silver, and W. B. Smith, "Radar echoes from Venus," *Science*, vol. 129, pp. 751–753; March, 1959.
[8] M. H. Cohen, "High-frequency radar echoes from the sun," (Correspondence), Proc. IRE, vol. 48, p. 1479; August, 1960.
[9] C. Stormer, "Short-wave echoes and the Aurora Borealis," *Nature*, vol. 122, p. 681; November, 1928.
[10] Balth. van der Pol, "Short-wave echoes and the Aurora Borealis," *Nature*, vol. 122, pp. 878–879; December 8, 1928.
[11] E. V. Appleton, "Short-wave echoes and the Aurora Borealis," *Nature*, vol. 122, p. 879; December 8, 1928.
[12] C. H. Mayer, T. P. McCullough, and R. M. Sloanaker, "Observations of Venus at 3.15-cm wave length," *Astrophys. J.*, vol. 127, pp. 1–10; January, 1958.
[13] C. H. Mayer, T. P. McCullough, and R. M. Sloanaker, "Observations of Mars and Jupiter at a wave length of 3.15 cm," *Astrophys. J.*, vol. 127, pp. 11–16; January, 1958.
[14] A. G. Smith and T. D. Carr, "Radio-frequency observations of the planets in 1957–1958," *Astrophys. J.*, vol. 130, pp. 641–647; September, 1959.
[15] B. Nichols, "Evidence of elongated irregularities in the ionosphere," *J. Geophys. Res.*, vol. 64, pp. 2200–2202; December, 1959.
[16] J. L. Heritage, S. Weisbrod, and W. J. Fay, "Evidence for 200-megacycles per second ionospheric forward scatter mode associated with the earth's magnetic field," *J. Geophys. Res.*, vol. 64, pp. 1235–1241; September, 1959.

The Stanford Microwave Spectroheliograph Antenna, a Microsteradian Pencil Beam Interferometer*

R. N. BRACEWELL†, fellow, ire, and G. SWARUP†

Summary—**A pencil beam interferometer has been constructed at Stanford, Calif., with multiple beams of 3.1 minutes of arc width to half power (0.8 microsteradian). It is composed of two equatorially-mounted, 16-element, Christiansen arrays of 3-m paraboloids, each 375 feet long (1255 wavelengths at a wavelength of 9.1 cm). The half power beamwidth of the fan beam of a single array is 2.3 minutes of arc. To form the pencil beam, the two arrays are switched together as in a Mills cross. Frequency range is from 2700 to 3350 Mc. Phase adjustment and monitoring are handled by a new technique of modulated, weakly reflecting gas-discharges maintained at the focus of the paraboloids. Television-type scanning yields maps of the sun (spectroheliograms) revealing fine details of the microwave source regions in the chromosphere and corona. All the transient bursts and a large fraction of the steady solar emission at 9.1 cm prove to originate in a small number of highly compact centers, whose brightness temperatures may exceed 5×10^5°K. The sensitivity of the instrument also allows the thermal emission from the moon (250°K) and a number of galactic and extragalactic sources to be studied with high angular resolution. Illumination of the moon by terrestrial radar can be detected. The pencil beam interferometer furnishes the finest beams currently available from pencil beam antennas of any type. Examination of the fundamentals of extracting high resolution details of a source from its radiation field indicates the fitness of pencil beam interferometers, incorporating steerable multielement arrays, for future development to higher resolving power. Adequate technique of phase preservation over wide spacings is available.**

* Received by the PGAP, October 10, 1960. This research was supported by the Office of Sci. Res. of the U.S.A.F., Air Res. and Dev. Command, under contract AF 18(603)-53.
† Radio Astronomy Inst., Radioscience Lab., Stanford University, Stanford, Calif.

I. Introduction

By 1954 it had become clear that a new type of pencil beam instrument could be built by combining the principles of the Christiansen array and the Mills cross. Practical feasibility of the one had been demonstrated by Christiansen and Warburton [1], [2] on a large, albeit economical, multi-element array, and of the other by Mills and Little [2]–[5] on a scale model designed for the purpose. It was therefore possible to plan an ambitious microsteradian pencil beam project with confidence that the basic principles were sound, an important prerequisite, because in each case objections had been entertained that could only be removed by test. The fruits of the new project would be microwave spectroheliograms, built up television-wise by scanning the sun with the pencil beam. During the tenure of a visiting professorship in the academic year 1954–55, in the Astronomy department of the University of California, Berkeley, the senior author studied the design of an instrument for a wavelength of about 10 cm. Execution of the design was proposed for Sydney (where, however, it was decided to embark on a different but similar project) and for California. The proposal [6] to build the present instrument was submitted to the Office of Scientific Research of the United States Air Force in September, 1955.

The purpose of the instrument was to study the chromospheric microwave emission with a view to ascertaining physical conditions in an optically transparent region which is the seat of important solar disturbance phenomena. Here, in the transition between the corona and the outer chromosphere, occurs the changeover between the steady optical sun and the spectacularly variable meter-wave sun. While the meter-wave radio emission is in itself fascinating, it is a secondary phenomenon associated with ejection of matter from lower levels. An attack on the very little known outer chromosphere therefore offered the possibility of coming to grips with the central problem of solar activity. In fact, as now appears, the maximum of emission from the active centers occurs around the selected wavelength of 9 cm; at shorter wavelengths their lack of opacity renders them less conspicuous, and at longer wavelengths the opacity of the overlying corona obscures them. In the vicinity of 9 cm the active centers have been up to 30 times brighter than the quiet sun.

Section II gives the principle of the instrument and Section III the basic design parameters. Section IV gives physical details of the installation. Section V discusses the vital item of technique on which the whole possibility of adjusting large arrays depends, namely the measurement, maintenance, and control of relative phase over great distances. Section VI gives samples of observations to illustrate the functioning of the instrument; their astronomical significance will be discussed elsewhere. Finally, in Section VII the significance of the instrument for antenna practice is discussed, with attention to possible future development to even greater resolution.

II. Basic Principle

Let an even number N of isotropic point sources be arranged in a straight line, each spaced at a distance d from the next. The field radiation pattern of one pair of identically excited sources at a distance nd apart will be

$$\exp\left[i\frac{2\pi}{\lambda}\,\tfrac{1}{2}\,nd\sin p\right]+\exp\left[-i\frac{2\pi}{\lambda}\,\tfrac{1}{2}\,nd\sin p\right],$$

where λ is the wavelength, and $nd \sin p$ is the path difference between two rays that make an angle p with the plane perpendicular to the line of the array. This expression is equal to $2\cos[(\pi/\lambda)\ nd \sin p]$. If now the whole array is considered to be composed of $\frac{1}{2}N$ symmetrical pairs, all equally excited, the field radiation pattern is proportional to

$$2\sum_{n=1,3,5\cdots}^{N-1}\cos\left[\frac{\pi}{\lambda}nd\sin p\right].$$

This is the Fourier series for a periodic function of $\sin p$ consisting of sharp fringes of the form

$$\frac{\sin\left(N\pi\dfrac{d}{\lambda}\sin p\right)}{\pi\dfrac{d}{\lambda}\sin p},$$

repeated with alternation of sign at intervals λ/d. In Fig. 1 this periodic function is plotted for $N=16$ and $d/\lambda=83.68$. The abscissa is 3438 $\sin p$, which is approximately equal to the angle between the ray direction and the median plane, measured in minutes of arc.

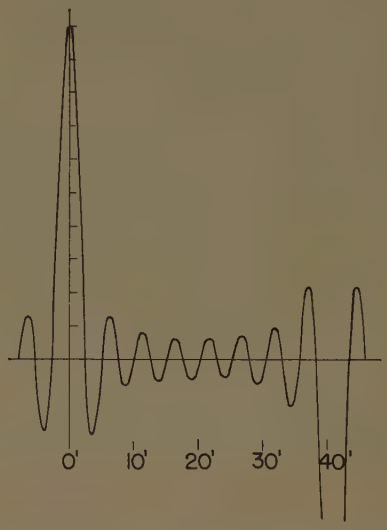

Fig. 1—Field radiation pattern of 16-element array (theoretical).

If now we sum the series by noting that the N exponential terms form a geometrical progression, we obtain the following closed expression for the field radiation pattern:

$$\frac{\sin\left(N\pi\dfrac{d}{\lambda}\sin p\right)}{\sin\left(\pi\dfrac{d}{\lambda}\sin p\right)}.$$

Now if the isotropic point sources are replaced by identical extended elements, the field radiation pattern of the whole is derived from the above by multiplication with the field pattern of a single element. The power pattern is the squared modulus.

It will be seen that when the individual elements are driven so as to track an object moving across the sky, the radiation pattern is the product of a moving envelope and the fixed pattern that is periodic in $\sin p$. Thus the object will be scanned by the sharp fringes of successive order, even though the individual antennas are tracking it.

The potential fringes form small circles on the sky, coaxial with the line of the array, in our case 167 in number (about 160 usable), and may be evoked in any neighborhood where the elements are (Fig. 2).

When one array is crossed with another the principle of the Mills cross enters. Let the voltages received by each array separately from a point source in the direction (θ, ϕ) be respectively $V_1(\theta, \phi)$ and $V_2(\theta, \phi)$. When the two arrays are connected together in phase, the voltage reception pattern of the combination is $V_1(\theta, \phi) + V_2(\theta, \phi)$, and if then a half wavelength of cable is inserted into the second arm before connecting the two, the pattern is $V_1(\theta, \phi) - V_2(\theta, \phi)$. The available power is

$$[V_1(\theta, \phi) \pm V_2(\theta, \phi)][V_1(\theta, \phi) \pm V_2(\theta, \phi)]^*,$$

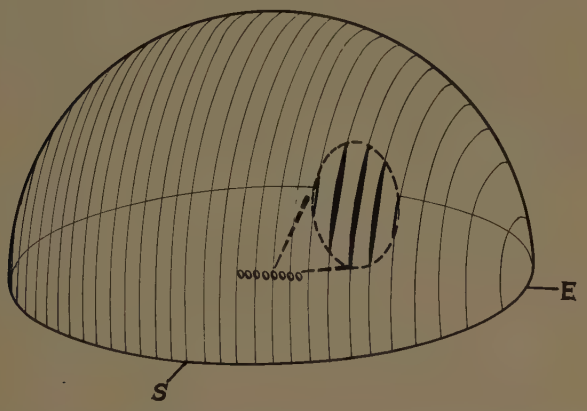

Fig. 2—Potential fringes (small circles) of a multi-element array and effective fringes (those enclosed within the outline representing the pattern of a single element).

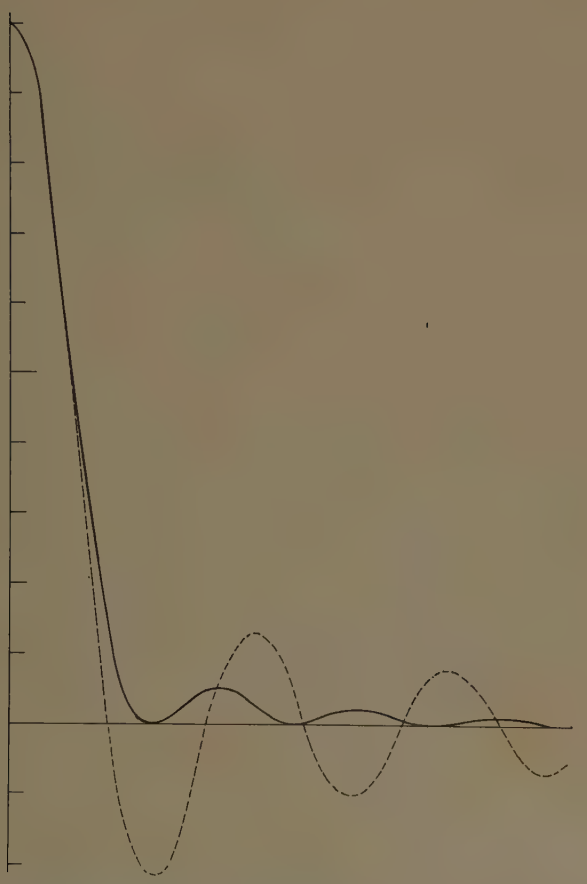

Fig. 3—Skew (heavy curve) and principal (broken curve) sections through the beam of an untapered cross of point sources.

the plus sign referring to the first condition and the minus sign to the second. If now the half wavelength is switched in and out at an audiofrequency (in our case 450 cps), and the receiver pays attention only to the alternating component of the available power, the response of the system as a function of direction will be the alternating part of the previous expression, namely

$$V_1(\theta, \phi)V_2^*(\theta, \phi) + V_2(\theta, \phi)V_1^*(\theta, \phi).$$

Thus the power response of the system to a point source is the scalar product of the voltage responses of the component arrays.

If the arrays produce sharp fringes, the net power response when they are switched together consists of pencil beams at the fringe intersections. The principal sections through the beam, those taken in planes containing one or other of the arrays, have the character of Fig. 1; *i.e.*, the power response may contain the negative lobes characteristic of a field radiation pattern. Sections through the beam in other directions tend towards shapes more usually associated with power patterns, *e.g.*, the 45° section is shown in Fig. 3 (heavy curve) in comparison with the principal section. The magnitude of all the sidelobes is shown in Table I which represents one complete quadrant of one periodic cell of the reception pattern; the ruled lines are null loci. The concentration of the field-type pattern along the principal sections (bold type) is well shown.

Useful alternative explanations that may be given in terms of sensitivity to spatial Fourier components of a source distribution [7], [8] should be referred to for dealing with refinements.[1]

[1] Such as, for example, the question of suitable array tapering, which is still under discussion.

TABLE I

LOBE MAXIMA FOR AN UNTAPERED CROSS OF POINT SOURCES
(PRINCIPAL SECTIONS IN BOLD TYPE)

$\bar{6}$	1	$\bar{1}$	$\frac{1}{2}$	$\overline{\frac{1}{2}}$	$\frac{1}{2}$	$\overline{\frac{1}{2}}$	$\frac{1}{2}$
7	$\bar{1}$	1	$\overline{\frac{1}{2}}$	$\frac{1}{2}$	$\overline{\frac{1}{2}}$	$\frac{1}{2}$	$\overline{\frac{1}{2}}$
$\bar{7}$	2	$\bar{1}$	$\frac{1}{2}$	$\overline{\frac{1}{2}}$	$\frac{1}{2}$	$\overline{\frac{1}{2}}$	$\frac{1}{2}$
8	$\bar{2}$	1	$\bar{1}$	$\frac{1}{2}$	$\overline{\frac{1}{2}}$	$\frac{1}{2}$	$\overline{\frac{1}{2}}$
$\overline{10}$	2	$\bar{1}$	1	$\bar{1}$	$\frac{1}{2}$	$\overline{\frac{1}{2}}$	$\frac{1}{2}$
13	$\bar{3}$	2	$\bar{1}$	1	$\bar{1}$	1	$\bar{1}$
$\overline{22}$	5	$\bar{3}$	2	$\bar{2}$	2	$\bar{1}$	1
100	$\overline{22}$	13	$\overline{10}$	8	$\bar{7}$	7	$\bar{6}$

III. Basic Design Parameters

As a minimum resolving power for revealing detail on the disk of the microwave sun, which has a diameter of about 33 minutes of arc, a beamwidth of 3 or 4 minutes of arc is a reasonable objective. This is about one milliradian. To obtain such a beamwidth an antenna aperture of about 1000 wavelengths is needed, say 100 m at a wavelength of 10 cm. Over the whole of this aperture the excitation has to be maintained constant in amplitude and phase to known tolerances [7], [9], [10] which, in the case of phase, require electrical and mechanical stability to a small fraction of a wavelength. The necessary stability of one part in 10^4 or 10^5 could be achieved only with great effort if the aperture had to be moved bodily to track the sun, especially in two dimensions.

The essence of Christiansen's multi-element interferometer is that the aperture is split into an array, each element of which tracks separately on its own modest mount. However, in doing this, one introduces a periodic variation along the antenna that results in the appearance of multiple beams; if there are N elements in the array, the multiple beams will appear at intervals of about N beamwidths.

The number of elements is consequently set by the requirement that the spacing of the multiple beams shall exceed the diameter of the object to be studied. Under this condition there can never be more than one beam on the object at any time and so the multiple beams can cause no confusion. With a 3 minute beam and a 33 minute sun (36 minutes when the spread due to antenna smoothing is allowed for) one could split the 1000-wavelength array into 12 elements. To allow for deterioration of the beam from various causes a narrower beamwidth was aimed for, however, and 16 elements were adopted.

The size of the individual elements is limited to rather less than the spacing of the elements; in fact unless there is room to spare, the elements will shadow each other when pointing out of the median plane (the plane perpendicular to the line of the array). The elements must be large enough that their combined collecting area is adequate for reception of the part of the source in the beam. While each element receives radiation from the whole source, the adjustment of the array is such that much of this energy is reradiated by other elements, only the contribution from within the 3-minute beam being delivered to the receiver. Standard spun aluminum paraboloids 10 feet in diameter and with 36 inch focal length were selected, and purchased from the Gabriel Company. Feed horns were designed for conservative illumination with low spillover, circular beam, and wideband match; a reflection-compensating window was incorporated in the prototype which was developed by K.-S. Yang. Prodelin Inc. manufactured the feeds complete with gooseneck waveguide supports.

Table II summarizes the design parameters for each of two identical arrays. Table III presents parameters of other existing multi-element arrays of related types, with literature references for further details.

TABLE II

Basic Design Parameters of Each Array

Latitude	37°24′ N
Longitude	122°11′ W
Elevation	20 m
Slope of north-south array	50.5′ (north end low)
Number of elements	16
Element spacing	25 feet (83.68λ)
Over-all length between centers of end elements	375 feet (1255.2λ)
Operating wavelength (frequency)	9.107 cm (3292.1 Mc)
Beamwidth to half power*	2.3′
Peculiar interval	1.28′
Spacing of beams	41′
Diameter of paraboloid	10 feet
Beamwidth of paraboloid	2.3°
Physical area of array	1257 feet² (117 m²)
Feed horn dimensions	3×4 inches
VSWR	<1.4 from 2700 to 3350 Mc <1.1 at 3292 Mc

* Theoretical value. From observations of the most compact solar spots available so far, it has been verified that the beamwidth is less than 2.5′. Under operation as a cross the half-power beamwidth is 3.1′ (theoretical value; observational verification so far, <3.3′).

TABLE III

Parameters of Existing Multi-element Arrays*

Location	Wavelength/ *cm*	Type of beam	Beam size	Elements		Spacing d/λ	Length $(N-1)d/\lambda$	Mounting	Present sensitivity 10^{26} Wm^{-2} $(c/s)^{-1}$
				N	Description				
Stanford	9.107	Pencil	3.1′×3.1′	16×16	3 m dishes	83.68	1255.2	Equatorial	12
		Fan	2.3′×2.3°	16					
Sydney [11]-[13]	21	Pencil	3′×3′	32×32	5.8 m dishes	58	1800	Equatorial	2000
		Fan	2′×2.5°	32					
Nançay [14]	3.2	Fan	4′×1.7°	16	1.1 m dishes	50	750	Meridian	3000
Nagoya [15]	3.18	Fan	2.25′×1.6°	16	1.2 m dishes	86.05	1290	Equatorial	3000
Nagoya [16]	7.5	Fan	4.5′×4°	8	1.5 m dishes	86.00	602	Equatorial	4000
Ottawa [17]-[18]	10	Fan	1.2′×2°	5	one 46×0.6 m V and four 3 m×2.4 m dishes	450	1800	Meridian	3000
Washington [19]	88	Fan	4.8′×15°	30	Helical antennas	22	640	Meridian	1000
Nançay [20]	177	Fan	3.8′×20°	32	5 m dishes	25	780	Meridian	10
Nançay [21]	177	Fan	7.5′×16°	8	10 m dishes	62	435	Meridian	
Santiago	171	Fan	4′×60°	16	10 yagis	47	700	Meridian	2000

* Other Christiansen arrays are being brought into operation in Berlin, The Netherlands, and the U.S.S.R. The 90-element array at Pulkovo, USSR, which is of a distinct type, is designed for a fan beam 1′×10′ at the zenith at 3 cm [30].

IV. Physical Description

Each element of the array is mounted on a concrete pier that rises 5 feet above ground level (Fig. 4). The piers extend about 8 feet below ground with a diameter of 30 inches. Bolted to the top of each pier is a machined and scribed cast-iron base-plate which was oriented, leveled, aligned and spaced before grouting. On the base-plate is a cannon-shaped housing containing the polar axle ($32\frac{1}{2}\times 3$ inches) and an oil-filled double worm reduction gear box (360:1). Keyed to the polar axle is a yoke carrying the declination axle ($28\frac{1}{2}\times 3$ inches), two castiron brake bands, and a worm box (20:1). Two cast-iron supporting arms keyed to the ends of the declination axle carry an adapting structure that finally bolts to the back-spinning of the paraboloid at four points on a $43\frac{1}{2}$-inch square. The back spinning is a pan that is riveted to the paraboloid on two circles about 68 and 23 inches in diameter. Counterweight arms bolted to the supporting arms give balance about the declination axis and two other counterweights attached to the polar axle bring the center of gravity down onto the polar axis at a point roughly above the pier.

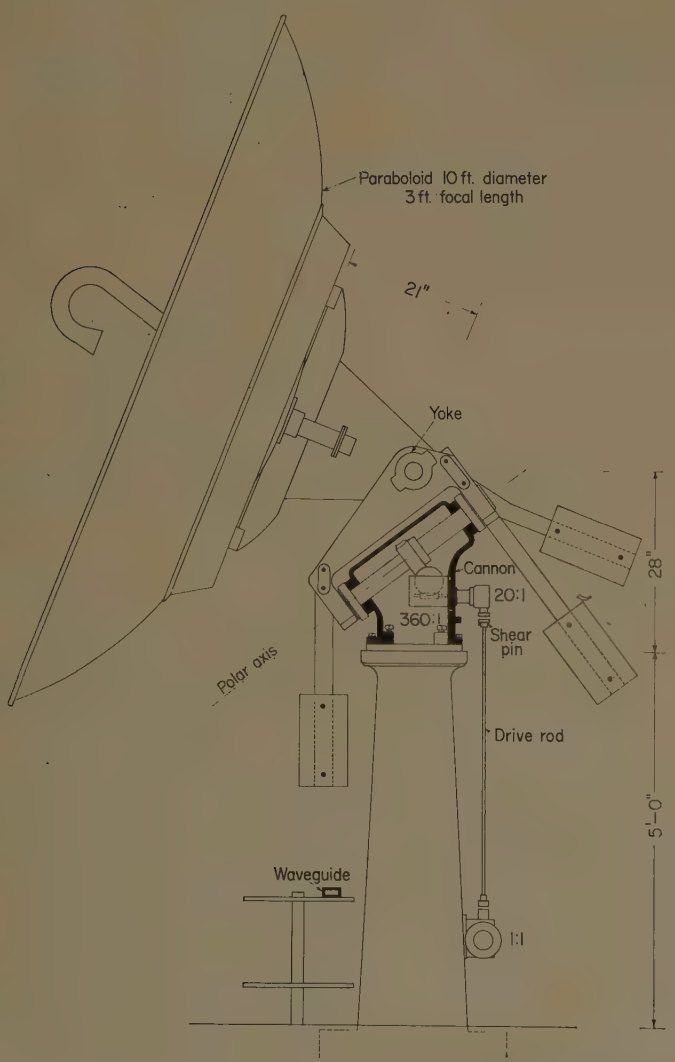

Fig. 4—Equatorial mount for the ten-foot paraboloids.

A mechanical drive system turns all the paraboloids in unison about their polar axes at a tracking rate of $\frac{1}{4}°$ per minute or a slewing rate of 5° per minute. Other rates are available. Two drive shafts, which run the whole length of each array, turn at 5 rpm (tracking) or 100 rpm (slewing) and have flexible couplings and bearings at $12\frac{1}{2}$ foot intervals.

When tracking, all 32 units are turned by a 1500 rpm, 1 hp synchronous motor. The slewing motor is a 1200 rpm, 3 hp induction motor connecting into the drive line through a differential, as shown in Fig. 5. The synchronous drive is accurate enough for tracking the sun, but evidently, whenever the slewing motor is used, absolute position is lost. For this, and other reasons, a further "correcting motor" is connected into the drive line.

If, during the course of the day, it is necessary to bring the antenna onto the sun, one first slews roughly into position and then turns on the tracking motor. A synchronous clock, that is never disconnected from the electrical supply, remembers where the sun should be. A subsidiary shaft S says where the antenna actually is, and a differential D_3 shows the discrepancy with the clock shaft on a counter. A switch on the counter turns on the correcting motor in the correct sense to cancel the discrepancy. The antenna is thus brought automatically onto the sun, after which the tracking

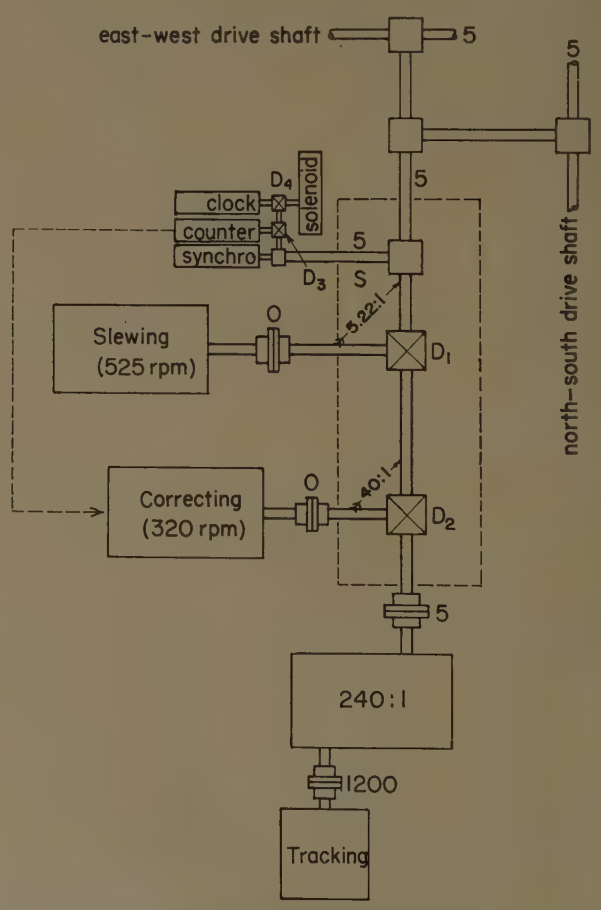

Fig. 5—Mechanical drive system. Numbers on shafts give speeds in rpm during tracking.

motor continues alone; provision is made for automatic slewing back at the end of a run and starting up on the sun the next morning. A synchro-transmitter shown in the figure conveys antenna position to the control console, where a digital indicator shows the "antenna time" (the hour angle at which the antenna is pointed, plus 12 h).

Corrections for equation of time are incorporated manually from the control console by pulsing a rotary solenoid that can insert a lead or lag in the clock shaft through the differential, D_4. The pulses also drive a digital time indicator, and the correct number of pulses has been sent when this indicator shows the sun's meridian transit time at Stanford.

This correction mechanism can also be used for setting on objects with other transit times, and for tracking at nonsolar rates.

The two hour-angle limit switches are located on a dummy polar axle geared to the subsidiary shaft S. They are readily accessible for resetting for special purposes. Two further limit switches, defining the range of safe operation, are actuated directly by the polar axle within the cannon of west no. 1 unit and cannot easily be changed; they are set to ± 4 h 20 m. Shear pins on the drive rods of each unit guard against accidents.

V. Phase Technique

The crucial step determining the success of a large array is the adjustment whereby the excitation of each element is brought into the same phase. Each element must also be excited with the same amplitude, but the measurement of amplitude is not especially difficult for a large array except insofar as the number of necessary measurements is large.[2] There is a basic difficulty in phase equalization over long distances, however, because the same absolute precision in fractions of a wavelength is required regardless of distance. Measuring to an accuracy of 1 mm in 50 m, *i.e.*, one part in 50,000, demands careful attention to mechanical stability, thermal effects, frequency stability, and all measurement procedures.

Swarup and Yang [22] have described the method originally used to bring the arms of the array into phase adjustment. The method which has subsequently proved most satisfactory [23] is to introduce a weakly reflecting, modulated gas discharge at the mouth of the horn of the element under test. When a test signal is sent out from the receiver room a faint, but modulated, reflection is returned from the electron cloud in the discharge. The modulation frequency component in the receiver output can be cancelled by combining the reflection with a strong quadrature reference signal. By sliding a probe in a slotted section of waveguide one finds a null setting that indicates the phase path to the discharge. The method has adequate accuracy and sensitivity for the present purpose, but is also susceptible of refinements suiting it to more extreme applications in the future. Phase path measurements through space by Swarup and Yang [24] show that the figure of giant paraboloids could be continuously monitored without further ado.

Assuming that the phases of both arrays have been adjusted, we would find the potential pencil beams at the intersection of the fringes of the arrays. The fringes of the east-west array lie in the directions where the path difference is an integral number of wavelengths m, *i.e.*, where

$$d \sin p = m\lambda.$$

In this equation, d is the spacing of the elements and p is the co-distance from the west point of the horizon. The number m is the order of interference of the fringes of the east-west array; the zero order fringe lies in the meridian plane. The fringes of the north-south array lie where

$$d \sin q = n\lambda.$$

Here q is the co-distance from the south point of the horizon, and n is the order of interference of the fringes of the north-south array, being zero on the east-west vertical circle (the prime vertical).

In terms of hour angle H and declination δ, coordinates forced on us by the earth's rotation,

$$\sin p = \sin H \cos \delta$$

$$\sin q = -\cos \Lambda \sin \delta + \sin \Lambda \cos \delta \cos H,$$

where Λ is the observing latitude.

To carry out scanning operations, the location of the fringes may be shifted by introducing a linear phase gradient along the north-south arm by means of phase shifters. If the phase gradient is such that the phase path from each element to the receiver exceeds that from its neighbor to the north by Φ meters, then the fringes of the north-south array will be displaced towards the south in accordance with the relation

$$d \sin q = n\lambda + \Phi.$$

Hence the location of the pencil beam of order (m, n) will be given by

$$\frac{m\lambda}{d} = \sin H \cos \delta,$$

$$\frac{n\lambda + \Phi}{d} = -\cos \Lambda \sin \delta + \sin \Lambda \cos \delta \cos H.$$

The following useful version of the formulas gives the coordinates of the pencil beam of order (m, n);

[2] When a signal generator is connected in place of the receiver, reflected waves will return from the elements themselves (due to mismatch) and from transmission system components, such as tee junctions. Some of this energy returns to the generator, but the bulk of it is redistributed among the elements, thus upsetting the amplitude of excitation. If the tee junctions are replaced by hybrid junctions with a matched termination on the fourth port, all returning reflections are absorbed. Excitation errors due to mismatch are then less.

$$\delta = \sin^{-1}\left\{\left[1 - \frac{m^2\lambda^2 + (n\lambda + \Phi)^2}{d^2}\right]^{1/2} \sin \Lambda - \frac{n\lambda}{d}\cos \Lambda\right\}$$

$$H = \sin^{-1}\left(\frac{m\lambda}{d}\sec \delta\right).$$

Values of δ and H for various values of (m, n) have been tabulated on an electronic computer.

To track with a pencil beam on a fixed declination as time elapses, one must vary Φ between scans. As an example, the required change $\Delta\Phi$ over an interval ΔH is given, on differentiation, by

$$\Delta\Phi = -d \sin \Lambda \cos \delta \sin H \, \Delta H.$$

To scan in television fashion, along parallel circles of declination, an additional change in Φ must be inserted between scans, according to the required spacing in declination.

We know by the discrete interval theorem (Bracewell and Roberts [25], Bracewell [26]) that the brightness distribution across the sun is completely determined by parallel scans spaced a distance $\lambda/Nd \cos q$ apart. Thus one can make N independent scans per unit of n, and provision must therefore be made for N path length increments Φ up to one full wavelength.

Of the various ways of inserting phase gradient we have chosen to place separate phase shifters at each element. They must then insert phase at rates proportional to $\pm 1, \pm 3, \pm 5, \cdots \pm 15$, in order to produce equal increments between one element and its neighbor.

The phase shifter is simply a piece of dielectric about 1 m long that can be rotated into and out of the strong electric field along the center line of the waveguide. The difference in phase delay between the extreme positions is exactly one wavelength. The dielectric is turned by a pulsed rotary solenoid through a gear that inserts the required factor mentioned above. A cam gives a linear relationship between the number of pulses to the solenoid and the amount of phase. Eighty pulses insert one half cycle into Number 1 unit, which changes Φ by one wavelength. At noon, five minus pulses (*i.e.*, 75) would be needed between successive scans, but as the sun begins to cross the fringes, the number of pulses alters, following a simple program. For example, for a map beginning at 11 hours 0.9 minutes 37 seconds at the equinox, the program is 9, 9, 8, 8, 7, 6, 5, 5, 5, 4, 2, 3, 2, 1, 1, 0, 79, 79, 77, $\cdots$, 2.79 minutes elapsing between each batch of pulses. The program can be punched on a card, inserted in a matrix switch on the control console, and followed automatically by a timer, or the program can be sent out manually. It is also practical to take maps with the unequal scanning intervals that result when the phase shifters are not used.

VI. Operational Behavior

Records taken with a single arm of the cross show that the design parameters have been essentially realized. Very sharp multiple beams have been observed, up to about the 80th order, located at equal intervals of sin p and in the calculated positions within about one minute of arc. A record taken tracking Cassiopeia A shows that the effective area remains substantially constant out to large hour angles, but that the beamwidth increases progressively. The precise value of the beamwidth has not yet been measured for want of a source of sufficiently small angular diameter. However, from the fact that ten or more maxima and minima have on occasion been observed within a half degree of the sun's diameter, it is clear that the beamwidth is approximately as planned. Occasionally, compact sources appear on the sun that permit an upper limit to be set to the beamwidth; from such cases we have concluded that the half power beamwidth of the east-west array is less than 2.5 minutes of arc. The expected value is 2.3 minutes.

Fan-beam scans of the sun are shown in Fig. 6. The repetitive character of the record is apparent and it will be seen that the repetition interval just exceeds the width of the sun. A transient event accompanying a solar flare may be seen taking place in one of the active centers.

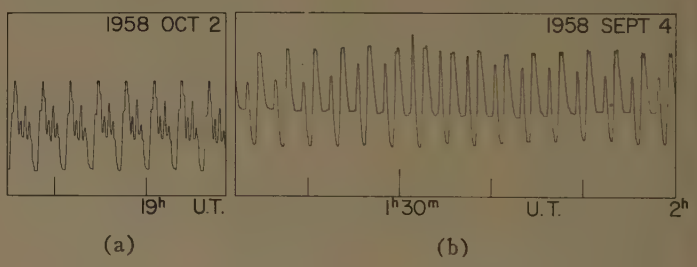

Fig. 6—Fan beam scans of the sun; (a) showing much fine structure, (b) showing a burst in one active center.

The effective area of the east-west array is now about 15 m²; *i.e.*, it is equivalent to a single paraboloid of about 6 m diameter. With the sun receiver, whose noise temperature is about 1500°K, this means that four or five of the brightest discrete sources, and the moon, have proved observable. Since at present the transmission system has an efficiency of only 25 per cent, there is a considerable margin in hand for high resolution studies of nonsolar sources, which can be exploited with superior receivers.

When the instrument is operated as a cross and used to map the solar emission, again it is apparent that the design has been realized. The procedure of phase adjustment is more critical for the cross than for the single arm, (Swarup and Yang [23]); and in fact the quality of the maps is a rather sensitive indicator of maladjustment. Fig. 7 shows a sample map, together with one of

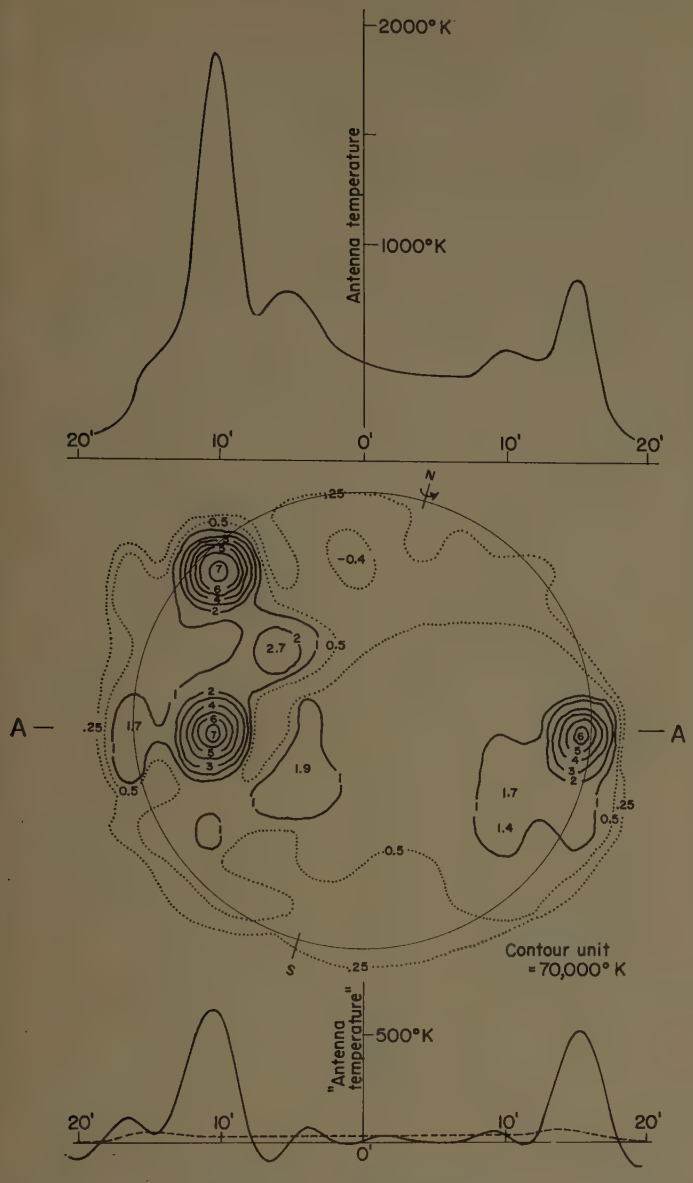

Fig. 7—A map of the 9-cm solar emission prepared from pencil beam scans such as that along A–A (below), together with a fan beam scan (above). May 30, 1960, 19–20h u.t.

the pencil beam scans and a fan beam scan taken after the map was completed. The extent to which the 9 cm emission is dominated by the active centers is much clearer from the maps than from fan beam scans. Sequences of these maps are being studied to obtain physical data on the emissive regions at the levels from which the 9 cm radiation comes.

A record of the moon passing through the fan beam, taken with a bandwidth of 300 Mc, is shown in Fig. 8. Sequences of such scans are being studied for evidence of monthly variation by D. Cudaback. Cudaback has also examined the moon under conditions of microwave illumination by a radar transmitter.

VII. Discussion

The instrument described in the preceding pages is significant both for astronomy, to be discussed elsewhere, and for antenna practice, with which we are concerned here. The fierce demand for resolving power, exerted from the beginning by the challenge of radio astronomy, and the competitive international atmosphere in which it flourishes, has called forth tremendous advances in antenna technique, so that at the present time the most refined antennas are those in the hands of radioastronomers. The development has followed several lines. In the category of pencil beam interferometers, to which our instrument belongs, the resolving power is unmatched in other branches of radio science and technology where antennas are used. Even higher resolving power is indeed attainable for special purposes by the techniques of variable-spacing two-element interferometry; but among pencil beam antennas of all kinds, both fixed and steerable, and including millimeter-wave paraboloids, the finest beams are those furnished by pencil beam interferometers.

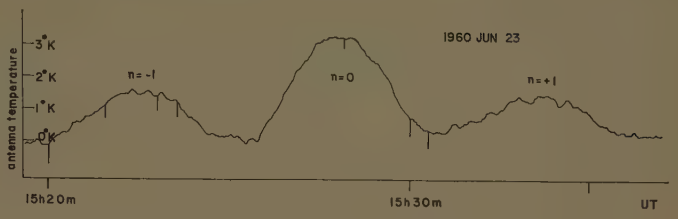

Fig. 8—Record made by D. Cudaback of a lunar passage through the fan beam. The antennas were stationary and a wide band used (300 Mc), so that the scans at $n = \pm 1$ are reduced and dispersed.

The demands of astronomy for resolving power are not satisfied, however. A fruitful approach to the question of resolving fine detail is to contemplate the radiation field on the ground and to ask how the information about the source that produced the field is spread over the ground [27]. Fundamental to the problem are the concepts of *complex coherence* and *principal solution*. If F_1 and F_2 are the field phasors at two points, the complex coherence Γ is defined as the normalized time average of the product $F_1F_2^*$; *i.e.*, $\Gamma = \langle F_1F_2^* \rangle / \langle F_1F_1^* \rangle$, and it depends only on the vector spacing of the two points. One can show [7], [28] that Γ, as a two-dimensional function of vector spacing, is the two-dimensional Fourier transform of the brightness distribution over the source. However, the vector spacings represented within a given antenna system, or accessible by variable-spacing interferometry, cover only a finite area; and the Fourier transform of the part of Γ within this area represents the best approximation to the actual brightness distribution (in the absence of outside information). This distribution, which is encountered in the antenna smoothing problem, is known as the principal solution [7], [25]. (In the presence of errors such that the signal-to-error ratio varies with spacing, as happens when redundant spacings are embraced, there is a modification to be allowed for [29]).

Two-element interferometry, or aperture synthesis, in which the accessible vector spacings are occupied sequentially, can be seen from this standpoint in its

relationship to pencil beam scanning, where the full range of spacings is embraced simultaneously, with much redundancy. The pencil beam interferometer, which is intermediate in character, avoids the slowness of sequential occupation of stations, and is economical as regards redundancy. It profits by the discrete interval theorem for discrete sources [28], in that many spacings may be left unoccupied.

These properties fit pencil beam interferometry, incorporating steerable multi-element arrays, for future progress to higher resolving power; we look forward confidently to the appearance of giant arrays composed of antenna units that are today considered large in themselves. The basic difficulty of coherence measurement, preservation of relative phase over great spacings, is under control by a technique that is not yet strained.

Acknowledgment

Financial support was provided by the Office of Scientific Research of the United States Air Force through the Physics Section under Dr. W. J. Otting. Day to day contact, initially with R. Heer, has been with Paul Johnson; the project has greatly benefited from Johnson's appreciation of the problems and his wise advice. While detailed design was in progress, but before the negotiation of the contract, a welcome grant was furnished by the Research Corporation through the kind offices of W. A. Woods. A good deal has been contributed to the project by Stanford University to whom we owe the land, buildings, roads, fences, earthmoving, maintenance and innumerable operations. The manifold services of the Stanford Electronics Laboratories have been indispensable; above all, administrative matters have been well cared for by the Associate Director, Dr. D. Bacon. A great number of students from the department of electrical engineering have contributed from time to time, major contributions having been made by R. Colvin, D. Cudaback, and K.-S. Yang. C. Sphar did the mechanical design, construction and surveying, and competently supervised a wide variety of technical tasks essential to the success of the project; C. C. Lee has ably maintained and operated the instrument. The project found its home at Stanford through the initiative of Prof. O. G. Villard, Jr., director of the Radioscience Laboratory, whose friendly interest throughout the whole project is here warmly acknowledged.

Bibliography

[1] W. N. Christiansen and J. A. Warburton, "The distribution of radio brightness over the solar disk at a wavelength of 21 centimetres, I," *Australian J. Phys.*, vol. 6, pp. 190–202; June, 1953.
[2] J. L. Pawsey and R. N. Bracewell, "Radio Astronomy," Oxford University Press, New York, N. Y.; 1955.
[3] B. Y. Mills and A. G. Little, "A high resolution aerial system of a new type," *Australian J. Phys.*, vol. 6, pp. 272–278; September, 1953.
[4] B. Y. Mills, A. G. Little, K. V. Sheridan, and O. B. Slee, "A high resolution radio telescope for use at 3.5 m," Proc. IRE, vol. 46, pp. 67–84; January, 1958.
[5] R. N. Bracewell, "A new instrument in radio astronomy," *Observatory*, vol. 73, pp. 200–201; October, 1953.
[6] R. N. Bracewell, "A Proposal for a Microwave Spectroheliograph," Radio Propagation Lab., Stanford University, Stanford, Calif., September 15, 1955.
[7] R. N. Bracewell, "Radio astronomy techniques," in "Handbuch der Physik," S. Flügge, Ed., vol. 54, Springer-Verlag, Berlin, Ger., to be published.
[8] R. N. Bracewell, "Interferometry and the spectral sensitivity island diagram," this issue, pp. 59–67.
[9] R. N. Bracewell, "Antenna tolerance theory," *Proc. Symp. on Statistical Methods in Radio Wave Propagation*, W. C. Hoffman, Ed., Pergamon Press, London, Eng., pp. 179–183; 1960.
[10] R. N. Bracewell, "Tolerance theory of large antennas," this issue, pp. 49–58.
[11] W. N. Christiansen, D. S. Mathewson, and J. L. Pawsey, "Radio pictures of the sun," *Nature*, vol. 180, pp. 944–946; November, 1957.
[12] W. N. Christiansen and D. S. Mathewson, "Scanning the sun with a highly directional array," Proc. IRE, vol. 46, pp. 127–131; January, 1958.
[13] W. N. Christiansen and D. S. Mathewson, "The origin of the slowly varying component," *Paris Symp. on Radio Astronomy*, R. N. Bracewell, Ed., Stanford University Press, Stanford, Calif., pp. 108–117; 1959.
[14] M. Gutmann and J. L. Steinberg, "Résultats préliminaires obtenus avec l'interféromètre à 8 antennes sur 3 cm de longueur d'onde," *Paris Symp. on Radio Astronomy*, R. N. Bracewell, Ed., Stanford University Press, Stanford, Calif., pp. 123–124; 1959.
[15] H. Tanaka, "An 8-element interferometer at 9,400 Mc," *Proc. Res. Inst. Atmosph.*, vol. 6, p. 67, 1959; vol. 8, to be submitted.
[16] H. Tanaka and T. Kakinuma, "Multiple element interferometer for locating sources of solar noise at 4000 Mc," *Proc. Res. Inst. Atmosph.*, vol. 2, pp. 53–76, 1954; pp. 102–109, 1955.
[17] A. E. Covington and N. W. Broten, "An interferometer for radio astronomy with a single-lobed radiation pattern," IRE Trans. on Antennas and Propagation, vol. AP-5, pp. 247–255; July, 1957.
[18] A. E. Covington, "Solar emission at 10-cm wavelength," *Paris Symp. on Radio Astronomy*, R. N. Bracewell, Ed., Stanford University Press, Stanford, Calif., pp. 159–165; 1959; "A compound interferometer," *J. Roy. Astron. Soc. Canada*, vol. 54, pp. 17–28, 58–68; February and April, 1960.
[19] J. Firor, "Solar radio bright spots at 88-cm wavelength," *Symp. on Radio Astronomy*, Paris, France, R. N. Bracewell, Ed., Stanford University Press, Stanford, Calif., pp. 136–139; 1959.
[20] E. J. Blum, J. F. Denisse, and J. L. Steinberg, "Radio astronomy at the Meudon Observatory," Proc. IRE, vol. 46, pp. 39–43; January, 1958; E. J. Blum, A. Boischot, and M. Ginat, "Le grand interféromètre de Nançay," *Ann. d'Astrophysique*, vol. 20, pp. 155–163; 1957.
[21] A. M. Malinge, E. J. Blum, M. Ginat, and M. Parise, "Labranche Nord-Sud du grand interféromètre de la station de-Nançay," *Comptes Rendus*, vol. 249, pp. 2009–2011; November, 1959.
[22] G. Swarup and K.-S. Yang, "Interferometer phasing problems at microwave frequencies," 1959 IRE WESCON Convention Record, pt. 1, pp. 17–24; 1959.
[23] G. Swarup and K.-S. Yang, "Phase adjustment of large antennas," this issue, pp. 75–81.
[24] G. Swarup and K.-S. Yang, "Monitoring paraboloidal antennas," Proc. IRE, vol. 48, pp. 1918–1919; November, 1960.
[25] R. N. Bracewell and J. A. Roberts, "Aerial smoothing in radio astronomy," *Australian J. Phys.*, vol. 7, pp. 615–640; December, 1954.
[26] R. N. Bracewell, "Two-dimensional aerial smoothing in radio astronomy," *Australian J. Phys.*, vol. 9, pp. 297–314; September, 1956.
[27] R. N. Bracewell, "Aerials and data processing," to be submitted for publication.
[28] R. N. Bracewell, "Radio interferometry of discrete sources," Proc. IRE, vol. 46, pp. 97–105; January, 1958.
[29] R. N. Bracewell, "Restoration in the presence of errors," Proc. IRE, vol. 46, pp. 106–111; January, 1958.
[30] S. E. Khaikin and N. L. Kaidanovskii, "A new radio telescope of high resolving power," *Paris Symp. on Radio Astronomy*, R. N. Bracewell, Ed., Stanford University Press, Stanford, Calif., pp. 166–170; 1959.

Two-Element Interferometer for Accurate Position Determinations at 960 Mc*

RICHARD B. READ†

Summary—A 960-Mc two-element interferometer using the twin 90-foot steerable paraboloids of the California Institute of Technology Radio Observatory is described. The response of the associated receiving equipment as it applies to interferometric position measurements is analyzed in some detail, and an advantage of not rejecting the image response of the receiver is mentioned. Finally, a brief account is given of the various ways the interferometer may be used to measure right ascensions and declinations with both an east-west and a north-south baseline.

Introduction

THE California Institute of Technology Radio Observatory is located in the Owens Valley of California at a latitude of 37°13′53.8″ north and a longitude of 118°17.6′ west, near the town of Bishop. The observatory is financially supported by the Office of Naval Research. The chief instruments of the observatory are two identical steerable paraboloids of 90-foot diameter. These antennas are of welded steel construction and were built on the observatory site during the summer of 1958. The steerable mounts are of the equatorial type, and the separation between the two antennas may be varied by moving the antennas on a very wide gauge railroad track to various stations along a 1600-foot east-west baseline or to various stations along a 1600-foot north-south baseline.

The 90-foot antennas may be used separately as two completely independent antennas,[1,2] or they may be used together as a two-element interferometer. The interferometer is useful for accurately measuring the positions of radio sources and for determining their angular extents. In addition, certain characteristics of the interferometer may sometimes be employed to great advantage for special experiments.[3] The discussion in this paper will be confined to the accurate measurement of positions.

Accurate position measurement is important in radio astronomy in that it frequently makes possible correlation of some of the sources observed by radio astronomers with certain objects observed by optical astronomers. When such a correlation can be convincingly made, the radio source is said to be identified with the optical object. It is obvious that the more accurately the position of the radio source can be determined, the greater is the probability of obtaining a convincing identification. While it is possible to measure the positions of sources to a small fraction of a beamwidth with a single antenna, the accuracy of the measurement is ultimately limited by the resolution of the antenna. The use of two simple antennas as an interferometer permits a high degree of resolution and hence positional accuracy without the expense of the enormous single antenna of equivalent resolution. Attractive as it may seem, however, this scheme has a serious drawback in that if the two antennas used for the interferometer have poor angular resolution, they are likely to see more than one radio source at a time. The resulting compound interference pattern in such cases is very difficult, if not impossible, to interpret. The two 90-foot steerable paraboloids of the California Institute of Technology Radio Observatory have sufficient angular resolution at 960 Mc so that the probability that they will see more than one source at a time is very small; thus, source confusion is not a problem. During the course of a position measurement, the paraboloids track the source being observed while it drifts through the interferometer lobe pattern.

Fig. 1—The twin 90-foot steerable paraboloids of the California Institute of Technology Radio Observatory.

* Received by the PGAP, September 16, 1960.

† Radio Observatory, California Institute of Technology, Owens Valley, Calif.

[1] D. E. Harris and J. A. Roberts, "Radio source measurements at 960 Mc/s," *Publications Astronomical Soc. Pacific*, vol. 72, pp. 237–255; August, 1960.

[2] R. W. Wilson and J. G. Bolton, "A survey of galactic radiation at 960 Mc/s," *Publications Astronomical Soc. Pacific*, to be published.

[3] V. Radhakrishnan and J. A. Roberts, "Polarization and angular extent of the 960 Mc/s radiation from Jupiter," *Phys. Rev. Letters*, vol. 4, pp. 493–494; May 15, 1960.

Geometry of the Interferometer

Consider two antennas a distance D apart receiving radiation from a source making an angle θ with the plane normal to a line through the two antennas (Fig. 2). The radiation reaching antenna no. 1 travels an extra distance of $D \sin \theta$ relative to radiation reaching antenna no. 2, and hence suffers a corresponding relative delay. Consider now the celestial hemisphere in Fig. 3.

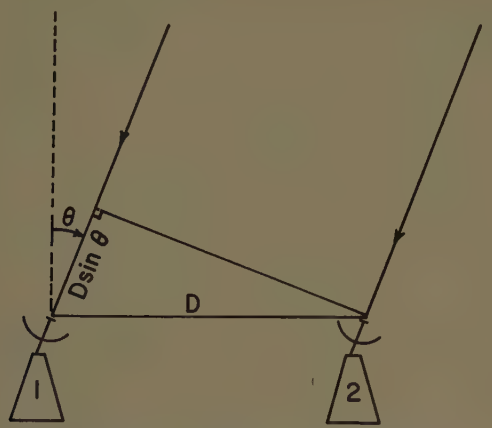

Fig. 2—Ray diagram showing the extra path length, $D \sin \theta$, traversed by the radiation striking antenna no. 1.

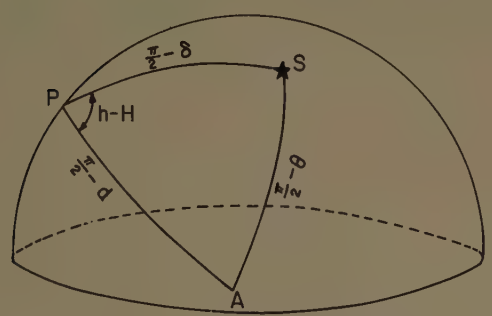

Fig. 3—The celestial hemisphere showing the relationships between various angles.

P is the north celestial pole, S is the radio source being observed, and A is the point representing the direction $\theta = \pi/2$. Let H be the hour angle of S, h be the hour angle of A, δ be the declination of S, and d be the declination of A. Then, by the relations in a spherical triangle we have

$$\cos\left(\frac{\pi}{2} - \theta\right) = \cos\left(\frac{\pi}{2} - d\right)\cos\left(\frac{\pi}{2} - \delta\right) + \sin\left(\frac{\pi}{2} - d\right)\sin\left(\frac{\pi}{2} - \delta\right)\cos(h - H), \quad (1)$$

which simplifies to

$$\sin\theta = \sin d \sin\delta + \cos d \cos\delta \cos(h - H). \quad (2)$$

The Receiver

Fig. 4 is a block diagram of the complete receiver. The receiver is operationally identical to the phase-switched type of interferometer[4] but does not employ any switching. Fig. 5 is a simplified block diagram for analysis of the receiver logic. For simplicity, it will be assumed that the high-frequency mixers merely multiply the signal by the local oscillator. Since only relative phase relations are desired in the following analysis, amplifier gains will be ignored. Let x, y, z be the electrical lengths of the cables connecting the mixer to the antenna, local oscillator, and multiplier, respectively, for antenna no. 2. Let $x+\Delta x$, $y+\Delta y$, $z+\Delta z$ be the corresponding cable lengths for antenna no. 1. Let I be the intensity of the signal, ω_{LO} be the angular frequency of the local oscillator, and ω_{IF} be the angular frequency of the IF amplifier response. Then $\omega_{LO} \pm \omega_{IF}$ are the angular frequencies of the signal and image. Note that there is no attempt in the receiver to discriminate against the image. An important reason for not doing so will be mentioned below. Since the signal being received by the interferometer is of the nature of random noise, there is no correlation between signal and image. The responses due to signal and image will therefore be worked out separately by carrying $\pm$ signs, and the combined response will then be computed.

Writing out the signals at the various points of Fig. 5 designated by letters (a)–(d), respectively, we have

$$\text{(a)} \quad I \sin[(\omega_{LO} \pm \omega_{IF})t], \quad (3)$$

$$\text{(b)} \quad I \sin\left[(\omega_{LO} \pm \omega_{IF})\left(t - \frac{x}{c}\right)\right], \quad (4)$$

$$\text{(c)} \quad \cos\left[\omega_{LO}\left(t - \frac{y}{c}\right)\right], \quad (5)$$

$$\text{(d)} \quad \frac{I}{2}\sin\left[(\omega_{LO} \pm \omega_{IF})\left(t - \frac{x}{c}\right) + \omega_{LO}\left(t - \frac{y}{c}\right)\right] + \frac{I}{2}\sin\left[(\omega_{LO} \pm \omega_{IF})\left(t - \frac{x}{c}\right) - \omega_{LO}\left(t - \frac{y}{c}\right)\right]. \quad (6)$$

The IF passband filter rejects the first term of (6) and introduces a phase shift ϕ. We thus have at (e), after replacing t by $t + \phi/\omega_{IF} - z/c$ and simplifying,

$$\pm\frac{I}{2}\sin\left[\omega_{IF}\left(t - \frac{x}{c} - \frac{z}{c}\right) + \phi \pm \omega_{LO}\left(\frac{y}{c} - \frac{x}{c}\right)\right]. \quad (7)$$

[4] J. L. Pawsey and R. N. Bracewell, "Radio Astronomy," Clarendon Press, Oxford, England, pp. 66–67; 1955.

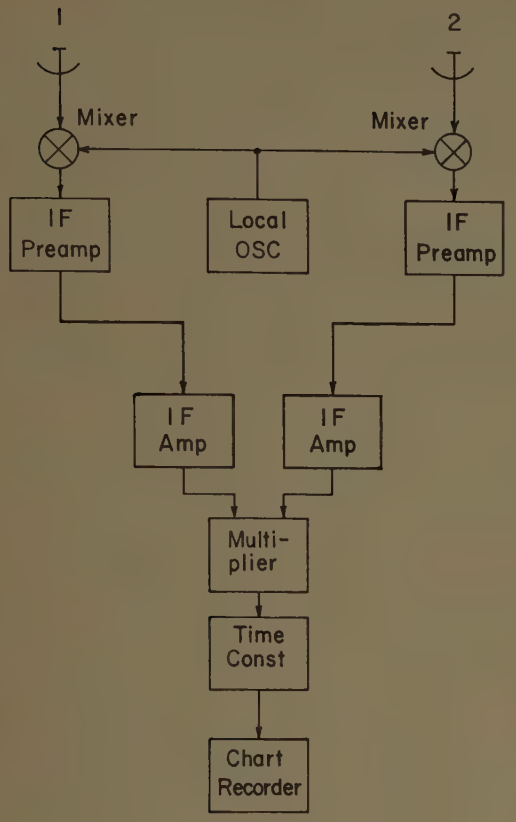

Fig. 4—Block diagram of the receiver.

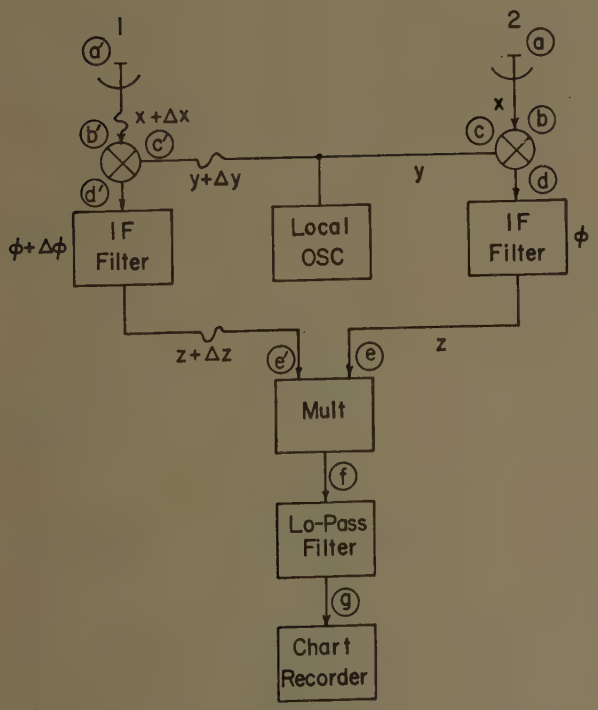

Fig. 5—Simplified block diagram for analysis of circuit logic.

A similar calculation for the primed letters taking into account the extra path length $D \sin\theta$ from Fig. 2 gives for (e′),

$$\pm \frac{I}{2} \sin\left[\omega_{IF}\left(t - \frac{D\sin\theta}{c} - \frac{x}{c} - \frac{\Delta x}{c} - \frac{z}{c} - \frac{\Delta z}{c}\right) + \phi + \Delta\phi \pm \omega_{LO}\left(-\frac{D\sin\theta}{c} + \frac{y}{c} + \frac{\Delta y}{c} - \frac{x}{c} - \frac{\Delta x}{c}\right)\right]. \quad (8)$$

Taking the product of (7) and (8) and employing a trigonometric identity gives at (f)

$$\frac{I^2}{8}\cos\left[\omega_{IF}\left(\frac{D\sin\theta}{c} + \frac{\Delta x}{c} + \frac{\Delta z}{c}\right) - \Delta\phi \pm \omega_{LO}\left(\frac{D\sin\theta}{c} + \frac{\Delta x}{c} - \frac{\Delta y}{c}\right)\right]$$
$$- \frac{I^2}{8}\cos\left[\omega_{IF}\left(2t - \frac{D\sin\theta}{c} - \frac{2x}{c} - \frac{\Delta x}{c} - \frac{2z}{c} - \frac{\Delta z}{c}\right) + 2\phi + \Delta\phi \pm \omega_{LO}\left(-\frac{D\sin\theta}{c} + \frac{2y}{c} + \frac{\Delta y}{c} - \frac{2x}{c} - \frac{\Delta x}{c}\right)\right]. \quad (9)$$

The low-pass filter rejects the second term of (9), leaving at (g)

$$\frac{I^2}{8}\cos\left[\frac{\omega_{IF}}{c}(D\sin\theta + \Delta x + \Delta z) - \Delta\phi \pm \frac{\omega_{LO}}{c}(D\sin\theta + \Delta x - \Delta y)\right]. \quad (10)$$

Now, taking the sum of the effect of the signal and the image, and employing another trigonometric identity, we find that the total deflection of the recorder is proportional to

$$\frac{I^2}{4}\cos\left[\frac{\omega_{IF}}{c}(D\sin\theta + \Delta x + \Delta z) - \Delta\phi\right] \cdot \cos\left[\frac{\omega_{LO}}{c}(D\sin\theta + \Delta x - \Delta y)\right]. \quad (11)$$

It should be noted that (11) was derived under the assumption that the intermediate-frequency bandwidth is infinitely narrow. In practice, however, the intermediate-frequency bandwidth is not infinitely narrow, and (11) must be integrated over the IF bandpass. If we denote the effective IF center frequency by ω_{IF_0}

and consider $\Delta\phi$ to be some function of ω_{IF}, then the integration yields, in general,

$$\frac{I^2}{4} p\left[\frac{\omega_{IF_0}}{c}(D\sin\theta+\Delta x+\Delta z)\right] \cdot\cos\left[\frac{\omega_{LO}}{c}(D\sin\theta+\Delta x-\Delta y)\right]. \quad (12)$$

It is difficult to evaluate the function p for any arbitrary frequency response of the IF bandpass. If, however, certain reasonable assumptions are made concerning the form of the frequency response, and if $\Delta\phi$ is assumed small, then

$$p \approx q\left[\frac{\omega_{IF_0}}{c}(D\sin\theta+\Delta x+\Delta z)\right] \cdot\cos\left[\frac{\omega_{IF_0}}{c}(D\sin\theta+\Delta x+\Delta z)\right], \quad (13)$$

where q is a bell-shaped function which is symmetrical about a maximum at an argument of zero. This form of response agrees closely with observations.

The quantities which are actually measured in a position determination are the sidereal times of the zero crossovers of (12) when p is near a maximum. The measured times are thus functions only of ω_{LO}/c (D sin $\theta+\Delta x-\Delta y$) and involve neither the difference in IF cable length Δz nor the differential phase shift $\Delta\phi$ of the IF tuned circuits. This insensitivity to Δz and $\Delta\phi$ is a direct consequence of accepting both signal and image and contributes markedly to the phase stability of the interferometer, since the differential phase shift $\Delta\phi$ produced by the many tuned circuits in the IF amplifiers is difficult to keep constant.

Measurement of Positions—East-West Interferometer

In order to minimize errors in reduction caused by an improper choice of a zero line when measuring times of zero crossovers of the recorder output, it is customary practice to compute a time which is the mean of two successive crossovers: one when the recorder output is going from negative to positive, and the other when it is going from positive to negative. Since sin θ may be regarded as a nearly linear function of time over short intervals, the cos $[\omega_{LO}/c\ (D\ \sin\theta+\Delta x-\Delta y)]$ term of (12) is essentially ± 1 at the computed time, and we may write

$$\frac{\omega_{LO}}{c}(D\sin\theta+\Delta x-\Delta y)=n\pi, \quad (14)$$

where n is an integer and where we denote the computed sidereal time for which (14) is valid as t_n.

For a true east-west baseline, $d=0$, $h=\pi/2$. In practice, however, the baseline may not be quite east-west or even level; we shall therefore define

$$h'=h-\frac{\pi}{2} \quad (15)$$

and consider both d and h' to be very small. Incorporating the above in (2) gives

$$\sin\theta=\sin d\sin\delta+\cos d\cos\delta\sin(H-h'). \quad (16)$$

The differential line lengths Δx and Δy may, in general, vary somewhat during the observing night due to temperature variations, etc. For simplicity, we shall regard them as an unknown function of time, and write

$$E(t)=\frac{-\Delta x+\Delta y}{D}. \quad (17)$$

Combining (14), (16) and (17),

$$\frac{n\pi c}{D\omega_{LO}}+E(t_n)=\sin d\sin\delta+\cos d\cos\delta\sin(H_n-h'). \quad (18)$$

In the measurement of right ascensions with the east-west interferometer, $n=n_0$ is chosen such that $H_{n_0}\approx 0$ (*i.e.*, a lobe near transit). By measuring the sidereal times t_{n_0} of this same lobe for several strong sources whose positions are well known (calibrators), and by employing the relation between sidereal time t, hour angle H, and right ascension α:

$$H=t-\alpha, \quad (19)$$

it is possible to plot $E(t)$ throughout the observing night. At the observatory the variation of $E(t)$ during any one night is equivalent to a variation of the time of transit of only $\frac{1}{2}$ to 1 second, and appears to be a smooth function. By interpolation, intermediate values of $E(t)$ may be found, and the right ascensions of sources whose positions are not accurately known may be determined from (18).

Declination measurements with the east-west interferometer are somewhat more complicated. Observations are made on each side of the meridian at $n=n_0-m$ and $n=n_0+m$ with the corresponding times t_{-m} and t_{+m} being measured. Inserting the two sets of quantities separately into (18) and subtracting gives

$$\frac{-2m\pi c}{D\omega_{LO}}+E(t_{-m})-E(t_{+m})=2\cos d\cos\delta\sin \cdot\left(\frac{H_{-m}-H_{+m}}{2}\right)\cos\left(\frac{H_{-m}+H_{+m}-2h'}{2}\right). \quad (20)$$

The value of $\pi c/D\omega_{LO}$ is determined by the observation of a strong source of known declination, and the difference $E(t_{-m})-E(t_{+m})$ is determined by interpolation as above. Since by (19) $H_{-m}-H_{+m}=t_{-m}-t_{+m}$, and since $H_{-m}+H_{+m}$ is very small, it is possible to solve (20) and obtain the declinations of sources whose positions are

not accurately known. It should be noted, however, that declination unfortunately enters (20) as cos δ, which means that for sources near the celestial equator (cos $\delta \approx 1$) the above method for measuring declinations loses accuracy. In practice, the east-west interferometer may be used successfully to measure declinations of sources which are more than 20° from the celestial equator.

Measurement of Positions—North-South Interferometer

With the north-south interferometer, it is possible to measure the declinations of sources regardless of their nearness to the celestial equator. The procedure is somewhat simpler than for the east-west interferometer, but requires a minor addition to the receiver logic. For an approximately north-south interferometer, d is approximately equal to the colatitude of the observatory, and h is approximately π. Let us define

$$h'' = h - \pi. \tag{21}$$

Then (2) becomes

$$\sin\theta = \sin d \sin\delta - \cos d \cos\delta \cos(H - h''). \tag{22}$$

In order to measure declinations, a device is added to the receiver which rotates the phase of the local oscillator signal sent to the mixer of antenna no. 1, while the phase of the local oscillator signal sent to the mixer of antenna no. 2 is unaffected. The phase is rotated at a uniform rate of 360° per minute, and an accurate timing mark is placed on the record for each revolution. The amount of local oscillator phase rotation corresponding to any point on the record may thus be determined. Let Φ be the amount of phase rotation. Replacing Δy by $\Delta y + (c/\omega_{LO})\Phi$ in (14) gives

$$\frac{\omega_{LO}}{c}(D\sin\theta + \Delta x - \Delta y) = n\pi + \Phi. \tag{23}$$

Combining (23) with (22),

$$\frac{c}{D\omega_{LO}}(n\pi + \Phi) + E(t) = \sin d \sin\delta - \cos d \cos\delta \cos(H - h''). \tag{24}$$

The measurement consists of determining Φ at a time when n is an integer, and cos $(H-h'')$ is essentially unity (transit). $E(t)$ is interpolated as before, from observations of calibrators, and the proper integral value of n may be chosen by a knowledge of the approximate position of the source. Thus, (24) may be solved for δ, the desired accurate declination of the source.

If (19) is substituted in (22), it will be noted that sin θ regarded as a function of sidereal time t is symmetrical about $t=\alpha+h''$:

$$\sin\theta = \sin d \sin\delta - \cos d \cos\delta \cos(t - \alpha - h''). \tag{25}$$

Thus, if h'' can be determined accurately by surveying, the north-south interferometer presents an interesting possibility of measuring right ascensions. Although untried at the observatory at the time of this writing, this method of right ascension measurement is intriguing because no calibrators are necessary to evaluate the unknown $E(t)$. As long as $E(t)$ remains essentially constant during an interval long enough to determine the time of symmetry of sin θ, then right ascensions may be measured on an absolute basis.

Results to Date

Extensive use was made of the 90-foot paraboloids at the observatory as an east-west interferometer for measuring positions during the first half of 1960. The data from these measurements are now being reduced, and it is expected that the results will be published shortly. During the fall of 1960, the antennas will be used for the first time as a north-south interferometer, with most of the effort being devoted to accurate measurement of declinations.

A 2–4 kMc Sweep-Frequency Receiver*

D. W. CASEY, II† AND J. W. KUIPER‡, MEMBER, IRE

Summary—**To study another octave of the solar radio-frequency spectrum, a new superheterodyne receiver using a video-frequency IF was developed. This receiver scans the 2000- to 4000-Mc octave in 0.1 sec by using a backward-wave oscillator as the local oscillator. A carefully designed balance mixer converts the incoming signal directly into a video signal, where it is amplified and displayed as an intensity-modulated trace on a high-resolution cathode-ray tube. The receiver has an average noise figure of 13.0 db, and a total gain variation of ±2 db over this octave. The receiver features power output stabilization of the local oscillator, a 2000- to 4000-Mc noise source, and highly stable video amplifiers.**

Introduction

RADIO-FREQUENCY radiation from the sun was discovered in 1942 and has been studied since 1945. In 1950, Wild and his associates began sweep-frequency recordings of meter-wavelength bursts,[1] and much progress was made in explaining the various types of radio bursts at these frequencies. At the University of Michigan, meter-wavelength observations started in September, 1957, using three mechanically-tuned sweep receivers, which scanned a total frequency range of 110 to 600 Mc in octave steps.[2,3]

The antenna for these receivers is a 28-ft equatorially-mounted radio telescope with four confocally-mounted antenna feeds, three of the antenna feeds covering the frequency range of 110 to 600 Mc, and the fourth covering from 2000 to 4000 Mc.[4]

Analysis of the meter-wavelength sweep-frequency solar data produced many theories and ideas on the origin, development, and propagation of this electromagnetic energy.[5,6] Several radio observatories saw the need for extending the frequency spectrum in order to obtain more complete sweep-frequency recordings. In general, the observations were extended toward the low-frequency end of the spectrum, some groups scanning as low as 18 Mc for solar emission. However, one group moved upward in frequency and started sweep-frequency observations from 500 to 950 Mc in July, 1959.[7,8]

The region above 1000 Mc was completely unexplored by the sweep-frequency technique. Single-frequency recordings at 2800 Mc have been taken at Ottawa, Canada, since 1947.[9,10] In Japan the intensity and polarization of solar radio bursts at 9400, 3750, 2000, and 1000 Mc, have been continuously observed since July, 1957.[11] Other groups have also observed solar emission at various centimeter and millimeter wavelengths.[12]

From these single-frequency recordings, several distinct classes of microwave bursts from the sun were observed, each class of bursts having a different magnitude of amplitude, duration, source diameter, structure, relative occurrence, rate of frequency drift, and wave polarization.

Several theoretical discussions predict a class of microwave bursts to be broad-band emission caused by synchrotron radiation from electrons with medium energies.[13,14]

Another observer has recently shown that this broad-band synchrotron emission is frequently associated with type IV meter-wavelength outbursts, and that the centimeter-wavelength broad-band burst is likely to be associated with polar-cap absorption events. This ionospheric absorption of cosmic noise in the polar region is in turn believed to be caused by the ionization of the upper atmosphere by fast protons emitted from the sun after a big flare.[15,16]

* Received by the PGAP, September 16, 1960.

† Space Commun. Lab., Kellogg Switchboard and Supply Co., Fort Wayne, Ind.

‡ Astronomy Dept., University of Michigan, Ann Arbor.

[1] J. P. Wild and L. L. McCready, "Observations of the spectrum of high-intensity solar radiation at metre wavelengths," *Australian J. Sci. Res.*, ser. A, vol. 3, Nos. 3 and 4, pp. 387–398, 399–408, 541–558; 1950; vol. 4, No. 1, pp. 36–50; 1951.

[2] F. T. Haddock, "Introduction to radio astronomy," PROC. IRE, vol. 46, pp. 8–9; January, 1958.

[3] J. Goodman and M. Lebenbaum, "A dynamic spectrum analyzer for solar studies," PROC. IRE, vol. 46, pp. 132–135; January, 1958.

[4] H. Jasik, "A wide-band antenna system for solar noise studies," PROC. IRE, vol. 46, pp. 135–142; January, 1958.

[5] F. T. Haddock, "Some characteristics of dynamic spectra of solar bursts," *Symp. on Radio Astronomy*, Paris, France, Stanford University Press, Stanford, Calif., pp. 188–193; 1959.

[6] J. A. Roberts, "Some aspects of type II bursts," *Symp. on Radio Astronomy*, Paris, France, Stanford University Press, Stanford, Calif., pp. 194–200; 1959.

[7] M. R. Kundu and J. A. Roberts, "A comparison of the dynamic spectra of solar radio bursts in the decimeter and meter wavelength ranges," submitted to *Astrophys. J.*

[8] C. W. Young, C. L. Spencer, G. E. Moreton, and J. A. Roberts, submitted to *Astrophys. J.*

[9] A. E. Covington and W. J. Medd, "Discussion of 10.7 cm solar radio flux measurements on an estimation of the accuracy of observations," PROC. IRE, vol. 46, pp. 112–119; January, 1958.

[10] A. E. Covington, "The solar emission at 10-cm wavelength," *Symp. on Radio Astronomy*, Paris, France; Stanford University Press, Stanford, Calif., pp. 159–166; 1959.

[11] H. Tanaka and T. Kakinuma, "Polarization of burst of solar radio emission at microwave frequencies," *Symp. on Radio Astronomy*, Paris, France; Stanford University Press, Stanford, Calif., pp. 215–217; 1959.

[12] Various articles in *Symp. on Radio Astronomy*, Paris, France; pt. 2, Stanford University Press, Stanford, Calif.; 1959.

[13] A. Boischot and J. F. Denisse, "Les émissions de type IV et l'origine des rayons cesmiques associés aux éruptions chromosphériques," *Compt. Rend. Acad. Sci.*, Paris, France, no. 245, pp. 2194–2197; December, 1957.

[14] T. Takakura, "Synchrotron radiation and solar radio outbursts at microwave frequencies," *Symp. on Radio Astronomy*, Paris, France; Stanford University Press, Stanford, Calif., pp. 562–570; 1959.

[15] G. C. Reid and H. Leinbach, "Low-energy cosmic-ray events associated with solar flares," *J. Geophys. Res.*, vol. 64, pp. 1801–1805; November, 1959.

[16] D. K. Bailey, "Abnormal ionization in the lower ionosphere associated with cosmic-ray flux enhancements," vol. 47, pp. 255–266; February, 1959.

Although the general frequency spectrum of centimeter-wave bursts could be inferred from single-frequency measurements, experimental sweep-frequency verification is needed to confirm theoretical studies, and also to give additional information for classifying the bursts.

System Design

The desired receiver was to cover the octave from 2000 tp 4000 Mc, to have a total gain variation with frequency of less than ± 3 db, and an image rejection of 50 db or better. It can be shown from a study of the single-frequency data taken at 2800 Mc that a noise figure of less than 12 db is necessary to detect a change in solar radio emission of 10^{-21} watt m^{-2} $(cps)^{-1}$. Three receiver system designs were studied before deciding on the final approach to this 2000- to 4000-Mc receiver.

One system considered was a superheterodyne receiver with a relatively high intermediate frequency. This receiver would use a bandpass filter to limit the total RF coverage from 2000 to 4000 Mc. To avoid spurious responses due to image-frequency signals, the center frequency of the first stages of IF amplification would be chosen at approximately 1200 Mc. The local oscillator is then tuned to the sum of the IF and received frequency.

This system has disadvantages of relative complexity and requires a balanced mixer with a flat response from 2000 to 5200 Mc.

Another system considered was the use of a traveling-wave tube amplifier ahead of a broad-band mixer. The local oscillator would be tuned near the signal to be received, thus converting the RF signal directly into video. This system would provide the necessary noise figure, but it is doubtful whether the gain variations with frequency could be kept within the desired limits of ± 3 db.

The third system, which was the one adopted, utilizes a carefully designed balanced crystal mixer in conjunction with a low-noise local oscillator to detect and convert the RF signal directly into video. With this arrangement, a low-noise video amplifier can immediately follow the mixer crystals and produce a good overall noise figure. The only gain variations with frequency will be those concerned with the operation of the mixer crystals, such as impedance matching and local oscillator drive. This system is also light in weight and simple to maintain, two important considerations when the RF unit must be mounted near the focus of the antenna.

General Description

The receiver was built in three separate units, one unit mounting near the focus of the antenna, the second placed at the base of the tower for the antenna, and the third placed in the control house (see Figs. 1 and 2).

The RF unit, mounted at the focus of the 28-ft antenna, is temperature stabilized and houses the balanced crystal mixer, a low-noise video preamplifier, a local oscillator power-leveling device, a noise source with its associated coaxial switch, a frequency-marker cavity, and a marker preamplifier.

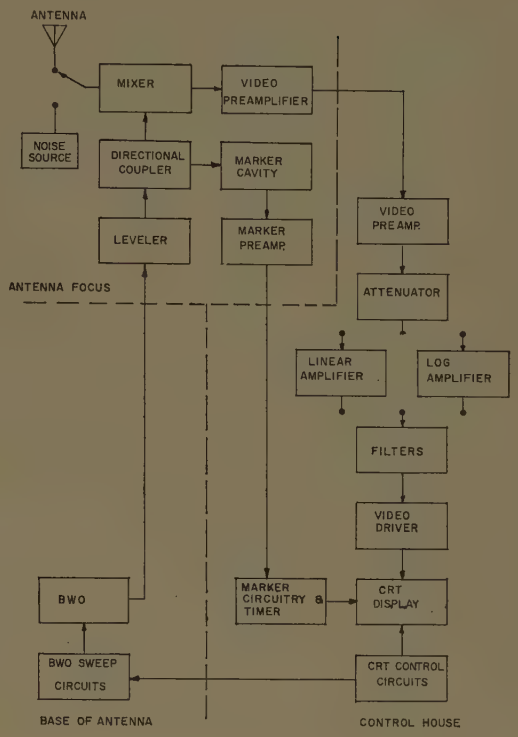

Fig. 1—Block diagram of the receiver.

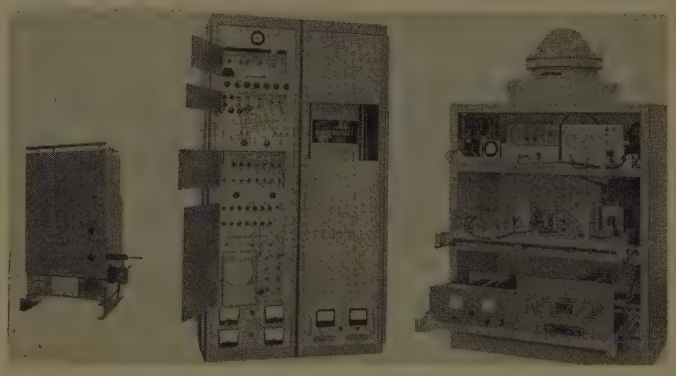

(a) (b) (c)

Fig. 2—Photograph of the receiver. (a) RF-unit. (b) Video amplifiers and display. (c) Local oscillator.

The Huggins HO-1 backward-wave oscillator and its solenoid, plus necessary power supplies and sweep circuits for this tube, are located at the base of the 28-ft antenna. Local oscillator power is transferred to the RF unit at the antenna focus by a low-loss coaxial cable.

The remaining unit houses the power supplies, video amplifiers, video band-pass filters, master sweep circuits, marker circuitry, the cathode-ray tube display, and the recording camera. The operator has a choice of using a linear response video amplifier with an effective dynamic range of 20 db or a logarithmic response video

amplifier with a dynamic range of 60 db. The low-frequency cutoff of the video amplifiers is fixed at 75 kc but the upper frequency cutoff can be selected at 1.0, 2.5, or 5.0 Mc. Provision is also made for calibrating the density of the film recording.

Detailed Description

Noise Figure Considerations

From single-frequency data taken at 2800 Mc, it is known that the minimum solar flux density is about 100 units (1 unit equals 10^{-22} watt m^{-2} $(cps)^{-1}$). From this value it was determined theoretically that the receiver noise figure should be less than 12 db (see Appendix) to detect a change of 10 units in solar emission.

In a typical microwave superheterodyne receiver using a 30 Mc (or higher) IF, noise contributions from the local oscillator are cancelled in a balanced mixer, and the $1/f$ spectrum noise of the crystals is masked by the other noise contributions in the system.

In designing a receiver with a video-frequency IF, the contributions of the $1/f$ spectrum noise of the crystals and the much larger noise output of the local oscillator at frequencies near the carrier frequency must not be neglected.

The $1/f$ noise spectrum of 1N23C crystals recently investigated by Newberg is of the order of 2×10^4 °K at 10 kc, and follows the $1/f$ law to about 1 Mc.[17]

A few measurements have been made on the noise spectrum and the spurious responses of the O-type carcinotron tube.[18,19] This carcinotron appears to have less noise output than a comparable klystron or magnetron. The problem of spurious responses has been studied for other *S*-band tubes,[20] but not for the Huggins HO-1 tube, although the manufacturer rejects those tubes which have spurious responses more intense than 35 db below the carrier level.

The noise figure of the receiver was measured by using the broad-band noise source and manually tuning the receiver to selected frequencies. The noise figure curve, shown in Fig. 3, averages about 13.0 db, with variations of ±1.5 db. The accuracy of measurement is about ±1.0 db or better.

The low receiver noise figure in the presence of many internal sources of noise is due to several precautions taken in the design. Choosing the video low-frequency cutoff sufficiently high eliminates most of the $1/f$ spectrum noise of the crystals and also removes much of the local oscillator noise. The balanced mixer cancels additional local oscillator noise. Finally, the video amplifier is low-noise, thus helping to minimize the total noise figure of the receiver.

Balanced Mixer

A balanced mixer, consisting of a 3-db hybrid coupler,[21] crystal holders and 1N21E and ER crystals, accepts signal power from the antenna. After the difficult design problem of the crystal holders was resolved, the mixer provided a response that was flat to within ±2 db across the band (see Fig. 4).

Several precautions have been taken to maintain a uniform gain and noise figure with frequency and time. These are: 1) matched crystals are used, 2) the mixer assembly and all RF components are maintained at constant temperature by a thermostatically controlled heating system, and 3) local oscillator power is held approximately constant over the band.

The local oscillator power is electronically controlled in order to maintain constant crystal current. This control is accomplished by comparing the crystal current

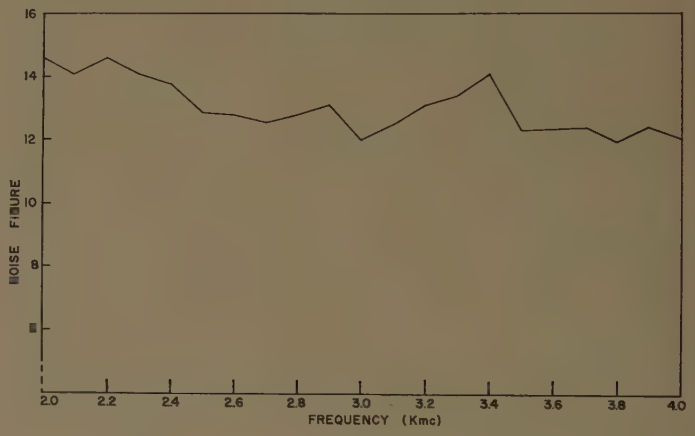

Fig. 3—Typical noise figure of the receiver.

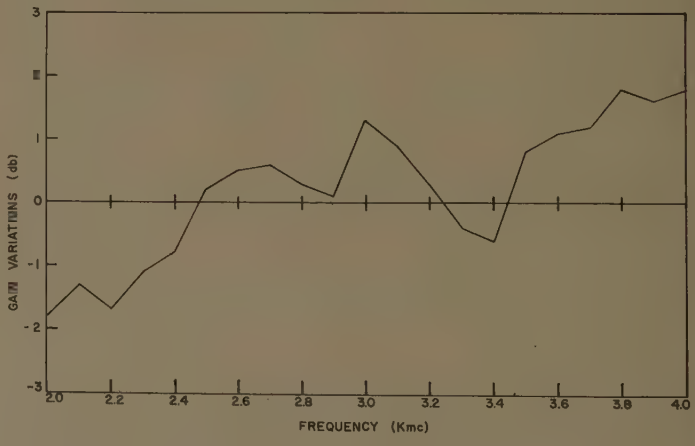

Fig. 4—Typical gain variation as a function of frequency.

[17] I. L. Newburg, "Video-Frequency Noise Measurements on Microwave Crystal Mixers," Mass. Inst. Tech., Cambridge, Rept. 7848-R-4; August, 1959.

[18] P. Palluel and A. K. Goldberger, "The O-type carcinotron tube," Proc. IRE, vol. 44, pp. 333–343; March, 1956.

[19] R. L. Krulee, "Carcinotron noise measurements," IRE Trans. on Electron Devices, vol. ED-1, pp. 131–133; December, 1954.

[20] R. E. Booth and R. G. Veltrop, "Detection and Measurement of Spurious Signals Generated by Microwave Oscillator Tubes," Sylvania Electric Products, Inc., Mountain View, Calif. Tech. Memo. EDL-M72; January 9, 1958.

[21] J. K. Shimizu, "Strip-line 3-db directional couplers," 1957 IRE WESCON Convention Record, pt. 1, pp. 4–15.

with a predetermined current reference. The resultant error current drives a transistorized chopper-stabilized dc amplifier which in turn controls an *S*-band ferrite attenuator. The attenuator, inserted between the local oscillator and the mixer, varies the local oscillator power in such a manner that the crystal current remains constant. By this method crystal conversion-loss variations are minimized.

Local Oscillator

In order to scan the frequency range of 2000 to 4000 Mc, the local oscillator is swept electronically at a rate of 10 sweeps per second in synchronism with the cathode-ray tube display sweep.

A backward-wave oscillator (BWO) requires the helix voltage to be varied in an exponential manner to insure a linear frequency-time relationship. To provide this characteristic, a direct-coupled bootstrap generator with positive feedback is used. When gated, this unit generates a voltage waveform which increases exponentially with time. Adjustments for varying sweep voltage amplitude and waveform permit replacement of the BWO and attainment of a frequency sweep linearity within ±5 per cent.

Since the sweep voltage range of the BWO is about 3000 volts, an adjustable high-voltage power supply of −4000 volts is provided. A block diagram of the BWO sweep control is shown in Fig. 5. The BWO and a

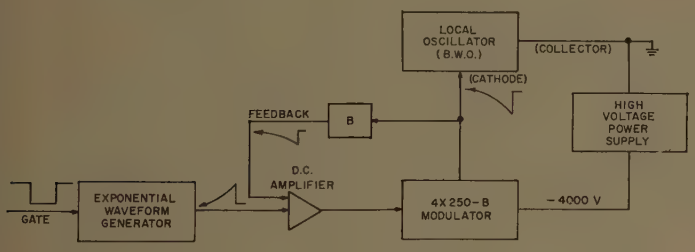

Fig. 5—Block diagram of the local oscillator sweep control.

4X250B sweep control tube are in series with the high-voltage supply and since the collector of the BWO is at ground potential, the cathode of the 4X250B is returned to the high voltage tap. Thus, varying the control-grid level (and hence the plate voltage) of the 4X250B will change the cathode voltage of the BWO. A dc amplifier is provided between the bootstrap generator and the sweep-control tube, with voltage feedback from the BWO cathode to the input of the amplifier. A large amount of dc and sweep signal stabilization is realized with this technique, thus insuring minimum frequency drift and maximum sweep linearity. The BWO frequency is manually controlled by replacing the bootstrap generator waveform with a variable dc voltage.

The highly-stabilized BWO anode and filament power supplies are referenced at the cathode potential. Power supply ripple and control-loop pickup have been minimized to prevent undesirable frequency modulation of the BWO power output.

Extensive use of protective devices and circuitry in the local oscillator sweep-control unit prevents damage to the BWO and associated power supplies due to primary power interruptions, thermal overload, or component failures.

Video Amplifiers

Operational use of the receiver in radio astronomy measurements requires a short-term gain stability of at least ±0.3 db per day, and a long-term gain change of less than 10 per cent after one month of operation.

It is also important that bandwidth stability be maintained. The receiver has selectable, stable video bandwidths of 1.0, 2.5, or 5.0 Mc which are determined by passive filters.

Each IF output of the crystal mixer is transformer-coupled to separate video cascode amplifiers. The transformers provide the required IF source impedance to the amplifiers for minimum noise figure. The output plates of the cascode-circuit tubes share a common load resistor. Thus the desired signal is added while the local oscillator noise is cancelled. The lower-frequency cutoff of these amplifiers is designed for 75 kc to prevent noise figure deterioration.

The cascode-circuit output is then amplified to a level sufficient for coaxial-line transmission to a remotely located video amplifier.

The signals from the RF-unit are amplified successively by a low-level video amplifier, a linear or a logarithmic response video amplifier, and a video driver unit. The output of the latter is sufficient to drive the grid of the cathode-ray display tube.

All the video amplifiers employ feedback-pair construction to insure maximum gain stability with time. Types 6688 and 5670 tubes make up the feedback pairs in all but a few instances where the type 5687 tube is substituted to accommodate higher signal levels. These tubes have a minimum transconductance variation with time, which improves long-time gain stability. The feedback pairs provide a very low dynamic output impedance.

Since the bandwidth cannot be stabilized with feedback-pair techniques, the bandwidth of each amplifier is maintained at approximately 3 to 4 times the desired over-all video bandwidth. An LC low-pass filter of 1.0, 2.5, or 5.0 Mc bandwidth maintains a stable bandwidth independent of amplifier bandwidth variations.

The logarithmic amplifier compresses a 60-db input range to a 20-db output range, approximating a true logarithmic characteristic within ±1 db. The amplifier contains seven feedback pairs and uses type 6688 and 5670 tubes. Interstage diode gain-switching techniques are used to compress the signal. A gain control at the

amplifier output provides more than 10 to 1 range of control.

The linear amplifier likewise consists of seven feedback pairs. This amplifier provides a 40-db dynamic voltage range while maintaining the response linear to within ±5 per cent. It has a maximum voltage gain of 85 db and the output gain control has a minimum of 10 to 1 range of control.

The video driver unit has a low output impedance and provides a maximum linear drive to the display tube of 35 volts peak-to-peak.

Display

To obtain the over-all frequency resolution in the display, it is necessary to consider the resolution of the receiver, the cathode-ray tube, the film, and the camera lens. When using the normal commercially developed 35-mm Plus-X film, and a high-quality lens, the receiver resolution is the limiting factor in the over-all resolution of the final record.

The display system consists of a synchronizer circuit, a sweep waveform generator, a sweep deflection amplifier, a high-resolution cathode-ray tube and its associated power supplies, and a special recording camera.

The synchronizer circuit is a free-running unsymmetrical multivibrator that provides time coincidence between the local oscillator and the display-tube sweep. The sweep duration is 90 msec and the retrace time is 10 msec, yielding a 10-cps sweep rate. One output from the multivibrator gates the sweep circuitry for the local oscillator, while a second output provides retrace blanking for the cathode-ray tube. A third output gates the cathode-ray tube horizontal sweep circuit.

The sweep generator of bootstrap design develops a very linear sawtooth voltage at the 10-cps rate. A gain control at the cathode-follower output of the generator varys the horizontal deflection amplitude.

A single-ended dc amplifier accepts the sweep voltage input and supplies the necessary current to drive the horizontal deflection coil. Linearity of the current output and stability of the amplifier are maintained by employing approximately 40 db of negative current feedback from the output to the input of the amplifier. A control provides adjustment of the static horizontal positioning of the trace.

The indicator tube is a DuMont type K1207PAX having a resolution of 1400 black and white lines across the 5-inch face, and is magnetically focused and deflected. Video and frequency-marker signals are applied to the control grid in order to obtain an intensity-modulated display. Since the horizontal sweep is linear and synchronous with respect to the local oscillator sweep, the camera photographs a frequency-time-intensity plot of solar radio emission. The retrace blanking waveform is applied to the cathode.

The cathode-ray tube high-voltage power supply is regulated to ±1 per cent and is controlled to prevent premature application of high voltage.

Both static and dynamic focus controls are provided, since the beam on a flat-faced display tube is either focused near the center of the trace or on the edges. Dynamic focus is achieved by integrating the sweep sawtooth waveform and using this signal to control the dynamic focus coil current. The static focus circuitry controls the steady-state focus current.

Frequency and Time Markers

Markers are obtained at 500 Mc intervals by coupling BWO energy through five resonant cavities. To obtain the necessary compact assembly, the cavities and crystal mount are integrated into a unit consisting of a coaxial-line crystal mount surrounded by five coaxial resonant cavities. The resonators are coupled to the crystal mount through a long aperture extending the full length of the housing. At each marker frequency a cavity is adjusted to resonate and absorb power, therefore the detected output exhibits a sharp dip when the input frequency from the local oscillator sweeps across a cavity frequency.

Since unwanted, although slower, voltage variations appear at the detected output in conjunction with the desired markers, a simple RC high-pass filter is provided to pass the markers and attenuate the unwanted variations. The markers are amplified by a video preamplifier to a level suitable for coaxial transmission to a remotely located marker unit.

This unit consists of three stages of video amplification, a Schmitt trigger circuit (which is adjusted to actuate on strong marker signals and is therefore insensitive to noise), and a blocking-oscillator output stage. Markers appear on the cathode-ray tube trace at predetermined time intervals spaced 500 Mc apart. (Markers are produced at 2.0, 2.5, 3.0, 3.5, and 4.0 kMc.)

Calibration System

It is desirable that solar sweep-frequency receivers include a calibration system. The equipment (excluding the display system) can be designed to be quite linear, but the characteristics of both the cathode-ray tube and the film are nonlinear. The calibration system incorporated into this receiver operates as follows: The input to the balanced mixer is transferred from the antenna to a broad-band noise source. This known noise temperature produces a given density on the film. Then the attenuation in the video amplifier is decreased in steps of 1 or 2 db, thereby giving stepped calibration densities on the film. This method does not take into account the effects of the antenna gain variations with frequency which requires a more elaborate calibration technique.

A special broad-band noise source was designed and developed for this equipment. It employs a fluorescent light discharge tube as the noise source. This noise source, which is located in the RF unit, consists of a waveguide mount for the discharge tube which matches the impedance of the noise source to the H_{10} waveguide

mode. A transition from the waveguide mode to the coaxial line furnishes a good impedance match over the entire range of 2000 to 4000 Mc. The over-all VSWR is shown in Fig. 6. The noise source is stabilized against temperature variations, and is remotely operated from the main control panel.

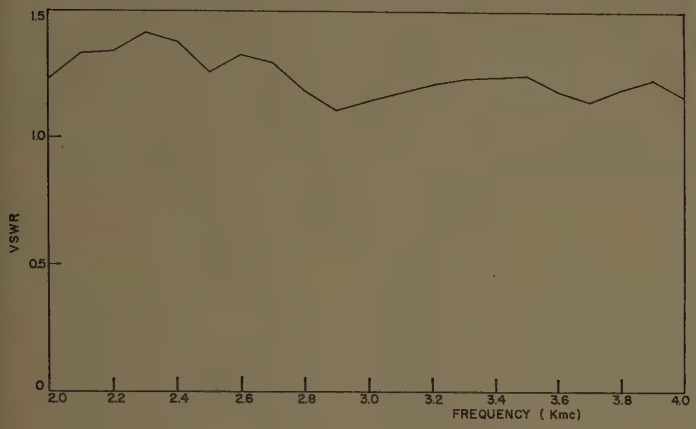

Fig. 6—VSWR of the 2000- to 4000-Mc noise source when fired.

It is interesting to note that the first noise source tried in the equipment was the coaxial type utilizing a neon gas discharge tube. Three units of the same model were tried in succession, but each exhibited the same detrimental characteristic. The gas discharge arc was not stable but moved in a cyclic manner at approximately a 50-kc rate. Local oscillator power entering the noise source from the mixer was modulated at this rate and fed back to the mixer whereupon a 50-kc component was added to the noise entering the video preamplifier. This component completely masked the desired calibration noise. Varying the noise source current and/or changing the gas pressure of the discharge tube had no effect.

Performance and Results

Every reasonable effort has been made to stabilize the receiver. The low voltage supplies maintain a 0.005 per cent voltage regulation, while the input line voltage is regulated to within 0.1 per cent.

The mixer assembly has been temperature-stabilized to prevent excessive conversion-loss variations. A uniform gain characteristic over the band is due to careful design of the microwave components, and gain-time stability is designed into all the video amplifiers by using a large amount of feedback.

Even with this care, various troubles have appeared in this equipment. Several of the components were just recently developed and must be further improved before maximum operational reliability of this receiver is achieved.

Fig. 7 shows one of two types of centimeter-wave bursts that have been recorded. Both types of bursts have a wide spectrum. One type occurs at the same in-

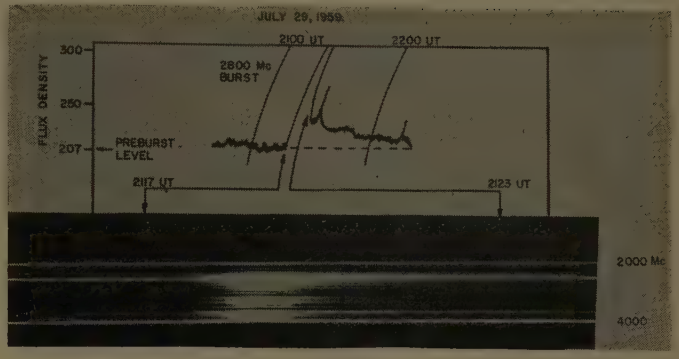

Fig. 7—Record of July 29, 1959, including a single-frequency recording from Ottawa, Canada.

stant as the type III meter-wave burst and is of short duration. The second type also occurs simultaneously with a type III meter-wave burst but with a type IV meter-wave burst following the type III. Only the more intense part of the storm is recorded.

Kundu and Haddock[22] present a more complete discussion of centimeter-wave solar bursts and these sweep-frequency recordings.

Other Applications

Although the receiver was originally designed for measurement of solar emission, its use and application are not limited to solar studies, or in fact, to *S* band. To the contrary, these techniques are applicable to *L*, *C*, *X*, and higher bands, wherever a wide-band, low-noise, gain-stable sweep receiver is required.

Appendix

The solar flux density S of the quiet sun is about 100×10^{-22} w m^{-2} (cps)$^{-1}$. The collecting area A of the 28-foot antenna is about 30 m^2. For one polarization, the power per cycle into the receiver terminals is as follows:

$$P_s = 1/2\ SA = 15 \times 10^{-20} \text{ w (cps)}^{-1}.$$

Converting to an equivalent antenna temperature,

$$T_a = \frac{P_s}{k} = 11{,}000°\text{K}.$$

For a sweep-frequency receiver the minimum detectable input temperature is limited by changes in receiver gain, attenuation and mismatch in the input circuitry, and statistical fluctuations of the noise from the antenna and the receiver.

Since the receiver is operated as a total-power receiver, the equivalent temperature fluctuations caused by changes in receiver gain are directly proportional to the fractional change in receiver gain times, the sum of the antenna and receiver temperatures.[23] Since this temperature term is large, it is necessary to stabilize the

[22] M. R. Kundu and F. T. Haddock, "Centimeter-wave solar bursts and associated effects," this issue, pp. 82–88.

[23] P. D. Strum, "Considerations in high-sensitivity microwave radiometry," Proc. IRE, vol. 46, pp. 43–53; January, 1958.

receiver gain by using well-regulated power supplies, large amounts of feedback in the video amplifiers, and temperature stabilization of the RF components.

Some improvement in the minimum detectable input temperature can be obtained by visual or photographic integration of the record. This improvement is proportional to the square root of the number of traces effectively integrated,[23] limited visually by the number of traces which the eye is capable of integrating and, photographically, by the amount of time resolution which is desired in the record.

Attenuation and mismatch in the input circuit up to the video amplifier reduces the signal power available at the input to the receiver and produces gain variations with frequency in the output record. If the gain variations with frequency are sufficiently large it makes integration and interpretation of the record difficult.

The tangential sensitivity due to statistical fluctuations of the noise, if given by the expression

$$\Delta T = \frac{K(T_R + T_A)}{\sqrt{B\tau}},$$

where

T_R = effective receiver noise temperature,
T_A = effective antenna temperature at the receiver input,
B = effective IF amplifier bandwidth,
K = system constant which depends upon the method of detection and filtering, and upon the operators skill at analysis of the record. The value for K generally varies between 2.5 and 5.0.[23]
τ = dwell time at any one frequency band of $2B$ at the receiver input (when B is larger than $\sqrt{(f_H - f_L)/2t_s}$, as is usually the case).

$$\tau = \frac{Bt_s}{\Delta f},$$

where

t_s = time of a scan, excluding retrace time,
Δf = total RF frequency range scanned by the receiver.

So

$$\Delta T = K \frac{(T_R + T_A)}{\sqrt{2B}} \frac{(\Delta f)^{1/2}}{(t_s)^{1/2}}.$$

Next, determine the relationship between T_R and the noise figure of the receiver. The average noise figure of a linear system is defined as the ratio of 1) the total noise power delivered by the system into its output termination when the noise temperature of its input termination is standard (290°K) at all frequencies, to 2) the portion thereof engendered by the input termination. For heterodyne systems, portion 2) includes only that noise from the input termination which appears in the output via the principal frequency transformation of the system, and does not include spurious contributions such as those from image-frequency transformations.[24]

For this receiver

$$F = \frac{2kT_RB + kT_0B}{kT_0B} = \frac{2T_R}{T_0} + 1.$$

When F equals 12 db or a ratio of 15.8, T_R equals about 2140°K. Let K be equal to 4, τ equal to 0.1 sec, and B equal to 5 Mc. Then ΔT equals 1050°K or an equivalent change to flux density of 9.6 units.

Acknowledgment

The authors express their appreciation to personnel of the Space Communications Laboratory of ITT-Kellogg, including R. J. Garcia, J. Hessler, and R. E. Allen, for their invaluable contribution to the microwave portions of the equipment, to H. R. Meadows for his valuable help in getting the receiver into operation, and to M. L. McCrea for his excellent assistance in the video circuitry development.

The authors also wish to thank Prof. F. T. Haddock and Dr. M. R. Kundu of the Radio Astronomy Project of the University of Michigan for the assistance they have given. Prof. Haddock outlined the requirements for the receiver, provided a summary of previous work in the centimeter-wavelength region, and made many valuable suggestions toward the successful operation of this receiver. Dr. Kundu has aided in the classification and theoretical presentation of the data, and has shown a continued interest in this area of research.

This work was supported by the Office of Naval Research Contract Nonr 1224 (16).

[24] "IRE standards on electron devices: methods of measuring noise," Proc. IRE, vol. 41, pp. 890–896; July, 1953.

Recent Developments and Observations with a Ruby Maser Radiometer*

M. E. BAIR†, J. J. COOK†, L. G. CROSS†, AND C. B. ARNOLD†

Summary—An *X*-band ruby maser radiometer is discussed. In particular, recent developments in the equipment design are detailed. Observations of radio sources are discussed, and response curves with and without the maser preamplifier are given. The detection of 3.45 cm radiation from the planet Saturn is reported, and the equivalent blackbody disk temperature calculated. The future of the maser amplifier in radio astronomy is considered.

Introduction

THE development and initial operation of an *X*-band ruby maser radiometer has been extensively discussed elsewhere.[1] Briefly, the radiometer system utilizes a four-level, push-pull, ruby maser preamplifier operating at 3.45 cm. The significant operating characteristics are approximately:

signal frequency = 8.72 Gc,
pump frequency = 22.4 Gc,
magnetic field = 3850 gauss,
angle; dc field to c-axis = $\theta = \cos^{-1} 1/\sqrt{3}$,
maser gain = 20–23 db,
maser voltage-gain bandwidth product = 300 Mc,
system bandwidth (IF limited) = 8 Mc,
maser gain stability
  short term: <10 minutes = 0.6 per cent,
    <30 minutes = 2.0 per cent,
  long term: >30 minutes = 5.0 per cent,
system noise temperature (equivalent input, excluding antenna temperature) <60°K,
rms noise fluctuations (12-second integration time) = <0.02°K.

The system bandwidth is limited by the intermediate frequency bandwidth to 8 Mc, since at the time of construction, a high performance 8 Mc receiver was available. The present receiver, following the maser, has a noise figure of about 8.5 db (including all noise resulting from components following the maser preamplifier). The maser bandwidth is about 30 Mc. The system gain stability is such that long integration times are possible (up to 42 seconds has been used). These long integration times are in general not usable, as the most reliable radio astronomy observation, the drift curve, does not normally allow the very slow response. Secondly, the system noise temperature and sensitivity of the maser radiometer are such that a 12-second integration time yields a signal-to-noise (peak-to-peak) ratio of about 2 to 1 for a 0.10°K source. Thus, for a very great amount of astronomical research, the maser performs suitably with time constants of 12 seconds or less. It is not until sensitivities below 0.10°K are desired that more integration, or drift curve averaging, becomes necessary.

The ruby maser radiometer is installed on the University of Michigan's 85-foot (26 meter) paraboloidal antenna. This antenna has an efficiency of approximately 50 per cent and a beamwidth of 6.1 minutes of arc at *X* band. These figures have been determined experimentally by observing standard sources.

Since the basic radiometer system has been reported in detail, this paper will concentrate upon the more recent developments and modifications aimed at increasing the sensitivity, reliability, and simplicity of operation. In the latter area, the operation is rapidly becoming routine, to the extent that the radio astronomy personnel, semitrained in maser techniques, are obtaining good results.

The Radiometer System

General

The radiometer is operated as a modified Dicke[2] system. The modification to the original system proposed by Dicke is in the balance of the two input arms. The input switching is between the antenna signal and a comparison source, the two being balanced to within 0.02°K off source on "cold" sky. Thus, the radiometer output is proportional to the difference in these two signals. The output rms noise fluctuation of this type of radiometer is given by[1]

$$\Delta T_{\text{rms}} = \frac{\pi}{2} \frac{(T_{\text{in}})_{\text{eff}}}{\sqrt{B\tau}} + \alpha(\gamma - 1)(|T_{\text{ant}} - T_{\text{comp}}|) \quad (1)$$

where

ΔT_{rms} = rms noise fluctuations at output, °K,
$(T_{\text{in}})_{\text{eff}}$ = total equivalent input noise temperature, °K,
B = system bandwidth, cps,
τ = integration time, seconds,
α = a detection factor ($\cong$1.0),
γ = gain variability factor = $1 + \delta G/G$ where G is maser power gain,
$(|T_{\text{ant}} - T_{\text{comp}}|)$ = input switching unbalance, °K.

* Received by the PGAP, September 21, 1960. This work was conducted by Project MICHIGAN under Dept. of the Army Contract DA-36-039-78801, administered by the U. S. Army Signal Corps, and by the Office of Naval Research, Contract Nonr-1224(16).

† Willow Run Labs., University of Michigan, Ann Arbor.

[1] J. J. Cook, L. G. Cross, M. E. Bair, and R. W. Terhune, "A low-noise *X*-band radiometer using maser," to be published in PROC. IRE.

[2] R. H. Dicke, "Measurement of thermal radiation at microwave frequencies," *Rev. Sci. Instr.*, vol. 17, pp. 268–275; July, 1946.

This expression shows the manner in which various parameters tend to limit the over-all system sensitivity. Further, (1) reveals the maser's major role in the radiometer system. Because of the very low inherent noise of the maser amplifier, the first term is about 20 times less than with a conventional receiver. Also, with the gain stability and balance available, the first term completely dominates (1); therefore, the factor of 20 is extremely significant.

Recent Developments

Recent developments in sensitivity and reliability have been directed to the variables of (1), resulting in several specially developed components and techniques. Although some of the designs are as yet not completely finalized, it is felt that preliminary results warrant their report.

Any Dicke system radiometer requires some source of comparison signal. In the present modified system, the magnitude of the comparison signal is chosen to be as near the off-source antenna signal as possible. Further, since the output is proportional to their difference, the two input signals should ideally be kept exactly balanced when off source. To date, three methods of obtaining the comparison signal have been used: a "cold sky" comparison horn, a cooled load, and the "double horn" technique.

The "cold sky" comparison employs a wide-beam horn pointed away from the antenna surface. Such a device gives an average sky temperature of 10–20°K, obviously dependent upon position and atmospheric conditions. This dependence is a decided disadvantage to this type comparison source. The antenna beam, being relatively small, is affected more by clouds than the wide beam horn. Thus, partly cloudy conditions result in very erratic output variations. Further, as the antenna is moved throughout the sky, the wide-beam comparison horn picks up varying amounts of ground radiation; this results in a varying input unbalance and, hence, output fluctuations. Referring to (1), if the quantity $(|T_{ant}-T_{comp}|)$ varies due to the changing T_{comp}, the instrument sensitivity is affected.

The cooled load system is an attempt to realize the seemingly ideal situation; that of being totally unaffected by either antenna position or atmospheric conditions. A cooled microwave load of sufficient loss radiates as a black body at its absolute temperature, and this can be as low as 4–5°K in liquid helium. This method, although theoretically sound, is practically very difficult. Not only must additional waveguide be cooled to liquid helium temperatures, but also the load material is very critical. At the present time, a completely satisfactory material has not been obtained. Commercial waveguide terminations of carbon base, as well as poly iron, have proven unsuitable, due to changing absorption characteristics at the extremely low temperatures.

In the case of small sources, possibly up to a beamwidth in extent, the "double horn" technique has proven to be a far superior method for obtaining the comparison signal. In this scheme, two identical horns are pointed at the antenna surface. By physically displacing these horns only a few inches, a rather large beam separation is possible. In this manner, one compares two signals originating from discrete areas of the sky. Due to the relatively close and nearly identical beams, the two signals are very closely balanced off source. Many of the problems of the wide beam, "cold sky" comparison scheme are overcome. The double horns are affected almost identically by antenna motion, as well as by clouds and atmospheric variations. Further, they can be constructed and positioned so as to present essentially the same spill-over and back-lobe noise. There is no need for continuous monitoring and correcting of the input balance, as is the case with "cold sky" comparison.

A more practical reason for the use of the double horn technique arises from the man hours required to produce a given amount of data. In the search for signals below the peak-to-peak noise level, standard practice is to average many drift curves. Here the observer is interested in obtaining as much data as possible under given conditions, and avoiding averaging data taken on many different days under perhaps widely varying conditions. By aligning the two horns in declination (a simple procedure), it is possible to use both on a single drift curve, and therefore approximately to double the amount of information possible from a given observation. This method has been successfully demonstrated in observations of the planet Jupiter.

One area for significant improvement is that of feed horn design. The off-source antenna temperature is presently about 30°K, largely due to spill-over and back-lobe radiation. Conventional horn designs which result in illuminations of 10 or even 20 db down at the dish edge are unsatisfactory for maser radiometer use. The illumination beyond the dish edge adds a variable input noise temperature, negligible with even a 1000°K system, but of great importance as the system temperature is reduced to the maser radiometer range.

Preliminary results indicate that it is possible to reduce the back lobes by using a conducting plate behind the feed horn. This radiation has been one of the major contributions to high antenna temperatures because of the close proximity to other equipment mounted at the apex. The mounting arrangement is such that the back lobes see essentially ambient temperature radiators.

Although it contributes to total system noise temperature, the back-lobe problem is of less concern than that of spill-over. Back-lobe noise is essentially constant, while spill-over noise varies as the antenna is moved. This variable input temperature causes an unbalanced switching signal. The varying unbalance has largely been overcome by use of the double horn technique, in

which the signal horn and the comparison horn both illuminate the reflector surface; thus we see comparable spill-over noise variations. The double horn technique, however, is not suitable for use in some observations, primarily because of the problems encountered in data reduction. Also, when observations are being made on extended sources, both horns may pass through portions of the same source. For these reasons, work is now being conducted to reduce the antenna temperature by lowering the spill-over noise contribution.

Preliminary investigations indicate that the most desirable horn design is a conical horn which makes use of its symmetry to illuminate the dish uniformly. This will improve the efficiency by utilizing more of the dish surface. A transition from rectangular to circular waveguide is required, and can be accomplished effectively by feeding from the TE_{11} mode in the circular guide to the TE_{10} mode in the rectangular guide. The circular guide would normally be prohibitive due to its larger insertion loss; however, for the short section required, its contribution to the system noise will be negligible. The authors are investigating the possibility of using concentric, conical horns to obtain an interference pattern to increase the usable area of the reflector, while yielding a sharper cutoff, which is 30 db down at the dish edge.

Regardless of the comparison source, some device to "balance out" the two input arms is necessary. If the input signal is large, say greater than 0.5°K (with a 2 per cent gain instability), the second term of (1) dominates the rms output fluctuation, and the over-all system sensitivity becomes gain-stability limited. Presently, switching unbalances as low as approximately 0.02°K are possible. This precise balance is obtained with variable attenuators in each input arm. In the case of the double horn technique, very little balancing is required, and the attenuators are designed to very strict specifications. Physically, a tiny strip of resistance card is inserted into the center of the wide wall of the *X*-band waveguide. The spring-loaded, tapered strip is cam-driven by a 1-rpm motor. The total loss is variable from <0.05 db to 0.25 db, resulting in a variation in equivalent input noise temperature of <3°K to 17°K in each input arm.

In order to measure antenna temperature, the radiometer must include some method of calibration. The calibration is accomplished in a unique and convenient manner, utilizing matched waveguide loads held at liquid nitrogen and ambient temperatures. These loads feed into the two input ports of a 3-port rotary switch. The output then enters the comparison arm of the radiometer through a 20-db crossguide directional coupler. With the 3-port switch in the ambient load position, the system is balanced and a change to the nitrogen load produces a signal (T_{test}) of approximately 2°K.

The test signal is a function of the ambient temperature according to

$$T_{test} = \frac{T_1 - T_2}{L_1 L_2}, \tag{2}$$

where T_1 is the temperature of the ambient or warm load, T_2 is the temperature of the cooled load, L_1 is the waveguide loss, and L_2 is the coupling at the signal frequency.

The cooled load temperature (T_2) is 77.2 ± 0.3°K, T_1 is ambient temperature for which we allow an error of ± 1.0°K. Measurements show the value of L_1 to be 0.2 ± 0.05 db, and L_2 to be 19.6 ± 0.1 db. Assuming the ambient temperature to be 300°K, a calculation for the test signal indicates $T_{test} = 2.34 \pm 0.06$°K.

The Maser Preamplifier

The maser "head," the heart of the radiometer system, is an original design which was developed specifically for this application [Fig. 1(a)]. The active element is a rectangular parallelopiped of silvered ruby, approximately 0.7 inch $\times$ 0.5 inch $\times$ 0.27 inch (for signal frequency of 8.72 Gc).[3] To allow for minor changes at liquid helium temperature, the coupling cavity, located

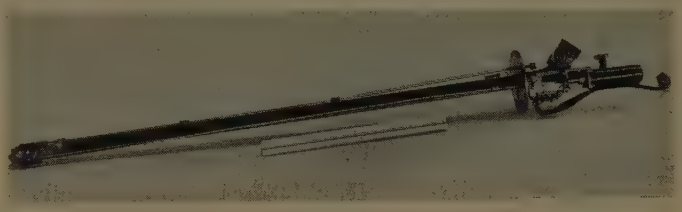

(a)

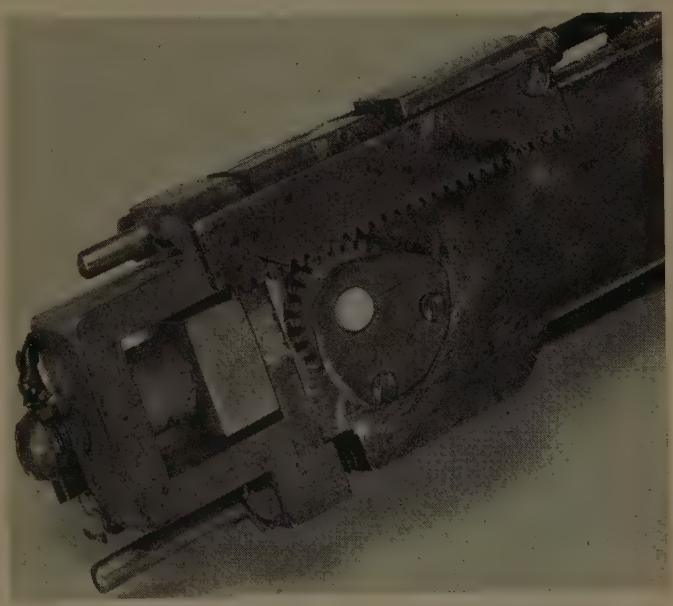

(b)

Fig. 1—(a) Maser "head" ruby maser radiometer. (b) Details of cavity assembly and controls.

[3] L. G. Cross, "Silvered ruby maser cavity," *J. Appl. Phys.*, vol. 30, p. 1459; September, 1959.

between the ruby and waveguide, is variable in frequency. This frequency is controlled by a rack and pinion arrangement, which rotates a teflon plug containing two small silver wires to perturb the resonance field of the coupling cavity. The preamplifier gain is variable, by magnetic tuning, from 10 to 30 db. Physically, a small piece of soft iron is moved near the cavity, producing a field inhomogeneity which broadens the resonance line. These controls are visible in Fig. 1(b).

Recent Astronomical Obervations

Early results with the radiometer have been reported elsewhere.[1,4] Several new observations are now available which are of interest not only in their demonstration of the maser's potential, but also for their contribution to radio astronomy.

[4] A. H. Barrett, M. E. Bair, J. J. Cook, L. G. Cross, and R. W. Terhune, "Preliminary Results with a Maser Radiometer at 3.45 cm," presented at the American Astronomical Society meeting, Pittsburgh, Pa.; April 18–21, 1960 (to be published in *Astronomical J.*).

Observations With and Without Maser

Starting with "relatively" insensitive operation, Fig. 2 shows drift curves of the standard source Cassiopeia A; Fig. 2(a) with the maser preamplifier, and Fig. 2(b) without the maser preamplifier. In obtaining these curves, the drift was first recorded with the maser operating at 17-db gain. The maser was immediately turned off and the drift repeated, using the otherwise identical radiometer system. Time lapse between the end of the curve in Fig. 2(a) and the start of the curve in Fig. 2(b) is less than two minutes. The post-maser IF gain was increased to compensate for the absence

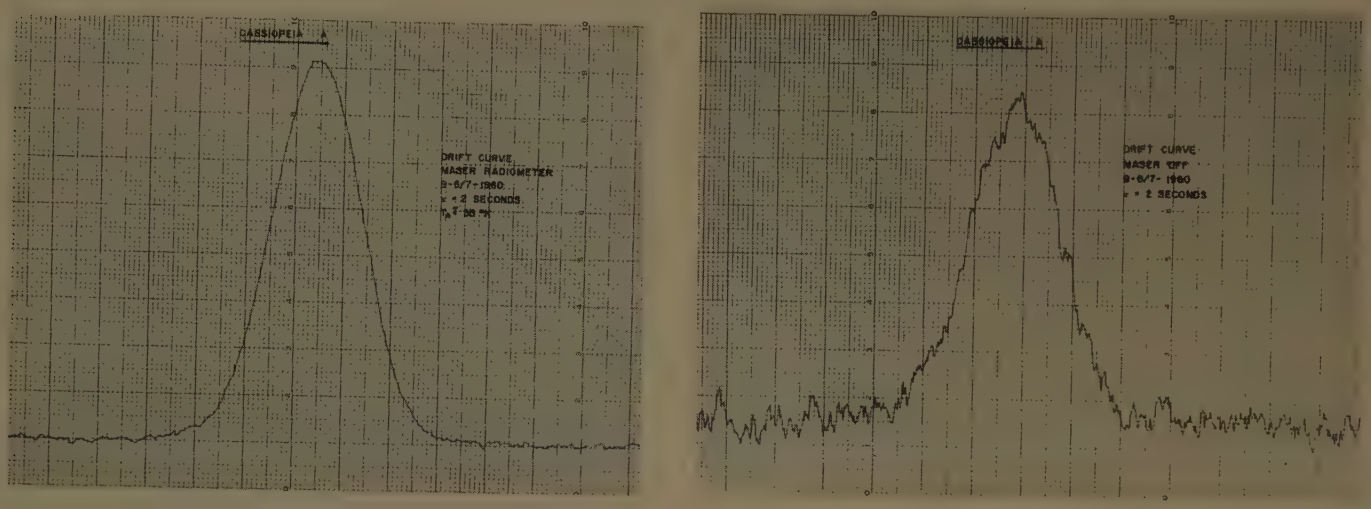

(a) (b)

Fig. 2—Drift curves of standard source Cassiopeia A. Both curves were obtained with the same system, except that (b) has the maser off and its gain replaced by IF gain. $\tau = 2$ seconds, $T_A \cong 35°K$, $\lambda = 3.45$ cm. (a) With maser preamplifier. (b) Without maser preamplifier.

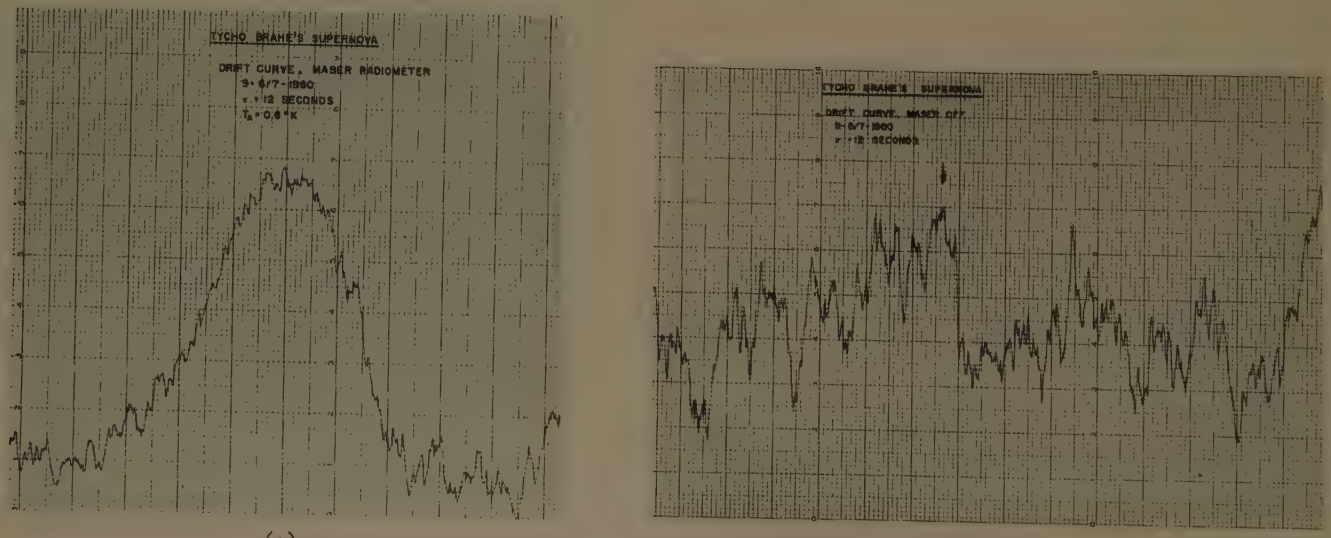

(a) (b)

Fig. 3—Drift curves of Tycho Brahe's Supernova IAU:OON6A. Both curves obtained with the same system, except that (b) has the maser off and its gain replaced by IF gain. $\tau = 12$ seconds. Arrow indicates source position in (b); $T_A = 0.6°K$; $\lambda = 3.45$ cm. (a) With maser preamplifier. (b) Without maser preamplifier.

of the maser gain in the curve of Fig. 2(b). The increase in signal-to-noise ratio, with maser, is obvious. Integration times for both curves is 2 seconds.

Fig. 3 shows similar drift curves for Tycho Brahe's Supernova IAU:OON6A. Again, the only change is the increase in IF gain to replace the maser gain in the curve of Fig. 3(b). Here the source is essentially lost without the maser. Integration time for both curves is 12 seconds.

Radio Detection of Planet Saturn

On August 25, 1960, the authors obtained seven drift curves across the planet Saturn, one of which is shown in Fig. 4. This represents a positive and unambiguous detection of radio emission from Saturn.[5] Although the increase at the planet's predicted position is visible on a single drift curve, the observation was repeated five days later, August 30, to eliminate any possibility of confusion with radiation from other extra-terrestrial sources. At the time of the second observation, the predicted average change in Saturn's right ascension was 37.3 seconds, westward, the measured average change was 36.5 ± 2 seconds, westward. These results are summarized in Fig. 5.

The peak antenna temperature of the first observation was 0.10 ± 0.028°K, while the second was 0.09 ± 0.028°K. The total of fourteen drift curves, with a "superposed epoch" reduction technique, yields a peak antenna temperature of 0.095 ± 0.02°K. This value indicates an equivalent black-body disk temperature of 106 ± 21°K, neglecting the effect of radiation from the rings. A correction factor of 2 per cent has been applied for terrestrial atmospheric absorption.

In these observations, the double horn technique was used. The two identical horns were aligned in right ascension, but separated by 3.5 beamwidths in declination. The entire fourteen drift curves were taken with an integration time of 12 seconds. Referring to Fig. 4, the peak-to-peak noise fluctuations are about 0.06°K. Thus, the rms value, taken as $\frac{1}{4}$ the peak-to-peak, is roughly 0.015°K. The maser radiometer is seen to produce a signal-to-noise (peak-to-peak) ratio of about 2 to 1 with a 0.10°K source, and 12-second integration time.

Long Integration Times

Although integration times longer than 12 seconds are of questionable value with a 6-minute beamwidth, they serve nicely to demonstrate the gain stability and extreme sensitivity of the maser radiometer. Fig. 6 show a 1.9°K test signal with an integration time of 42 seconds. The over-all time shown here is 13 minutes, but the actual stability test ran for 30 minutes with no change other than the slight base line drift shown. The noise is essentially nonexistent; however, if one attempts to evaluate the off-source rms noise fluctuation ($\frac{1}{4}$ peak-to-peak), it is roughly 0.005°K. This seems certain to be the lowest rms output fluctuation demonstrated to date.

Other recent maser radiometer observations have been conducted by the authors and Drs. A. H. Barrett and W. E. Howard of the Radio Astronomy Observatory of The University of Michigan. Among these has been the establishment of upper limits on radio emission of several celestial objects. These are summarized in Table I.

Future of Radio Astronomy Maser Systems

It now seems feasible to construct maser radiometer systems with an order of magnitude greater sensitivity. Such advancement will make maser receivers an order of magnitude more sensitive than even the very optimistic estimates of conventional receivers. Although great advances in traveling-wave systems will continue, the maser has merely begun to show its potential. At *X* band, cavity maser bandwidths seem certain to be extended to 100 Mc or more, while the over-all system noise temperature will be pushed to below 50°K. These values will allow rms threshold sensitivities of a few millidegrees, with integration times of 10 seconds or less.

Further, the use of mechanical refrigerators, although raising the initial cost, will greatly reduce the operational costs of maser receivers. Continual cooling will practically eliminate the need for time-consuming maser adjustments. This will relieve the present need for maser experience in routine operation. One-man operation, at the flip of a switch, is conceivable in the reasonably near future.

Although the atmospheric limitations are not known, there is some feeling that greater sensitivities will be useless, as long as the observer must confine his efforts to the earth's surface. However, the removal of this limitation is definitely only a matter of time.

However, if the greater sensitivities are usable, through the earth's atmosphere, there are almost limitless applications for the future maser's sensitivity.

Planets[6]

Mercury: As yet, no detection has been published. The predicted black-body radiation should be observable on a single drift curve, with future maser systems.

Mars: Very little observational data is presently available. Black-body temperature should be deter-

[5] The peak antenna temperature of Saturn is about 350 times less than that measured from the standard source Cassiopeia A with the same system. In 1957 Brake and Ewen, using a 28-foot antenna and a TWT radiometer at 3.75 cm, reported an antenna temperature of 0.04°K for Saturn. This reported detection was from one "off-on-off" type observation. This same paper reports an antenna temperature of 2°K from Cassiopeia A. Their ratio of 50 would predict an antenna temperature of about 0.7°K from Saturn with the University of Michigan's 85-foot antenna, as opposed to our measured 0.10°K. The solid angle subtended by the planet during our measurements was the same as during the Drake and Ewen measurement of 1957. See F. D. Drake and H. I. Ewen, "A broad-band microwave source comparison radiometer for advanced research in radio astronomy," Proc. IRE, vol. 46, pp. 53–60; January, 1958.

[6] Prof. F. T. Haddock, W. E. Howard, and A. H. Barrett, private communication.

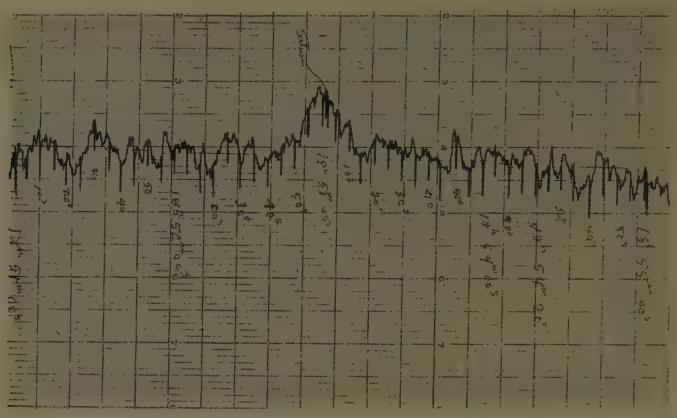

Fig. 4—Drift curve of the planet Saturn, obtained with the maser radiometer, August 25, 1960. $\tau=12$ seconds, $T_A=0.10°K$, $\lambda=3.45$ cm.

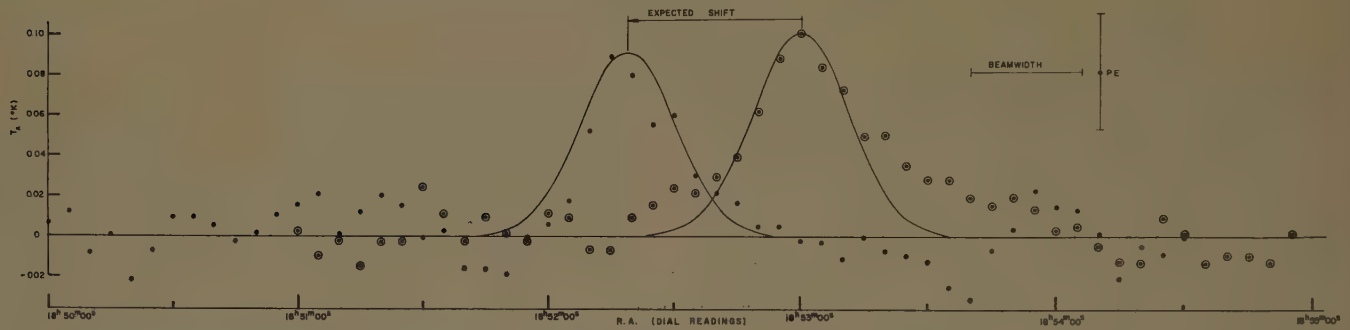

Fig. 5—Drift curves of planet Saturn taken five days apart. Each curve is the average of 7 individual drift curves. Solid lines are Gaussian representation at the expected average shift in right ascension. $\lambda=3.45$ cm. ⊙=August 25–26, 1960. ●=August 30–31.

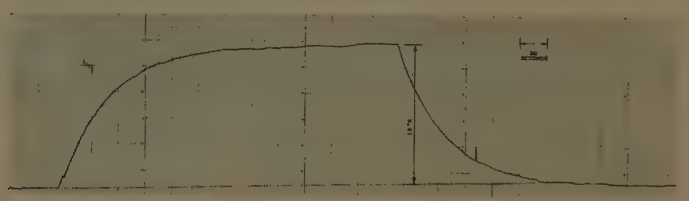

Fig. 6—1.9°K test signal, maser radiometer, March 11, 1960. $\tau=42$ seconds. ΔT_{rms} roughly 0.005°K over 30-minute stability test. $\tau=42$ seconds. $\Delta T_{rms}\cong 0.005°K$.

TABLE I

Object	Date	Antenna Temperature (Upper limit)	Flux (Upper limit)
Nova Hassell 1960	3/10–11/1960	0.07°K	8×10^{-27} w/m² cps
Comet Burnham (1959K)	4/27–28/1960	0.06°K	7×10^{-27} w/m² cps
Supernova in NGC4496	5/ 2– 3/1960	0.09°K	9×10^{-27} w/m² cps

mined with a smaller probable error. Future maser systems will be admirably suited to this type of measurement.

Saturn: Although the present maser system has readily detected this planet, future systems will make extensive studies much more practical.

Uranus: With a predicted antenna temperature of only a few thousandths of a degree, the detection of this planet seems to demand the sensitivity of advanced maser receivers.

Galactic Objects[6]

Ionized Hydrogen Regions: An advanced maser should make possible the mapping of several such regions. Such observations promise to yield valuable information on electron densities in these objects, with resulting in-

formation on physical conditions in the interstellar medium.

Planetary Nebulae: The present maser system has produced the first positive detection of any planetary nebulae, at any radio frequency.[7] Future maser radiometers should make several more of these sources available for study.

Supernovae: Sources such as Tycho's Supernova and Kepler's Supernova are so weak as to require the maser's sensitivity for good high-frequency measurements. Several such sources should become available for study as thresholds are reduced.

Extra Galactic Objects[6]

Other Galaxies: Most of these sources have such steep spectra as to be unobtainable with conventional receivers. Detection and measurement of several galaxies should be realized with advanced maser radiometers having sensitivities of a few millidegrees.

Since this list is not at all exhaustive, the maser's radio astronomy future looks very bright indeed.

[7] A. H. Barrett, W. E. Howard, F. T. Haddock, M. E. Bair, J. J. Cook, and L. G. Cross, "Measurement of Microwave Radiation at 3.45 cm from the Planetary Nebula NGC 6543", paper presented at American Astronomical Society meeting, New York City, N. Y., December 28–31, 1960.

Conclusions

The positive detection of the planet Saturn and the first detection of a planetary nebula (NGC 6543), has proven the effectiveness of the ruby maser in radio astronomy. On a single drift curve, the maser radiometer is capable of detecting sources with antenna temperatures of 0.10°K using a 12-second integration time. Conventional receivers would require much longer integration times. In general, good drift curves cannot be obtained with integration times much greater than 12 seconds. However, conventional radiometers, using 12 seconds integration time, require many drift curves and a detailed averaging process to detect a 0.10°K signal.

Therefore, in radio astronomy the maser has definitely established its usefulness as a low-noise, stable preamplifier.

Acknowledgment

The authors wish to thank G. Makhov and Prof. F. T. Haddock for continued interest and support. They wish to express their gratitude to A. H. Barrett and W. E. Howard for their guidance and support. Special acknowledgment is due J. Tanner, B. Gary, R. Yorks, J. Talen, G. Latimer, R. Banta, F. Alred, and W. Flowers for technical assistance.

Tolerance Theory of Large Antennas*

R. N. BRACEWELL†, FELLOW, IRE

Summary—**The design of an antenna calls for definite amplitudes and phases of the currents, but when the antenna has been constructed and adjusted, there will be departures from the design currents because of several factors. The customary procedure of taking radiation patterns and making the final adjustments semi-empirically has usually been satisfactory, but two difficulties have been setting in with the trend towards large antennas of high gain. First, it is impossible to measure the radiation pattern of the largest existing antennas; even the determination of single sections through the pattern or the gain in one direction presents difficulty. Second, the adjustments themselves are more laborious on larger antennas. It is therefore very desirable that the theory of antenna tolerances should be pursued so that the effect of departures can be taken into account, statistically or otherwise, during the design.**

This paper considers the effects of systematic and random errors on the radiation pattern of antennas representable by a field distribution over an aperture, such as paraboloidal reflectors and large arrays of small elements. In the case of paraboloids, the deterioration in directivity is found to depend on the mean square departure of the surface from the paraboloid of best weighted least-squares fit and on the two-dimensional autocorrelation function of the departure. The variation of directivity with wavelength of a particular paraboloid is deduced by leaving out of account those two-dimensional Fourier components of the departure with spatial periods less than a wavelength.

Practical steps are considered for unifying testing, adjusting, and design so as to lead to the greatest relaxation of the mechanical tolerances imposed on construction.

* Received by the PGAP, September 14, 1960. This research was supported by the U. S. Air Force Office of Scientific Research under contract number AF 18(603)-53.

† Radio Astronomy Inst., Radioscience Lab., Stanford Univ., Stanford, Calif.

I. Introduction

A GOOD deal of detailed work, from various standpoints, has been done on tolerances in antennas. This paper attempts to provide a physical basis from which tolerance studies can be approached. Very often numerical results can readily be derived along the lines indicated here, but the main emphasis is on the picture provided by rather simple ideas of classical diffraction. These ideas are reviewed in Section II.

Many particular cases are studied in Section III in order to show the effect of errors on the directivity of an antenna. In Section IV, other parameters of the radia-

tion pattern are considered and finally, in Section V, features of the theory peculiar to large paraboloids are discussed.

II. The Fourier Transform Relation

It is well known that the relationship between the radiation diagram of an antenna and its aperture distribution involves a Fourier transform; in fact, it is often loosely said that the field radiation pattern is the Fourier transform of the aperture distribution. A more rigorous statement of the Fourier transform relation is needed in the present paper, where some of the principal results depend on intricacies which, in other connections, can sometimes be overlooked.

The Fourier transform relation is based on the fact that the field F over a plane $\zeta=0$ can be expressed as a sum of plane waves as follows:

$$F(\xi/\lambda, \eta/\lambda) = \int_{-\infty}^{\infty}\int_{-\infty}^{\infty} P(l, m) \exp [i2\pi(l\xi + m\eta)/\lambda]dldm,$$

where l, m, n are direction cosines in the right-hand coordinate system, ξ, η, ζ, and

$$P(l, m) \exp [i2\pi(l\xi + m\eta + n\zeta - ct)/\lambda]dldm$$

represents the field vector at (ξ, η, ζ) because of waves in the interval l to $l+dl$, m to $m+dm$. It follows from the two-dimensional Fourier theorem that the inverse relationship

$$P(l, m) = \int_{-\infty}^{\infty}\int_{-\infty}^{\infty} F(\xi/\lambda, \eta/\lambda) \cdot \exp [-i2\pi(l\xi + m\eta)/\lambda]d(\xi/\lambda)d(\eta/\lambda)$$

also holds, and it is worth noting that in order to achieve this symmetrical statement, it is necessary to choose as independent variables 1) direction cosines, not angles, and 2) distances measured in wavelengths.

These simple mathematical relationships between the aperture distribution F and the angular spectrum[1] P disguise a number of physical subleties. For example, the power radiated per unit solid angle in the direction (l, m) is proportional to

$$PP^*(1 - l^2 - m^2)^{1/2},$$

since the directions within dl of l, and dm of m, fill a solid angle

$$\frac{dldm}{(1 - l^2 - m^2)^{1/2}}.$$

Evidently, therefore, the radiation pattern, which is an expression of radiated power per unit solid angle as a function of direction, is a more complicated thing than simply PP^*; and there is a further complication. The set of direction cosines l, m, n is subject to the relation

$$l^2 + m^2 + n^2 = 1;$$

hence, when $l^2+m^2>1$, the quantity n becomes imaginary. Under these conditions, the plane wave

$$P(l, m) \exp [i2\pi(l\xi + m\eta + n\zeta - ct)/\lambda]dldm$$

assumes the evanescent form

$$\exp [-2\pi(l^2 + m^2 - 1)^{1/2}\zeta/\lambda]P(l, m) \exp [i2\pi(l\xi + m\eta - ct)/\lambda]dldm,$$

which decays exponentially with ζ and therefore does not contribute to the radiation field.

From this discussion it is clear that the radiation pattern A, as ordinarily understood, is related to the angular spectrum P by

$$A = PP^*(1 - l^2 - m^2), \qquad l^2 + m^2 < 1.$$

A suppressed proportionality factor containing the intrinsic impedance of free space may be reinserted as required, once it is stated whether P represents an electric or magnetic field. However, it is just as well to keep to the simpler expression since the radiation pattern is frequently renormalized, sometimes so that unit effect is produced in some principal direction, *e.g.*,

$$A(0, 0) = 1,$$

and sometimes so that the radiated power is unity, *i.e.*

$$\int\int A dldm = 1,$$

where the integral is taken over values of l and m such that $l^2+m^2<1$.

The aperture distribution function F contains its own subtleties. It is a vector quantity, and for any given P will have a component perpendicular to the aperture plane $\zeta=0$. One often thinks of imposing tangential fields over an aperture, but of course normal components will set themselves up in accordance with Maxwell's equations. The character of the normal field depends on polarization; consequently aperture distributions of tangential field which are symmetrical in ξ and η, *e.g.*, a uniform tangential distribution, do not give rise to radiation symmetrical in l and m. If the distribution is polarized like a sheet of dipoles parallel to the ξ-axis, then a ray proceeding at an angle $\frac{1}{2}\pi-\theta$ to the ξ-axis is reduced by a factor $\cos\theta=(1-l^2)^{1/2}$; the angle which it makes with the η-axis does not matter. Assuming that polarization is constant in direction over the aperture, and aligned with either the ξ- or η-axes, we have finally the relationship between radiation pattern and an imposed

[1] The term "angular spectrum" was introduced by H. G. Booker and P. C. Clemmow, *Proc. IEE*, vol. 97, pp. 11–16; January, 1950.

tangential (electric) field distribution E:

$$A(l, m) = (1 - l^2 \text{ or } m^2)^{1/2} \times \iint_{l^2+m^2<1} E(\xi/\lambda, \eta/\lambda) \cdot \exp\left[-i2\pi(l\xi + m\eta)/\lambda\right] d(\xi/\lambda) d(\eta/\lambda) \times \text{conjugate}$$

The inverse relationship is of course indeterminate.

The foregoing summary lays the basis for the following work which is thus subject to the assumptions incorporated in this section. A physical interpretation which is helpful below is included here and completes the groundwork.

Fig. 1 represents a plane aperture $\zeta = 0$ over which is maintained a tangential field distribution of the form

$$\cos(2\pi\xi/\lambda_1) \cos(2\pi\eta/\lambda_2) \exp i\omega t.$$

Any field distribution can be built up by superposition of components of this form with various values of λ_1 and λ_2, and each such component gives rise to four rays OA, OB, OC, OD for which

$$l = \pm \sin\theta = \pm \lambda/\lambda_1$$

$$m = \pm \sin\phi = \pm \lambda/\lambda_2,$$

as may be deduced by substituting (l, m), $(-l, m)$, $(l, -m)$, $(-l, -m)$, in the earlier expression for a plane wave, and adding the four results together. Conversely, four rays inclined as shown describe the general situation in a rectangular waveguide carrying a single mode. The familiar relations between the propagation constant, the angles of inclination, and the transverse dimensions can be interpreted in terms of the present problem, as also can the cutoff property. As the spatial structure of the Fourier component becomes finer, the four waves spread apart until in the limit of $l = \pm 1$, $m = \pm 1$, λ_1 and λ_2 become equal to λ. If either λ_1 or λ_2 is smaller than λ, then that component sets up an evanescent wave, but it is not necessary for either λ_1 or λ_2 actually to be less than λ for this to happen. The necessary condition for nonevanescence, *viz.*,

$$l^2 + m^2 < 1,$$

becomes

$$\frac{1}{\lambda_1^2} + \frac{1}{\lambda_2^2} < \frac{1}{\lambda^2}.$$

III. Effect of Errors on Directivity

The Directivity Achievement Factor

Directivity is one of the most important design parameters of an antenna, since it measures the success with which the total power radiated from an antenna is concentrated toward a direction of special interest. By the reciprocity theorem, it also measures the sensitivity to reception from that direction, relative to other directions on the average, of suitably polarized signals. The directivity is not invariably of prime importance, but its alternative interpretation as the reciprocal of the effective solid angle of the beam indicates its basic nature.

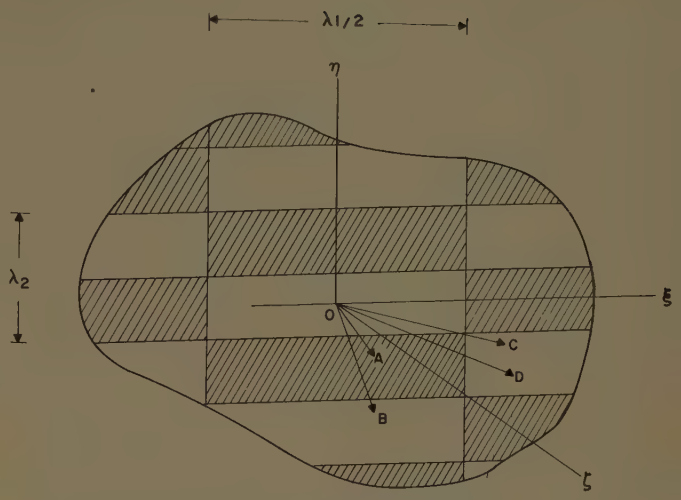

Fig. 1—Rays produced by a cosinusoidal field distribution over an infinite plane aperture.

The directivity is defined by

$$D = \frac{\text{power radiated per unit solid angle in direction of maximum response}}{\text{average power radiated per unit solid angle}}.$$

We wish to relate the radiated power to details of the aperture field distribution E. To do this, we introduce H, the area of the aperture, and E_m, the mean value of E over the aperture:

$$E_m = \frac{1}{H}\iint_H E(\xi/\lambda, \eta/\lambda) d\xi d\eta.$$

Then we can show that D depends on the aperture distribution as follows:

$$D = \frac{4\pi H/\lambda^2}{\frac{1}{H}\iint_H \left(\frac{E}{E_m}\right)\left(\frac{E}{E_m}\right)^* d\xi d\eta}.$$

Or, introducing the compact notation,

$$\langle \cdots \rangle \equiv \frac{1}{H}\iint_H \cdots d\xi d\eta,$$

we can write

$$D = \frac{4\pi H/\lambda^2}{\langle (E/E_m)(E/E_m)^* \rangle}.$$

The assumptions entering into the derivation of this formula are very important for the present subject, but for purposes of continuity the derivation and discussion are relegated to the Appendix. It is sufficient at this stage to note that the assumption of high directivity is involved but that suitable interpretation of E reinstates the formula for use when irregularities in the aperture distribution introduce important side radiation.

When $E=E_m$; that is, when the aperture distribution is uniform, we have

$$D = \frac{4\pi H}{\lambda^2},$$

and we see that departures from uniformity will invariably reduce the directivity.[2]

The factor by which D falls below $4\pi H/\lambda^2$ is defined as the directivity factor $\mathfrak{D}$:

$$\mathfrak{D} = \frac{1}{\langle (E/E_m)(E/E_m)^* \rangle}.$$

In cases of nonuniform distribution, let the complex fractional departure from uniformity ϵ be defined by

$$E = E_m + \epsilon E_m.$$

Then by the definition of E_m, the average value of ϵ over the aperture is zero:

$$\langle \epsilon \rangle = 0.$$

In terms of ϵ, the directivity factor becomes

$$\mathfrak{D} = \frac{1}{\langle (1+\epsilon)(1+\epsilon)^* \rangle} = \frac{1}{1 + \langle \epsilon\epsilon^* \rangle}.$$

The quantity $<\epsilon\epsilon^*>$, the mean squared modulus of the complex fractional departure from the mean aperture distribution, is conveniently described as the variance of ϵ and will be so written; thus,

$$\text{var}\,\epsilon = \langle \epsilon\epsilon^* \rangle = \frac{1}{H}\int\int_H \epsilon\epsilon^* d\xi d\eta,$$

and

$$\mathfrak{D} = \frac{1}{1 + \text{var}\,\epsilon}.$$

As a simple illustration of this formula, consider a rectangular aperture of unit width in the ξ-direction, over which the aperture distribution is $\cos \pi\xi$ (independent of η). Then $E/E_m = \frac{1}{2}\pi\cos\pi\xi$ and $\epsilon = \frac{1}{2}\pi\cos\pi\xi - 1$, with a mean square value of $\pi^2/8 - 1$, whence $\mathfrak{D} = 8/\pi^2$, the familiar result for the directivity of a rectangular horn excited in the TE_{01} mode.

The formula for the directivity factor which has just been derived is immediately applicable to the problem of the effect on directivity of errors in the realization of a design calling for a uniform aperture distribution. In the more general case, the directivity factor will fall below unity for two separate reasons, partly because of design and partly because of errors. It is convenient therefore to introduce a "directivity achievement factor" ζ which measures the extent to which the directivity achieves the design value. Let the antenna be built with actual directivity factor $\mathfrak{D}'$ and actual complex fractional departures ϵ' from the mean actual aperture distribution, the design values being $\mathfrak{D}$ and ϵ. Then

$$\zeta = \frac{\mathfrak{D}'}{\mathfrak{D}} = \frac{1 + \text{var}\,\epsilon}{1 + \text{var}\,\epsilon'}.$$

Random Errors

Consider a large batch of antennas which have been built to a particular design with certain tolerances, or potential antennas which could be built. It may happen that the actual or potential fractional departure from the mean value of the designed aperture distribution can be expressed in the form $\epsilon + \epsilon_r$, where ϵ_r is a random component. By this, we mean that our information about ϵ_r is only partial; *i.e.*, it is of a statistical character and is such that on an average over the batch we would expect ϵ_r to be uncorrelated with ϵ and to be distributed about zero mean value; *i.e.*,

$$\text{expected value of } \langle \epsilon\epsilon_r^* \rangle = 0$$

and

$$\text{expected value of } \langle \epsilon_r \rangle = 0.$$

Assuming for the moment that the random errors are small, we can write the actual complex fractional departure ϵ' from the actual mean in a particular case as

$$\epsilon' = \epsilon + \epsilon_r,$$

and for the mean square modulus of ϵ' we have

$$\text{var}\,\epsilon' = \text{var}\,\epsilon + \text{var}\,\epsilon_r + \langle \epsilon\epsilon_r^* \rangle + \langle \epsilon^*\epsilon_r \rangle,$$

whence

$$\zeta = \frac{1 + \text{var}\,\epsilon}{1 + \text{var}\,\epsilon'} = \frac{1}{1 + \mathfrak{D}(\text{var}\,\epsilon_r + \langle \epsilon\epsilon_r^* \rangle + \langle \epsilon^*\epsilon_r \rangle)}.$$

Averaging ζ over the whole batch we have for the expected value $\bar{\zeta}$

[2] This accords with experience of high gain antennas. The moderate increases obtainable in practice with low gain arrays result in a sense from a different definition of the physical area H. The unlimited *theoretical* possibilities of "super-gain" are, however, included in the formula as interpreted in the Appendix.

$$\bar{\zeta} = (1 + \mathfrak{D}\,\overline{\text{var}\,\epsilon_r})^{-1},$$

where $\overline{\text{var}\,\epsilon_r}$ is the batch average of var ϵ_r.

This very simple result enables many practical questions on tolerances to be answered. It shows that the directivity achievement factor for a uniform array falls below unity by an amount which is about equal to the batch average of the square modulus of the fractional excitation error averaged over the aperture. The effect of designing for nonuniform aperture excitation is always to improve the achievement factor, and is fully taken into account by multiplying in the *design* directivity factor $\mathfrak{D}$.

If the random errors were not small it would be necessary to take account of $\langle\epsilon_r\rangle$. In that case,

$$\epsilon' = \frac{\epsilon + \epsilon_r - \langle\epsilon_r\rangle}{1 + \langle\epsilon_r\rangle}.$$

Random Errors in Arrays

In general the quantity ϵ_r is complex,

$$\epsilon_r = \rho \exp i\delta$$

and

$$\epsilon_r \epsilon_r^* = \rho^2.$$

Therefore, in general,

$$\text{var}\,\epsilon_r = \text{var}\,\rho,$$

and

$$\bar{\zeta} = \frac{1}{1 + \mathfrak{D}\,\overline{\text{var}\,\rho}}.$$

This formula now assumes a special significance in the case of arrays whose elements are designed to be matched to their respective feeder lines but which, in fact, give rise to reflections. Then it will be realized that, in the case of a uniformly excited array, ρ can be interpreted as the modulus of the reflection coefficient on the feeder to each element.[3] As we have shown, the phase angle δ drops out, and so the reflection coefficient need not refer to the precise position of the radiating element. In other words, a knowledge of the standing wave ratio S suffices, for the modulus of the reflection coefficient is given by

$$K = \frac{S - 1}{S + 1},$$

or, in the case of small reflections, by

$$\tfrac{1}{2}(S - 1).$$

For a uniform array of well-matched elements, we have approximately

$$\bar{\zeta} = \frac{1}{1 + 1/4\,\overline{\text{var}\,(S - 1)}}$$

In the general case of a nonuniformly excited array, we must weight the reflection coefficients according to the (modulus of the) aperture distribution. Thus, the design excitation $E_m(1+\epsilon)$ becomes, if the fed element has a reflection coefficient $K \exp i\psi$,

$$E_m(1 + \epsilon)(1 + K \exp i\psi),$$

and this is what we have called $E_m(1+\epsilon+\rho \exp i\delta)$. Hence,

$$\rho = |1 + \epsilon|\, K$$

and

$$\bar{\zeta} = \frac{1}{1 + \mathfrak{D}\,\overline{\text{var}\,(|1 + \epsilon|\, K)}}.$$

Pure Amplitude Errors

It may happen that the excitation of the elements of an antenna is subject to amplitude errors only, or it may be desired to consider amplitude separately from phase. Let the amplitude at a particular element be p per cent wrong, high or low. Weight this by a factor $|1+\epsilon|$ representing the aperture distribution, so that if the excitation of that element is weak, the effect of the error is correspondingly reduced, and let M be the mean square value of $|1+\epsilon|\,p/100$. Then $\zeta = (1+\mathfrak{D}M)^{-1}$ as before, but there is one practical point which must be watched when the errors are not random. If the excitation of all elements is 10 per cent low, obviously no loss of directivity is to be expected. Therefore, in calculating the percentage errors p, calculate them with respect to the *perturbed* mean.

Pure Phase Errors

Of course a pure phase error, if large enough, becomes an amplitude error. We therefore refer to small phase errors of excitation ϕ. If ϕ is measured in radians, then the weighted value $|1+\epsilon|\,\phi$ is the quantity whose mean square value enters into the usual formula. Here again, it is important to omit any net phase shift common to all elements by referring phase errors to the phase of the mean perturbed aperture distribution.

Systematic Errors

Squint: Let the phase error vary linearly with ξ by an amount α radians per meter. Then

$$\zeta = \left(\frac{E_m'}{E_m}\right)\left(\frac{E_m'}{E_m}\right)^*$$

$$= \left[\frac{1}{H}\int\int_H (1 + \epsilon) \exp(-i\alpha\xi)\,d\xi\,d\eta\right] \times \text{conjugate}$$

$$= \frac{PP^*|_\Theta}{PP^*|_0}$$

[3] It is assumed that the junctions of the feeder lines are so designed that reflection from one element of the array does not enter other elements.

where

$$\Theta = \frac{\alpha\lambda}{2\pi}.$$

The loss of directivity is thus entirely caused by a displacement of the pattern PP^* through an angle $\alpha\lambda/2\pi$ without change of shape. Evidently, for many purposes, loss of directivity in this way would not matter. Therefore, before evaluating the effect of phase errors, one subtracts not only the mean phase, but also any linear phase variation, when appropriate.

Monotonic Taper: Let the amplitude of a nominally uniform array vary linearly by plus and minus a fraction Δ over the width W of the aperture. Then

$$\epsilon = \frac{2\Delta}{W}\xi,$$

$$\text{var } \epsilon = \frac{1}{W}\int_{-\frac{1}{2}W}^{\frac{1}{2}W}\left(\frac{2\Delta\xi}{W}\right)^2 d\xi$$

$$= \Delta^2/3$$

and

$$\zeta = (1 + \Delta^2/3)^{-1}$$

This is a remarkably small effect on directivity, *e.g.*, if Δ is twenty per cent, the loss of directivity is $\frac{1}{2}$ db, and if Δ is one hundred per cent, the loss is 1.2 db. The effect on beam shape is considered later.

Quadratic Phase Error: Let the phase error vary as the square of ξ, building up to a maximum Δ at the extremities of the aperture. Then, for uniform excitation, the phase of the perturbed mean excitation is shifted by $\Delta/3$. Hence,

$$\zeta \approx 1 - \text{var}\,[\Delta(\xi/\tfrac{1}{2}W)^2 - \Delta/3]$$

$$= 1 - 4\Delta^2/45.$$

If the aperture is circular and the error varies as $\xi^2+\eta^2$, the result is approximately the same ($\zeta = 1-\Delta^2/12$), and if the excitation is nonuniform, the loss of directivity is diminished and may be calculated by weighting the phase errors as described in the earlier paragraph on pure phase errors.

General Features of Tolerance Theory

The foregoing sections permit several aspects of the antenna tolerance problem to be clarified. For want of better knowledge, tolerances are often quoted in terms of limits which shall not be exceeded, and in any case, this kind of specification would often be desired on grounds of convenience; furthermore, in homogeneous circumstances, as on a production run, it would be appropriate. What we have found here, however, is that it is the mean square error which is significant. Therefore, in a special job, setting an outside limit may impose a penalty; and a manufacturing or adjusting procedure aimed at holding down extreme variations may be different from a procedure for holding down mean square error. This all depends on the error distribution, a function which can assume three very different shapes under outside limit conditions. 1) The error may be truncated Gaussian with root-mean-square breadth much less than the truncation width. In this case, tolerances can be greatly relaxed. 2) The truncation width may be small, so that the error distribution is practically uniform up to the limit. 3) The errors may be concentrated at the limits.

Obviously, there would be quite a difference of approach to the design of a sheet reflector according as rivet heads were required to be less than $\frac{3}{8}$ inch high, maximum height or rms height. Two rivets of maximum height allowed are as acceptable as one under condition 1) but not under condition 2).

The first feature to be emphasized, therefore, is that the mean square error is the significant quantity, and that the directivity factor $\mathfrak{D}$ must be taken into account with it.

Next is the result that departures from the *perturbed* mean, not from the design, are to be held in check. This result shows up in many different ways, usually with the effect that tolerances based on stricter ideas may be relaxed.

Third, in applying these requirements, we do not have to worry about Fourier components in the aperture distribution whose spatial period is less than the wavelength. In reflectors this means that fine corrugations can be left out of account, but in the case of broadside arrays this matter will be automatically allowed for, if the elements are not spaced closer together than half a wavelength.

Finally, before setting the absolute magnitude of the tolerance on a standing wave ratio or a dimension, it is necessary to decide what achievement factor is required. Tolerances are no doubt often set without any clear idea of the effect on the achievement factor and of course it is often necessary for the designer to set tolerances in the absence of full theory. Usually they will be stricter than necessary. The purpose of the present paper is to show how tolerances may be relaxed safely in the case of large and costly antennas where full advantage of theory must be taken. It will be realized how inadequate is a specification calling for a paraboloid of a certain focal length and diameter, "the surface to be true within $\lambda/8$."

Many of the foregoing ideas already have some currency, especially in optics, where the ideas of mean square errors and achievement factor were introduced by Rayleigh.[4] A "Rayleigh criterion" is often quoted in antenna design, sometimes, as in the example above, without mention of mean squares, paraboloid of best

[4] Lord Rayleigh, "Scientific Papers," Cambridge University Press, Cambridge, Eng., pp. 415–459; 1899.

fit, fine structure, directivity factor or achievement factor. Often, however, one or more of these ideas is encountered in correct form.

It remains to emphasize that tolerances applied according to these ideas have the effect of maintaining the *directivity* near to the design value. They are not concerned with radiation proceeding along other directions than the axis of the main beam.

To control the effect of errors on the beamwidth, the beamshape, the side radiation level and other quantities of interest such as lobe structure and depth of nulls, is a different matter which is taken up in the following section.

The basic new feature that appears is that account must now be taken not only of the size of errors, but also of their character, and in more detail than previously, when we merely rejected fine structure.

IV. Effect of Errors on Radiation Pattern

The superposition principle enables us to analyze an actual aperture distribution into two parts, the design distribution and an error distribution. Then the radiation pattern of the error distribution tells us how the actual radiation pattern will depart from the design pattern. By Fourier analysis of the error distribution, we can determine the directions where the effects will be produced, *viz.*, in the directions (l, m) where

$$l = \pm \frac{\lambda}{\lambda_1}$$

$$m = \pm \frac{\lambda}{\lambda_2},$$

and where λ_1, λ_2 are the spatial periods of the Fourier component. Of course, this result is more useful for qualitative or theoretical consideration than for numerical calculations, which would hardly ever be carried out.

The appearance of errors in an aperture distribution will cause a redistribution of directions in which energy is radiated, and, as has been shown under the assumptions stated for random errors, the energy radiated along the main axis is reduced relative to the total radiation. Errors which vary slowly across the aperture will give rise to radiation components at small angles to the axis, influencing the beamwidth and beamshape. More rapidly-varying errors will produce side radiation away from the main beam, and Fourier components which are sufficiently fine structured will not affect the radiation pattern at all (but may introduce selectivity and sensitivity to neighboring objects).

To describe the angular distribution of the error radiation field, one needs to know the spatial spectrum of the error distribution (strictly, that part of it coarser than the wavelength), and if radiated phase is unimportant, as when the error radiation dominates rather than interferes with the design radiation field, then the spatial "power" spectrum, or the autocorrelation function of the error distribution, suffices.

Beamwidth

Beamwidth can be defined in different ways, and the differences are critical in the present discussion. First, consider the effective solid angle Ω, defined as that solid angle into which radiation at the axial intensity would equal the total radiation. We know that

$$\Omega = 4\pi/D.$$

Therefore, the effective solid angle is increased in the presence of errors by a factor equal to the reciprocal of the directivity achievement factor, which we have already shown how to calculate.

The 3- and 10-db beamwidths behave differently. Suppose that a highly directional antenna has small fine-scale random errors which abstract radiation from the main beam and spread it thinly over all directions. Then the main beam will be diminished in strength, there will be a loss of directivity, but no important change in beamwidth at the half and one-tenth power levels. Now, if the errors are enough to have an appreciable effect, the beamwidth to half-power will depend on the error radiation in the directions near the half-power directions. This, in turn, is determined by the spectrum of the error distribution at spatial frequencies of one or two cycles per aperture width. Slowly varying effects such as excitation taper, warp or sag of reflectors therefore make their presence felt as changes in half-power beamwidth. Many special cases can be worked out, allowing for the phase with which the error field combines with the design field in the particular case. However, the following general approximation can often be made. If there are no errors other than the slowly-varying kind, and if considerations of symmetry indicate that changes in radiated power will be the same in both wings of the beam, then the increase in beamwidth may be taken approximately from the effective solid angle. If the bulk of the error radiation does not go into symmetrical fattening of the main beam, this approximation cannot be made.

Beamshape

Enough has been said to indicate qualitatively how errors affect the beamshape. Two examples discussed earlier will illustrate the approach.

Let an aperture designed for uniform excitation have a small monotonic taper in the ξ direction. The error distribution is proportional to ξ times the design distribution, and therefore the error field radiation pattern is proportional to the derivative of the design field radiation pattern and is in phase quadrature (Theorem VI, Appendix). Because of the quadrature relationship, the power patterns add. Now the derivative is a maximum near the points where the design pattern has its nulls.

The principal effect of gradual taper is, therfore, to fill in the nulls. With increasing taper the effect is felt closer in on the main beam where it increases the beamwidth to half power. We note that all the nulls are destroyed, but that the bulk of the error radiation is directed into the vicinity of the first pair of nulls.

Consider now a linear phase shift across a uniform array. The error field radiation pattern is just the same as in the previous case, except that there is no longer phase quadrature. The main error fields are produced in the directions of the first pair of nulls, but on one side of the beam axis the error field is in phase and on the other side in antiphase. Therefore, less power is radiated on one side than before, and more on the other. This qualitative reasoning, which could easily be made quantitative, agrees with what we found before, *viz.*, that the beam shifts without change of shape.

Side Radiation

By side radiation is meant any radiation from an antenna proceeding in directions other than along the main axis. There is very little distinction in application, therefore, between the terms "side radiation" and "radiation pattern." The term sidelobe is sometimes used as a synonym for side radiation, which can lead to confusion in discussing the parts of the radiation pattern just off the main axis. The term sidelobe is here defined as one of the domains, not containing the main axis, into which the radiation pattern is divided by valley lines.

Some important types of side radiation, such as spillover from feeds used with reflectors, reflections from the ground, and effects resulting from feed supporting structures, are not discussed here at all.

Precise detail in the side radiation is not often of much interest; generally its strength is more important. In directions where the error radiation field is comparable with the side radiation expected by design, complicated details can be expected. Even here, however, where the design goes through a null, the strength of the minimum which replaces it can be deduced from the error radiation, and upper limits can easily be placed on the maxima in such a region.

Well away from the main beam, where the design side radiation is very small, the errors may be the principal cause of radiation. One can then calculate the side radiation level directly from the error, or estimate average side radiation from some statistical description of the error distribution, such as its autocorrelation function.

As a special case, consider a highly directional antenna with a random error distribution of such fine structure as to scatter side radiation equally in all directions per elementary solid angle $dldm$. The power radiated in the design pattern is reduced by a factor ζ and the scattered power forms a fraction $1-\zeta$ of the total power radiated. The average scattered power per unit solid angle relative to the axial intensity is

$$\frac{1-\zeta}{2\pi} \Big/ \frac{\zeta D}{4\pi} = 2(\zeta^{-1}-1)/D$$

$$= 2\mathfrak{D} \operatorname{var} \epsilon_r / D.$$

This very interesting result relates the side radiation level to the roughness of a reflector.

V. Paraboloids

The construction of the 250-, 210-, and 150-foot steerable paraboloids at Manchester, Sydney, and Stanford, and plans for others over 100 feet in diameter in the near future have brought special attention to bear on tolerance theory for large paraboloids. The problem for the designers, mainly radio astronomers, has been to make a compromise between the size and highest frequency of operation permitted by surface inaccuracy on the one hand, and cost on the other. In the 50- to 90-foot size range, the problem has not been insuperable, but with cost tending to rise as the cube of the diameter, even a small relief from the direction of tolerance theory is welcome in planning for future very large structures.

In this section, it is assumed that deformation of a paraboloid reflector produces changes of phase, but not amplitude, in the aperture distribution at the point indicated by ray theory. In some parts, also, we ignore the inclination of the paraboloid to the aperture plane, and assume large focal ratios. Some of the assumptions could be improved with care in particular problems, but the main objective here is to explore the subject along the physical line of approach adopted in this paper, and the assumptions seem appropriate to a first-order discussion of the effects of errors.

A practical scheme to measure the deformations of the surface of a large steerable paraboloid is described by Swarup and Yang.[5,6] Modulated reflection produced by a discharge tube placed on the surface of the paraboloid is used to measure the magnitude and phase of the electric field distribution.

Systematic Errors

Squint: Various distortions of the paraboloid and structure supporting the feed at the focus will be examined. Consider, first, the effect of the feed point moving away from the focus of the paraboloid, in a direction perpendicular to the axis. Since the paraboloid is very large relative to the wavelength, and we do not contemplate shifts of more than a wavelength or so, insignificant amplitude changes result from the shift. The principal effect is a progressive phase change across the aperture, in the direction of displacement of the feed, by amounts easily calculated from the geometry. For high focal ratios, it is essentially a linear phase change, with slope proportional to the displacement,

[5] G. Swarup and K. S. Yang, "Monitoring paraboloidal antennas," Proc. IRE, vol. 48, p. 1918; November, 1960.

[6] G. Swarup and K. S. Yang, "Phase adjustment of large antennas," this issue, pp. 75–81.

and therefore gives rise principally to an angular displacement of the beam without change of shape, as discussed in Section III. When this technique is deliberately used for beamswinging, directivity deteriorates at high displacements by an amount which is approximately calculable by subtracting the linear component of phase shift and examining the residual phase and amplitude departures from the design aperture distribution on a ray basis. Since, for most purposes, it is suitable to point an antenna by "peaking up" on a signal, a small amount of squint is acceptable. Variable squint caused by wind, vibration, or temperature change is in a different category, but variable squint dependent on the angle of elevation of a paraboloid on an altazimuth mounting can be calibrated or compensated for. At a certain antenna size, which for some users has already been reached, elevation-dependent squint becomes more acceptable than the structural and cost penalties of a more rigid feed support.

Defocus: Displacement of the feed point axially also produces phase errors, in this case mainly quadratic, but easily calculable in detail from ray geometry. The effect is to reduce the directivity and fatten the beam. As mentioned in Section III, the reduction in directivity with a quadratic phase error building up to a maximum of Δ over a uniformly excited circular aperture is given by

$$\zeta = 1 - \frac{\Delta^2}{12}.$$

Therefore, for a reduction to 90 per cent, a maximum phase error of 1.1 radians can be tolerated, or an axial displacement of rather less than $\lambda/6$, depending on the focal ratio, and rather less than $\lambda/4$ when conventional amplitude distributions are considered.

It is clear that with a large reflector there is very little difference between an axial motion of the feed point and distortion of the paraboloid which simply changes the focal length. Distortion of a paraboloid under its own weight when pointing to the zenith and distortion caused by slow temperature change would be expected to contain a principal component of this character, to which the remarks of the previous paragraph would therefore apply.

Astigmatism: Distortion of the paraboloid in such a way that the circular sections become elliptical can be expected from a variety of causes, notably gravity, temperature gradient, wind gradient, etc. The parabolic sections remain parabolic, but the focal lengths of the parabolas range between extreme values in two perpendicular axial planes, and on a ray approximation, energy received from the axial direction is brought to focus, not at a single point, but at points along a segment of the axis. The extremities of this segment are the foci of the extreme parabolas.

Under these conditions, if a point source is placed on the axis, there will be a loss of directivity, the best position being midway between the extremes. The phase error in the aperture distribution will be approximately of the form

$$\delta = \alpha'\xi^2 + \beta'\eta^2,$$

which can be rewritten

$$\delta = \alpha(\xi^2 + \eta^2) + \beta(\xi^2 - \eta^2).$$

The first pair of terms represents a quadratic phase error of the type we have already considered under the heading of defocus. If we were to remove this pair of terms entirely by adjusting the position of the feed on the axis to the midpoint of the focal segment, the remaining antisymmetrical phase error would constitute the condition referred to as astigmatism. The astigmatic coefficient β measures the extension of the focal segment.

If the extreme phase errors over a circular aperture caused by astigmatism are $\pm\Delta$, then we find by integration that

$$\langle\beta^2(\xi^2 - \eta^2)^2\rangle = \frac{\Delta^2}{4},$$

and so the loss of directivity resulting from astigmatism is given by

$$\zeta = \frac{1}{1 + \frac{1}{4}\mathfrak{D}\Delta^2}.$$

Appendix

We require the following theorems relating to a function of two variables $f(x, y)$ and its two-dimensional Fourier transform $F(u, v)$.

$$F(u, v) = \int_{-\infty}^{\infty}\int_{-\infty}^{\infty} f(x, y) \exp\left[-i2\pi(ux + vy)\right]dxdy,$$

$$f(x, y) = \int_{-\infty}^{\infty}\int_{-\infty}^{\infty} F(u, v) \exp\left[i2\pi(ux + vy)\right]dudv.$$

Theorem I

The two-dimensional Fourier transform of the convolution $h(x, y)$ of two functions $f(x, y)$ and $g(x, y)$ is the product of the transforms of the two functions. We write

$$h(x, y) = f(x, y) * g(x, y)$$

$$\equiv \int_{-\infty}^{\infty}\int_{-\infty}^{\infty} f(x - x', y - y')g(x', y')dx'dy'.$$

Theorem II

The infinite integral of a function is equal to the value of its transform at the origin:

$$\int_{-\infty}^{\infty}\int_{-\infty}^{\infty} f(x, y)dxdy = F(u, v)\Big|_{u=v=0}.$$

Theorem III

The infinite integral of the convolution of two functions is equal to the product of their infinite integrals:

$$\int_{-\infty}^{\infty}\int_{-\infty}^{\infty} h(x, y)dxdy = \int_{-\infty}^{\infty}\int_{-\infty}^{\infty} f(x, y)dxdy \int_{-\infty}^{\infty}\int_{-\infty}^{\infty} g(x, y)dxdy.$$

Theorem IV

The transform of the complex conjugate of a function is the conjugate of the reverse of its transform, *i.e.*, the transform of $f^*(x, y)$ is $F^*(-u, -v) \equiv F_r^*(u, v)$.

Theorem V

According to this theorem, which is referred to in the text, a linear phase gradient $\Theta\lambda/2\pi$ radians per unit distance in the xy plane is associated with a shift θ in the uv plane:

$$F(u - \Theta, v - \Phi) = \int_{-\infty}^{\infty}\int_{-\infty}^{\infty} \exp\left[i2\pi(\Theta x + \Phi y)\right] f(x, y) \cdot \exp\left[-i2\pi(ux + vy)dxdy.\right.$$

Theorem VI

The transform of the derivative of a function with respect to x is $i2\pi u$ times the transform of the function:

$$i2\pi u F(u, v) = \int_{-\infty}^{\infty}\int_{-\infty}^{\infty} \frac{\partial}{\partial x} f(x, y) \exp\left[-i2\pi(ux + vy)\right]dxdy.$$

By definition

$$D = \frac{\text{power radiated per unit solid angle in specified direction}}{\text{average power radiated per unit solid angle}} = \frac{PP^*\big|_{l=m=0}}{\frac{1}{4\pi}\iint_{l^2+m^2<1} PP^*dldm}.$$

If the contributions to the angular spectrum P are concentrated within a range of directions well away from $l=m=1$, *i.e.*, if we are dealing with an ordinary highly directive antenna, then the precise limits placed on the double integral are unimportant, provided they include the radiating regime. We can then say, from Theorems I, II, and IV, that the radiated power is given by

$$\int_{-\infty}^{\infty}\int_{-\infty}^{\infty} PP^*dldm = E^*E_r^*\Big|_{\xi=\eta=0} = \int_{-\infty}^{\infty}\int_{-\infty}^{\infty} EE^*d(\xi/\lambda)d(\eta/\lambda)$$

and from Theorems I, II, III, and IV,

$$PP^*\big|_{l=m=0} = \int_{-\infty}^{\infty}\int_{-\infty}^{\infty} (E^*E_r^*)d(\xi/\lambda)d(\eta/\lambda)$$

$$= \int_{-\infty}^{\infty}\int_{-\infty}^{\infty} Ed(\xi/\lambda)d(\eta/\lambda) \int_{-\infty}^{\infty}\int_{-\infty}^{\infty} E_r^*d(\xi/\lambda)d(\eta/\lambda)$$

$$= H^2E_mE_m^*/\lambda^4.$$

Thus,

$$D = \frac{H^2E_mE_m^*/\lambda^4}{\frac{1}{4\pi}\int_{-\infty}^{\infty}\int_{-\infty}^{\infty} EE^*d(\xi/\lambda)d(\eta/\lambda)} = \frac{4\pi H/\lambda^2}{\frac{1}{H}\int_{-\infty}^{\infty}\int_{-\infty}^{\infty}\left(\frac{E}{E_m}\right)\left(\frac{E}{E_m}\right)^* d\xi d\eta}$$

This is the result used in the paper. The restriction imposed by the substitution of infinite limits can be removed as follows:

$$\iint_{l^2+m^2<1} PP^*dldm = \int_{-\infty}^{\infty}\int_{-\infty}^{\infty} \pi(l, m)PP^*dldm,$$

where $\pi(l, m)$ is a function which is zero where $l^2+m^2>1$, equal to unit where $l^2+m^2<1$, and has a known transform

$$q(\xi/\lambda, \eta/\lambda) = \frac{J_1(2\pi\sqrt{\xi^2+\eta^2}/\lambda)}{\sqrt{\xi^2+\eta^2}/\lambda}.$$

Since we now have infinite limits, the theorems apply exactly and the final result may be obtained by replacing E (which was the transform of P) by the transform of $\pi(l, m)P$, *viz.*, $q * E$. We then have the rigorous result (after applying Theorems II and III to show that E_m is unchanged),

$$D = \frac{4\pi H/\lambda^2}{\left\langle\left(\frac{q*E}{E_m}\right)\left(\frac{q*E}{E_m}\right)^*\right\rangle}.$$

Since $q * E$ is derived from E by removal of those components for which $l^2+m^2>1$, we may interpret it physically as that part of the aperture distribution which remains after removal of those (nonradiating) high-frequency Fourier components with period less than λ. A practical point worth mention is that nonradiating components may have a period greater than λ in a *one-dimensional* slice across an aperture.

A point of interest in relation to theoretical supergain antennas is that $q * E$ may extend beyond the limits outside which E was zero. For ordinary high-gain antennas this fringing field adds a negligible fraction to the physical area, which is a well-defined quantity; but it is significant for small arrays, especially if deliberately intensified. However, the phenomenon of supergain disappears if the increased extent of the impressed field is taken into account (by deeming the physical extent equal to the separation of points between which there is negligible correlation).

Interferometry and the Spectral Sensitivity Island Diagram*

R. N. BRACEWELL†, FELLOW, IRE

Summary—Basic principles of radio interferometry are expounded and a special diagram is established which helps with problems on interferometers, especially those with phase switching or other complications.

The information on a record, or interferogram, made by scanning a compact source or target with an interferometer comprising an antenna with two well-spaced parts, is all in one complex number, the *complex visibility* of the interference fringes. Under appropriate conditions, the complex visibility observed is equal to the *complex coherence* of the field produced by the source between the points occupied by the two elements of the interferometer. (If the elements are not infinitesimal in extent, the complex visibility is equal, instead, to a weighted mean of the values of complex coherence between the pairs of points embraced by the elements.) Furthermore, this quantity gives the strength of one *spatial Fourier component* of the source distribution in amplitude and phase. To know all Fourier components would require the use of all spacings—two dimensions, this means all vector spacings.

Measurements at a finite number of spacings yield the *principal solution;* if the source is finite in extent, only certain discrete spacings need be used. *Spectral sensitivity* of antennas depends on the *complex autocorrelation function* of the antenna aperture distribution. For interferometers, the spectral sensitivity is confined to islands in the spatial frequency plane whose shorelines may be delineated by a simple graphical procedure. The *spectral sensitivity island diagram* offers an alternative approach to interferometer problems. In an application of the diagram, it is explained how the resolving power of a Mills cross is not impaired by deleting half of one arm.

I. Interferometers

An interferometer will be defined for the purposes of this paper as an antenna with two, or more, well-separated parts.[1] In Fig. 1, a two-element microwave interferometer is shown, and, according to our definition, this is a single antenna. Clearly one might also describe it as two antennas whose feeder lines happen to be connected together, but it proves to be advantageous to select a reference point beyond the confluence of the waveguides and to regard this as the input or output of one composite antenna.

This antenna, then, has its own peculiar radiation pattern with nulls in some directions, *viz.*, where the contributions of the two paraboloids cancel. This happens along small circles on the celestial sphere where the path difference p (Fig. 2) is an odd number of half-wavelengths, *i.e.*, where

$$p = d \cos\theta = n\frac{\lambda}{2}, \qquad n = 1, 3, 5, \cdots.$$

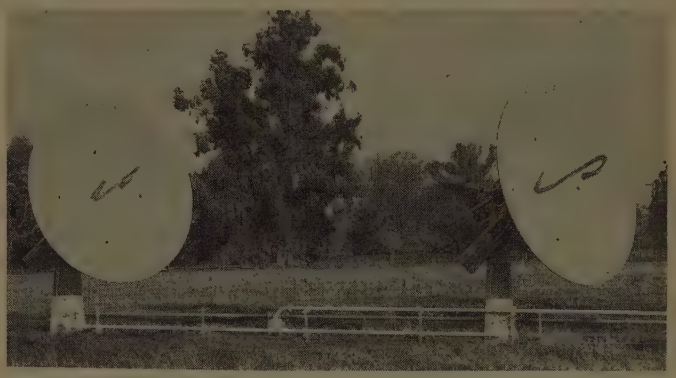

Fig. 1—A two-element interferometer comprising two equatorially mounted paraboloidal reflectors connected together at a central waveguide T junction.

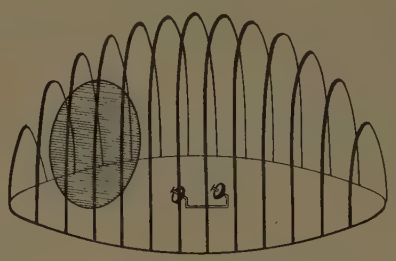

Fig. 2—Small circles showing the interference nulls of an interferometer.

In this equation, d is the spacing of the paraboloids, θ is the angle between any direction and the line joining the paraboloids, and λ is the wavelength of the monochromatic radiation to which attention is being paid. We have assumed that there is an interference maximum on the symmetry plane $\theta = \pi/2$. Evidently, the greater the spacing d, the closer the interference nulls are packed.

While it is true that the small circles $p = n\lambda/2$ are nulls of the radiation pattern of the interferometer, this fact is not very important in directions where the paraboloids are not pointed. The shaded area in Fig. 2 delineates the half-power beam of a single paraboloid. Well outside this area, the interference nulls and intervening maxima are merely potential.

Though interference plays an important role in the formation of the beam of any antenna array, we restrict the name interferometer to antennas whose radiation patterns remind us of the striated interference patterns of optics. Well-separated parts ensures this. For example, in Fig. 3 we see the radiation that was recorded at 9 centimeters as the sun passed through the beam of a stationary interferometer consisting of two 10-foot paraboloids spaced 25 feet apart.

* Received by the PGAP, September 14, 1960. This paper was originally presented at the URSI-IRE meeting, San Diego, Calif., October 19–21, 1959, under the title "Switched Interferometers." The research was supported by the U.S.A.F. Office of Sci. Res. under Contract No. AF18(603)-53.

† Radio Astronomy Inst., Radioscience Lab., Stanford University, Stanford, Calif.

[1] J. L. Pawsey and R. N. Bracewell, "Radio Astronomy," Clarendon Press, Oxford, Eng.; 1955.

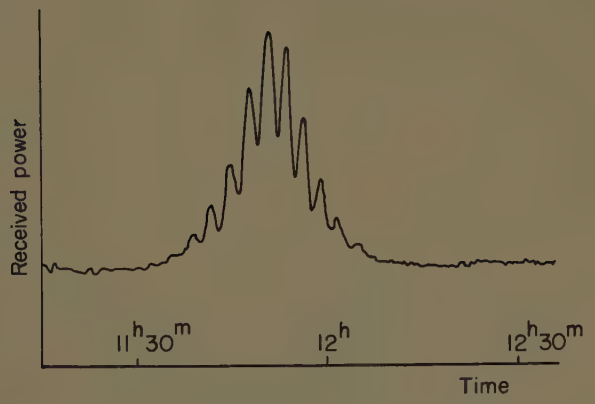

Fig. 3—Microwave radiation received as the sun passed through the beam of an interferometer on September 17, 1957, at Stanford, Calif.

If, instead of the sun, a point source had passed through the interferometer beam, we should have recorded the radiation pattern of the interferometer, complete with nulls formed as the point source crossed the nulls of the interference pattern [Fig. 4(a)]. Since the sun is an extended source, it straddles each null so that the signal received from it (Fig. 3) does not fall to zero until it moves well out of the beam. If the sun were bigger (which it is at longer wavelengths), the depth of modulation recorded would be even less [Fig. 4(b)]. Furthermore, if the antennas were spaced more widely, the depth of modulation probably would be less again, for the interference nulls would be closer together. Fig. 4(c) shows the faster and weaker fringes which one would expect.

Thus, it is clear that the way in which the depth of modulation of the interferogram falls off with increasing spacing depends on the diameter and other details of the source structure.

Although we have used the sun for our example and, following the practice in radio astronomy, have spoken of the celestial sphere, any kind of incoherent radio source or radar target may be substituted. Thus, when we speak of details of source structure, we could be referring to the number and distribution of elements in a cluster of radar point targets.

Furthermore, the scanning produced by the earth's rotation may be replaced by the rapid lobe sweeping technique of Little and Payne-Scott[2] or by simultaneous recording of sum and difference channels as in monopulse radar.[3]

Interferometry furnishes a general tool for bringing high definition to bear in antenna applications. As described here, the two-element interferometer gives one-dimensional resolution; or alternatively, observations

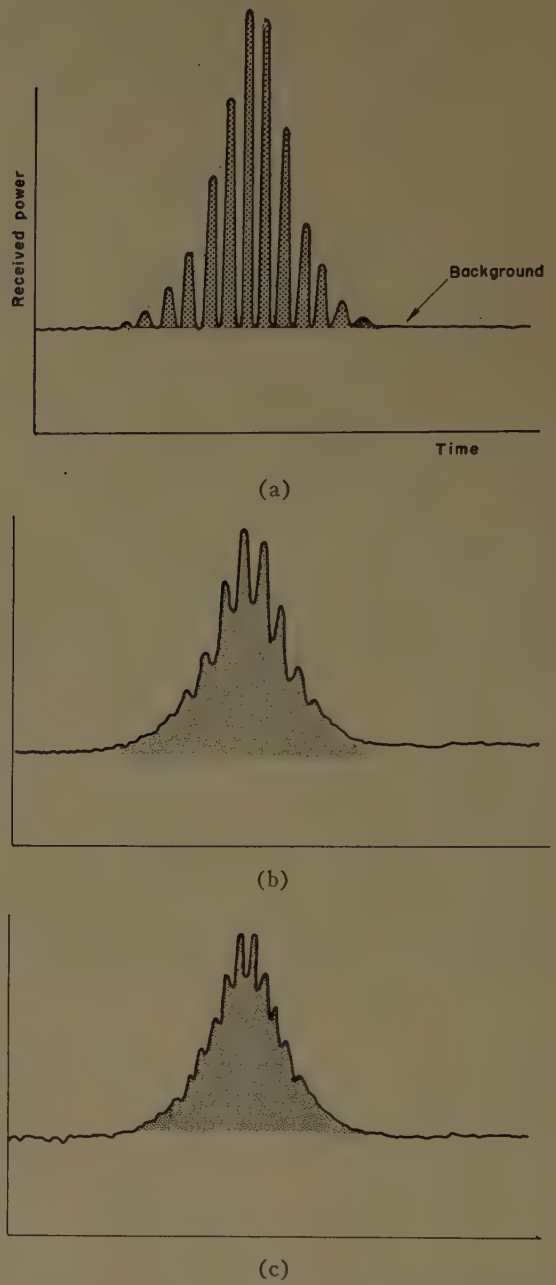

Fig. 4—(a) The radiation received from a point source would trace out the radiation pattern. (b) An extended source (*e.g.*, the sun) gives fringes of lower visibility (less depth of modulation). (c) An extended source, observed with wider spacing of the interferometer elements, exhibiting weaker and faster fringes.

with an interferometer with a baseline extended in one direction only gives information about the equivalent one-dimensional, or line-integrated, source. The reconstitution of a two-dimensional distribution from line-integrated profiles is a soluble problem in integral equations.[4]

II. Procedure for Interferometry

A standard procedure for interferometry is to take interferograms at different spacings d up to as far as is

[2] A. G. Little and R. Payne-Scott, "The position and movement on the solar disc of sources of radiation at a frequency of 97 Mc/s, pt. I—equipment," *Australian J. Sci. Res.*, Ser. A, vol. 4, pp. 489–507; December, 1951.

[3] D. R. Rhodes, "Introduction to Monopulse," McGraw-Hill Book Co., Inc., New York, N. Y.; 1959.

[4] R. N. Bracewell, "Strip integration in radio astronomy," *Australian J. Phys.*, vol. 9, pp. 198–217; June, 1956.

possible or sufficient. The results of this procedure are expressed in terms of the complex visibility v of the interference fringes, as a function of interferometer spacing.

The modulus of the complex visibility is $\mathcal{V}$, the "depth of modulation" of the interferogram, defined by

$$V = \frac{P_{\max} - P_{\min}}{P_{\max} + P_{\min}},$$

where $P_{\max} - P_{\min}$ is the range of received power and $P_{\max} + P_{\min}$ is twice the average received power. As shown in Fig. 5, $P_{\max}$ is the upper envelope and $P_{\min}$ the lower envelope of the interference fringes.

The phase σ of the complex visibility expresses the asymmetry of the interferogram. Thus, if the greatest interference maximum follows the envelope maximum with a time delay T_1, and T is the time interval between successive maxima, then we define σ by

$$\sigma = \frac{2\pi T_1}{T}.$$

Thus,

$$\mathcal{V} = Ve^{i\sigma}.$$

Data from a set of interferograms may be presented as in Fig. 6, where the visibility modulus V is plotted as a function of spacing s measured in wavelengths. The convenient quantity s is defined by

$$s \equiv \frac{d}{\lambda}.$$

As the spacing approaches zero, the interference nulls fall further apart, sources tend effectively to point sources, and V approaches unity. As the spacing increases, V falls off, and may oscillate, but is, in general, not known beyond some finite spacing.

III. Interferograms Measure Complex Coherence

Even though the various parts of a radio source, such as the sun, radiate incoherently,[5] it is apparent that there is coherence between the electric fields $\mathcal{E}_1(t)$ and $\mathcal{E}_2(t)$ which the sun produces at distinct points on the earth's surface. Fig. 3 proves that there is such coherence; if there were not, there would be no rise and fall due to interference.

As a measure of the dependence of the field $\mathcal{E}_1(t)$ at one point on the field $\mathcal{E}_2(t)$ at another point s wavelengths away, we might form the time average of the product, *viz.*,

$$\langle \mathcal{E}_1 \mathcal{E}_2 \rangle \equiv \lim_{T \to \infty} \frac{1}{2T} \int_{-T}^{T} \mathcal{E}_1(t)\mathcal{E}_2(t)\,dt.$$

[5] In this paper, two stationary time-varying quantities are taken to be incoherent if the average of their product, taken over a sequence of time intervals of increasing duration, tends to zero.

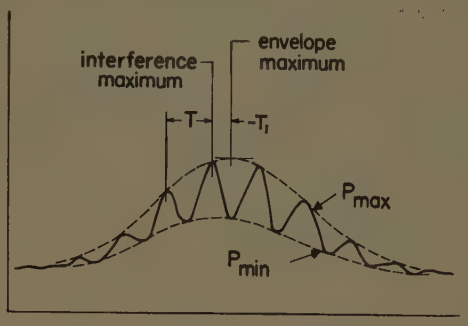

Fig. 5—Defining complex visibility.

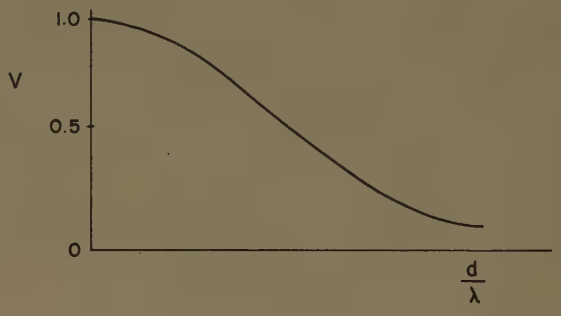

Fig. 6—Fringe visibility V as a function of spacing in wavelengths.

Dividing by the value $\langle \mathcal{E}_1^2 \rangle$ that is assumed when the two points coincide, we obtain the correlation coefficient

$$C(s) = \frac{\langle \mathcal{E}_1 \mathcal{E}_2 \rangle}{\langle \mathcal{E}_1^2 \rangle},$$

which is equal to unity for zero spacing and falls off indefinitely as the spacing increases, *i.e.*,

$$C(0) = 1$$

and

$$\lim_{s \to \infty} C(s) = 0.$$

The precise way in which the correlation coefficient $C(s)$ falls off with spacing is determined by the source diameter and structure. Conversely, however, if we have $C(s)$ for all spacings, we find that we have only one half of the available information. Essentially, this is because fields which are interdependent but in quadrature (related as sin t is to cos t) do not contribute to the correlation coefficient; this is remedied by taking into account the quadrature components of $\mathcal{E}_1$ and $\mathcal{E}_2$.

Let $\hat{\mathcal{E}}_1$ be the quadrature component corresponding to $\mathcal{E}_1$, *i.e.*, what we obtain if, in the Fourier analysis of $\mathcal{E}_1$, we replace each cosine by sine and each sine by minus cosine. Let

$$\mathcal{F}_1(t) = \mathcal{E}_1(t) + j\hat{\mathcal{E}}(t)$$

and

$$\mathcal{F}_2(t) = \mathcal{E}_2(t) + j\mathcal{E}_2(t),$$

where the complex time functions $\mathcal{F}_1(t)$ and $\mathcal{F}_2(t)$ are such that

$$\mathcal{E}_1(t) = \mathcal{R}\mathcal{F}_1(t),$$
$$\mathcal{E}_2(t) = \mathcal{R}\mathcal{F}_2(t),$$

and thus resemble the rotating vectors used to represent alternating quantities.

Now define the complex coherence $\Gamma(s)$ by

$$\Gamma(s) = \frac{\langle \mathcal{F}_1 \mathcal{F}_2^* \rangle}{\langle \mathcal{F}_1 \mathcal{F}_1^* \rangle}.$$

The asterisks represent complex conjugates. We can show in a few lines that

$$\mathcal{R}\Gamma = C.$$

Thus,

$$\begin{aligned} \mathcal{R}\langle \mathcal{F}_1 \mathcal{F}_2^* \rangle &= \langle \mathcal{R}\mathcal{F}_1 \mathcal{F}_2^* \rangle \\ &= \langle \mathcal{E}_1 \mathcal{E}_2 + \hat{\mathcal{E}}_1 \hat{\mathcal{E}}_2 \rangle \\ &= 2\langle \mathcal{E}_1 \mathcal{E}_2 \rangle, \end{aligned}$$

hence,

$$\mathcal{R}\frac{\langle \mathcal{F}_1 \mathcal{F}_2^* \rangle}{\langle \mathcal{F}_1 \mathcal{F}_1^* \rangle} = \frac{\langle \mathcal{E}_1 \mathcal{E}_2 \rangle}{\langle \mathcal{E}_1^2 \rangle} = C.$$

The complex coherence, or complex degree of coherence, as defined here, is a slight but obvious generalization of the quantity introduced by Zernike under the same name. A slightly restricted definition may be given[6] for quasimonochromatic variation at frequency ω in terms of a time-varying phasor $F(t)$ such that $\mathcal{E}(t) = \mathcal{R}F(t)e^{j\omega t}$. Then $\Gamma = \langle F_1 F_2^* \rangle / \langle F_1 F_1^* \rangle$.

A very close relationship exists between the complex coherence $\Gamma(s)$ of a radiation field and the complex visibility $\mathcal{V}$ measured from an interferogram taken at spacing s. When the interferometer is composed of two small equal antennas connected by equal feeders,

$$\mathcal{V} = \Gamma.$$

If the elements of the interferometer are not small,

$$\mathcal{V} = \Gamma_{av},$$

where Γ_{av} is a weighted average coherence taken over the range of spacings embraced by the extended elements.[7] If the two elements have unequal gain, whether due to unequal apertures or feeder efficiencies, then

$$\frac{1}{2}\left(r^{1/2} - r^{-1/2}\right)V = |\Gamma|,$$

where r is the ratio of the power available from each element separately just at the feeder junction. Derivations of these results have been given by Bracewell.[6,8]

An interferometer is to be regarded, then, as an instrument for measuring the complex coherence of a radiation field, in terms of spacing. This function has been emphasized by Wolf[9] in connection with optical interference.

Ability to measure coherence depends on ability to measure power and to bring to one point the signals extracted from the field at two separated points.

IV. Coherence Determines Source Distribution

From interferometer observations of the radiation field of a source, the distribution of intensity over the source can be deduced by taking the Fourier transform of the complex coherence function.[6,8] This result is deducible from the original application by McCready, Pawsey and Payne-Scott[10] of radio interferometry in radio astronomy. The limitation arising from the finite range of spacings that can be attained in practice has been clarified by Bracewell and Roberts,[11,12] in terms of their *principal solution.*

When we make an observation at one spacing (with small elements), we measure one Fourier component of the source distribution; all spacings give us all the Fourier components.

In two dimensions the result is the same: we must then deal in vector spacings, each one of which gives the amplitude and phase of one two-dimensional Fourier component. The interferometer spacing in wavelengths gives the spatial frequency of the component (in cycles per radian) and the orientation of the interferometer baseline gives the orientation of the component (after allowance for projection).

To observe with vector spacings as the independent variable means a lot of work, which, however, is minimized by the use of a theorem[6] which limits the necessary observations to a *finite number* depending on the dimensions of the antenna and the source.

V. Spectral Sensitivity of an Antenna

The spectral sensitivity function helps to handle the concepts which have been introduced. By spectral sensitivity we mean a property of an interferometer, or

[6] R. N. Bracewell, "Radio interferometry of discrete sources," Proc. IRE, vol. 46, pp. 97–105; January, 1958.

[7] Since fine detail in the visibility vs spacing curve is smoothed out by the use of a large antenna, it would seem that information was lost. Clearly, however, the lost detail relates to parts of the sky, well away from the beam axis, that should be pointed at directly if they are of interest.

[8] R. N. Bracewell, "Radio astronomy techniques," in "Handbuch der Physik," vol. 54, Springer-Verlag, Berlin, Germany; 1960.

[9] E. Wolf, "A macroscopic theory of interference and diffraction of light from finite sources. II. Fields with a spectral range of arbitrary width," *Proc. Roy. Soc. (London) A*, vol. 230, pp. 246–265; June, 1955.

[10] L. L. McCready, J. L. Pawsey, and R. Payne-Scott, "Solar radiation at radio frequencies and its relation to sunspots," *Proc. Roy. Soc. (London) A*, vol. 190, pp. 357–375; August, 1947.

[11] R. N. Bracewell and J. A. Roberts, "Aerial smoothing in radio astronomy," *Australian J. Phys.*, vol. 7, pp. 615–640; December, 1954.

[12] R. N. Bracewell, "Two-dimensional aerial smoothing in radio astronomy," *Australian J. Phys.*, vol. 9, pp. 297–314; September, 1956.

any antenna, which tells us its sensitivity to spatial Fourier components of a source distribution. Thus, if a sinusoidal source distribution were scanned by an antenna, the received power would vary sinusoidally with a certain amplitude and phase depending on the spatial frequency. When suitably normalized, this amplitude and phase would constitute one complex value of the spectral sensitivity function. A filter characteristic is analogous. Bracewell and Roberts[11] showed that the spectral sensitivity function is given by the complex autocorrelation function of the antenna aperture distribution. An independent approach has been reported by Spencer.[13]

It is in fact clear that the sensitivity to a particular sinusoidal source component is measured by the number of ways in which the aperture embraces the spacing appropriate to that spatial frequency. By displacing the aperture relative to itself (Fig. 7), by the amount of that spacing, and by multiplying the excitations and integrating, we can count the number of ways, suitably weighted. But this is what we know as the autocorrelation.

Fig. 7 shows the spectral sensitivity function for a simple two-element interferometer, normalized so that the sensitivity to zero spatial frequency is unity. We see that it is sensitive to a band of high spatial frequencies corresponding to spacings embraced by the two elements jointly, and to a band of low spatial frequencies corresponding to spacings contained within each element separately. The sensitivity to a spatial frequency of, say, n cycles per radian is proportional to the number of ways a spacing of n wavelengths can be found.

The spectral sensitivity in a sensitive band can be restored to uniformity by cutting down by $1/m$ the spectral contribution associated with a spacing that occurs in m ways. This important topic in the analysis of antenna observations, usually referred to as restoration, is developed elsewhere.[11,12,14]

In a phase-switched interferometer such as the one Ryle[15] first introduced for studying discrete radio sources, a half-wave section of feeder is alternately switched in and out of one arm of the transmission system. Then a filter is inserted at the receiver output, which accepts only the component fluctuating at the switching frequency. The behavior of the phase-switched interferometer has been adequately explained. In Fig. 8(a) and 8(b) we see the spectral sensitivity of

Fig. 7—An interferometer aperture distribution and its spectral sensitivity function.

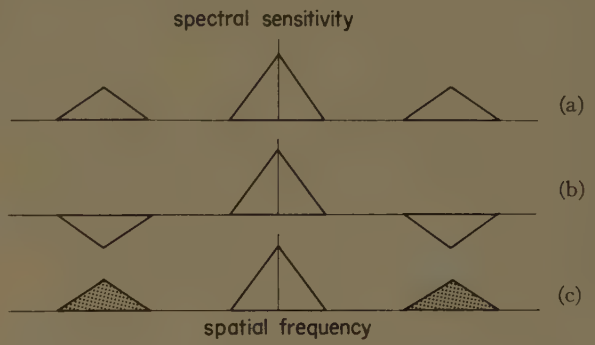

Fig. 8—Explaining the spectral sensitivity (shaded triangles) of a phase-switched interferometer.

the interferometer in each of its two states. When it is being switched between its two states, the shaded areas in Fig. 8(c) alternate in sign; hence, the shaded portion alone represents the spectral sensitivity of the phase-switched system. The sensitivity to low spatial frequencies disappears, and from this follows the ability to reject galactic background noise.

Since phase switching followed by square-law detection represents a method of pure multiplication, the results apply also to interferometers which use some other method of multiplying. In one modification,[16] separate preamplifiers and mixers are used and the phase of a common local oscillator is switched.

In another,[17] one of the signals is converted to a slightly different frequency by the insertion of a steadily rotating phase-changer in one arm. The two signals are then applied to separate grids of a nonlinear tube, whose response contains the squares and product of the signals. The product appears sinusoidally modulated at the difference frequency, a fact which allows it to be separated from the square terms.

From the preceding example it is clear that the rejection of extended backgrounds is not peculiar to phase switching but is rather a consequence of separating the product term $\mathcal{F}_1\mathcal{F}_2^*$ from the single-element terms $\mathcal{F}_1\mathcal{F}_1^*$ and $\mathcal{F}_2\mathcal{F}_2^*$ which occur in the output of a simple interferometer. Thus, one may extract the two quantities $\mathcal{F}_1+\mathcal{F}_2$ and $\mathcal{F}_1-\mathcal{F}_2$ simultaneously by connecting the two arms of the interferometer in a hybrid junction. Then,

[13] R. C. Spencer, "Antenna scanning problems in radio astronomy," *Proc. NEC*, vol. 11, pp. 506–522; 1955

[14] R. N. Bracewell, "Correction for Gaussian aerial smoothing," *Australian J. Phys.*, vol. 8, pp. 54–60; March, 1955.
—— "Chord construction for correcting aerial smoothing," *Australian J. Phys.*, vol. 8, pp. 200–205; June, 1955.
—— "Simple graphical method of correcting for instrumental broadening," *J. Opt. Soc. Am.*, vol. 45, pp. 873–876; October, 1955.
—— "Restoration in the presence of errors," PROC. IRE, vol. 46, pp. 106–111; January, 1958.

[15] M. Ryle, "A new radio interferometer and its application to the observation of weak radio stars," *Proc. Roy. Soc. (London) A*, vol. 211, pp. 351–375; March, 1952.

[16] B. Y. Mills, "The radio brightness distributions over four discrete sources of cosmic noise," *Australian J. Phys.*, vol. 6, pp. 452–470; December, 1953.

[17] R. Hanbury Brown, H. P. Palmer, and A. R. Thomson, "A rotating lobe interferometer and its application to radio astronomy," *Phil. Mag.*, vol. 46, pp. 857–866; August, 1955.

using separate detectors and recording the difference of the detected outputs, one obtains the normal phase-switched record, without the complication of switching but at the expense of two channels.

VI. Spectral Sensitivity Islands

In the foregoing treatment, the one-dimensional situation has been described in order to achieve as clear an explanation as possible of the concepts involved. The generalization to two dimensions, which is the most common situation, is straightforward; for example, the two-dimensional spectral sensitivity function is again derived as the two-dimensional complex autocorrelation function of the aperture distribution.[8,12]

Let x and y be rectangular coordinates in the aperture plane across which the excitation is $E(x/\lambda, y/\lambda)$. Then the spectral sensitivity function is

$$\frac{\iint E\left(\frac{x}{\lambda}-s_x,\frac{y}{\lambda}-s_y\right)E^*\left(\frac{x}{\lambda},\frac{y}{\lambda}\right)d\left(\frac{x}{\lambda}\right)d\left(\frac{y}{\lambda}\right)}{\text{normalizing factor}}.$$

This expression simply directs, as before, that the aperture distribution is to be given a vector displacement (components s_x and s_y) relative to itself as indicated in Fig. 9. The product of the unshifted distribution with the conjugate of the shifted distribution (shaded) is then integrated over the intersection (darker shading). Finally the result is normalized, so that the spectral sensitivity at $s_x=s_y=0$ is unity; we then have the spectral sensitivity at the point P whose coordinates are s_x and s_y.

To clarify the meaning of this value, let us state that it gives the sensitivity to a harmonic source distribution of spatial frequency OP, *i.e.*, $(s_x^2+s_y^2)^{1/2}$, with crest lines oriented at right angles to the direction OP of the displacement. The spectral sensitivity, which is generally complex, allows for the possibility that a cosinusoidal source distribution such as that shown in Fig. 9(c) (positive areas indicated by shading) may be perceived by the antenna as having a spatial displacement depending on the spatial frequency.

The complete spectral sensitivity diagram for a uniformly excited rectangular aperture a wavelengths long and b wavelengths wide, which is shown in Fig. 10, can easily be shown to be given by

$$\left(1-\frac{|s_x|}{a}\right)\left(1-\frac{|s_y|}{b}\right)$$

inside the rectangle $2a\times 2b$, and by zero outside.

An important property of this and of all other spectral sensitivity diagrams for finite antennas is that the sensitivity is zero outside some boundary or boundaries. For this reason it is referred to as a spectral sensitivity island diagram.

While the details of topography within an island depend on details of the aperture excitation and may require effort to evaluate, the island boundaries can be established easily. We shall see that an island diagram consisting of shorelines alone is a powerful and easily acquired tool for thinking with some of the more complicated situations in interferometry.

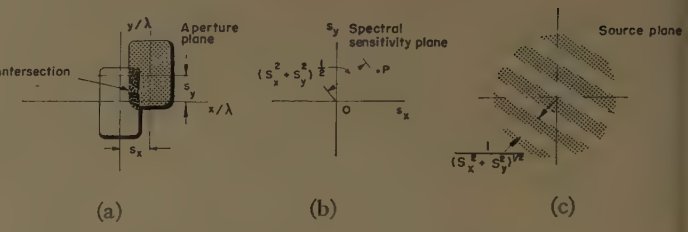

Fig. 9—Procedure for autocorrelation.

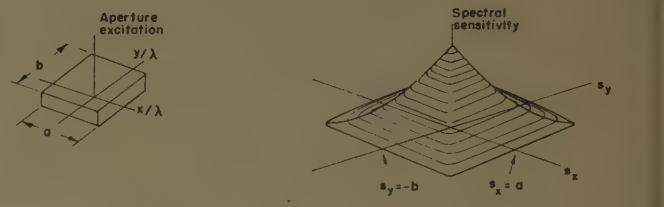

Fig. 10—Spectral sensitivity island for uniform rectangular aperture.

Consider a general two-element interferometer whose aperture distribution is broken into two separated parts A and B in Fig. 11. Trace the outlines of the aperture distribution on a piece of tracing paper (faintly shaded). Now displace the tracing paper, without rotation, so that the outline remains tangent to itself. The displaced origin O' then traces out the boundaries of the spectral sensitivity islands. As a matter of practical convenience, to avoid superposition, we use a pencil to follow the point of an arrow marked at one edge of the moving paper. (Alternatively, one can trace onto the moving paper the locus of a point on the fixed sheet below.)

It is desirable to repeat the construction of Fig. 11 for practice and to experiment with various practical shapes. Re-entrant shapes and distributions with a higher order of connectivity can be handled readily. Overlapping of some of the islands proves to be a regular feature.

When the interferometer is phase-switched, some of the islands are affected by the switching and some are not. Thus, if part B is subject to phase reversal, so are the shaded islands in Fig. 11. The two central islands representing the response of single elements alone therefore drop out of the spectral sensitivity diagram for the phase-switched device. This is true for any multiplying arrangement, phase-switched or not, where the single-element terms are separated from the product term.

Note that the shaded islands surround spatial frequencies corresponding to vector spacings between pairs of points chosen so that one is in one part of the interferometer and one is in the other. Some special examples to illustrate this are shown in Fig. 12. Thus, the

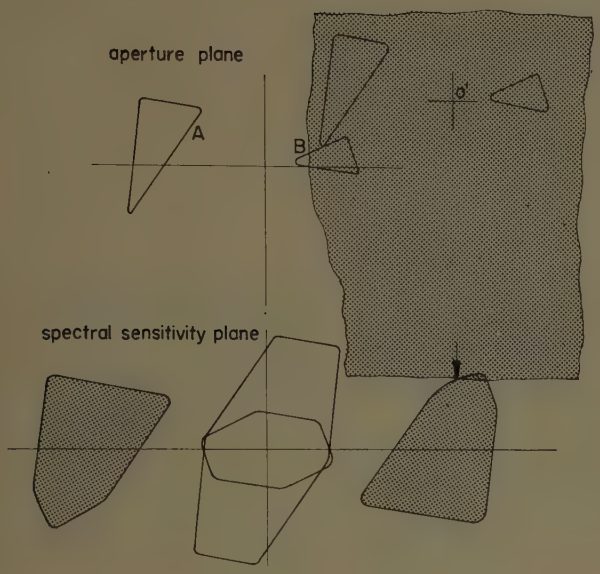

Fig. 11—Tracing out the shorelines of an island diagram.

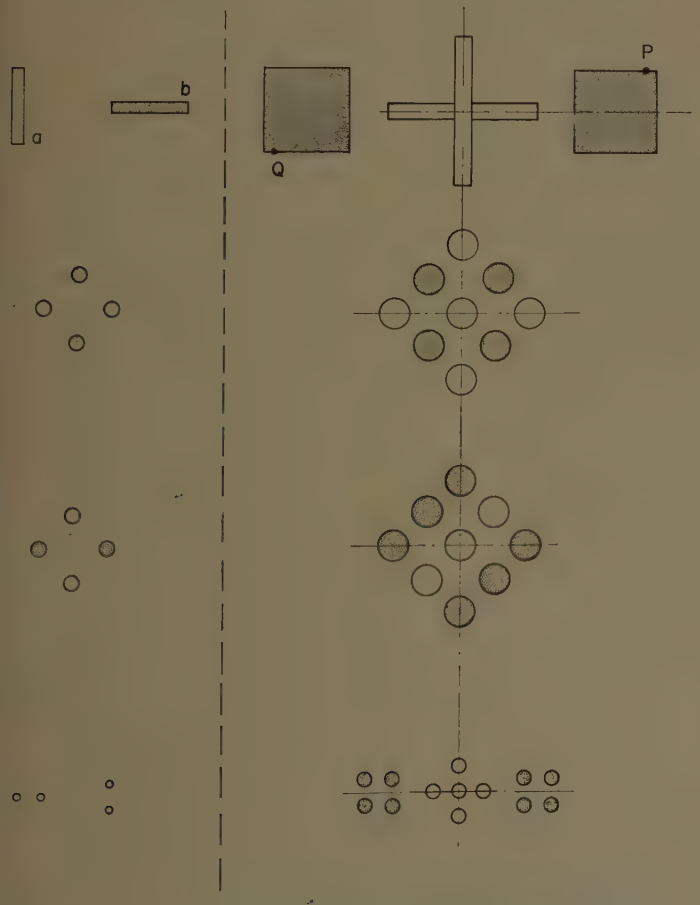

Fig. 12—Spectral sensitivity island diagrams (right) chosen to illustrate how the regions of sensitivity (shaded) of switched interferometers correspond to vector spacings between pairs of points of which one is, and one is not, in the switched part of the interferometer.

vector spacing ab between the point a in one array and point b in the other is represented by the point P on a spectral sensitivity island of the switched interferometer. The point Q, which represents the vector spacing ba, of necessity is also in one of the islands, and shows that the diagram must be unchanged by a rotation π. This kind of symmetry corresponds to the evenness possessed by one-dimensional spectral sensitivity functions.

VII. Applications of the Island Diagram

A variety of interferometers are in use, some of which are shown in Fig. 13. There is no doubt that many of these systems are rather subtle to understand. Yet many qualitative and quantitative conclusions can be drawn from the spectral sensitivity diagram, even in many cases from the island outlines alone. Indeed, with a little practice, one can dispense with the diagram and focus attention directly on the possible vector spacings embraced by the interferometer. This is the fundamental point. The interferometer perceives the field coherence only at the vector spacings actually represented within its aperture distribution.

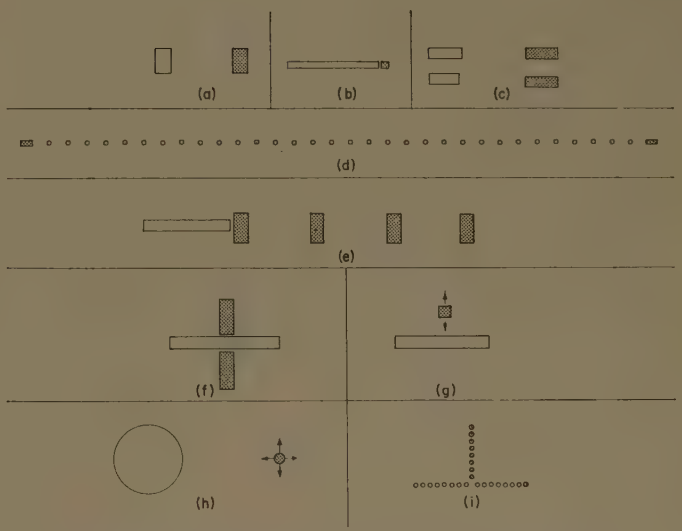

Fig. 13—Some interferometric arrangements used in practice. Typical dimensions range up to several thousand wavelengths.

All the examples given in Fig. 13 may be studied with profit. Fig. 13(a) represents a switched interferometer comprising two rectangular apertures, whose spectral sensitivity will be concentrated in two rectangular islands, each of the character shown in Fig. 10. This arrangement is the earliest form of two-element interferometer.

In Fig. 13(b), an interesting principle is illustrated. If we choose elements a and b, as in Fig. 12, one from each part of the switched interferometer of Fig. 13(b), then each spacing from zero up to the full length of the aperture is represented the same number of times. The spec-

tral sensitivity is, therefore, uniform from zero up to the maximum spatial frequency. In contrast, the spectral sensitivity of a single uniform aperture of the same extent falls off linearly to zero at the maximum spatial frequency accepted. The switching scheme thus yields directly what one seeks to obtain from fan beam observations by the restoration procedures mentioned in Section V; the "principal solution" is observed directly. It should be noted that the collecting area is reduced, in comparison with the single aperture, by approximately the ratio of the areas of the two parts.

Fig. 13(c) represents the large interferometer[18] used in the Cambridge surveys of discrete radio sources, in one of the various ways in which its four elements can be combined by switching. The antennas are parabolic cylinders 320 by 40 feet situated at the corners of a rectangle 1900 by 168 feet.

Fig. 13(d) shows how to suppress all but the zero-order interference fringe of a multielement spaced array by incorporating elongated apertures equal in length to the spacing between elements. Clearly, the many spacings not embraced by the spaced array alone are included between the two parts of this switched system. Only one of the two elongated apertures is necessary, but in the case of the 1.5 km 32-element interferometer at Nançay[19] two are preferred for practical reasons connected with collecting area and phase-symmetry of the transmission lines.

Fig. 13(e) illustrates Covington's scheme[20] for obtaining a one-minute-of-arc fan beam for solar studies at 10 centimeters. In principle, it is the same as the preceding, but it evolved from the elongated aperture (a 150-foot horn) by addition of extra elements. As in the cases of Fig. 13(b) and 13(d), the spectral sensitivity is uniform, with the consequence that the beamwidth is about one half what it would be with a uniform aperture of the same over-all extent. The possibility of so doubling the resolution expected from a given aperture has been adequately confirmed by solar observation. There is no terrestrial method of verifying the beamwidth, since the beam only forms well out in outer space.[21]

Although in the usual sense the resolution of a spaced array is improved by switching it with an elongated aperture, it is, nevertheless, not always desirable. Elimination of all but the zero-order fringe confines operations to the vicinity of the plane perpendicular to the line of the array in the case of the large systems mentioned. In Christiansen's original multielement array[22] of equatorially mounted paraboloids, on the other hand, the higher orders of interference are depended on to permit operation in almost any direction, unwanted fringes being suppressed by the primary directivity of the paraboloidal elements. This principle is followed in the Stanford-U. S. Air Force microwave spectroheliograph shown in Fig. 14.

Fig. 14—The Stanford-USAF microwave spectroheliograph. Supported by the AF Office of Scientific Research for research in radio astronomy, this Mills cross composed of Christiansen-type multielement spaced arrays, with its pencil beam of less than 2 square milliradians, has the highest resolving power among antennas in the United States.

Fig. 13(f) represents the standard Mills cross composed of continuous arrays, which is in use in many locations, with dimensions now exceeding a kilometer.[23,24] Fig. 13(g) is a synthetic system formed by moving a small antenna to successive stations on a line perpendicular to a large linear array.[25] It accumulates sequentially the same information as would be obtained with a Mills cross. Fig. 13(h) represents a large aperture antenna supplemented by a smaller mobile one. By suitable stationing of the smaller element at the points of a certain rectangular lattice in accordance with a discrete spacing theorem[6] mentioned in Section IV, a large effective aperture can be synthesized.

Fig. 13(i) is a tee composed of spaced multielement arrays; it raises interesting questions which have been studied in theory and practice by Swarup and Yang.[26] We shall study this case from the standpoint of spectral sensitivity islands. Suppose we have a Mills cross, *i.e.*, a phase-switched interferometer consisting of two long

[18] M. Ryle and A. Hewish, "The Cambridge radio telescope," *Mem. Roy. Astron. Soc.*, vol. 67, pp. 97–105; 1955.

[19] E. J. Blum, A. Boischot, and M. Ginat, "Le grand interféromètre de Nançay," *Ann. Astrophys.*, vol. 20, pp. 155–164; July-August, 1957. See also *Paris Symp. on Radio Astronomy*, R. N. Bracewell, Ed., Stanford University Press, Stanford, Calif., p. 495; 1959.

[20] A. E. Covington and W. N. Broten, "An interferometer for radio astronomy with a single-lobed radiation pattern," IRE TRANS. ON ANTENNAS AND PROPAGATION, vol. AP-5, pp. 247–255; July, 1957.

[21] A. E. Covington, "Solar emission at 10-cm wavelength," *Paris Symp. on Radio Astronomy*, R. N. Bracewell, Ed., Stanford University Press, Stanford, Calif., p. 159; 1959.

[22] W. N. Christiansen and J. A. Warburton, "The distribution of radio brightness over the solar disc at a wavelength of 21 cm. I. A new highly directional aerial system," *Australian J. Phys.*, vol. 6, pp. 190–202; June, 1953.

[23] B. Y. Mills, A. G. Little, K. V. Sherican, and O. B. Slee, "A high resolution radio telescope for use at 3.5 m," PROC. IRE, vol. 46, pp. 67–84; January, 1958.

[24] C. A. Shain, "The Sydney 19.7-Mc radio telescope," PROC. IRE, vol. 46, pp. 85–88; January, 1958.

[25] M. Ryle, "The Mullard Radio Astronomy Observatory, Cambridge," *Nature*, vol. 180, pp. 110–112; July, 1957.

[26] G. Swarup and K. S. Yang, "Interferometer phasing problems at microwave frequencies," 1959 WESCON CONVENTION RECORD, pt. I, pp. 17–24.

—— "Phase adjustment of large antennas," this issue, pp. 75–81.

perpendicular arrays. We then remove one-half of one arm. What is the effect on the angular resolution of the system?

In Fig. 15, we see the island diagram for the cross and for the tee. It is immediately clear that the shaded islands have the same extent in each case and we can verify directly that no vector spacing between arm elements occurs in the cross that does not also occur in the tee. Furthermore, the distribution of weight over the islands is the same. The angular resolution of the smaller system is, consequently, the same as for the larger. This is an example of direct reasoning, permitted by the concepts of this paper, in relation to a problem whose answer is not at all obvious, judging by the reaction of colleagues more familiar with other approaches to antennas. The result can, of course, also be verified by calculating the beamwidth without recourse to the domain of spatial frequencies.

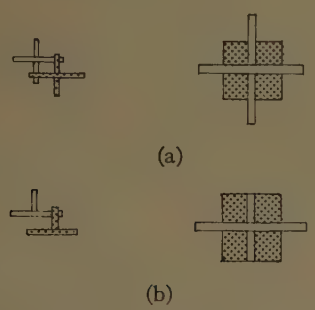

FIG. 15—Island diagrams for (a) a cross and (b) a tee. Note that every spacing *ab* contained between the two arms of the cross is also contained by the tee.

Although the bulk of the applications of switched interferometers in their early phase of development has been to radio astronomy, it is to be expected that the principles will find application also in other fields of radio science and technology when the need for high resolving power demands it. The well-known Minitrack antenna was an early example of precision position-finding technique borrowed from radio astronomy.

VIII. Conclusion

Although interferometers are included within the class of antennas and are therefore susceptible to treatment by any approach that is applicable to antennas in general, they possess features which have not been customary with conventional antennas. For this reason, a new approach may sometimes have advantages. The concept of complex coherence of the radiation field in which the interferometer is immersed is not used in connection with ordinary antennas that do not have the gaps characteristic of interferometers, but is most significant for interferometry.

The author has defined a *complex visibility* of the fringes of an interferogram and shown that under suitable adjustment of the interferometer the complex visibility is exactly equal to a weighted average of the complex coherence. Interferometry may thus be regarded as a rather direct method of observing the degree of field coherence.

As the coherence produced by a radiation source is the Fourier transform of the intensity distribution of the source, we are led naturally into considerations of the spatial harmonic components of the source distribution and thus, in turn, to the sensitivity of the interferometer to a sinusoidal source distribution of given spatial frequency. The spectral sensitivity function of an antenna is precisely equivalent to the power radiation pattern, the two forming a Fourier pair.

Thus, the method of this paper is complementary to more familiar methods, and in any given problem may furnish a powerful alternative tool. This is particularly so in interferometry and especially in two-dimensional interferometry, where the easily visualized spectral sensitivity island diagram brings welcome clarity.

Stepped Cylindrical Antennas for Radio Astronomy*

L. RONCHI†, V. RUSSO†, AND G. TORALDO DI FRANCIA†

Summary—**In this paper a stepped cylindrical mirror is described which satisfies the following requirements: 1) it is free from spherical aberration for a point source at infinity on the axis, 2) both off-axis spherical aberration and coma vanish for fixed values of the field angle, $\bar{\Omega}$, and of the aperture, $\bar{\alpha}$.**

The analysis has been carried out, in the approximation of parageometrical optics, by considering a diffraction grating of the generalized type, equivalent to the stepped mirror.

Three interesting results are obtained, and precisely: 1) independently of the values of $\bar{\Omega}$ and $\bar{\alpha}$, the equivalent diffraction grating has a quasi-parabolic cross section, 2) the off-axis spherical aberration turns out to be negligible over the whole aperture 0–$\bar{\alpha}$, for fields angles up to at least 20 degrees, 3) the residual coma turns out to be well corrected, too.

I. Introduction

In the last years, antennas for radio astronomy have been built in larger and larger sizes, in order to be able both to detect weak sources and to achieve a fine resolving power.

However, increasing the antenna size leads to difficult practical problems. The cost of a steereable mount for scanning the sky is very great because it is very difficult to maintain the proper tolerances. On the other hand, a conventional telescope with a spherical or parabolic mirror, cannot be used in a fixed position because its field angle is very limited. Consequently, while the antenna may work perfectly when the feeder is placed on the axis, the performance rapidly deteriorates when the feeder is moved off the axis because of the strong aberrations which are introduced.

A good solution to these problems is to use a fixed paraboloid and in addition, a flat reflector which deflects the descending radio waves into the paraboloid.[1] In this way a large field angle can be reached, but only in a plane.

Recently, two of us[2] described a stepped zone spherical mirror which collimates a beam with substantial values of the aperture and field angles.[3,4] The design requirements were to obtain a spherical aberration equal to zero for all values of the aperture for a point source at infinity on the axis, and, at the same time, to make the offense against the sine condition vanish. A similar antenna was tested by Ramsay and Jackson.[5] Dasgupta and Lo[6] have developed the diffraction theory of such antennas. This system enables one to use a fixed standing mirror without the additional steerable flat reflector, the scanning being obtained by moving the feeder along the focal surface.

However, the zone spherical mirror presents residual astigmatism and off-axis spherical aberration, which become very strong for large field angles. Besides, there is some higher order coma.

In order not to bother about the astigmatism, one can use a cylindrical mirror based on the same principle as the spherical mirror.

However, we note that the vanishing of the offense against the sine condition, which is ensured by the focus being at the center of the circular cross section of the mirror, is not the best requirement from a practical point of view. If one wants to attain a great field angle, a better compromise is represented by the coma vanishing for a given value $\bar{\Omega}$ of the field angle Ω and a given value $\bar{\alpha}$ of the aperture α.

This condition may be easily satisfied in the case of a stepped cylindrical mirror, with circular mean cross section, by requiring the focus to be at a certain distance d from the center of the cross section. Obviously, d turns out to be a function of $\bar{\Omega}$ and $\bar{\alpha}$.

Further, by giving up the condition that the cross section should be a circle, one can satisfy additional requirements. For example, one can require that both coma and off-axis spherical aberration should be corrected.

In this paper we will consider the case when the cross section is a general second order curve, and will require the correction of both coma and off-axis spherical aberration for a given value of $\bar{\Omega}$ and a given value of $\bar{\alpha}$. Of course, the requirement will be maintained that the spherical aberration be identically zero over the whole aperture, for $\Omega=0$. The results obtained seem to be very promising.

* Received by the PGAP, May 25, 1960. This research has been sponsored by the Air Res. and Dev. Command, USAF, under Contract AF 61(052)-234, through the European Office ARDC.

† Centro di Studio per la Fisica delle Microonde, Florence, Italy.

[1] J. D. Kraus, "Radio telescope antennas of large aperture," PROC. IRE, vol. 46, pp. 92–97; January, 1958.

[2] L. Ronchi and G. Toraldo di Francia, "An application of parageometrical optics to the design of a microwave mirror," IRE TRANS. ON ANTENNAS AND PROPAGATION, vol. AP-6, pp. 129–133; January, 1958.

[3] G. Toraldo di Francia, L. Ronchi, and V. Russo, "Experimental test of a stepped zone mirror for microwaves," IRE TRANS. ON ON ANTENNAS AND PROPAGATION, vol. AP-7, pp. 125–131; December, 1959.

[4] G. Toraldo di Francia, P. F. Checcacci, L. Ronchi, and V. Russo, "Design, Development, and Test of an Advanced, Fixed Position Astronomy Antenna," Centro Microonde, Florence, Italy, Final Rept , Contract AF 61(052)-234; April, 1960.

[5] J. F. Ramsay, and J. A. C. Jackson, "Wide-angle scanning performance of mirror aerials," *Marconi Rev.*, vol. 19, pp. 119–140; July–October, 1956.

[6] S. Dasgupta and Y. T. Lo, "A Study of the Coma Corrected Zone Mirror by Diffraction Theory," Antenna Lab., University of Illinois, Urbana, Ill., Tech. Rept. No. 40, Contract AF 33(616)-6079; July, 1959.

II. The Local Periodicity of the Equivalent Diffraction Grating

Let us consider a cylindrical mirror, whose cross section is a conic section Σ (Fig. 1). The actual mirror will consist of a number of metallic plates intersecting Σ at suitably chosen points P_i. Once Σ and F have been so determined as to satisfy the prescribed conditions, it is an easy matter to specify the intersection points P_i and the shape of the steps. However, in order to determine the shape of Σ and the position of F, we will consider a diffraction grating of the generalized type,[7] covering Σ. Of course, the problem requires only a two-dimensional treatment.

It is well known that, in the two-dimensional case, the following relation holds:

$$\sin \alpha_n = \sin \alpha^i + A \tag{1}$$

where α^i is the angle ($\leq \pi/2$) between a ray incident on Σ (Fig. 2) and the normal N to Σ through the incidence point P, α_n the angle between the nth order diffracted ray at P and N, and finally A is a quantity which depends on the characteristics of the grating and on the coordinates of P, but is independent of α^i. Precisely, if p denotes the local periodicity of the grating, we have $A = n\lambda/p$.

The quantity A must be determined by prescribing the condition that the spherical aberration be identically zero for all values of the aperture α and for a point source at infinity on the axis. To this end, let us refer to a system of polar coordinates ρ, θ with the origin at the focus O of the conic section Σ next to the vertex V of the mirror and the polar axis in the direction OV. The equation of Σ may be written as

$$\rho = \frac{p}{1 + e \cos \theta} \tag{2}$$

where p and e are two positive constants. The condition to be fulfilled requires that the reflected ray s_n should be directed towards the focus F of the mirror, when the incident ray s^i is parallel to the axis OV (Fig. 3).

In this case, if ϕ indicates the angle OPQ, and β the angle OPF, we can write

$$\alpha^{0i} = \theta - \phi \tag{3}$$

and

$$\alpha_n{}^0 = \phi - \beta \tag{4}$$

where α^{0i}, $\alpha_n{}^0$ represent the values of α^i and α_n respectively, when the field angle Ω is equal to zero.

The value of β may be derived from the triangle OPF. By indicating by d the distance OF (positive

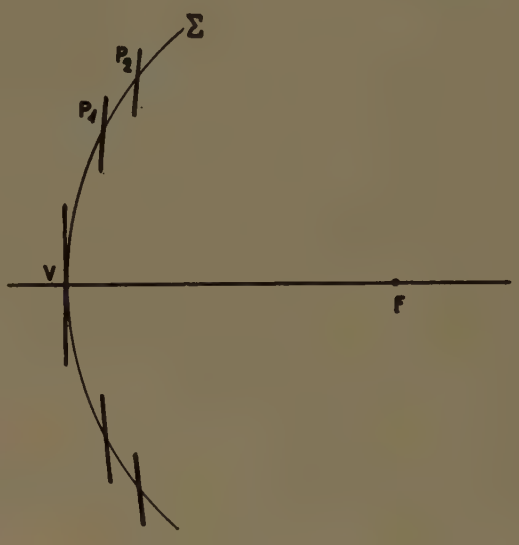

Fig. 1.

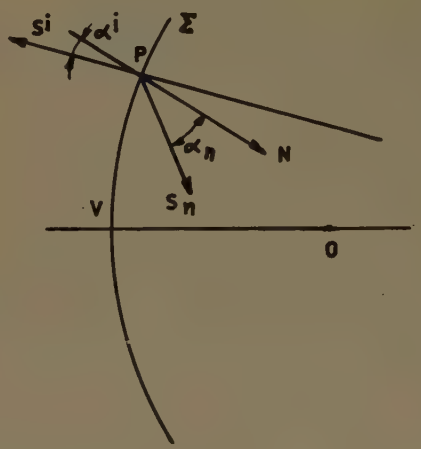

Fig. 2.

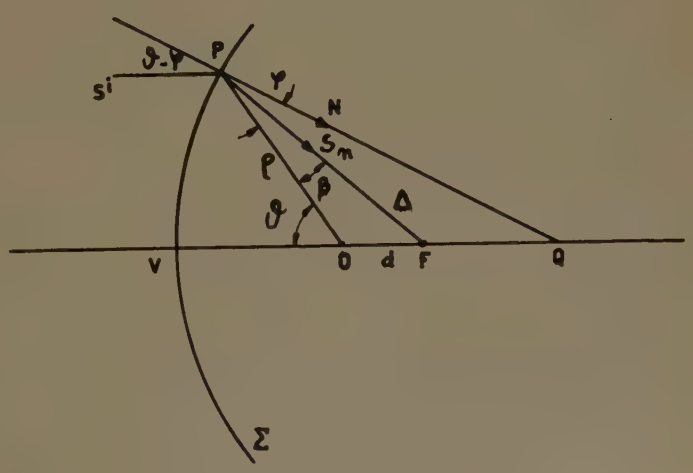

Fig. 3.

[7] G. Toraldo di Francia, "Electromagnetic Waves," Interscience Publishers, New York, N. Y., p. 234; 1956.

when F is on the right of O), and by Δ the length of PF, one has

$$\Delta^2 = \rho^2 + d^2 + 2\rho d\cos\theta \tag{5}$$

$$\sin\beta = \frac{d}{\Delta}\sin\theta; \qquad \cos\beta = \frac{\rho + d\cos\theta}{\Delta}. \tag{6}$$

The value of ϕ can be easily expressed in terms of θ and e, for example by recalling that $2\phi = OPO'$, if O' is the other focus of Σ. It is found

$$\sin\phi = \frac{e\sin\theta}{\sqrt{1 + e^2 + 2e\cos\theta}}, \qquad \cos\phi = \frac{1 + e\cos\theta}{\sqrt{1 + e^2 + 2e\cos\theta}}. \tag{7}$$

By introducing (7) and (6) into (3) and (4), one can write

$$\sin\alpha^{0i} = \frac{\sin\theta}{\sqrt{1 + e^2 + 2e\cos\theta}} \tag{8}$$

$$\sin\alpha_n{}^0 = \frac{\rho e - d}{\Delta}\,\frac{\sin\theta}{\sqrt{1 + e^2 + 2e\cos\theta}} \tag{9}$$

respectively, and finally, by introducing (8) and (9) into (1), one obtains

$$A = \left[\frac{\rho e - d}{\Delta} - 1\right]\frac{\sin\theta}{\sqrt{1 + e^2 + 2e\cos\theta}}. \tag{10}$$

We have thus determined the quantity A, which is inversely proportional to the local periodicity of the grating.

III. Conditions for the Correction of Spherical Aberration and Coma

When s^i is not parallel to the axis OV, one has

$$\alpha^i = \theta - \phi - \Omega \tag{11}$$

where Ω is the field angle (Fig. 4).[8] The corresponding direction of s_n is then derived from (1) with the help of (10).

It is to be noted that in our representation, α_n is positive when s_n and N have the relative position shown in Fig. 4.

Let us now introduce rectangular coordinates, with the origin at O (Fig. 4), the x-axis parallel to OV directed from left to right. The unit vectors in the directions of x and y will be denoted by i, j respectively. For s_n we have

$$s_n = \cos(\theta - \phi + \alpha_n)i - \sin(\theta - \phi + \alpha_n)j. \tag{12}$$

[8] We will adopt the usual convention, to count Ω as positive when the radiation comes from below the axis OV, as in Fig. 4.

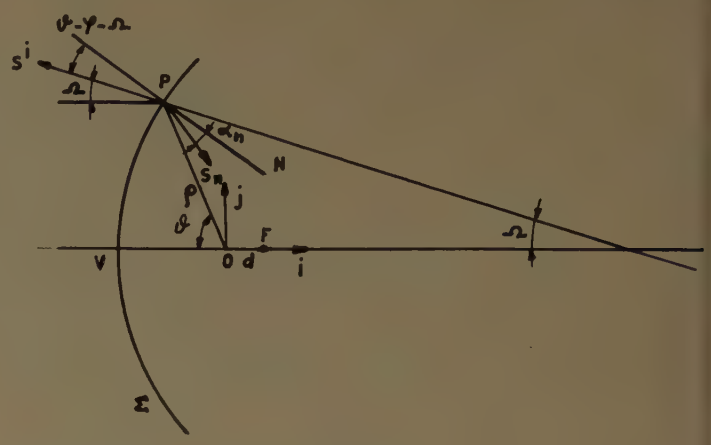

Fig. 4.

Accordingly, the equation of the ray diffracted at P in the direction s_n is

$$\frac{x + \rho\cos\theta}{\cos(\theta - \phi + \alpha_n)} = -\frac{y - \rho\sin\theta}{\sin(\theta - \phi + \alpha_n)}. \tag{13}$$

This equation is to be used together with (2), (7) and (1). Eq. (1) can be rewritten, by recalling (11) and (10), as

$$\sin\alpha_n = \sin(\theta - \phi - \Omega) + \left[\frac{\rho e - d}{\Delta} - 1\right]\frac{\sin\theta}{\sqrt{1 + e^2 + 2e\cos\theta}}. \tag{14}$$

In the sequel all the rays considered will be assumed to have the same value of n (diffracted wave of the nth order).

Now we have to determine e and d/p in such a way that both the coma and the spherical aberration vanish for $\Omega = \bar{\Omega}$ and $\theta = \pm\bar{\theta}$. First, we will determine the coordinates $\bar{x}$, $\bar{y}$ of the focus $\bar{F}$ corresponding to the field angle $\bar{\Omega}$ (and to $\theta = 0$). Then we will consider the two rays diffracted at the points $P = (\rho, \theta)$ and $P' = (\rho, -\theta)$, respectively, and determine their intersections P_1, P_1' with the straight line $x = \bar{x}$. Let y_1 and y_1' be the ordinates of P_1 and P_1', respectively. Since $A = 0$ for $\theta = 0$, as is shown by (10), the ray $V\bar{F}$ makes an angle equal to $\bar{\Omega}$ with the axis OV, so that the following relation holds:

$$\bar{y} = (\bar{x} + \bar{\rho}_0)\tan\bar{\Omega} \tag{15}$$

where $\rho_0 = |OV| = \rho(\theta = 0) = p/(1 + e)$.

If no coma exists for the two rays PP_1, $P'P_1'$, the situation is that represented in Fig. 5, where PP_1 and $P'P_1'$ intersect $V\bar{F}$ at the same point B. In this condition, P_1 and P_1' are nearly symmetric with respect to $\bar{F}$. Accordingly, the condition that no coma exists for the field angle $\bar{\Omega}$ and the given aperture $\bar{\theta}$ may be written as

$$\tfrac{1}{2}(y_1 + y_1') = \bar{y}. \tag{16}$$

In general, we will define as coma the quantity

$$C(\Omega, \theta) = \tfrac{1}{2}(y_1 + y_1') - \bar{y}. \tag{17}$$

The distance $|B\overline{F}|$ represents the spherical aberration of the two rays PP_1, $P'P_1'$. In a first approximation this spherical aberration may be expressed by

$$S(\Omega, \theta) = \frac{1}{2\theta}(y_1' - y_1). \tag{18}$$

Accordingly, in order to obtain a vanishing spherical aberration for given values of $\bar{\Omega}$ and $\bar{\theta}$, one must set

$$y_1'(\bar{\Omega}, \bar{\theta}) = y_1(\bar{\Omega}, \bar{\theta}). \tag{19}$$

The two conditions for both coma and spherical aberration may be summarized as

$$y_1(\bar{\Omega}, \bar{\theta}) = y_1'(\bar{\Omega}, \bar{\theta}) = \bar{y}(\bar{\Omega}). \tag{20}$$

From these equations, the quantities e, d/p can be determined.

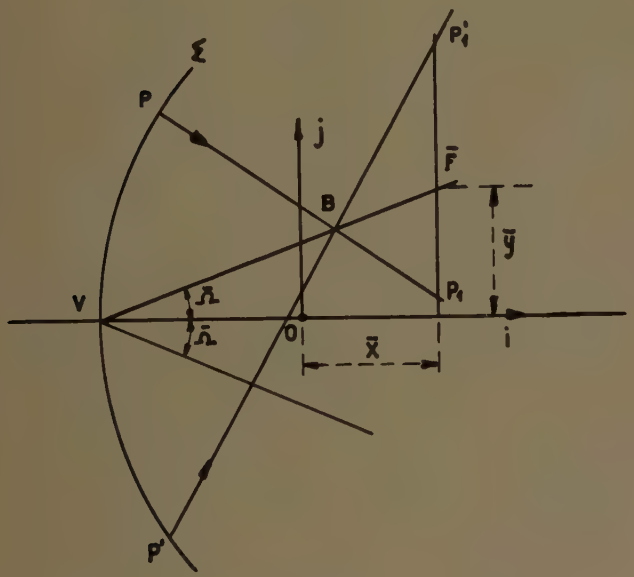

Fig. 5.

IV. Determination of $\overline{F}$ in Terms of e, d/p, $\bar{\Omega}$

In order to determine the coordinates $\bar{x}$, $\bar{y}$ of $\overline{F}$, we will consider the intersection of the general diffracted ray with the ray $V\overline{F}$. Next we have to find the limit for $\theta \to 0$. Eq. (13) gives

$$y - \rho \sin\theta = \tan(\theta - \phi + \alpha_n)(x + \rho\cos\theta) \tag{21}$$

while the equation of $V\overline{F}$ is

$$y = (x + \rho_0)\tan\bar{\Omega}. \tag{22}$$

By introducing (22) into (21) one obtains

$$x[\tan\bar{\Omega} + \tan(\theta - \phi + \alpha_n)]$$
$$= \rho\sin\theta - \rho_0\tan\bar{\Omega} - \rho\cos\theta\tan(\theta - \phi + \alpha_n). \tag{23}$$

When $\theta \to 0$, x tends to $\bar{x}$, but, to evaluate the limit of the other quantities, one has to take into account infinitesimals of the order of $\sin\theta$. Accordingly, one can simply substitute ρ_0 for ρ and 1 for $\cos\theta$. It is easy to find the following relations from (7):

$$\sin\phi \to \frac{e}{1+e}\sin\theta, \qquad \cos\phi \to 1$$

whence

$$\sin(\theta - \phi) \to \frac{1}{1+e}\sin\theta, \qquad \cos(\theta - \phi) \to 1.$$

From (14) and (15) we have

$$\sin\alpha_n \to -\sin\bar{\Omega} + \frac{1}{1+e}\sin\theta\left[\cos\bar{\Omega} + \frac{e\rho_0 - d}{\rho_0 + d} - 1\right]$$

$$\tan\alpha_n \to -\tan\bar{\Omega} + \frac{1}{1+e}\frac{\sin\theta}{\cos^3\bar{\Omega}}\left[\cos\bar{\Omega} - 1 + \frac{e\rho_0 - d}{\rho_0 + d}\right]$$

whence

$$\tan(\theta - \phi + \alpha_n) = \frac{\tan\alpha_n + \tan(\theta - \phi)}{1 - \tan\alpha_n\tan(\theta - \phi)}$$
$$\to -\tan\bar{\Omega} + \frac{\sin\theta}{1+e}\frac{1}{\cos^3\bar{\Omega}}\left[2\cos\bar{\Omega} - 1 + \frac{e\rho_0 - d}{\rho_0 + d}\right].$$

Finally, (23) gives

$$\bar{x} = -\rho_0 + p\frac{\cos^3\bar{\Omega}}{2\cos\bar{\Omega} - 1 + \dfrac{e\rho_0 - d}{\rho_0 + d}}. \tag{24}$$

Therefore, recalling (15)

$$\bar{y} = p\frac{\sin\bar{\Omega}\cos^2\bar{\Omega}}{2\cos\bar{\Omega} - 1 + \dfrac{e\rho_0 - d}{\rho_0 + d}}. \tag{25}$$

Eqs. (24) and (25) are the parametric equations (parameter $\bar{\Omega}$) of the focal line for given values of e and d.

V. Evaluation of the Quantities e and d

In order to evaluate $y_1(\bar{\Omega}, \bar{\theta})$, one has simply to substitute $\bar{x}$ as given by (24), for x into (13), and $\bar{\theta}$ for θ. One obtains

$$y_1 = \rho\sin\bar{\theta} - \tan(\bar{\theta} - \phi + \alpha_n)(\bar{x} + \rho\cos\bar{\theta}) \tag{26}$$

where the quantities ρ, ϕ are evaluated for $\theta = \bar{\theta}$, and α_n for $\theta = \bar{\theta}$ and $\Omega = \bar{\Omega}$.

For symmetry reasons, one can write

$$y_1'(\bar{\theta}, \bar{\Omega}) = -y_1(\bar{\theta}, -\bar{\Omega}). \tag{27}$$

In other words, one may evaluate y_1' with the same formula (26), where α_n must be now evaluated for $\theta = \bar{\theta}$ and $\Omega = -\bar{\Omega}$.

We are now in a position to solve (20). To this end, having selected the values of $\bar{\Omega}$ and $\bar{\theta}$, and assuming p as unit of length, we evaluated y_1, y_1' and $\bar{y}$ for a num-

ber of values of e and d. Precisely, $y_1(\bar{\Omega}, \bar{\theta}, e, d)$, $y_1'(\bar{\Omega}, \bar{\theta}, e, d)$, $\bar{y}(\bar{\Omega}, e, d)$ were plotted against d (Fig. 6) for a fixed value e. In this way we were able to find, by interpolation, the two values d_1, d_1' of d such that

$$y_1(\bar{\Omega}, \bar{\theta}, e, d_1) = \bar{y}(\bar{\Omega}, e, d_1)$$

$$y_1'(\bar{\Omega}, \bar{\theta}, e, d_1') = \bar{y}(\bar{\Omega}, e, d_1').$$

Then, by varying e, it was possible to plot both d_1 and d_1' versus e, as shown in Fig. 7, and to determine the values $\bar{e}$, $\bar{d}$ of e and d corresponding to $y_1=\bar{y}=y_1'$. These values represent the coordinates of the point S of Fig. 7.

This procedure has been applied for a number of values of $\bar{\Omega}$ and $\bar{\theta}$. The results obtained are shown in Table I.

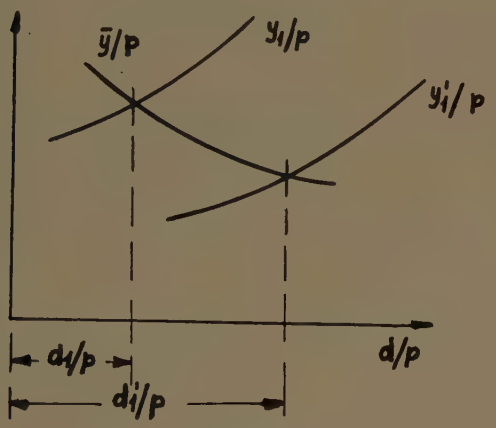

Fig. 6.

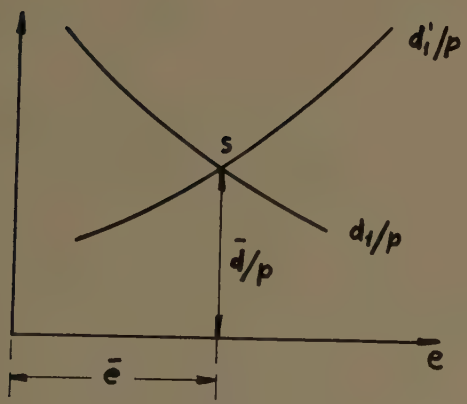

Fig. 7.

TABLE I

$\bar{\Omega}$	$\bar{\theta}$	$\bar{e}$	$\bar{d}/p$	f/p	$\bar{\alpha}$
20°	60	0.9400	0.5490	1.06446	33°
	45°	0.9720	0.5011	1.00820	24°
	30°	1.0000	0.4720	0.97200	16°
15°	60°	0.9260	0.5710	1.09021	33°
	45°	0.9675	0.5250	1.03326	24°
	30°	1.0000	0.4950	0.99500	16°

Here $f=\bar{d}+\rho_0$ is the distance from the vertex V to the optical focus[9] F (Fig. 3); *i.e.*, the focal length of the diffraction grating for the nth diffracted wave, and $\bar{\alpha}$ is the semiaperture angle VFP (Fig. 3) corresponding to $\theta=\bar{\theta}$.

It is interesting to note that the excentricity $\bar{e}$ of Σ turns out to be close or equal to unity, for all the values of $\bar{\Omega}$ and $\bar{\theta}$ considered. In other words, Σ turns out to have a quasi-parabolic shape. However, it will be emphasized that the focal length is about twice the focal length of a conventional parabolic mirror.

VI. The Residual Aberrations

The above values of e and f correspond to a mirror free from spherical aberration for a point source at infinity on the axis and free from both coma and spherical aberration at a given value of the field angle $\bar{\Omega}$ and of the aperture $\bar{\alpha}$. It is of interest to evaluate coma and spherical aberration for different values of α and Ω (residual aberrations). To this end, (17) and (18) can be used. The results are shown in Figs. 8–11.

Figs. 8(a), (b) and (c) show coma and spherical aberration plotted against α for the three cases of correction at $\Omega=20°$ and $\bar{\alpha}=16°$, 24°, 33°, respectively.

Figs. 9(a), (b), and (c) refer to the cases $\bar{\Omega}=15°$ and $\bar{\alpha}=16°$, 24°, 33°.

Figs. 10(a) and (b) show the residual aberrations at $\Omega=15°$ and $\Omega=10°$, respectively, for the same mirror as that to which Fig. 8(b) is referred.

Fig. 11(a), and (b) show the residual aberrations at $\Omega=15°$ and $\Omega=10°$, respectively, for the same mirror as that to which Fig. 8(c) is referred.

The most remarkable result is that the off-axis spherical aberration turns out to be practically negligible over the whole aperture $0-\bar{\alpha}$ and the whole field $0-\bar{\Omega}$.

The residual coma turns out to be more appreciable; however, its maximum value, which occurs at $\Omega=\bar{\Omega}$ is a small fraction of the focal length, and precisely:

$$C_{max} \simeq 0.006 f \quad \text{for } \bar{\Omega} = 20°, \quad \bar{\alpha} = 33° \ (\bar{\theta} = 60°)$$

$$C_{max} \simeq 0.002 f \quad \text{for } \bar{\Omega} = 20°, \quad \bar{\alpha} = 24° \ (\bar{\theta} = 45°).$$

For comparison, Fig. 12 shows the coma and the spherical aberration for $\Omega=20°$ and α up to 40° for the step mirror with circular cross section ($e=0$, $d=0$) described in L. Ronchi *et al.*[2] Of course, in the case of a circular mirror with $d=0$, α and θ coincide.

Table II shows a comparison between the aberrations of two quasi-parabolic step mirrors corrected for given values $\bar{\Omega}$ and $\bar{\alpha}$, for which $\bar{\alpha}$ represents also the maximum semiaperture, and the aberrations of the circular step mirrors having the same semiaperture. The first row corresponds to the mirror corrected for $\bar{\Omega}=20°$ and $\bar{\alpha}=33°$ (diameter $D=1.1\ f$). The second row cor-

[9] The optical focus F must not be confused with the geometrical foci O, O' of the conic section Σ.

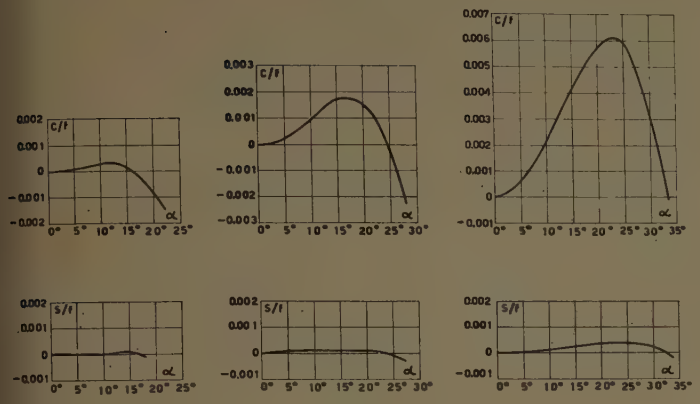

Fig. 8—Coma and spherical aberration plotted vs α, at $\Omega=20°$ for the three cases of correction: (a) at $\bar{\Omega}=20°$ and $\bar{\alpha}=16°$, (b) at $\bar{\Omega}=20°$ and $\bar{\alpha}=45°$, and (c) at $\bar{\Omega}=20°$ and $\bar{\alpha}=33°$.

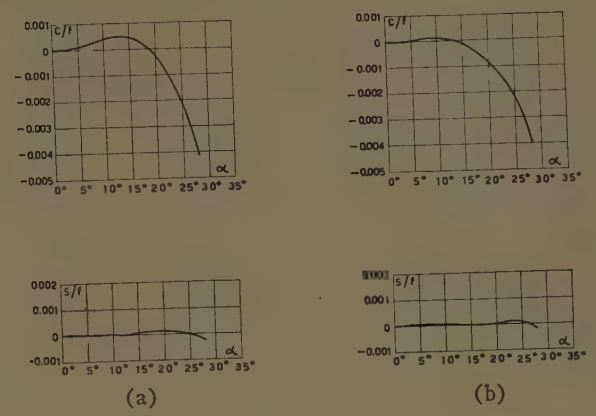

Fig. 10—Residual coma and spherical aberration plotted against α, (a) at $\Omega=15°$, (b) at $\Omega=10°$, for the case of correction at $\bar{\Omega}=20°$ and $\bar{\alpha}=24°$.

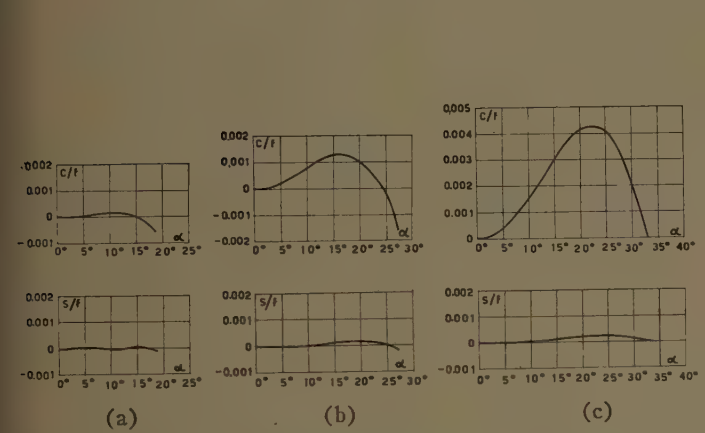

Fig. 9—Coma and spherical aberration plotted vs α, at $\Omega=15°$, for the three cases of correction: (a) at $\bar{\Omega}=15°$ and $\bar{\alpha}=16°$, (b) at $\bar{\Omega}=15°$ and $\bar{\alpha}=24°$, and (c) at $\bar{\Omega}=15°$ and $\bar{\alpha}=33°$.

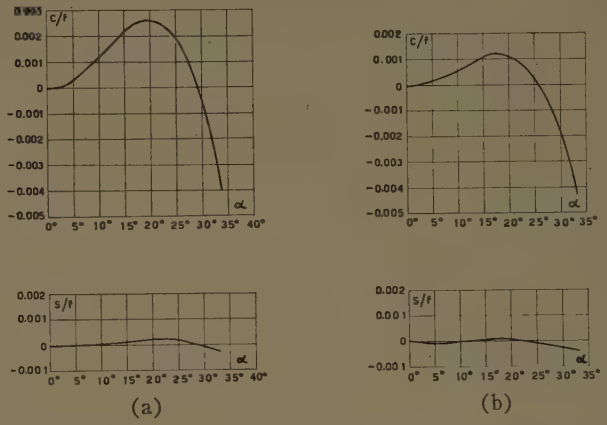

Fig. 11—Residual coma and spherical aberration plotted against α, (a) at $\Omega=15°$, (b) at $\Omega=10°$, for the case of correction at $\bar{\Omega}=20°$ and $\bar{\alpha}=33°$.

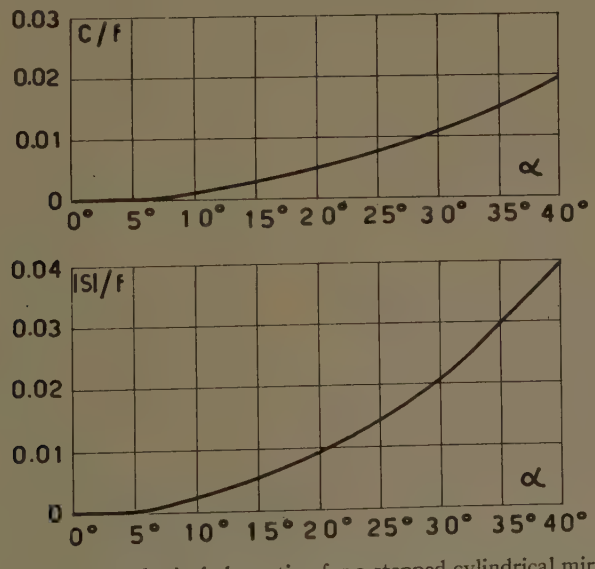

Fig. 12—Coma and spherical aberration for a stepped cylindrical mirror with circular cross section, plotted against α and evaluated at $\Omega=20°$.

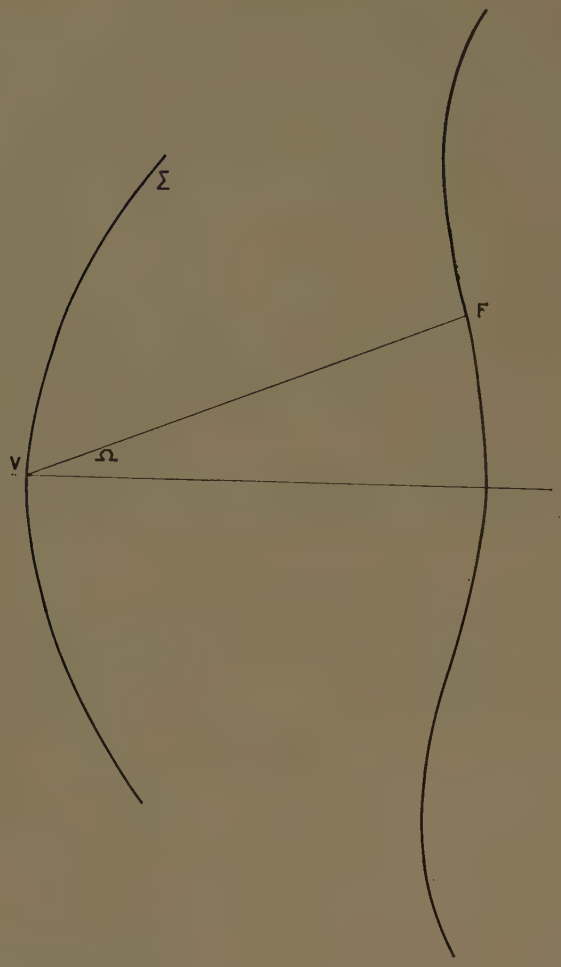

Fig. 13—Locus of the focus F for a variable field angle Ω for the mirror Σ corrected at $\bar{\Omega}=20°$ and $\bar{\alpha}=33°$.

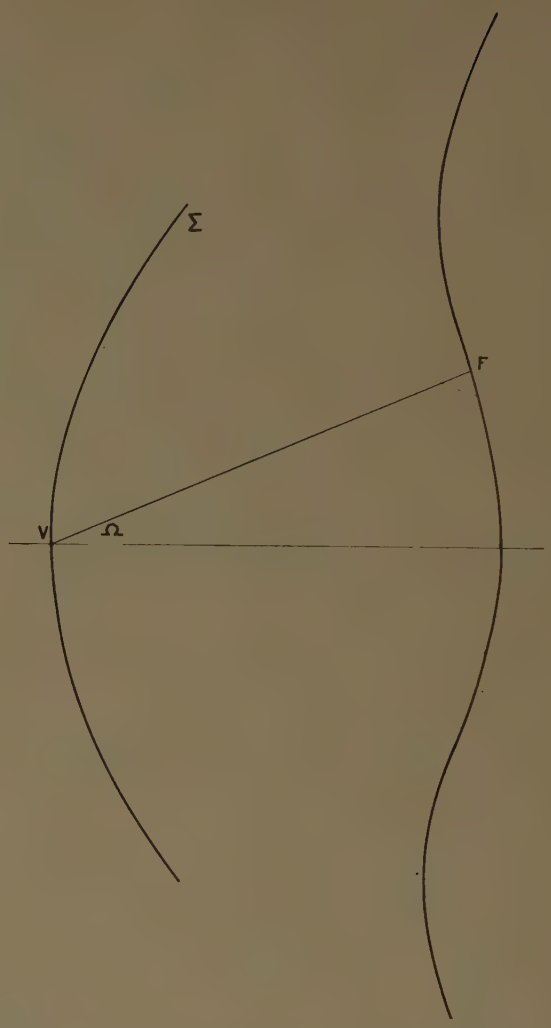

Fig. 14—Locus of the focus F for a variable field angle Ω for the mirror Σ corrected at $\bar{\Omega}=20°$ and $\bar{\alpha}=24°$.

responds to $\bar{\Omega}=20°$ and $\bar{\alpha}=24°$ ($D=0.83\,f$). The subscript c refers to the circular mirrors, while the symbols without subscript refer to the quasi-parabolic mirrors.

TABLE II

$\bar{\Omega}$	$\bar{\alpha}$	C	C_c	S	S_c
20°	33°	$0.006f$	$0.014f$	$0.0004f$	$0.026f$
20°	24°	$0.002f$	$0.008f$	$0.0001f$	$0.013f$

It appears from this table that the main improvement with respect to the circular mirrors is represented by the great reduction of the spherical aberration, which practically disappears.

The small values of C and S allow large antenna sizes to be attained. For example, for the value $D=300\lambda$ in the case $\bar{\alpha}=33°$, corresponding to a beamwidth of about 12′ and to $f=271\,\lambda$, one has $C=1.6\,\lambda$ and $S=0.11\,\lambda$, which are very little values.

In order to complete the results, it is of interest to draw the locus of the focus for a variable field angle. This is shown in Figs. 13 and 14 for the two mirrors corrected at $\bar{\Omega}=20°$ and $\bar{\alpha}=33°$ and $\bar{\alpha}=24°$, respectively.

VII. Conclusion

The theoretical results obtained for the cylindrical stepped mirrors of noncircular cross section seem to be very encouraging. One can scan a total field angle of at least 40° with a relative aperture D/f of the order of unity, without appreciable aberrations. It is most probable that even at much larger field angles the aberrations should remain reasonably small. An actual experimental test is desirable.

For radioastronomical work the mirror could be mounted with the axis of the cylinder vertical and a tiltable plane mirror should be placed in front of it. In order to collect more energy, one or both mirrors can have a slight curvature also in the vertical plane.

Of course, the very good qualities of the antenna are partially counterbalanced by a shortcoming, represented by the very limited bandwidth. It can easily be shown[4] that the frequency bandwidth is about $8\,cf/D^2$, where c is the velocity of light. Once the desired resolving power is selected, the value of D is derived as a consequence and the bandwidth turns out proportional to the focal length f.

Phase Adjustment of Large Antennas*

G. SWARUP† AND K. S. YANG†

Summary—**A technique is described for adjustment of phase paths within large antenna arrays or paraboloidal surfaces which are now in use, or are planned, for radio astronomy. After large paraboloids have been constructed, they suffer distortions which are very difficult to investigate and for which photogrammetry, millimeter-wave radar and optical survey have been suggested. A new suggestion, based on experiment at Stanford with phase measurement of long paths, is to place modulated gas discharge tubes, acting as scatterers, at various points on the paraboloidal surface and to monitor the phase path from a signal generator through the feed at the focus to each discharge tube in turn, and back. By means of a second probe, say a dipole situated at the vertex of the paraboloid, it is possible to triangulate on deflections. The feasibility of this scheme has been established in connection with the large Stanford cross antenna which has an aperture of 1339 wavelengths at 9.1 cm. The phase of the modulated reflected wave produced by the discharge tube is determined by adding it to a reference continuous wave of large amplitude and applying the resultant to a receiver sensitive to the modulating frequency. A null is obtained when the two waves are in quadrature. The coherent detection system allows measurement of the phase of the modulated reflection even when its amplitude is below −130 dbm. Using a 10-mw *S*-band signal generator, no difficulty was found in detecting the reflection from a small discharge tube placed 100 feet away from a 3 by 4 inch horn, which is sufficient range for applying the method to large paraboloids.**

I. Introduction

THE most highly directional antennas now in use depend critically for optimum performance on the adjustment of phase paths within the antenna. From the theory of antenna tolerances, discussed by Bracewell,[1,2] one can calculate the loss in directivity to be expected from given misadjustments of phase, both systematic and random. For smaller antennas, mechanical construction within the tolerances needed for adequate performance is possible.

For the larger antennas, those with apertures exceeding a thousand wavelengths (beamwidths less than a milliradian), it is necessary either to go to extremes of geodetic survey technique[3] or to make phase adjustments after construction.[4–6] Even in large paraboloids, which are now reaching apertures measured in hundreds of wavelengths, it is becoming customary to provide for phase adjustment by forming the surface with movable panels; it is not clear, however, that the best method of controlling the adjustment has been discovered. Suggestions include millimeter-wave radar, photogrammetry, and theodolite survey.[7]

In the case of large antenna arrays and interferometers, one of the chief problems is the adjustment of the transmission line connecting the various elements to the receiver. Phase path measurements require considerable care and effort, particularly if the transmission line between antennas is several hundred wavelengths long and there are many elements. The adjustment of an interferometer with phase-switching, such as a Mills cross[4] or a tee antenna[8] is even more arduous because it is more sensitive to adjustment errors. An example of a large phase-switched interferometer is the cross antenna that has been constructed recently at Stanford University, for operations at *S* band. Its design has been discussed by Bracewell and Swarup.[9] The antenna has an aperture of 1255 wavelengths. The crucial phase-paths are those of the branched *S*-band waveguide system feeding the 32 paraboloids of the interferometer. In this antenna it is absolutely necessary to make electrical determinations of phase path, physical length measurements being invalidated by dependence of phase velocity on the guide width.[10] Our original technique of adjustment of this antenna (Fig. 1) was based on phase equalization of all adjacent pairs of paraboloids, thus minimiz-

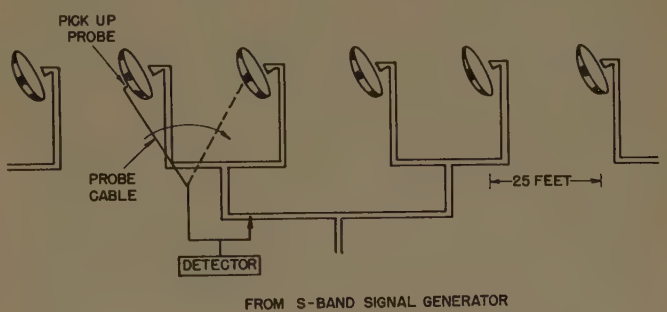

Fig. 1—Phase adjustment by equalization of adjacent pair using a movable probe cable.

* Received by the PGAP, May 18, 1960. This research was supported by the USAF Office of Sci. Res. under Contract No. AF 18(603)-53.

† Radio Astronomy Inst., Radioscience Lab., Stanford University, Stanford, Calif.

[1] R. N. Bracewell, "Radio astronomy techniques," in "Handbuch der Physik," Springer Verlag, Berlin, Germany, vol. 54 (in press).

[2] R. N. Bracewell, "Tolerance theory of large antennas," this issue, pp. 49–58; also, "Antenna tolerance theory," *Statistical Methods in Radio Wave Propagation*, Pergamon Press, Inc., New York, N. Y., p. 179; 1960.

[3] S. E. Khaĭkĭn and N. L. Kaĭdanovski, "A new radio telescope of high resolving power," *Paris Symp. on Radio Astronomy*, R. N. Bracewell, Ed., Stanford University Press, Stanford, Calif., pp. 166–170; 1959.

[4] B. Y. Mills, A. G. Little, K. V. Sheridan, and O. B. Slee, "A high resolution radio telescope for use at 3.5 m," PROC. IRE, vol. 46, pp. 67–88; January, 1958.

[5] W. N. Christiansen and J. A. Warburton, "The distribution of radio brightness over the solar disk at a wavelength of 21 cm, I," *Australian J. Phys.*, vol. 6, pp. 190–202; June, 1953.

[6] W. N. Christiansen and D. S. Mathewson, "Scanning the sun with a highly directional array," PROC. IRE, vol. 46, pp. 127–131; January, 1958.

[7] R. M. Emberson and N. L. Ashton, "The telescope program for the National Radio Observatory at Green Bank, West Virginia," PROC. IRE, vol. 46, pp. 23–35; January, 1958.

[8] G. Swarup and K. S. Yang, "Interferometer phasing problems at microwave frequencies," 1959 WESCON CONVENTION RECORD, pt. 1, pp. 17–24.

[9] R. N. Bracewell, and G. Swarup, "The Stanford microwave spectroheliograph antenna, a microsteradian pencil beam interferometer," this issue, pp. 22–30.

[10] Twelve-foot lengths of standard precision waveguide (drawn over a mandrel after extrusion) show variations in electrical length of up to one centimeter.

ing the phase paths to be measured. Pickup probes were placed in identical positions at the vertices of adjacent paraboloids, and the receiver was replaced by a signal generator. A reference voltage was extracted through a slot in the transmission line common to a pair of adjacent antennas. The voltages picked up by the two identical probes were then successively compared in phase with the reference voltage by means of the same probe cable.[11] The method is difficult, using microwaves, but was rendered feasible by the following precautions: (1) strap probe cable to a rigid strut, (2) surround probe cable with thermal insulation, (3) insert thermally insulated compensating cable length into reference arm to avoid errors arising because of frequency variations. Without these precautions, spurious phase changes, some mechanical, some due to the redistribution of sunlight and shade, occur when the probe cable is moved. A suitable, movable probe cable proved more practical than an elaborate multi-cable scheme used by Swarup and Yang[8] in which the cables are not required to move.

One might consider the possibility of placing a reflecting termination at each paraboloid in turn and noting the phase of the reflection returned to the signal generator. A basic difficulty is that 3 db of loss occurs at each branch point, of which ten all told are encountered on a round trip if the interferometer has 32 elements. Hence, there is a 30-db reduction due to this cause alone; consequently, the wanted return from a fully reflecting termination is indistinguishable from small reflections due to acceptable mismatches. One might work on small sections of transmission line at a time, but it would be laborious and the errors would be cumulative. Furthermore, if there were any discontinuities in the transmission line, it would be necessary to make measurements for several positions of the reflecting termination, as in a nodal-shift experiment.[12]

The method evolved here depends on a gas discharge, acting as a scatterer, maintained at the mouth of the feed horn at the focus of each paraboloid. The discharge is confined within a small fluorescent tube 13 cm long and 1.4 cm in diameter. A small reflection is produced by the glass of the tube, and the electron content of the discharge itself produces a small reflection. By imposing square-wave modulation on the discharge current, one causes part of the reflection to carry the modulation. Now, even though the reflection returned to the center of the feeder system is minute, it is separable from the other unmodulated reflections. This method has great promise for absolute phase measurement over unusually long distances and through heavy attenuation. It reduces considerably the effort required in doing the phase path adjustment of large antennas.

Automatic phase path control is clearly derivable from this method of phase path measurement by driving a phase shifter from the difference voltage of two probes straddling a null. Such automatic control is required in some applications, for example for the klystrons of very long microwave linear accelerators. It will also be required in due course for large radar antennas that have to be quick acting. An automatic null-seeking phasemeter for use in field exploration by means of the conventional probe method has been described by Bacon.[13]

A further possibility, of phase path measurement through space, presents itself. Short microwaves would be very suitable for monitoring the shape of large paraboloids, but in order to resolve small enough areas of the surface, only millimeter-wave radar has seemed appropriate. Now, by means of a modulated gas discharge which could be moved about on the surface, fine spatial resolution could be provided, at the wavelengths for which the normal feed system and transmission line were designed. Suitable modulated elements might include antennas, such as horns or corner reflectors that could be mismatched by a discharge or microwave diode, or mechanically vibrating or rotating elements.

The principle has been used previously by Richmond,[14] in connection with experimental studies of the near field of a horn radiator. In his modification of Justice and Rumsey's scatter techniques[15] for exploring a diffraction field, the requirements of stability and tuning adjustments were relaxed if the dipole scatterer was periodically detuned by a series germanium diode.

Dr. J. W. Findlay of the National Radio Astronomy Observatory has informed us that a phase measurement scheme was proposed in 1957 by N. Pedersen and R. Fleischer of Rensselaer Polytechnic Institute in an application to the U. S. Patent Office, and has been tested by General Bronze Corporation. We are grateful to Dr. Fleischer for information that his scheme is essentially similar to ours.

II. Theory of the Modulated Reflection Method

Fig. 2 shows the arrangement of the essential components for the measurement of phase shift and attenuation of an unknown feeder using a modulated gas discharge. A signal generator is connected to a matched antenna through a slotted line, an isolator, a directional coupler, and the feeder of unknown length. The gas dis-

[11] S. Silver, "Microwave antenna theory and design," Mass. Inst. Tech., Rad. Lab. Ser., McGraw-Hill Book Co., Inc., New York, N. Y., pp. 564–570; 1949.

[12] E. L. Ginzton, "Microwave measurements," McGraw-Hill Book Co., Inc., New York, N. Y., pp. 278–285; 1957.

[13] J. Bacon, "An *X*-band phase plotter," *Proc. NEC*, vol. 10, pp. 256–263; 1954.

[14] J. H. Richmond, "A modulated scattering technique for measurement of field distributions," IRE Trans. on Microwave Theory and Techniques, vol. MTT-3, pp. 13–15; July, 1955.

[15] R. Justice and V. H. Rumsey, "Measurement of electric field distribution," IRE Trans. on Antennas and Propagation, vol. AP-3, pp. 177–180; October, 1955.

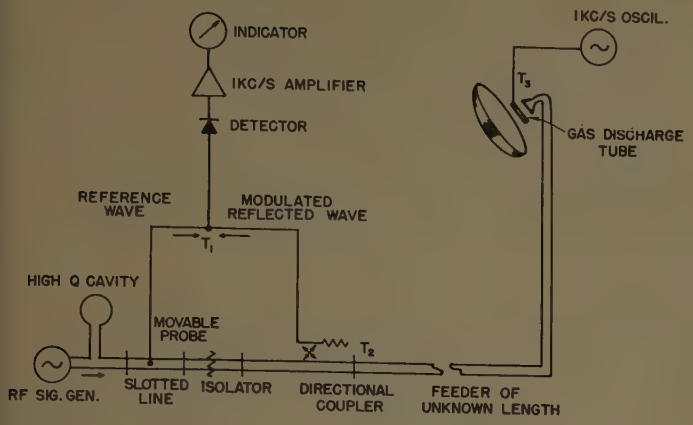

Fig. 2—Schematic circuit for the measurement of phase shift and attenuation using a modulated gas discharge tube.

charge is situated in a convenient position at the antenna. In the presence of a discharge, the electrons interact with the microwave field, the heavy ions (argon, mercury) being unimportant. The theory of the reflection produced by the discharge is treated in the Appendix. The current of the discharge tube shown in Fig. 2 is modulated at a convenient audio frequency, say 1 kc, to produce a reflected wave which is modulated. The reflected wave passes through the unknown network and is separated from the forward wave by a good directional coupler. The reflected wave is then added to a reference wave derived from the slotted line. The resultant wave, which is the sum of the reference wave, the modulated reflected wave, and some stray unmodulated wave, is impressed on a receiver consisting of a detector, a narrow-band 1-kc amplifier, and an indicator. The amplitude of the reference wave is made much stronger, say 40 db or more, compared to the amplitude of other waves. It is shown below that a null is obtained on the indicator when the very weak, modulated reflected wave is nearly in *quadrature* with the reference wave, and a maximum is obtained when the two are in phase. The phase and amplitude of the reflected wave is obviously dependent upon the constants of the measuring circuit and upon twice the phase path length and attenuation of the unknown network. The effect of phase constants of the measuring circuit can be easily eliminated by removing the unknown network and determining a reference plane on the slotted line for the null condition. A null is then obtained with the unknown network connected. One-half of the difference of the two positions of the probe determines the phase path length of the unknown network. The attenuation of the network can be determined by noting the amplitude of the receiver output for the position of the probe when a maximum is obtained and by calibration of the receiver law. The accuracy of attenuation measurements can of course be improved by the usual substitution method.

As mentioned above, the voltage wave impressed on the detector is the sum of the reference wave, the modulated reflected wave, and a stray unmodulated wave that is caused by an imperfect directional coupler and some small steady reflections in the circuit. The amplitude and phase of these voltages may be represented as follows:

$$\text{reference wave} = v_r = V_r \cos(\omega_c t + \phi),$$

$$\text{modulated reflected wave} = v_m = V_m(1 + m\cos\omega_m t)\cos(\omega_c t + \theta),$$

$$\text{stray unmodulated wave} = v_s = V_s \cos(\omega_c t + \psi). \quad (1)$$

Let us at first ignore the presence of the stray unmodulated wave. The voltage wave v impressed on the detector is then the sum of the reference wave v_r and the modulated reflected wave v_m, *i.e.*,

$$v = V_r \cos(\omega_c t + \phi) + V_m(1 + m\cos\omega_m t)\cos(\omega_c t + \theta). \quad (2)$$

For simplicity, we assume that the detector is a full-wave, square-law detector whose output current i_d is given by

$$i_d = Av^2, \quad (3)$$

where v is the instantaneous input voltage.

Substituting (2) in (3) yields, after some reduction:

$$i_d = \text{dc component} + [(AmV_m^2 + AmV_rV_m\cos(\phi - \theta)]\cos\omega_m t + \tfrac{1}{4}Am^2V_m^2\cos 2\omega_m t + \text{RF components}. \quad (4)$$

If the detector output is connected to a narrow-band amplifier tuned to the modulating frequency, the receiver responds only to the term at the modulating frequency. The indicator current i_0 is given then by

$$i_0 = GAmV_m[V_m + V_r\cos(\phi - \theta)], \quad (5)$$

where G is the gain of the audio amplifier.

When the position of the probe in the slotted line is altered, the phase of the reference wave changes, and it is seen from (5) that this varies the receiver output current. The condition for a minimum or null of the output current is dependent upon the amplitudes of the modulated reflected wave and the reference wave. Let us examine (5) for three cases, as follows:

1) $V_r < V_m$. The amplitude of the reference wave is smaller than that of the modulated reflected wave. It is obvious that a minimum is obtained when

$$\phi = \theta \pm (2n + 1)\pi,$$

where n is any integer 0, 1, · · · .

2) $V_r = V_m$. If the amplitudes of the reference wave and of the modulated reflected wave are equal, a null is obtained for the case of

$$\phi = \theta \pm (2n + 1)\pi.$$

The nulls correspond to positions of the probe in the slotted line that are one wavelength apart.

3) $V_r \gg V_m$. The amplitude of the reference wave is much larger than the amplitude of the modulated reflected wave. A null is obtained when

$$V_m = -V_r \cos(\phi - \theta).$$

That is, when either

$$\phi = \theta + \sin^{-1}\left(\frac{V_m}{V_r}\right) + (\pm 2n + \tfrac{1}{2})\pi,$$

or

$$\phi = \theta - \sin^{-1}\left(\frac{V_m}{V_r}\right) + (\pm 2n - \tfrac{1}{2})\pi.$$

If the reference wave is made 40 db stronger than the modulated reflected wave, then $\sin^{-1} V_m/V_r = 0.6°$. In this case, the nulls correspond to positions of the probe in the slotted line which are nearly one-half wavelength apart. The phase of the output current that is varying at the modulating frequency reverses at each null. The output current has a maximum amplitude when v_r and v_m are in phase or out of phase. For the in-phase case,

$$|i_{0\,\max}| = GAmV_m(V_r + V_m). \tag{6}$$

For the out-of-phase case,

$$|i_{0\,\max}| = GAmV_m(V_r - V_m). \tag{7}$$

The adjacent maxima are nearly equal if $V_r \gg V_m$.

Fig. 3 illustrates the relative value of the output current as a function of the probe position for the above three cases. The maximum amplitude of the output current becomes larger as the amplitude of the reference wave is increased. If the receiver does not start saturating, it can be shown that this method of coherent detection by introducing a large reference wave makes it possible to detect an amplitude modulated wave whose power is only a few times greater than $kT\Delta f$, where T is the equivalent temperature of the receiver and Δf is the bandwidth of the amplifier tuned at the modulating frequency. The thermal noise emitted by the discharge tube does not depend on the oscillator signal level and can be made negligible by a suitable choice of the oscillator level.

Let us now consider the effect of the stray unmodulated wave $v_s = V_s \cos(\omega_c t + \psi)$. It may be shown that the indicator current is then given by

$$i_0 = GAmV_m[V_m + V_r \cos(\phi - \theta) + V_s \cos(\psi - \theta)]. \tag{8}$$

This differs from (5) by the presence of the term $V_s \cos(\psi - \theta)$.

In an experimental case described in Section III, the unknown network had an attenuation of 20 db. The small perturbation produced an amplitude-modulated reflection which was 30 db weaker than the incident wave. Thus, the amplitude of the modulated wave at terminals T_2 was about 70 db lower than that of the incident wave. In comparison, a small mismatch at terminals T_2, in Fig. 2, corresponding to a standing-wave ratio

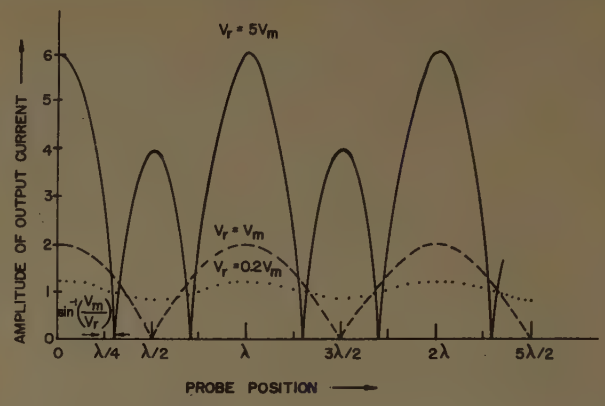

Fig. 3—Relative amplitude of output current as a function of probe position for the cases of

$V_r = 0.2\ V_m$ (dotted line),
$V_r = V_m$ (broken line), and
$V_r = 5\ V_m$ (full line),

where V_r is the amplitude of the reference wave and V_m is the amplitude of the modulated reflected wave.

of 1.02 produces a stray unmodulated wave which is only 40 db lower than that of the forward-going wave. Thus, we conclude that in many practical cases the amplitude of the stray wave is much larger than that of the modulated wave. This is the main reason for our making the amplitude of the reference wave much larger than that of the other waves in this phase-measurement technique (see case 3, above). The maximum error $\epsilon_{\max}$ in phase measurement of the unknown network in the presence of the stray wave is given by $\epsilon_{\max} = \sin^{-1} V_s/V_r$. This is a small angle of 0.6° if the reference wave is made 40 db larger than the stray wave.

The principle of the modulated discharge method of phase measurement can be visualized quickly by considering the frequency spectrum of the various voltage waves. Fig. 4 shows the spectrum of the voltage waves existing at the input and output of the receiver (see Fig. 2). For convenience, the phase of the modulated reflected wave is taken to be zero. The wave at the input of the receiver consists of a carrier wave of frequency ω_c whose amplitude and phase is nearly the same as that of the reference wave, for the case when $V_r \gg V_s \gg V_m$, and the two sidebands at frequencies of $(\omega_c + \omega_m)$ and $(\omega_c - \omega_m)$ whose phase and amplitude are dependent on the constants of the unknown network. Now, it can be shown that the output of a linear or a square-law detector does not contain a term at the modulating frequency if the phase of the sidebands is 90° away from that of the carrier wave. Thus, when the very strong reference wave and the modulated reflected wave are in quadrature, we obtain a null on the output indicator.

Suppose a square-wave modulation is imposed on the discharge. It can be shown that the audio component of the detector output is also a square wave, and that the term at the modulation frequency has the same form as (8). Again a null is obtained when the strong reference wave is in quadrature to the modulated wave.

When the discharge produces a combined amplitude and phase modulation, the corresponding sideband fre-

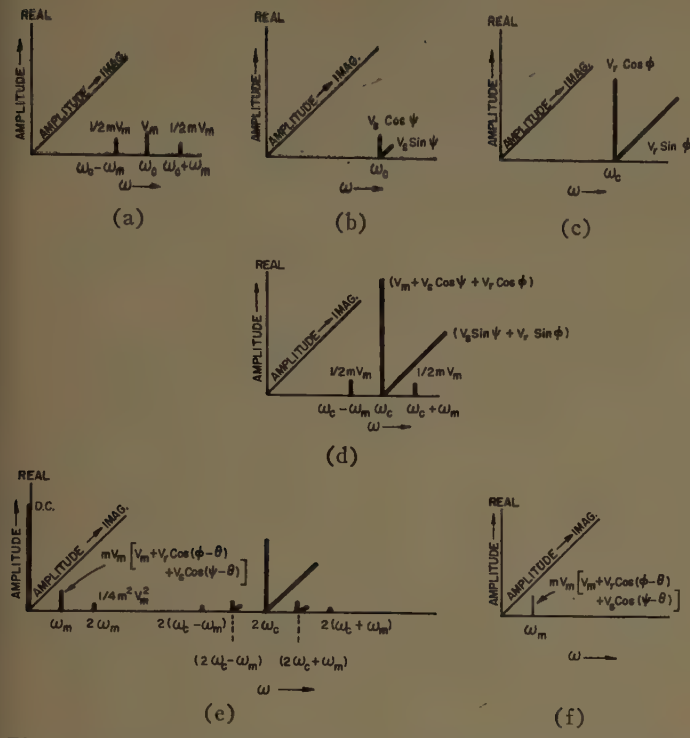

Fig. 4—Spectrum of the voltages existing at the input and output of the receiver shown in Fig. 2. (a) Modulated reflected wave. (b) Stray unmodulated wave. (c) Reference wave. (d) Resultant wave at input of receiver. (e) Detector output. (f) 1-kc amplifier output.

quencies on the opposite sides of the carrier do not necessarily have the same amplitude any more (for a square-wave modulation there is always symmetry). In this case only a minimum, not a null, is obtained when the strong reference wave is in quadrature to the modulated wave.

A number of refinements can be made to the simple technique described in this paper. One possible variation is to place a magic tee and a pair of balanced detectors at the junction T_1 in Fig. 2, instead of a simple tee and a single detector. As shown by Richmond,[14] this procedure suppresses the stray unmodulated wave. Another possibility is offered when we are required to equalize amplitude and phase of fields impressed on a system like a multi-element interferometer shown in Fig. 1. Two discharge tubes are used. One is placed near a reference antenna and the second is placed successively near the other elements of the interferometer. A modulating voltage is applied in phase opposition to the two tubes. Each tube produces a modulated reflected wave. If the amplitude and phase of the two RF waves are identical but the phase of the modulation is in opposition, it is easily seen that the resultant wave does not contain any variation at the modulating frequency. Hence, a suitable equalization procedure can be easily developed. Another possible refinement is to use a phase detector instead of an amplitude detector in the indicator at the output of the receiver shown in Fig. 2. This improves the signal-to-noise ratio. Also, if an amplitude detector is used, the measurements of the phase-path of the unknown network may have an ambiguity of multiples of $\lambda/4$; whereas, for the case of a phase detector, there is obtained only an ambiguity of multiples of $\lambda/2$. This ambiguity can be eliminated by making a pair of phase path measurements at two slightly different frequencies of the signal generator. We have also found it convenient to verify freedom from ambiguity by making brief solar observations with adjacent pairs of elements.

III. Experimental Results

The method described here was applied in adjusting the transmission line of the Stanford cross antenna that is shown in Fig. 5. The antenna has been constructed to obtain daily pictures of the sun at a wavelength of 9.1 cm. It consists of an E-W and a N-S multi-element interferometer, each containing 16 ten-foot paraboloid reflectors situated 25 feet apart. The two arrays are phase-switched to provide pencil-shaped beams with a half-power width of nearly 3.1 minutes of arc. The separation between the adjacent beams is more than 41 minutes of arc, and therefore, there is only one beam on the solar disk at a time.

Fig. 5—The 32-element cross antenna at Stanford for operation at 9.1 cm.

The paraboloids are illuminated by waveguide horns of mouth 3 inches×4 inches which are situated at the focus. The horn feeds are connected to a receiver through a branched system of transmission line. The transmission line between each horn and the receiver is approximately 300 feet long. The attenuation between a horn and the receiver is nearly 20 db, of which 15 db is due to the fact that 32 elements are connected in parallel. Fig. 2 shows the experimental setup employed for the measurement of attenuation and phase path of this feeder system. A well-matched magic tee was used as a directional coupler. A sliding screw tuner was placed between the magic tee and the feeder system to minimize the amplitude of any stray unmodulated wave reaching the detector. The modulated discharge tube placed at the horn was a Westinghouse 4-watt standard fluorescent tube. The tube was placed in succession just outside the mouth of the 32 horns and was located in the direction of the *H* plane. The tube produced a small standing-wave ratio of 1.05 at zero current which increased to 1.10 at 30 ma and to 1.16 at 100 ma. The tube current was square-wave modulated between 15 and 45 ma at a frequency of 1 kc. It is to be noted that

proper care should be taken in choosing the modulating frequency, since a fluorescent tube usually oscillates by itself at some audio frequency dependent upon the parameters of the discharge.[16] The oscillations can be prevented by increasing the discharge current. In the present case, the frequency of oscillation was around 1.9 kc, which was found to be sufficiently remote from 1 kc since the tuned voltage amplifier employed in the receiver had a half-power bandwidth of only 38 cps centered around 1 kc (Hewlett-Packard model 415B). Further, the amplitude of the 1.9 kc oscillation was reduced to a value about one-tenth that for the 1 kc square-wave modulation by proper choice of the external circuit. Fig. 6 shows the circuit of the power supply used with the fluorescent tube.

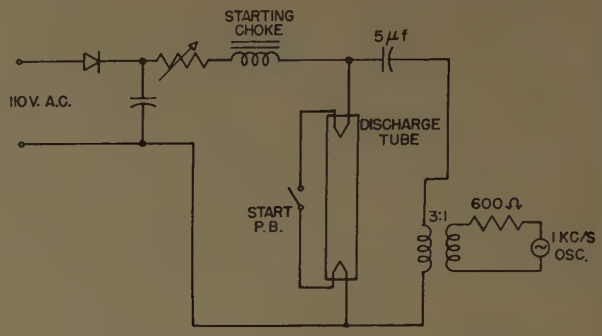

Fig. 6—Circuit of the power supply for the discharge tube.

The current and location of the discharge tube were chosen to produce a small reflection; otherwise, a large error could occur, since each junction of the transmission line system contains a large discontinuity. The accuracy of measurement of the over-all system was checked by inserting a variable precision phase-shifter and attenuator of known calibration between one horn and the 300-foot transmission line. The measurements were then made at the other end of the transmission line, using the procedure outlined in Section II, for various positions of the phase-shifter and the attenuator. The insertion of the phase-shifter changes the position of the probe in the slotted line for the condition of the null. Half the difference between two values of the probe position gives the phase path difference. The insertion of the attenuator changes the value of the indicator current for the condition of maximum. If the detector has a square-law characteristic, the power attenuation is given directly by the ratio of the two values of the indicator current. This is because the modulated reflected wave travels the unknown network twice, and the indicator current is directly proportional to the amplitude of the modulated reflected wave [see (6) and (7)]. Fig. 7 shows the error found between the measured and the actual value using the modulated discharge method for attenuation and phase measurement. The errors are sufficiently small. Using a signal generator with output of 10 mw, an audio amplifier with gain of 60 db, and a small perturbation that produces a reflection 30 db below the incident power, it was found possible to measure attenuation of the feeder accurately up to about 25 db.

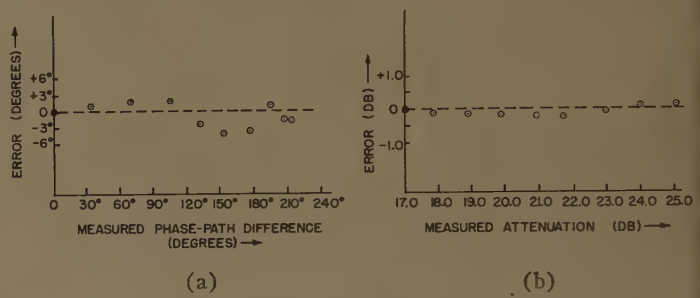

Fig. 7—Error in the measurements of (a) phase path difference, (b) phase path attenuation.

The accuracy of phase path measurement of long transmission line is dependent upon the frequency stability of the RF signal generator. The frequency can be monitored using a high Q cavity. The requirement on the stability of the signal generator is relaxed by placing a reference discharge tube at one of the antennas. The square-wave modulation is first applied to the tube at the reference antenna and a few seconds later to the tube at the antenna to be measured. We are thus able to measure accurately the amplitude and phase of the fields imposed on all 32 antennas in the course of a few hours. The measurement time could be reduced further by using 32 discharge tubes and applying modulation to them in succession.

The technique described above would be very suitable for investigating any constructional errors occurring in the surface of a large paraboloidal antenna,[17] and in particular, for monitoring displacements of the surface that arise when the large paraboloid is pointed in various directions or subjected to thermal or wind stress. Several discharge tubes could be placed at different points on the surface and their distance to the feed at the focus measured by applying modulation to them in succession. The positions of the tubes could be triangulated by making further sets of measurements to other feeds, *e.g.*, a quarter-wave dipole situated at the vertex of the paraboloid. The method was applied to a 10-foot paraboloid of the Stanford cross antenna, and the change in phase path within the paraboloid and its feed structure due to antenna pointing was measured to be less than 2°. In a special test, it was found possible to measure small displacements of a 4-watt fluorescent tube placed 100 feet away from a 3×4-inch horn to an accuracy of ±0.1 inch, while using a 10-mw S-band signal generator. A sensitive receiver with a noise factor

[16] H. Johnson and K. R. DeRemer, "Gaseous discharge superhigh-frequency noise source," Proc. IRE, vol. 39, pp. 908–914; August, 1951.

[17] G. Swarup and K. S. Yang, "Monitoring paraboloidal antennas," Proc. IRE, vol. 48, pp. 1918–1919; November, 1951.

of 8 db, which incorporated a phase detector, was employed. The scattering cross section of the modulated 4-watt discharge tube was measured to be 0.4 square cm at a wavelength of 9.1 cm which is consistent with the theoretical estimates of the scattering produced by the tube (see the Appendix). This provides sufficient range for applying the method to the largest existing paraboloids.

Appendix

Radio Reflections from a Discharge Tube

The theory of the scattering of radio waves by an ionized cylinder has been treated in detail by several authors[18–21] in connection with the study of meteor trails. The strength of the reflection is primarily dependent upon the diameter of the column, electron line density, and the direction of the electric field within the column. When the electron density in the column is less than the critical density, and the diameter of the tube is much less than the wavelength, so that the wave affects all the electrons uniformly, then the electrons scatter coherently and freely, and the scattering cross section of the ionized column is given by

$$\sigma = \frac{\mu_0^2 e^4}{6\pi m^2} N^2_{\text{tot}}$$

$$= 6.65 \times 10^{-29} N^2_{\text{tot}} \text{ meter}^2 \qquad (9)$$

where $\mu_0^2 e^4/6\pi m^2$ is the classical scattering cross section of an electron and N_{tot} is the total number of electrons contained in the discharge. If the electron volume density exceeds the critical density, the electrons inside the skin depth are shielded and do not provide their full effect. But if the diameter of the discharge column is less than the skin depth, the above equation is still valid, provided the incident electric field vector is parallel to the discharge. When the electric vector is normal to a narrow ($<\lambda$) ionized column, a resonant scattering may occur at a frequency for which the dielectric constant of the medium is -1. The plasma resonance occurs because the normal incident wave induces a space charge in the sharp boundaries of the column. The theoretically expected resonance effect has been confirmed experimentally by Romell,[22] who studied the scattering of 30-cm radio waves by a mercury discharge in a 3-cm diameter tube. However, if the diameter of the discharge column is much higher than the skin depth, the reflection is the same as that produced by a metal cylinder with the dimensions of the discharge. It can be shown that the skin depth equals the diameter of an ionized column if the electron line density is $\simeq 10^{14}$ electrons per meter.

The effect of electron collisions is to reduce the scattering cross section of (9) by $[1+(\nu/\pi f)^2]^{-1}$, where ν is the collision frequency and f is the frequency of the radio waves. In a discharge tube, ν is of the order of 10^9 to 10^{10} collisions per second and the effect of damping is not very large.

Our measurements showed that the scattering cross section of a 4-watt fluorescent tube 13 cm long and 1.4 cm in diameter varied by 0.4 square cm as its current was altered from 15 ma to 40 ma. Substituting this in (9), we deduce the corresponding variation in the volume electron density of the tube to be of the order of 10^{17} electrons per cubic meter, which is consistent with our estimates of the density in the tube.

If the discharge tube is placed in a transmission line, we can calculate the reflection produced by the discharge by considering the equivalent dielectric constant and propagation constant of the ionized medium. Each electron acts like an inductance m/e^2 in series with resistance $m\nu/e^2$ shunted across the guide, where e, m, and ν are the charge, mass, and collision frequency of an electron.[23] Let us consider, as a special case, the reflection produced by a slab of electrons of length L situated between parallel strip lines of width b and separation a. If $L<\lambda$, the electron slab effectively causes a shunt lumped admittance ξ across the guide which, after normalization by the parallel strip admittance ($377\ a/b$), is found to be

$$\xi = \frac{\dfrac{a}{b}377}{\dfrac{a}{b}\dfrac{m(\nu+j\omega)}{Ne^2}\dfrac{1}{L}},$$

$$= \frac{377e^2NL}{m(\nu+j\omega)},$$

where N is the volume electron density. Thus, we expect a reflection coefficient of

$$\Gamma = \frac{1-Y_L}{1+Y_L} = \frac{1-(1+\xi)}{1+(1+\xi)},$$

$$\cong -\frac{377e^2NL}{2m(\nu+j\omega)}.$$

Acknowledgment

The authors are indebted to Prof. R. N. Bracewell for many valuable discussions on the problems encountered in this work.

[18] A. C. B. Lovell and J. A. Clegg, "Characteristics of radio echoes from meteor trails, I," *Proc. Phys. Soc.*, vol. 60, pp. 491–498; May, 1948.

[19] N. Herlofson, "Plasma resonance in ionospheric irregularities," *Arkiv för Fysik*, vol. 3, pp. 247–297; August, 1951.

[20] V. R. Eshleman, "The Mechanism of Radio Reflections from Meteoric Ionization," Electronics Labs., Stanford University, Stanford, Calif., Tech. Rept. no. 49; July, 1952.

[21] T. R. Kaiser and R. L. Closs, "Theory of radio reflections from meteor trails: 1," *Phil. Mag.*, vol. 43, pp. 1–32; January, 1952.

[22] D. Romell, "Radio reflections from a column of ionized gas," *Nature*, vol. 167, pp. 243–244; February, 1951.

[23] R. N. Bracewell, "Analogues of an ionized medium," *Wireless Engr.*, vol. 31, pp. 320–326; December, 1954.

Centimeter-Wave Solar Bursts and Associated Effects*

M. R. KUNDU† SENIOR MEMBER, IRE AND F. T. HADDOCK†, MEMBER, IRE

Summary—**Most of our knowledge of solar bursts in the meter-wave region has been derived from dynamic spectral observations. Systematic spectral observations have led to the classification of meter-wave bursts into distinct spectral types. No such classification exists for cm-wave bursts because spectral observations are only just beginning. However, recent interferometric measurements have enabled the cm-wave bursts to be classified into a number of distinct types. The properties of such different types of cm-wave bursts are discussed in relation to their associated effects.**

Dynamic spectral observations of cm-wave bursts obtained at the University of Michigan show that cm-wave burst emission is a broad-band continuum, similar in nature to meter-wave type-IV and type-V emission.

Introduction

SPORADIC bursts of radio-frequency radiation from the sun have been observed and studied since 1945. Little progress was made in classifying and explaining the various types of radio bursts until 1950 when Wild and McCready [1] obtained a variety of wide-band dynamic spectra of meter wavelength bursts.

Although the variety and diversity of solar bursts at cm wavelengths is several times *less* than for meter waves, not as much is known about them because sweep-frequency receiver observations have only been initiated recently.

Two dynamic spectra of solar bursts obtained at the University of Michigan on July 29, 1959, and January 12, 1960, in band of 2000–4000 Mc are discussed in association with meter-wave emission in [19].

Within the last year or two, the importance of cm-wave bursts has been stressed, particularly because of their association with sudden ionospheric disturbances, geomagnetic and cosmic-ray storms, auroras, gamma-ray bursts, etc. In view of the apparent importance of cm bursts and their associated effects, it seems valuable at this time to present an up-to-date review of our knowledge of cm-wave bursts and to make it readily available, particularly to cosmic-ray physicists and geophysicists.

Classification of Centimeter-Wave Solar Bursts

Meter-wave bursts have been classified into a number of distinct types. This classification has been possible due to systematic spectral studies by Wild [1]. No such classification exists for cm-wave bursts. The reason is mainly the lack of spectral studies. However, records of total solar radiation during bursts have led Covington to give a morphological classification of 10-cm bursts [2]. Recent interferometric measurements by Kundu [3] have shown that the bursts observed on cm waves can be considered to be composed fundamentally of three distinct types:

Type A: The simple burst is characterized by a rapid rise to a peak value and a subsequent decline. It is short in duration (1–5 minutes) and seems to be impulsive in nature. About 60 per cent of these bursts are found to be partially polarized. The partial polarization may be circular or linear. The source of the burst has an average diameter of about 1 minute of arc when its intensity is small and of about 1.6 minutes of arc when its intensity is large. The corresponding equivalent temperatures are of the order of 10^{6}°K for weak bursts and usually 10^{7}°K to 10^{9}°K for strong bursts.

Type B: The post-burst follows a simple burst or a group of simple bursts (in the case of a complex structure). It has a duration of several minutes to several hours. The partial polarization of this burst is the same as the simple or complex burst associated with it. Usually its source appears to be a diffuse zone of relatively large diameter (>3 minutes of arc). Its equivalent temperature usually lies between 10^{5}°K and 10^{7}°K.

Type C: The gradual rise and fall is characterized by a slow rise to a maximum intensity and comparably slow decline to the preburst level. Its duration is usually of the order of 10 minutes. It is, in most cases, partially polarized, the polarization being always circular. Its source is a localized hot region of small diameter (<1 minute of arc) with an equivalent temperature usually less than 10^{6}°K.

One or a combination of these different basic types usually constitutes the burst or outburst event.

Microwave Outbursts

Great solar bursts on centimeter waves—microwave outbursts—are very complex in structure, being usually composed of types A and B. These are different from the other cm bursts only in their intensity, the intensity being greater than a certain value $I(f)$. The peak flux density (part A) on 3-cm wavelength is usually greater than 100[1] units. They have a very complex structure and have several maxima of comparable intensity (type A), that is, they consist of several type A bursts usually followed by a post-burst (type B). Sometimes they are preceded by one or two bursts (type A or C) called precursors. At the end of the precursor, the intensity increases very rapidly and reaches its peak value after a time of 1–3 minutes (type A). The short rise time to maximum and the short duration of the peak intensity displays an impulsive character of the burst at its be-

* Received by the PGAP, September 12, 1960. This work was supported by Office of Naval Res. Contract Nonr 1224(16).

† The Observatory, University of Michigan, Ann Arbor.

[1] One unit of radio flux density at the earth in this discussion is 10^{-22} watt meter^{-2} (cps band)$^{-1}$.

ginning. Shortly after the maximum (type A), the intensity of the post-burst (type B) decreases very slowly and comes to the normal pre-burst value after a time of about 10 minutes to several hours. The diameter of these outbursts at the instant of maximum intensity (type A) usually lies between 1.5 minutes of arc and 2 minutes of arc, the average value being about 1.6 minutes of arc. The dimension of the source increases after the maximum intensity, its value being usually greater than 3 minutes of arc (type B). The post-burst (type B) source appears as a diffuse region of rather large diameter. Majority of these microwave outbursts (about 70 per cent on a wavelength of 3 cm) are partially circularly polarized. Linear partial polarization has, however, been observed in some cases. Study of polarization of the microwave outbursts reveals that *sometimes* the source is composed of two regions: 1) a narrow region of small intensity and of long duration mainly responsible for the polarization of the emitted radiation, and 2) a rather large region of high intensity and of shorter duration, which does not seem to contribute to the polarization of the emitted radiation [4]. The equivalent temperatures of these outbursts usually exceed 10^7°K and can attain a value of 10^9°K on 10-cm waves. An interferometric record of a typical cm-outburst is shown in Fig. 1.

Rare Short Outburst

Occasionally 3-cm outbursts from the sun have been observed which have a very short duration and a large diameter. The intensity rises to the peak value unusually fast and the impulsive period (type A) does not normally last more than a minute. The post-burst (type B) is either absent or very much shorter than in the case of usual microwave outbursts. The total duration of the event is of the order of 2 to 3 minutes. No data are available for the polarization of these short outbursts. Their diameter (>2.5 minutes of arc) is larger than that of the usual outbursts (diameter <2.5 minutes of arc). In some cases, it can have a value as large as 5 minutes of arc, as in the case of the March 20, 1958 event shown in Fig. 2. The equivalent temperature is of the same order as that of other outbursts.

It is to be noted that the 3-cm solar burst characteristics of that event (rapid rise, short duration, large diameter) also apply to the 10-cm and 21-cm burst event. The intensity of the burst decreases very sharply from a value of more than 900 units on 3-cm wavelength and 350 units on 10 cm to less than 25 units on 21 cm. The diameter, on the other hand, increases rapidly from about 5 minutes of arc on 3-cm to about 10 minutes of arc on 21-cm wavelength.

The essential difference between "microwave outburst" and "rare short outburst" is in their duration and their diameter. In addition, the "microwave outburst" has a broad spectrum extending down to meter waves,

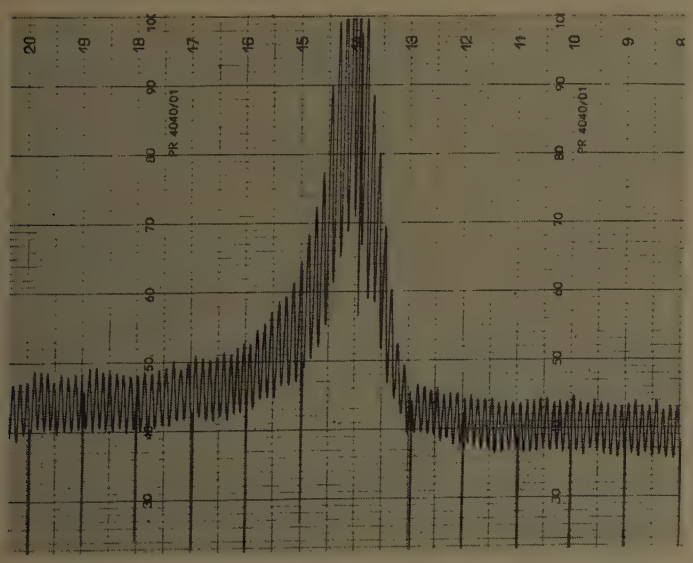

Fig. 1—Record of a microwave outburst by a two-element interferometer on 3 cm. The angular resolution is 1'8.

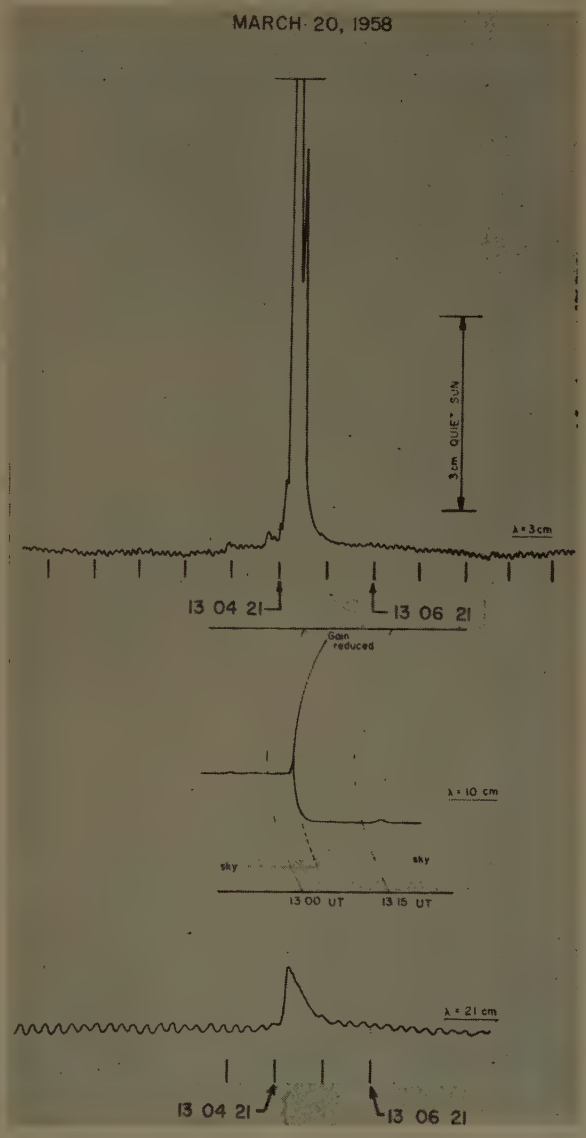

Fig. 2—Records of a "rare short outburst" on 3-cm, 10.7-cm and 21-cm wavelengths. The 10.7-cm burst was recorded by a single antenna at Ottawa, whereas the 3-cm and 21-cm bursts were recorded by two-element interferometers at Nançay, France.

but the "rare short outburst" has a very sharp low-frequency cutoff spectrum. The outburst of March 20, 1958 has a spectrum as shown in Fig. 3(a). In contrast, an ordinary microwave outburst may have an average spectrum like that shown in Fig. 3(b).

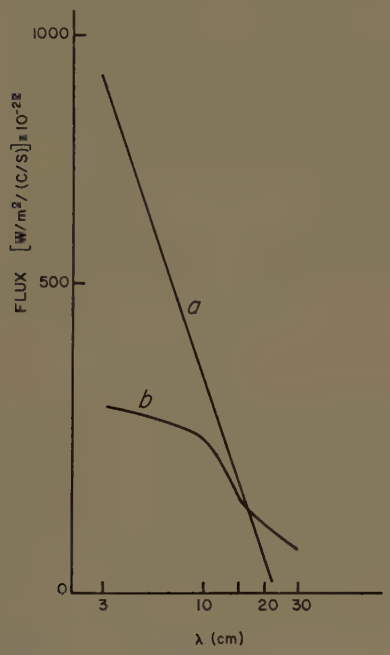

Fig. 3—Peak flux vs wavelength of (*a*) a "rare short outburst," (*b*) an average microwave outburst.

Other Nomenclature

The classification of cm-wave bursts by Covington [13] gives different classes of bursts. As we have mentioned earlier, all these different classes of bursts are composed fundamentally of three distinct emissions when source size and polarization are taken into account. For the sake of future nomenclature, these emissions have been called emissions of type A, type B, and type C. Table I (opposite) shows the relation between these types and the classes of bursts according to Covington. Also listed in the same table are the distinctive features of these emissions.

Great bursts in Covington's classification have been classified as microwave outbursts and rare short outbursts, which are distinguished from the other cm-wave bursts principally by their great intensity. They are basically composed of emissions of types A and B. Their main features are listed in Table II.

Frequency of Occurrence

Microwave outbursts are less frequent than the other, less intense, bursts. The frequency of occurrence of bursts decreases with the increase of their peak intensity. The frequency distribution of cm bursts as a function of their intensity is expressed [3] by

$$f(I) \sim I^{-1.5}$$

where $f(I)$ is the frequency of occurrence corresponding to intensity I.

Position and Movement of Burst Sources

The cm-wave bursts have been observed to originate at the same place in the solar atmosphere as the origin of the slowly varying component [3] (radio condensations). In fact, there is a close relationship between the intensity of the radio condensations and the probability of occurrence of cm-wave bursts [3]. However, during periods of strong activity, very weak bursts of type A (micro-bursts) have been found to occur at places other than the radio condensations [3].

Although interferometric measurements have been made to find the movement of cm-wave bursts by means of observed phase shifts, no phase shift has been observed for most of the bursts. However, in some exceptional cases, phase shifts have been observed corresponding to velocities of burst sources of the order of 1000 ± 300 km/second [3]. It is difficult to ascertain the significance of this result.

Association with Optical Flares

The association of cm outbursts with solar flares is well established. All cm-wave *outbursts* are associated with solar flares, and solar flares of importance greater than 2 are associated with cm-wave bursts in 75 per cent of cases [3]. The association is less for weaker cm-wave bursts and for solar flares of importance less than 2. The flare-associated cm-wave bursts follow the flares with an average delay of about 1 minute. On the average, the 3-cm burst reaches its maximum intensity before the solar flare maximum and ends sooner than the optical event.

Distribution of Centimeter-Wave Bursts on Solar Disk

In view of the difficulty of determining with sufficient accuracy the positions of cm-wave bursts, the optical positions have been used for the distribution of flare-associated bursts on solar disk. The observed distribution presents a center-to-limb effect which is less for 3-cm bursts than for 10-cm bursts [3]. That is, the 3-cm bursts are less directionally beamed than are the 10-cm bursts.

Association with Meter-Wave Bursts and Expected Dynamic Spectrum

Before we discuss the association of cm-wave bursts with meter-wave bursts, and draw conclusions regarding their expected dynamic spectrum, it seems necessary to give a brief résumé of the different spectral types of meter-wave bursts:

Type I: Noise storms are enhancements of radio emission lasting for hours or days during which the level shows a series of bursts of seconds' duration superposed on a more slowly varying background. The bursts

TABLE I

TYPES OF CENTIMETER-WAVE SOLAR BURSTS

Example	Type	Description (Covington)	IGY Key	Typical Duration (minutes)	Wave Polarization	Source Angular Size	Maximum Equivalent Temperature	Radiation Mechanism
	A	Simple burst-impulsive	1, 2, 6, 8, 9	1 to 5	Random or partial (circular or linear)	<2′30″	10^6 to 10^9°K	Synchrotron
	B	Post-burst-slow decay	4	10 to 200	Random or partial (circular or linear)	>3′	10^5 to 10^7°K	Synchrotron. Some probably thermal.
	C	Gradual rise and fall	3	10 to 100	Random or partial (circular)	<1′	<10^6°K	Same as slowly varying component. Thermal.
		Absorption following burst	5	10 to 100	?	?	?	?
		Fluctuations	7	30 to 150	?	?	?	?

TABLE II

CENTIMETER-WAVE SOLAR OUTBURSTS

Example	Name	Description	Typical Duration (minutes)	Rise Time (minutes)	Wave Polarization	Source Diameter	Maximum Equivalent Temperature	Associated Phenomena
	Microwave outburst (common)	Simple with a post-burst A plus B	10 to 200	1 to 3	Random or partial (circular)	<2′30″	10^7 to 10^9°K	Solar flares, hard X rays or Lyman α (?) (SID), cosmic-ray and geomagnetic storms, meter-wave bursts.*
	Rare short outburst (3 cases)	Simple A or simple with a post-burst A plus B	1 to 3	<½	?	>2′30″	>10^7°K	Solar flares, gamma rays (one case).

* A type-III group followed by type-II and -IV or a type-III group with a type-V.

(type I) are of narrow bandwidth (~5 Mc) and the background is a broader continuum. The radiation is strongly circularly polarized and it is statistically related to the presence of visible active regions on the disk.

Type II: These are intense "outbursts" of radio emission, lasting for some minutes and fluctuating violently. The radiation is randomly polarized and it is closely related to solar flares. The radio spectrum of these bursts shows emission details slowly drifting in frequency (at a rate of about ¼ Mc) toward the lower frequencies, indicating that the exciting source travels outward through the solar atmosphere with velocities of the order of 1000 km. This has been confirmed by recent interferometer observations [5].

Type III: These bursts are intense shortlived bursts, lasting a few seconds, whose frequency of maximum intensity drifts rapidly (at a rate of about 20 Mc) from high to low frequencies. The radiation of some bursts is partially polarized, and they are sometimes related to solar flares. Their rapid frequency-drift indicates a source traveling outward with velocities up to 10^5 km/sec, and this deduction also has been confirmed by recent interferometer observations [5].

Type IV: This burst is a very broad-band emission, free of details in time and frequency and lasting from 20 minutes to a few hours. The radiation is partially circularly polarized, and on long meter-waves it usually follows a group of type-III bursts and type-II bursts. Observation shows it to be a continuum with all frequencies arriving from about the same source position. The source has been found to have a transverse velocity of a few thousands of km/sec. The source size is usually greater than 5 minutes of arc on meter waves.

Type V: This burst is another broad-band emission, lasting only a few seconds to a few minutes. It usually is accompanied by a group of type-III bursts. It has a transverse velocity of the same order as the type-IV burst.

Until now, lack of available dynamic spectrum records of cm-wave bursts has made it impossible to classify the cm-wave bursts into spectral types in the same way as it has been possible for meter-wave bursts. However, systematic studies of single-frequency cm-wave bursts over several years have revealed certain facts. The microwave *outbursts* are mostly associated with meter-wave bursts of either types II or III whether or not followed by type-IV bursts. In fact, the comparison of cm-wave bursts with those observed on meter waves shows that certain bursts occur almost simultaneously on all frequencies and are therefore identifiable with type-III bursts. But on meter waves type-III bursts last only several seconds, whereas on cm waves they last a few minutes. This duration is comparable with type-II bursts, but the cm-wave bursts do not exhibit the violent fluctuations typical of type-II bursts.

Bursts of type IV on meter waves are nearly always associated with microwave outbursts. This close association with type-IV bursts, and the fact they do not show features of types II and III, has led us and others to think that cm-wave outbursts are probably of the same nature as type-IV bursts. Indeed, their properties (smoothness, polarization, broad-band spectrum, and duration) tend to support this assumption. On the other hand, it has been observed [6] that a group of type-III bursts has greater probability of being associated with a cm-wave burst if it has an associated type V in the range 40–240 Mc. This observation suggests that some cm-wave bursts may be of the same nature as type V.

Observed Dynamic Spectrum of Cm-Wave Bursts

A dynamic spectrum analyzer sweeping the band of 2000–4000 Mc (*S* band) was recently operated at the University of Michigan Radio Astronomy Observatory at Peach Mountain, Mich. The first cm-wave dynamic spectrum of a burst was recorded with this equipment on July 29, 1959. A type-III burst group was recorded simultaneously with the Michigan dynamic spectrum analyzer sweeping the band of 100–600 Mc. These two records are shown in Fig. 4. Also shown in the same figure is the single-frequency record of the outburst obtained on 10.7 cm by Covington in Ottawa.

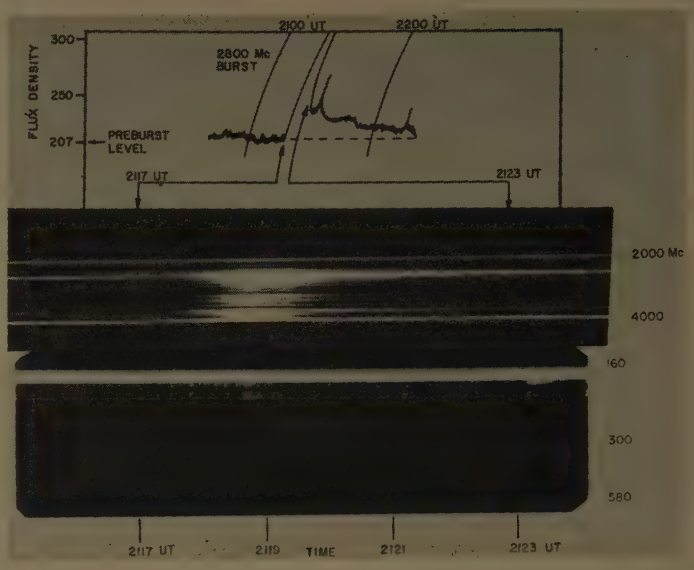

Fig. 4—Dynamic spectrum record of a microwave outburst in the range of frequencies 2000–4000 Mc as obtained at the University of Michigan on July 29, 1959. Also shown are the 2800-Mc record of the burst obtained by Covington at Ottawa and the dynamic spectrum record of Michigan in the range 100–300 Mc.

The 10.7-cm record shows that the outburst began at 2117.5 UT and consisted of an intense impulsive burst of type A, on which was superposed peaks of small intensity. The maximum of this burst occurred at about 2119 UT. This was followed by a post-burst (type B) of small intensity, on which was superposed at about 2129 UT another simple burst of type A. The dynamic spectrum record in the 2000- to 4000-Mc band shows that the burst emission is a broad-band continuum lasting from 2117.5 to about 2130 UT, with its maximum intensity at about 2119 UT and a secondary maximum at about 2129 UT (not shown in the figure). These two maxima correspond to the two peaks of 10.7-cm record. The post-burst spectrum is not evident on this record because of insufficient sensitivity of the equipment. The dynamic spectrum record in the 100- to 600-Mc band shows several groups of type-III bursts in the 160–320-Mc band between 2117.5–2124 UT. It appears that these events were simultaneous with the 10.7-cm peaks. There is no event in this range corresponding to the peak at 2129 UT and the post-burst observed on 10.7 cm.

An interesting result occurs from the comparison of the two dynamic radio spectra with the single frequency record at 10.7 cm. This is that the impulsive phase (type A) as well as the post-burst (type B) of the cm-wave burst emission is a broad-band continuum. The comparison shows further that the cm-wave burst in its impulsive phase is associated with a group of type-III bursts in the 160- to 320-Mc band. The simultaneous beginning of cm-wave outbursts with some type-III bursts had previously led to the suggestion that the

impulsive phase of the cm-wave outburst may be a type-III burst, although the duration did not correspond to that of type-III bursts. From the 2000- to 4000-Mc dynamic spectrum recorded on July 29, 1959, it is clear that the type-III burst does not extend to the cm wavelengths, although it is associated with a broadband cm-wave continuum emission. The 10.7-cm record shows that the post-burst (not very evident on the *S*-band spectrum record due to insufficient sensitivity) lasts about an hour. This duration corresponds to type-IV emission. Another example is a burst observed on January 12, 1960 (Fig. 5), which shows that the cm-wave burst is a broad-band continuum emission of very short duration. In the meter-wave region, this burst is associated with two groups of type-III bursts. The short duration of the cm-wave burst continuum emission corresponds to that of type-V emission. In view of the above considerations, it appears likely that cm-wave outbursts are continuum emissions of the same nature as type IV and type V.

Association with Cosmic Ray Storms and Geomagnetic Storms

Australian, Japanese, and French workers have established a good correlation between type-IV bursts and geomagnetic storms. More recently an association between type-IV bursts and cosmic ray storms has been found by Japanese and American workers. The published data shows that all the type-IV bursts involved are associated with cm outbursts. Since we consider cm-wave outbursts as emissions of types IV and V, it will be of interest to study the correlation between cm outbursts and cosmic-ray and geomagnetic storms, irrespective of their association with type-IV bursts on the meter waves. The reason is that type-IV bursts may sometimes have a low-frequency cutoff, as in the case of March 20, 1958. This event was not observed below 1400 Mc, thus indicating a sharp low-frequency cutoff [Fig. 3(a)]. This rare microwave outburst was accompanied by a short, intense gamma-ray burst [7], [14]. In view of its distinctive features (its strong intensity, short duration, large diameter and sharp low-frequency cutoff), this outburst has been classified in a separate class called "rare short outburst."

The good correlation observed previously between certain type-II bursts and geomagnetic storms was probably due to the fact that type-IV bursts were associated with them. According to recent analysis, type-II bursts, without type-IV bursts following them, show but weak association with geomagnetic storms. The correlation between type-III bursts and cosmic-ray storms has also been looked for but without much success [12]. However, it might be of interest to study this correlation, taking only those type-III bursts which are usually associated with a type-V in the 40- to 240-Mc band, where the type-V intensity can reach 10,000 units, or 10^{-18} watt m^{-2} $(cps)^{-1}$.

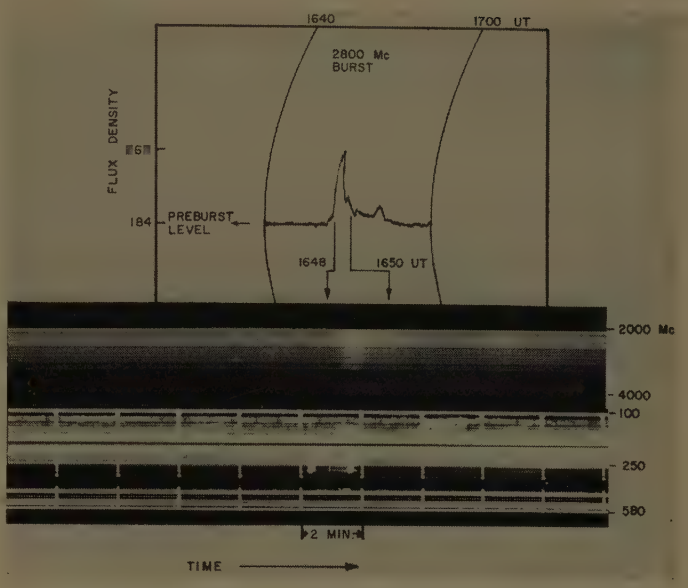

Fig. 5—Dynamic spectrum record of a microwave burst in the range of frequencies 2000–4000 Mc as obtained at the University of Michigan on January 12, 1960. Also shown are the 2800-Mc record of the burst obtained by Covington at Ottawa and the dynamic spectrum record of Michigan in the range 100–580 Mc.

Association with Polar Cap Absorption

Ionospheric absorption of cosmic noise in polar regions (called polar cap absorption) is believed to be caused by ionization of the upper atmosphere by fast protons (in the energy range of 10–50 Mev) emitted from the sun after big flares. Direct balloon and satellite observations of protons have confirmed this hypothesis. It has been found that intense broad-band cm-wave outbursts [16], [18] and type-IV meter-wave outbursts of continuum radiation [15], [17] are closely associated with polar cap absorption events. The occurrence of a type-IV outburst on meter waves alone is not sufficient for its association with polar cap absorption, but it must be simultaneous with an intense cm-wave outburst observed over the whole wavelength range of 3 to 30 cm [18].

Association with D-Layer Ionization

It is known that the ionization in the *D* layer is greatly increased during chromospheric flares and causes absorption phenomena. Nothing definite is known about the association between these abnormal absorption phenomena and the radio bursts observed on cm waves. However, it has been found [9] that the intensity variation of the ionizing radiation responsible for the nondeviative absorption in the *D* layer during a sudden ionospheric disturbance (SID) is in qualitative agreement with the intensity variation of 3-cm burst emission. Thus, it is suggested that the 3-cm burst emission and the ionizing radiation (X rays or Lyman alpha radiation) responsible for the *D* layer both originate from the region in the solar atmosphere, and are both generated by associated emission mechanisms.

Discussion

Most of our knowledge of meter-wave bursts has been derived from dyanmic spectral observations. Unfortunately, spectral observations for the cm-wave bursts are only just beginning. The cm-wave burst emission, however, seems to be different from meter-wave burst emission. The extremely brief emissions of types I and III, characteristic of meter-wave bursts, do not exist on cm waves. The duration of cm-wave bursts corresponds to type-II or type-V bursts, but the violent fluctuations typical of type-II bursts do not exist on the cm-wave bursts.

The high equivalent temperatures (10^7–10^{5}°K) of the cm-wave outbursts (type A plus type B) suggest their nonthermal origin. In fact, their duration, smoothness, polarization, and spectra have been explained by synchrotron radiation from electrons with medium energies [10]. The cm-wave outbursts are closely associated with type-IV and type-V emission observed on the meter waves, which have also been interpreted as synchrotron radiation from relativistic electrons [11]. As a result, one can suggest that cm-wave outbursts are emissions of the same nature as type IV and type V. This seems to be confirmed by the 2000–4000-Mc dynamic spectrum observations at the University of Michigan.

It is not known whether all cm-wave bursts (types A and B) are of the same nature as type-IV and type-V bursts. However, there are weak cm-wave bursts (types A and B) whose equivalent temperatures do not seem to exceed 10^6°K. Consequently, one cannot altogether exclude the possibility of a thermal origin for these bursts.

The long enduring bursts of type C (gradual rise and fall) have equivalent temperatures of less than 10^6°K. Moreover, they have been observed to have properties (intensity, duration, polarization, size) similar to those of radio condensations, responsible for the slowly varying component of decimeter- and cm-wave solar radiation. Thus (like the slowly varying component of solar radiation) bursts of type C may be generated by thermal processes related to the heating of a localized region in the solar atmosphere in the presence of a magnetic field. They differ from radio condensations only in their intensity and duration, exhibiting the same intensity-duration relationship as the radio condensations [13], [7]. Because of the similarity of their behavior, these bursts have been called "micro-condensations" [7].

It is expected that systematic dynamic spectral observations will shed much light on the mechanism of generation of centimeter-wave bursts.

Aknowledgment

The authors wish to thank James Kuiper of the radio astronomy group for obtaining the dynamic spectra of solar bursts.

Bibliography

[1] J. P. Wild and L. L. McCready, "Observations of the spectrum of high-intensity solar radiation at meter wavelengths," *Australian J. Sci. Res.*, ser. A, vol. 3, pp. 387–398; September, 1950.
[2] A. E. Covington, "Some characteristics of 10.7 cm solar noise," *J. Roy. Astronomical Soc. Canada*, vol. 45, pp. 49–61; March, 1951.
[3] M. R. Kundu, "Structures et propriétés des sources d'activité solaire sur ondes centimétriques," *Ann. Astrophys.*, vol. 22, pp. 1–100; January, 1959.
[4] M. R. Kundu, "Étude interférométrique des sources d'activité solaire sur 3 cm de longueur d'onde," *Paris Symp. on Radio Astronomy*, R. N. Bracewell, Ed., Stanford University Press, Stanford, Calif., pp. 222–236; 1959.
[5] J. P. Wild, "The transverse motions of the sources of solar radio bursts," *Paris Symp. on Radio Astronomy*, R. N. Bracewell, Ed., Stanford University Press, Stanford, Calif., pp. 176–183; 1959.
[6] A. A. Neylan, "An association between solar radio bursts at meter and centimeter wavelengths," *Australian J. Phys.*, vol. 12, pp. 399–403; December, 1959.
[7] J. F. Denisse, "Les sources d'emissions radioélectriques du soleil," *Paris Symp. on Radio Astronomy*, R. N. Bracewell, Ed., Stanford University Press, Stanford, Calif., pp. 81–88, 237–239; 1959.
[8] D. J. McLean, "Solar radio emission of spectral type IV and its association with geomagnetic storms," *Australian J. Phys.*, vol. 12, pp. 404–417; December, 1959.
[9] O. Hachenberg and H. Volland, "Vergleich zwischen 3.2 cm-radiostrahlung der Sonne und ionosphärischer Dämpfung im D-Gebiet während einer Sonnen eruption," *Z. Astrophys.*, vol. 14, pp. 69–80; February, 1959.
[10] T. Takakura, "Synchrotron radiation and solar radio outbursts at microwave frequencies," *Paris Symp. on Radio Astronomy*, R. N. Bracewell, Ed., Stanford University Press, Stanford, Calif., pp. 562–569; 1959.
[11] A. Boischot and J. F. Denisse, "Les émissions de type IV et l'origine des rayons cosmiques associeés aux éruptions chromosphériques," *Compt. rend. acad. sci. (Paris)*, no. 245, pp. 2194–2197; December, 1957.
[12] A. R. Thompson, "The correlation of solar radio bursts with magnetic activity and cosmic rays," *Paris Symp. on Radio Astronomy*, R. N. Bracewell, Ed., Stanford University Press, Stanford, Calif., pp. 210–213; 1959.
[13] A. E. Covington, "Solar emission at 10 cm wavelength," *Paris Symp. on Radio Astronomy*, R. N. Bracewell, Ed., Stanford University Press, Stanford, Calif., pp. 159–165; 1959.
[14] L. E. Peterson and J. R. Winckler, "Gamma-ray burst from a solar flare," *J. Geophys. Res.*, vol. 64, pp. 697–707; July, 1959.
[15] Y. Hakura and T. Goh, "Pre-sc polar cap ionospheric blackout and type IV solar radio outbursts," *J. Radio Lab. Japan*, vol. 6, pp. 635–650; June, 1959.
[16] Y. Avignon and M. Pick, "Relation entre les émissions solaires de rayons cosmiques et les sursauts de type IV," *Compt. rend. Acad. sci. (Paris)*, no. 249, pp. 2276–2278; November, 1959.
[17] A. R. Thompson and A. Maxwell, "Solar radio bursts and low-energy cosmic rays," *Nature*, no. 185, pp. 89–90; January, 1960.
[18] M. R. Kundu and F. T. Haddock, "A relation between solar radio emission and polar cap absorption of cosmic noise," *Nature*, no. 186, pp. 610–612; May, 1960.
[19] F. T. Haddock and J. W. Kuiper, "Spectral characteristics of centimeter-wave bursts," in preparation.

Radio Star Scintillation and Multiple Scattering in the Ionosphere*

DIMITRI S. BUGNOLO†, MEMBER, IRE

Summary—**Recent experimental evidence of radio star scintillation indicates that multiple scattering effects are of importance in the ionosphere. It is therefore of interest to apply the transport equation for the expectation of the photon density function to this problem. The solution of the transport equation is used to predict the mean-squared scattering angle and corresponding size of the ionospheric irregularities as measured on the earth. The particular example discussed in detail is based on a Gallet model for turbulence in the underside of the *F* layer under nighttime conditions. However, if should be noted that the general theoretical results can be applied to any other model as well.**

I. Introduction

RECENT experimental investigations of radio stars at Cornell University appear to indicate that multiple scattering effects are of importance in the ionosphere.[1] In view of this it is of some importance to apply the present theory of multiple scattering[2,3] to this problem.

As was the case for scattering in the troposphere the theoretical analysis to date has been restricted to a first Born approximation. This in effect assumes that all sections of the scattering volume "see" the unperturbed incident field. In other words, no ray of the incident field can be scattered more than once. The reader is referred to a recent paper by Booker for a complete review of the current theory and experimental verification.[4] Booker's paper also contains a brief consideration of the multiple scatter problem.

The statistical parameters of interest in the study of the irregular ionosphere by the use of radio stars are:

1) mean free path for scattering,
2) mean squared scattering angle (variance),
3) scale of irregularities as measured by spaced receivers on the earth.

The above will be considered in detail under the assumption of a Gallet layer in the underside of a number of typical models for the nighttime *F* region. The transport equation for the expectation of Poynting's vector will be used to predict the above three parameters. It will be shown that

1) mean free path (MFP),

$$\text{MPF} \sim \frac{1}{l_0^3} \frac{f^4}{f_{cr_M}{}^4},$$

where l_0 is the mean blob size in the Gallet layer, f the frequency of observation, and f_{cr_M} the maximum critical frequency in the *F* layer;

2) mean-squared scattering angle

$$\sigma^2 = 4\left(\frac{\lambda}{2\pi l_0}\right)^2 \xi,$$

where λ is the wavelength of the observation, and ξ the path length measured in mean free paths;

3) scale of irregularities (L_M) as measured on the ground,

$$L_M \sim L/\sqrt{\xi},$$

where L is the scale as deduced from single-scatter (high-frequency) observations.

II. A Model for the Turbulent *F* Layer

A. Models for the *F* Layer

It would appear that turbulence in the *F* layer is restricted to its underside at moderate latitudes and occurs mainly at night.[5] During this period the underside of the region assumes a nearly parabolic form.[6] This is in contrast to the Chapman form suitable for daytime prediction. Appropriate equations for the two models in terms of the number of electrons per cubic meter N are

$$N = N_M \exp\left\{1 - z - \sec x\epsilon^{-z}\right\} \quad \text{Chapman} \qquad (1)$$

$$N = N_M\left\{1 - Z^2/4\right\} \quad \text{parabolic} \qquad (2)$$

where X is the solar zenith angle.

The distance Z is measured in scale heights H from the position of maximum electron density. The two models are sketched in Fig. 1 for comparison below N_M.

* Received by the PGAP, April 25, 1960; revised manuscript received, July 1, 1960. This research was supported in whole or in part by the USAF under Contract No. AF 49(638) 350 monitored by the Air Force Office of Scientific Research. Work performed at Columbia University, New York, N. Y.

† Bell Telephone Labs., Inc., Holmdel, N. J.; formerly with Dept. of Elec. Engrg., Columbia University, New York, N. Y.

[1] H. G. Booker and B. Nichols, private communication.

[2] D. S. Bugnolo, "A Transport Equation for the Spectral Density of a Multiply Scattered Electromagnetic Field," Columbia University, New York, N. Y., Tech. Rept. no. T-3/D, April, 1960; to be published in *J. Appl. Phys.*, vol. 31, pp. 1176–1182; July, 1960.

[3] D. S. Bugnolo, "On the question of multiple scattering in the troposphere," *J. Geophys. Res.*, vol. 65, pp. 879–884; March, 1960.

[4] H. G. Booker, "The use of radio stars to study irregular refraction of radio waves in the ionosphere," PROC. IRE, vol. 46, pp. 298–314; January, 1958.

[5] D. F. Martyn, "The normal *F* region of the ionosphere," PROC. IRE, vol. 47, pp. 147–155; February, 1959. See especially p. 155.

[6] *Ibid.*, p. 152.

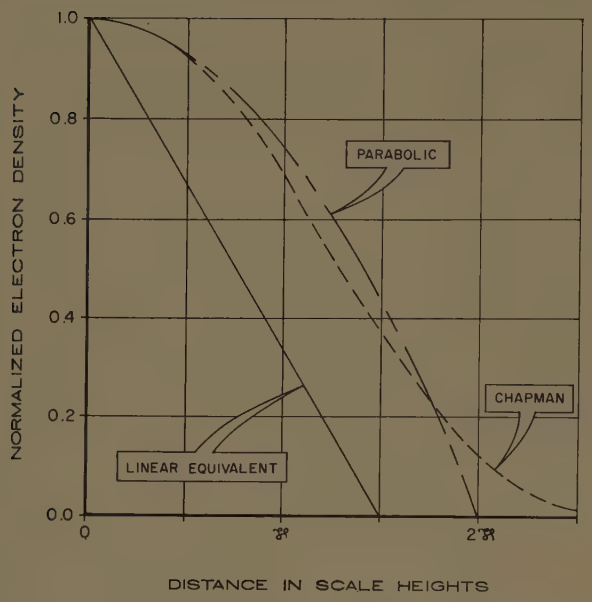

Fig. 1—Comparison of models for the underside of the F layer.

B. Model for Turbulence

If turbulence in the underside of the F layer is caused by the vertical transport of electrons then Gallet has shown that the mean-squared variation in the electron density is given by[7]

$$\overline{\left|\frac{\Delta N}{N}\right|^2} \cong \frac{l_0^2}{3}\left|\frac{\nabla N}{N}\right|^2 \tag{3}$$

where l_0 is the mean scale size.

C. Model for the RMS Dielectric Noise

The index of refraction $n(\theta)$ in an ionized layer in the presence of a static magnetic field H_0 is given by the usual Appleton-Hartree formula.[8]

In the northeastern section of the United States it is reasonable to assume a longitudinal mode of propagation. The effective dielectric constant for this mode is the usual

$$\epsilon = \epsilon_0\left\{1 - \frac{\omega_{cr}^2}{\omega(\omega \pm \omega_H)}\right\} \tag{4}$$

where

ϵ_0 = dielectric constant of free space,
ω_{cr} = critical frequency in radians/seconds,
ω_H = gyro frequency in radians/seconds.

The rms magnitude of the dielectric noise is given by a differentiation of (4). Substituting for the rms electron noise from (3), we have

$$\overline{\left|\frac{\Delta\epsilon}{\epsilon}\right|^2} \cong \frac{l_0^2}{3}\left\{\frac{\omega_{cr}^2}{\omega(\omega \pm \omega_H) - \omega_{cr}^2}\right\}^2\left|\frac{\nabla N}{N}\right|^2. \tag{5}$$

Particular Examples: It is convenient to find the particular form for the rms dielectric noise given a model for the underside of the F layer. Two models will be considered in detail.

a) Parabolic layer: Substitution of (2) and (3) into (5) and taking ω such that

$$\omega > \sqrt{10}\,\omega_H; \qquad \omega > \sqrt{10}\,\omega_{cr},$$

$$\overline{\left|\frac{\Delta\epsilon}{\epsilon}\right|^2} \cong \frac{l_0^2}{12}\left(\frac{\omega_{cr_M}}{\omega}\right)^4\frac{x^4}{H^4}. \tag{6}$$

b) Linear approximation: As a linear approximation for the parabolic model, consider

$$N = N_M\{1 - z/b\} \tag{7}$$

where b will be adjusted later. Substituting (7) and (3) into (5) and taking $\omega > 10\omega_H$ and ω_{cr},

$$\overline{\left|\frac{\Delta\epsilon}{\epsilon}\right|^2} \cong \frac{l_0^2}{3b^2}\left(\frac{\omega_{cr_M}}{\omega}\right)^4. \tag{8}$$

The linear approximation is of interest since the resulting dielectric rms noise is independent of the scale height Z. This can be used to simplify the general theory since the notion of mean free path is of significance.

III. A Transport Equation for the Photon Density Function

The properties of the electromagnetic field scattered by a random space-time dielectric fluctuation have been considered in detail for the *single-scatter* case. A recent paper by Wheelon contains eighty-one references.[9]

A classical example of the multiple scattering effect is the Milne problem of astronomy. The reader is referred to the discussion of this problem by Morse and Feshbach.[10] As originally presented, the theoretical analysis is limited to a discussion of the rms value of the scattered radiation. In a recent paper, the author has generalized the results to permit a prediction of the spectral density as well.[2]

In general, the electromagnetic parameters of interest are the expectation of the energy density $U(\boldsymbol{r}, t)$ and Poynting's vector $\boldsymbol{P}(\boldsymbol{r}, t)$. The desired results could be obtained as a special case of the general theory previously given by the author;[2] however, it is instructive to consider the particular example in detail.

Let a density function $f(\boldsymbol{r}, \boldsymbol{v})$ for the number of photons in an element of positional velocity space $(\boldsymbol{r}, \boldsymbol{v})$ be defined such that the *expectation* for the num-

[7] R. M. Gallet, "Electron density fluctuations in turbulent ionized layers," Proc. IRE, vol. 43, pp. 1240–1252; October, 1955.
[8] H. Bremmer, "Terrestrial Radio Waves," Elsevier Publishing Co., New York, N. Y., ch. 11; 1949.
[9] A. D. Wheelon, "Radio scattering by tropospheric irregularities," *J. Res., NBS*, vol. 63 D, pp. 205–234; September–October, 1959.
[10] P. M. Morse and H. Feshbach, "Methods of Theoretical Physics," McGraw-Hill Book Co., Inc., New York, N. Y.; 1953.

ber of photons per unit volume at r, $\langle N(r)\rangle$, is given by

$$\langle N(r)\rangle = \int f(r, v)dV_v \tag{9}$$

where dV_v signifies an integration over all velocity space. It should be noted that this definition differs from the usual as given by Morse and Feshbach[10] since the photon density function is related to the *expectation* of the field. It also follows that the expectation of the energy density per unit volume at the point r is related to the density function f by

$$\langle U(r)\rangle = \hbar\omega_0 \int f(r, v)dV_v \tag{10}$$

where ω_0 is the center frequency of the incident radiation. The expectation of Poynting's vector $P(r)$ at the point r is given by

$$\langle P(r)\rangle = \hbar\omega_0 \int vf(r, v)dV_v. \tag{11}$$

As previously noted by the author,[2] the expectation of Maxwell's equations can be used to construct a transport equation for the spectral density of a multiply scattered field, or in this case, for the rms value. Let

$\sigma(r, v, v')$ = the cross section for scattering per unit volume per unit solid angle at the point r for an incident and scattered vector velocity number v and v' respectively.

$Q_s(r)$ = the total cross section for scattering per unit volume at the position r.

$$Q_s(r) \equiv \int \sigma(r, v, v')dV_v.$$

It is possible to show that the density function as defined by (9) satisfies the transport equation when the process is statistically stationary.[2]

$$\hat{v}\cdot\nabla f = \int \sigma(r, v, v')f(r, v')dV_{v'} - Q_s(r)f(r, v). \tag{12}$$

This corresponds to the so-called "steady-state" solution[11] of the usual transport theory. The analogy is a direct result of the assumption of statistical stationarity since the expectation of the time rate of change of the energy density will vanish everywhere.[2]

IV. Solution of the Transport Equation

A. Reduction to a Partial Differential Equation

In order to reduce the radio star problem to one possible solution it is necessary to assume a plane earth. The geometry is thereby reduced to the case of a plane wave source radiating into a slab characterized by the scattering cross section σ (Fig. 2). It is evident that the photon density function on the far side of the slab will depend on the distance X and the directional angle θ as illustrated in Fig. 2. The transport equation (12) reduces to

$$u\frac{\partial f}{\partial x} = \int \sigma(x, u, u')f(x, u')d\Omega' - Q_s(x)f(x, u) \tag{13}$$

where $u = \cos\theta$, and $d\Omega$ signifies integration over a solid angle.

The method of solution will depend on the character of the differential cross section σ. When the scattering is primarily forward as is the case in the ionosphere the transport equation can be reduced to a partial differential equation by a method introduced by Morse and Feshbach.[12] Let $f(x, u')$ be expanded in a Taylor series about the point u,

$$f(x, u') \cong f(x, u) + (u' - u)\left.\frac{\partial f}{\partial u'}\right|_{u'=u} + \frac{(u' - u)^2}{2}\left.\frac{\partial^2 f}{\partial u'^2}\right|_{u'=u}. \tag{14}$$

The angles of importance are illustrated by Fig. 3. It follows that

$$u' - u = u(\cos\theta' - 1) - \sin\theta'\sqrt{1 - u^2}\cos\beta. \tag{15}$$

Substituting (14) into (13) we have

$$u\frac{\partial f}{\partial x} = \int d\Omega'\sigma(x, u')\sum_{m=0}^{2}\frac{(u' - u)^m}{m!}\left.\frac{\partial^m f}{\partial u'^m}\right|_{u'=u} - Q_s f.$$

The term $m = 0$ just cancels the terms $Q_s f$ from the definition of the total cross section. The remaining two terms yield the partial differential equation

$$u\frac{\partial f}{\partial x} = \alpha_1^2(x)\left\{\frac{u^2 - 1}{2}\frac{\partial^2 f}{\partial u^2} + u\frac{\partial f}{\partial u}\right\} + \alpha_2^2(x)u^2\frac{\partial^2 f}{\partial u^2} \tag{16}$$

where

$$\alpha_1^2(X) \equiv 2\pi\int \sigma(X, \theta)(\cos\theta - 1)\sin\theta d\theta$$

$$\alpha_2^2(X) = 2\pi\int \sigma(X, \theta)(\cos\theta - 1)^2\sin\theta d\theta.$$

B. A Model for the Dielectric Noise

Since very little is known about the exact nature of turbulence in the ionosphere it will be assumed that the space correlation function R of the dielectric noise is isotropic and best fitted by any one of the possible Bessel models given by Norton.[13]

$$R(r) = \frac{2^{1-\mu}}{\Gamma(\mu)}\left(\frac{r}{l_0}\right)^{\mu}K_\mu(r/l_0) \tag{17}$$

[10] *Ibid.*, p. 897

[12] *Ibid.*, p. 1750, Problem 12.14.

[13] K. A. Norton, Natl. Bur. of Standards, Washington, D. C., Memo. Rept. No. PN-83-21; August, 1959.

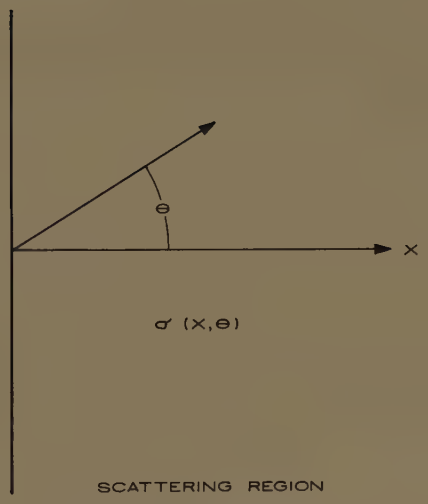

Fig. 2—Geometry for scattering.

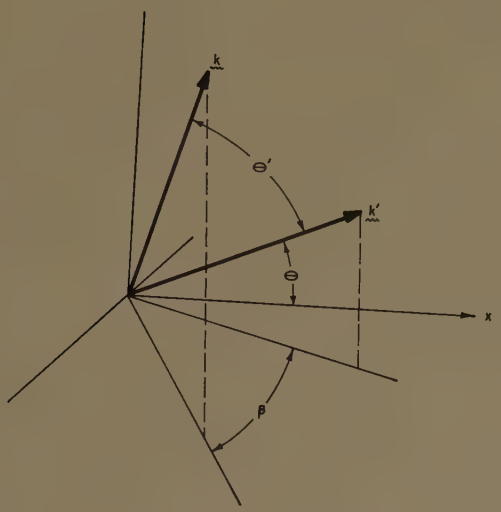

Fig. 3—Geometry for scattering.

where K_μ is a modified Hankel function. It should be noted that the usual exponential model is a special case of the above for $\mu = \frac{1}{2}$.

The cross section per unit volume per unit solid angle is given by a substitution into the results for the space-wise spectrum S given by Norton.[13]

$$\sigma(x, K) = \frac{\pi^2}{\lambda^4} S\left\{x, \frac{4\pi}{\lambda} \sin \frac{\theta}{2}\right\}.$$

Hence

$$\sigma(x, K) = \frac{\frac{\sqrt{\pi}}{\lambda}\left(\frac{2\pi l_0}{\lambda}\right)^3 \frac{\Gamma(\mu + 3/2)}{\Gamma(\mu)} \langle \Delta\epsilon^2(x) \rangle}{\left\{1 + 4\left(\frac{2\pi l_0}{\lambda}\right)^2 \sin^2 \frac{\theta}{2}\right\}^{\mu+3/2}} \tag{18}$$

where

l_0 = mean "blob" size

and

$$K = \frac{4\pi}{\lambda} \sin \theta/2.$$

The cross section σ may be a function of the position x since the rms dielectric noise may depend on the scale distance z as noted in Section II.

We are now in a position to calculate the moments of the cross section as defined by (16). The parameter of interest is the ratio

$$\frac{2\pi l_0}{\lambda}.$$

Since $2\pi l_0$ is of the order of 5 km in the ionosphere[14] it follows that

$$\frac{2\pi l_0}{\lambda} > 10$$

for frequencies above 1 mc. Under this condition it follows that

$$\alpha_1^2 \cong \frac{1}{4\mu^2 - 1} \frac{\sqrt{\pi}}{l_0} \frac{\Gamma(\mu + 3/2)}{\Gamma(\mu)} \overline{\left|\frac{\Delta\epsilon}{\epsilon}\right|^2} \tag{19}$$

for $\mu > \frac{1}{2}$, and

$$\alpha_1^2 \cong \frac{\pi}{16 l_0}\left\{\ln\left[1 + 4\left(\frac{2\pi l_0}{\lambda}\right)^2\right] - 1\right\} \overline{\left|\frac{\Delta\epsilon}{\epsilon}\right|^2} \tag{20}$$

for $\mu = \frac{1}{2}$. A similar calculation for the second moment α_2^2 can be used to show that

$$\alpha_2^2 \ll \alpha_1^2$$

and can therefore be neglected in the ionosphere.

Consequently the partial differential equation for the photon density function reduces to

$$u \frac{\partial f}{\partial x} = \alpha_1^2(x)\left\{\frac{u^2 - 1}{2} \frac{\partial^2 f}{\partial u^2} + u \frac{\partial f}{\partial u}\right\}. \tag{21}$$

C. Solution for Small θ

When the radio star is directly overhead or nearly so such that θ is small it is possible to reduce (21) to an equation that can be solved in closed form. Using the connection $\mu = \cos\theta$ we have for small θ

$$\frac{1}{\alpha_1^2(x)} \frac{\partial f}{\partial x} - \frac{\partial^2 f}{\partial \theta^2} + \frac{1}{\theta} \frac{\partial f}{\partial \theta} = s(x, \theta) \tag{22}$$

where $s(x, \theta)$ is the source.

Let the Hankel transform for f be defined by:

$$F(x, g) = \int_0^\infty J_0(g\theta) f(x, \theta) \theta d\theta.$$

[14] Booker, *op. cit.*, p. 311.

Applying this to the partial differential equation yields

$$\frac{1}{\alpha_1^2(x)}\frac{dF}{dx} + g^2F(x, g) = \Psi(x, g) \tag{23}$$

where

$$\Psi(x, g) = \int_0^\infty J_0(g\theta)s(x, \theta)\theta d\theta. \tag{24}$$

The general solution for (24) is then given by

$$F(x, g) = \exp\left\{-g^2\int \alpha_1^2(x)dx\right\}$$
$$\cdot\left[\int \Psi(x, g)\exp\left[\int g^2\alpha_1^2(x)dx\right]dx + 1\right]. \tag{25}$$

1) *Solution for a Normally Incident Plane Wave:* If the plane wave source is normally incident on the ionosphere then the source $s(x, \theta)$ is given by

$$s(x, \theta) = \frac{\delta(\theta)}{\theta}\delta(x)$$

where δ is the Dirac delta function. Substituting into (24) and (25), it follows that

$$F(x, g) = \exp\left[-g^2\int_0^X \alpha_1^2(x)dx\right].$$

The density function $f(X, \theta)$ is given by the inverse transformation of this result.

$$f(X, \theta) = \int_0^\infty J_0(g\theta)\exp\left[-g^2\int_0^X \alpha_1^2(x)dx\right]gdg. \tag{26}$$

Let

$$\Phi(X) \equiv \int_0^X \alpha_1^2(x)dx$$

where X is the path length in the scattering medium. Then the solution for the photon density function is given by

$$f(X, \theta) = \frac{1}{2\Phi}\exp\left[-\theta^2/4\Phi\right]. \tag{27}$$

2) *Moments of the Distribution:* The second central moment of the distribution or the "mean-squared scattering angle" is of interest in the observation of radio stars. This is given by

$$\sigma^2 = \int_0^\pi \theta^2 f(\theta)\sin\theta d\theta;$$
$$\therefore\ \sigma^2 = 4\Phi. \tag{28}$$

It is also of interest to note that

$$\int_0^\pi f(\theta)\sin\theta d\theta = 1$$

as expected.

3) *Mean Free Path for Scattering:* The probability $P_1(X)$ that a ray has gone a distance X *without* scattering is given by[15]

$$\frac{d}{dx}P_1(x) = -Q_s(x)P_1(x) \tag{29}$$

where $Q_s(X)$ is the total cross section per unit volume for scattering. This is related to cross section σ by an integration over all possible directions.

$$Q_s(x) = \int \sigma(x, \theta)d\Omega. \tag{30}$$

The solution of (29) with the boundary condition $P(0) = 1$ is

$$P_1(X) = \exp\left[-\int_0^X Q_s(x)dx\right]. \tag{31}$$

The probability that a ray *will be* scattered *at least once* in the distance R is given by

$$P_1(r \leq R) = 1 - \exp\left[-\int_0^R Q_s(x)dx\right].$$

The corresponding density function is given by

$$f_1(R) = Q_s(R)\exp\left[-\int_0^R Q_s(x)dx\right].$$

It is of interest to find the first moment of the distribution or the *mean free path* for scattering. For the density function of unity measure we have

$$\text{MFP} = \langle R\rangle = \int_0^\infty RQ_s(R)\exp\left[-\int_0^R Q_s(x)dx\right]dR. \tag{32}$$

For the case where Q_s is independent of position it is evident that this result reduces to that given by Morse and Feshbach.[15]

$$\text{MFP} = 1/Q_s.$$

D. Application to the Parabolic Model

We are now in a position to apply the above results to a particular model for the underside of the F layer.

As noted in Section II the parabolic model is a good approximation for the underside of the F layer under night-time conditions. The electron density profile is given by

$$N = N_M\{1 - z^2/4\}$$

where

$$z = \frac{h - h_M}{H} = \frac{x}{H}$$

[15] Morse and Feshbach, *op. cit.*, p. 179.

is measured in scale heights H below the level of maximum electron concentration h_M. Under the assumption that the frequency f was

$$f > \sqrt{10}\, f_{cr}; \qquad f > \sqrt{10}\, f_H,$$

it was shown that the rms dielectric noise is (6),

$$\overline{\left|\frac{\Delta\epsilon}{\epsilon}\right|^2} \cong \frac{l_0^2}{12}\left(\frac{f_{cr_M}}{f}\right)^4 \frac{x^2}{H^2}. \tag{33}$$

It therefore follows from (19) and (33) that the moment α_1^2 is a function of x^2 in the Gallet region.

$$\alpha_1^2(x) = \frac{\sqrt{\pi}}{4\mu^2 - 1}\,\frac{\Gamma(\mu - 3/2)}{\Gamma(\mu)}\,\frac{l_0}{12}\left(\frac{f_{cr_M}}{f}\right)^4 \frac{x^2}{H^2} \tag{34}$$

for $\mu > \frac{1}{2}$,

$$\alpha_1^2(x) = \frac{\sqrt{\pi}}{96}\left\{\ln\left[1 + 4\left(\frac{2\pi l_0}{\lambda}\right)^2\right] - 1\right\}\left(\frac{f_{cr_M}}{f}\right)^4 \frac{x^2}{H^4} \tag{35}$$

for $\mu = \frac{1}{2}$. We are now in a position to find the second moment of the distribution as given by (28):

$$\sigma^2 = 4\int_0^{2H} \alpha_1^2(x)\,dx.$$

Hence

$$\sigma^2 = \frac{8}{4\mu^2 - 1}\,\frac{\sqrt{\pi}}{9}\,\frac{\Gamma(\mu + 3/2)}{\Gamma(\mu)}\left(\frac{f_{cr_M}}{f}\right)^4 \frac{l_0}{H} \tag{36}$$

for $\mu > \frac{1}{2}$.

As noted by (32), it is possible to define a mean free path for the parabolic model. Unfortunately, the resulting integral cannot be solved in closed form. Since the notion of mean free path is a useful one, it is convenient to define an equivalent linear model for the electron profile. This will be done in such a way as to make the probability $P_1(X)$ as defined by (29) an invariant. This will insure the same result for the second moment of the distribution σ^2.

E. An Equivalent Linear Model

Let the electron density profile for the underside of the nighttime F layer be given by

$$N = N_M(1 - x/b)$$

where b is an adjustable number. Under the assumption that the frequency f of the incident plane wave was

$$f > \sqrt{10}\, f_{cr}; \qquad f > \sqrt{10}\, f_H,$$

it was shown that the rms dielectric noise is (8),

$$\overline{\left|\frac{\Delta\epsilon}{\epsilon}\right|^2} \cong \frac{l_0^2}{3b^2}\left(\frac{f_{cr_M}}{f}\right)^4.$$

The moment α_1^2 is no longer a function of x. Substituting the above result into (19) and (20), we have

$$\alpha_1^2 = \frac{\sqrt{\pi}}{4\mu^2 - 1}\,\frac{\Gamma(\mu + 3/2)}{\Gamma(\mu)}\,\frac{l_0}{3b^2}\left(\frac{f_{cr_M}}{f}\right)^4 \tag{37}$$

for $\mu > \frac{1}{2}$, and

$$\alpha_1^2 = \frac{\pi}{16}\left\{\ln\left[1 + 4\left(\frac{2\pi l_0}{\lambda}\right)^2\right] - 1\right\}\frac{l_0}{3b^2}\left(\frac{f_{cr_M}}{f}\right)^4 \tag{38}$$

for $\mu = \frac{1}{2}$. It is also of interest to note that the total cross section Q_{s_L} as defined by (30) is *independent* of position.

$$Q_{s_L} = \frac{2\pi^{3/2}}{2\mu + 1}\,\frac{\Gamma(\mu + 3/2)}{\Gamma(\mu)}\,\frac{2\pi l_0}{\lambda^2}\left(\frac{f_{cr_M}}{f}\right)^4 \frac{l_0^2}{3b^2} \tag{39}$$

for $\mu > \frac{1}{2}$. The author has previously shown that this implies that the scattering process is Marhoffian.[3]

As mentioned previously the parameter will be chosen such that the probability $P_1(X)$ is an invariant. From (31) it follows that

$$\int_0^{2H} Q_s(X)\,dx = \int_0^{b} Q_{s_L}\,dx$$

where $Q_s(X)$ is the total cross section for the parabolic model and Q_{s_L} is the equivalent for the linear model. It follows after some algebra that

$$b = 3H/2$$

where H is the scale height. Consequently the mean free path in the equivalent model is given by

$$\text{MFP} = \frac{2\mu + 1}{2\pi^{3/2}}\,\frac{\Gamma(\mu)}{\Gamma(\mu + 3/2)}\,\frac{\lambda^2}{2\pi l_0}\left(\frac{f}{f_{cr_M}}\right)^4 \frac{27}{4}\left(\frac{H}{l_0}\right)^2 \tag{40}$$

for $\mu > \frac{1}{2}$. Under this constraint the second moment of the photon density function is given by the result for the parabolic model (36). However, we are now in a position to express this result in equivalent mean free paths, ξ. Let

$$\xi = \text{path length/MFP}. \tag{41}$$

If the plane wave is normally incident on the ionosphere then the path length is just the effective thickness b. Hence

$$\varepsilon_N = \frac{\sqrt{\pi}}{2\mu + 1}\,\frac{\Gamma(\mu + 3/2)}{\Gamma(\mu)}\left(\frac{2\pi l_0}{c}\right)^2 \frac{2}{9}\,\frac{l_0}{H}\,\frac{f_{cr_M}^4}{f^2}. \tag{42}$$

The mean-squared scattering angle follows directly from (37).

$$\sigma_N^2 = \frac{4}{2\mu - 1}\left(\frac{\lambda}{2\pi l_0}\right)^2 \xi_N = \frac{4\alpha_1^2}{Q_s}\,\xi_N. \qquad (43)$$

It follows that σ^2 is inversely proportional to f^4. This result is to some extent similar to that given by Booker,[14] in that both are directly proportional to the expected number of scatterings. Since

$$\frac{4\alpha_1^2}{Q_s}$$

is just the mean-squared scattering angle under single scatter conditions it follows that the "blob" size L as measured in the ground is given by

$$L = l_0/\sqrt{\xi} \quad \text{for} \quad \xi \geq 1. \qquad (44)$$

The theoretical results above are restricted to $\xi \geq 1$ since the transport equation assumes at least one scattering on the average.

F. Solution for Oblique Incidence

The above results assume that θ is small. For arbitrary θ it is necessary to solve (21). This could be done by defining a transform based on the Legendre function of the first kind. However, a very good and straightforward approximation to the result can be obtained by noting that the rms dielectric noise is still obtained by a gradient in the normal direction while the distance in mean free paths depends on the direction of propagation. Consider Fig. 4. The path length h' in the ionosphere is given by

$$h' = r\left\{\left[\cos^2\beta + 2\frac{l+h}{r} + \left(\frac{l+h}{r}\right)^2\right]^{1/2} - \left[\cos^2\beta + 2\frac{l}{h} + \left(\frac{l}{h}\right)^2\right]^{1/2}\right\}. \qquad (45)$$

For $\beta \leq 60$ this reduces to

$$h' \cong h/\cos\beta. \qquad (46)$$

However, this is *not* a good approximation for $\beta > 60°$. Since most multiple scattering data is restricted to low angles of elevation the complete result (44) should be used. The effective length ξ in mean free paths can be found by using (40), (41), (45) and noting that

$$h = 3H/2.$$

V. A Particular Example

In order to illustrate better the multiple scatter theory as developed in this paper, it is useful to consider an example in detail. The example has been based on the latest data available to the author with the hope that it is a "typical" illustration.

From the standpoint of experimental verification it is convenient to calculate the effective path length ξ in mean free paths as a function of f_c the critical frequency,

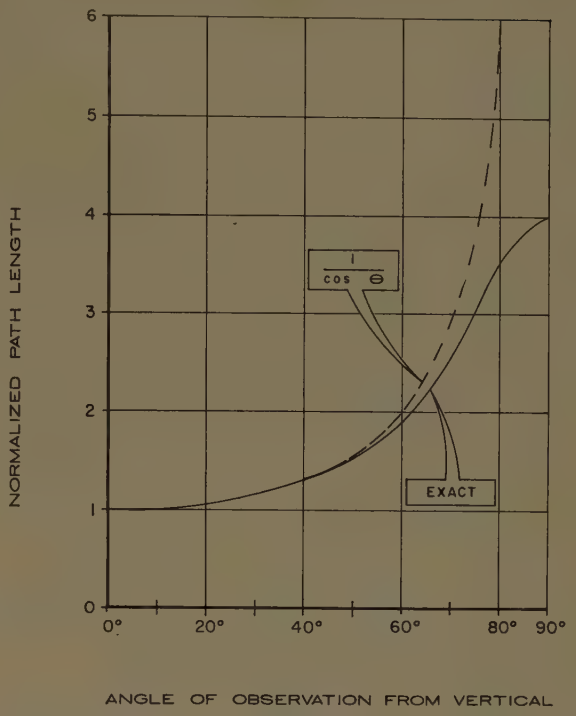

Fig. 4—Normalized path length in the F layer as a function of the angle of observation.

f the frequency of observation, and β the angle of observation as measured from the zenith. This will be done for the special case when

$$2\pi l_0 = 5 \text{ km} \qquad \mu = 1/2$$
$$H = 55 \text{ km} \qquad \beta = 0°, 90°$$
$$d = 300 \text{ km, level of } N_M.$$

The results have been plotted in Figs. 5 and 6. The above selection is based on those given by Booker[4] and Martyn.[5] The critical frequency will be taken as either 5 or 10 Mc. It is evident from (42) and (44) that the scale of irregularities as measured on the earth is a linear decreasing function of frequency below the point where the propagation path is just equal to one mean free path. This has been plotted in Figs. 5 and 6. Above this point the result is just that given by single-scatter theory which yields a mean-squared scattering angle σ_{ss}^2 of

$$\sigma_{ss}^2 = \frac{4}{2\mu - 1}\left(\frac{\lambda}{2\pi l_0}\right)^2.$$

The abrupt transition from single-scatter to multiple-scatter effects as predicted by these results will not be observed experimentally. Instead we might expect a gradual transition to the point where the path length is equal to the "critical distance" in the ionosphere. The notion of critical distance has been defined by the author in a previous paper[3] as that distance where the probability that any ray of the incident field is scattered at least twice is exactly one half. This point has been denoted by a ⊗ on the results plotted in Figs. 7 and 8.

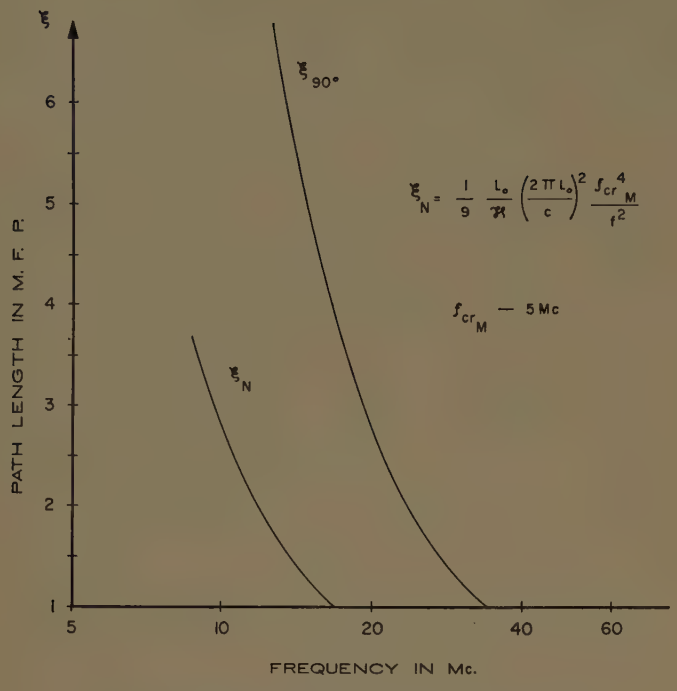

Fig. 5—Path length in the *F* layer in mean free paths as a function of frequency.

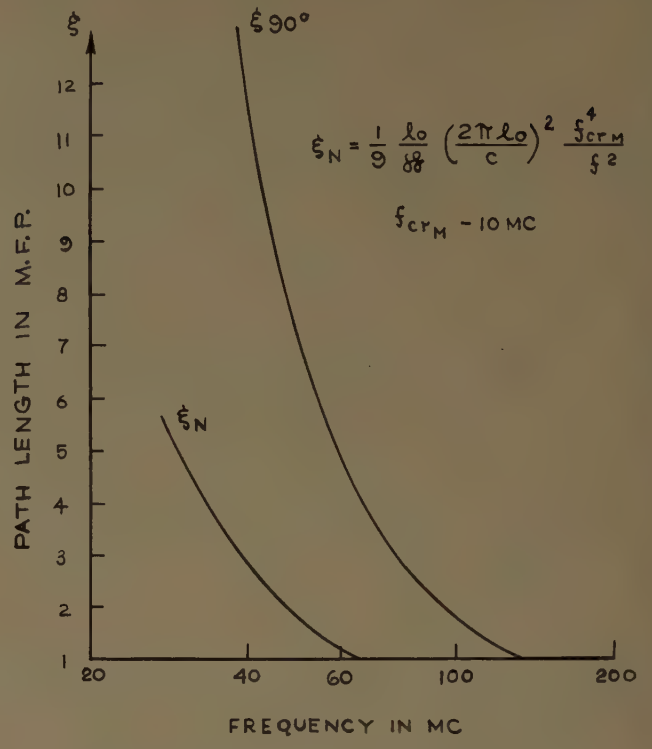

Fig. 6—Path length in the *F* layer in mean free paths as a function of frequency.

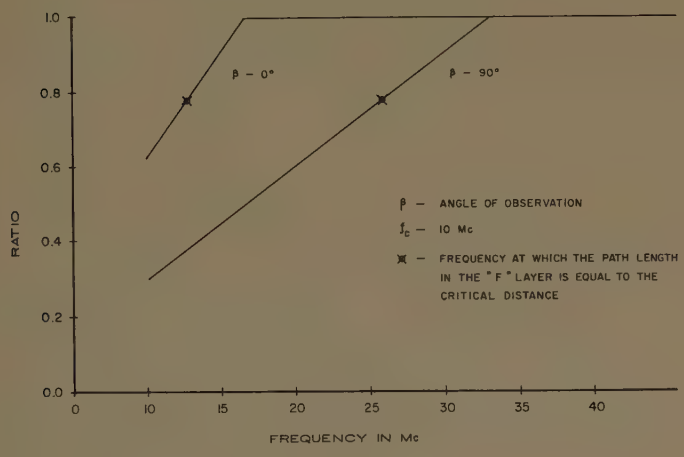

Fig. 7—Ratio of multiple to single scattering "blob" size as measured by spaced antenna.

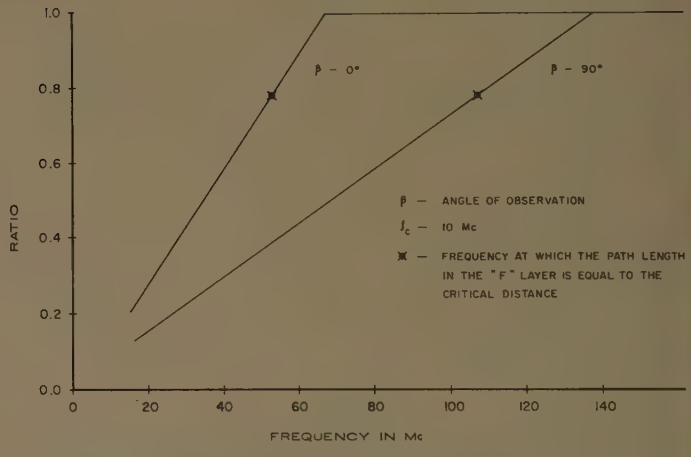

Fig. 8—Ratio of multiple to single scattering "blob" size as measured by spaced antenna.

VI. Conclusions and Recommendations

Let us briefly review the problem and the progress we have made towards its solution. The transport equation for the expectation of the photon density function has been briefly redeveloped (12). A solution has been developed for the special case of forward scattering by an inhomogeneous dielectric noise (27). The result has been applied to mean-squared scattering angle as observed on the earth for the case of a parabolic (36) and equivalent linear (37) model for the underside of the *F* layer under nighttime conditions. The mean free path for scattering has been used to estimate the size of irregularities as measured on the earth (44).

Numerical results have been presented for the case of a plane wave incident on two typical models for the underside of the nighttime *F* layer. An application of the results to other typical cases is straightforward and consequently left to the interested reader. The results indicate that multiple scattering effects should be observable at frequencies well above 50 Mc if the observation is directed towards the horizon.

The above results have been based on a Gallet model for the electron noise. However, it should be noted that the general solution (27) can be applied to any model for turbulence. If the Gallet approximation should prove to be incorrect it is only necessary to recompute the rms dielectric noise.

communications

The Utility of the Array Pattern Matrix for Linear Array Computations*

MURRAY HOFFMAN†, MEMBER, IRE

Summary—**Operations with a class of matrices called pattern matrices represent essentially every step in the numerical calculation of the patterns of linear arrays. These matrices are especially suitable for use with high speed computers. The inverses of pattern matrices always exist so that they can be used for purposes of array pattern synthesis via Lagrangian interpolation.**

Securing a good fit to the specified pattern would call for many radiators, thus requiring the inversion of a matrix of high order. Consequently, a class of uniform pattern matrices is defined whose inversion can be accomplished by inspection, which is sufficiently general to be useful for most practical problems of interest. Uniform pattern matrices generate the coefficients of the Fourier expansion of the specified pattern and can be used, therefore, to help minimize the integral of the square of the deviation of the synthesized and specified patterns as functions of the phase variable, ψ.

Method Formulation

In array theory, the power pattern of an array is expressed using the notation of Silver,[1] as

$$P(\theta, \Phi) = P_0(\theta, \Phi) \left| \sum_{m=1}^{r-1} a_m \exp\left(jm(2\pi(s/\lambda)\cos\theta - \delta)\right) \right| \quad (1)$$

where $P_0(\theta\Phi)$, the a_k, s, λ, δ and θ all have their usual meanings. Schelkunoff[2] pointed out that the sum inside the absolute value brackets is a polynomial defined over the unit circle in the complex z plane in the form

$$f(z_k) = a_0 + a_1 z_k + a_2 z_k^2 + a_3 z_k^3 + \cdots a_{r-1} z_k^{r-1}, \quad (2)$$

where

$$z_k = \exp\left(j2\pi(s/\lambda)\cos\theta_k - \delta\right) = \exp j\psi_k.$$

For most P_0, the pattern of the array is largely determined by the square of this polynomial and must be computed by first laboriously evaluating the complex function $f(z)$ at a set of values z_k as closely spaced on the unit circle as may be desired for accuracy. This computation produces a set of complex numbers which represent the phase and amplitude of the far field at the angles θ_k corresponding to the values of z being used. The power pattern can then be computed from the sequence of field values $f(z_k)$.

The process can be represented in matrix notation[3] as

$$\begin{bmatrix} 1 & z_1 & z_1^2 & z_1^3 & \cdots & z_1^{r-1} \\ 1 & z_2 & z_2^2 & z_2^3 & \cdots & z_2^{r-1} \\ \cdot & \cdot & \cdot & \cdot & & \cdot \\ \cdot & \cdot & \cdot & \cdot & & \cdot \\ \cdot & \cdot & \cdot & \cdot & & \cdot \\ 1 & z_k & z_k^2 & z_k^3 & \cdots & z_k^{r-1} \end{bmatrix} \cdot \begin{bmatrix} a_0 \\ a_2 \\ \cdot \\ \cdot \\ \cdot \\ a_{r-1} \end{bmatrix} = \begin{bmatrix} f(z_1) \\ f(z_2) \\ \cdot \\ \cdot \\ \cdot \\ f(z_k) \end{bmatrix} \quad (3)$$

* Received by the PGAP, March 8, 1960. The work in this paper was partially supported by the Wright Air Dev. Ctr. Air Materiel Command under Contract AF 33(600)-35616 at Litton Industries, Maryland Div., College Park, and by the U. S. Army Signal Res. Dev. Labs. under Contract DA-30-039-SC-78134 at the Philco Corp. Res. Div., Philadelphia, Pa.

† Philco Corp., Philadelphia, Pa.

[1] S. Silver, "Microwave Antenna Theory and Design," McGraw-Hill Book Co., Inc., New York, N. Y., pp. 257–281; 1949.

[2] S. A. Schelkunoff, "A mathematical theory of linear arrays," *Bell Sys. Tech. J.*, vol. 22, p. 80; January, 1943.

[3] R. A. Frazer, W. J. Duncan, and A. R. Collar, "Elementary Matrices," Cambridge University Press, Cambridge, England; 1900.

Eq. (3) can be written more briefly as

$$Z(A) = F, \tag{4}$$

where Z stands for the matrix of complex numbers little z, (A) is the column vector of complex coefficients a_k, and F is the column vector representing the pattern in field amplitude and phase computed for each z. The matrix Z is not square because the pattern can be calculated at as many points as desired.

The labor saving feature of the matrix point of view is that a pattern matrix Z may be composed once, stored in the memory of a computer, and used for almost every array pattern calculated which might be of interest regardless of the s/λ ratio or, within reason, the number of radiators.

Because all z's lie on the unit circle, one z is distinguished from another by arg $z=\psi$. This is given by

$$\psi = 2\pi(s/\lambda)\cos\theta - \delta. \tag{5}$$

The correct physical angle θ at which to plot the value of power density computed for a row generated from a given z_k of arg ψ_k is

$$\theta_k = \cos^{-1}\left(\frac{\lambda}{2\pi S}(\psi_k + \delta)\right). \tag{6}$$

When $s>\lambda/2$, portions of the unit circle are traversed more than once so that the pattern repeats itself either in whole or in part. It is easy to keep track of portions of the pattern that repeat by means of the unit circle as explained in Silver.[1]

Application to Synthesis

As pointed out by Taylor and Whinnery,[4] there is not a unique array polynomial which will produce a given array pattern specified in power. However, when the pattern is specified in field amplitude and phase at a set of angles in the far field equal in number to the radiators in the array, the array polynomial is unique.

Finding the array polynomial is the familiar problem of solving a set of n linear equations in n unknowns as displayed explicitly by (3). The formal solution is to multiply both sides of (4) by the inverse of the matrix Z, thus yielding the column vector A as the product of the inverse of a square pattern matrix Z and the column vector of field values, F; *i.e.*,

$$(A) = Z^{-1}(F). \tag{7}$$

It will now be proved that the inverse of the square pattern matrix always exists. A sufficient condition for the existence of an inverse of a matrix[3] Z is that it must not have a nontrivial null vector. That is, no V exists, such that if $V\neq O$,

$$Z(V) = O. \tag{8}$$

The proof follows: Any set of n coefficients A determine a polynomial of order $n-1$, which is our associated polynomial $f(z)$. When we multiply these coefficients arranged in a column by a row of our pattern matrix Z, the polynomial is evaluated for a particular value of z. If this is repeated n times with a square matrix and if A is to be a nontrivial null vector, all the evaluations must be zero. However, the order of the polynomial is $n-1$ and, by the fundamental theorem of algebra, the polynomial has no more than $n-1$ zeros. Therefore, not all of the n row-by-column multiplications can yield zero no matter what set of A's are used, and no null vector can exist. Hence, for any square pattern matrix the inverse Z^{-1} always exists.

The nonexistence of a nontrivial null vector is equivalent to the nonvanishing of the determinant of Z, the necessary and sufficient condition that the solution given by (7) exists and is unique.

Matrix Synthesis

Matrix operations offer a rapid means of array synthesis if one can control the pattern at many points. However, controlling at many points involves the inversion of matrices of very high order, a task which taxes the capabilities of even high speed computing machines.

A class of matrices, easy to invert, exists which for convenience will be referred to as "uniform pattern matrices." The members of this class are composed of rows generated from selected values of z on the unit circle. The selected values are those values of z at the midpoints of intervals which divide the halves of the unit circle from O to π and from π to 2π into n equal parts.

For these selected z's

$$\arg z_k = \psi_k = \frac{1}{2}(2k-1)\frac{\pi}{n} = \frac{(2k-1)\pi}{2n}. \tag{9}$$

The index k goes from 1 to $2n$ to produce a square matrix having $2n$ elements on a side. The element of such a matrix in the kth row and pth column is given by

$$(z_k)^{p-1} = \exp j(2k-1)(p-1)\pi/2n. \tag{10}$$

The inverse of this matrix is given by $1/2n$ times its conjugate transpose. Consider the result of multiplying the pth column of a square uniform pattern matrix by the lth row of its conjugate transpose. This scalar product, of course, produces the element I_{lp} in the lth row and the pth column of the product matrix, which

[4] T. T. Taylor and J. R. Whinnery, "Applications of potential theory to the design of linear arrays," *J. Appl. Phys.*, vol. 22, p. 19; January, 1951.

is given by

$$I_{lp} = \sum_{k=1}^{2n} z_{lk} z_{kp} = \sum_{k=1}^{2n} \exp\left(j \frac{(2k-1)\pi}{2n} (p-l)\right). \quad (11)$$

Eq. (11) is a geometric progression of ratio $\exp j(p-l)2\pi/2n$ whose sum is given by

$$I_{lp} = \frac{\exp j \dfrac{(p-l)\pi}{2n} \left\{\left[\exp\left(j \dfrac{(p-l)2\pi}{2n}\right)\right]^{2n} - 1\right\}}{\exp j \dfrac{(p-l)2\pi}{2n} - 1}. \quad (12)$$

Because $(p-l)$ is always smaller than $2n$, the denominator of (12) is not zero for $p \neq l$, whereas the quantity in brackets in the numerator is zero for integral $(p-l)$.

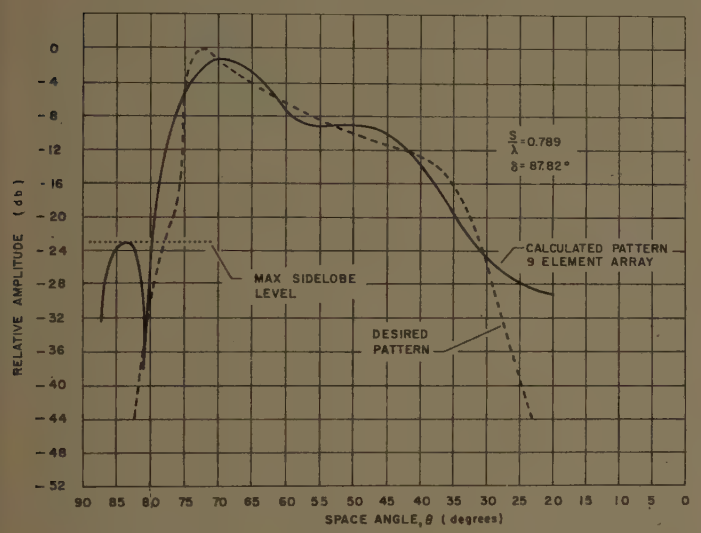

Fig. 1.

Therefore, in all cases $I_{lp} = o$, $l \neq p$; $I_{lp} = 2n$, $l = p$, and the assertion is proved.

Relationship to Fourier Methods

The form of the inverse just constructed bears a strong relationship to the Fourier series. To synthesize a desired pattern, one specifies it as a column vector and multiplies it from the left by the inverse matrix.

TABLE I

Coefficient Vector E-31

Reals	Imaginaries
−0.2148268	−0.2616114
−0.1701754	−0.3756549
−0.0330758	−0.4598802
+0.1049999	−0.5715767
+0.3073646	−0.5802840
+0.5897243	−0.6692145
+0.7493487	−0.6052777
+1.2035549	−0.4562292
+1.3773297	−0.4565782
+1.8041235	+0.1498776
+2.4008505	+0.1254140
+2.5114346	+1.2429506
+4.3066226	+1.8854050
+3.9128238	+3.1464932
+9.3294481	+7.5479766
+16.7900000	0.0000000
+9.3294481	−7.5479766
+3.9128238	−3.1464932
+4.3066226	−1.8854050
+2.5114346	−1.2429506
+2.4008505	−0.1254140
+1.8041235	−0.1498776
+1.3773297	+0.4565782
+1.2035549	+0.4562292
+0.7493487	+0.6052777
+0.5897243	+0.6692145
+0.3073646	+0.5802840
+0.1049999	+0.5715767
−0.0330758	+0.4598802
−0.1701754	+0.3756549
−0.2148268	+0.2616114

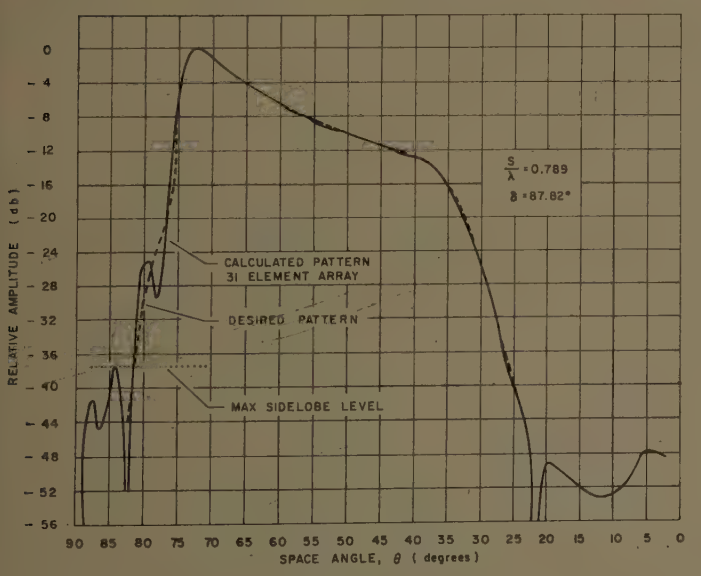

Fig. 2.

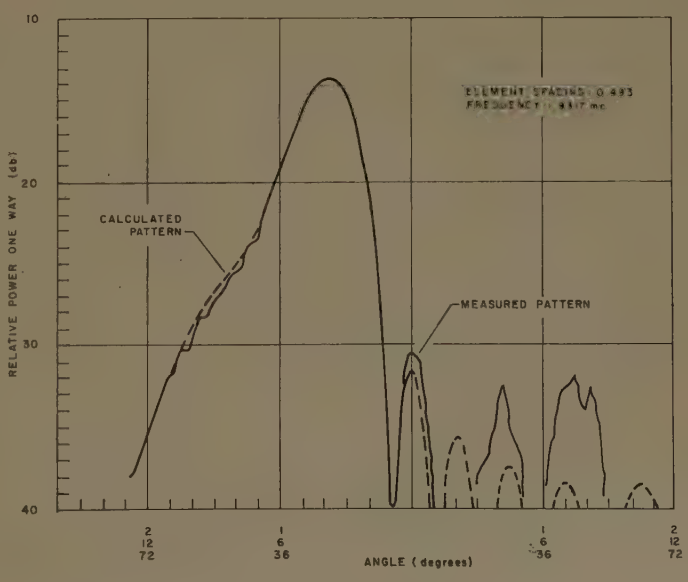

Fig. 3.

A given row-by-column multiplication has the form

$$A_l = \sum_{k=1}^{2n} \exp(-jl\psi_k) \cdot f(\psi_k). \tag{13}$$

If $f(\psi)$ is a real function, then the process becomes the numerical procedure for getting the Fourier coefficient in the complex Fourier expansion of the function $f(\psi)$, as set forth by Sommerfeld;[5]

$$f(\psi) = \sum_{l=-\infty}^{\infty} A_l \exp(jl\psi) \tag{14}$$

$$A_l = \frac{1}{2\pi}\int f(s) \exp(-jls)ds. \tag{15}$$

The coefficients in the expansion, (14), symmetrically placed about A_0, are complex conjugates of each other. Eq. (13) numerically calculates (15), and, therefore, the coefficients for a real pattern are the same as the Fourier coefficients.

The close relationship affords a choice in the design of an array. Either the $2n$ coefficients generated by the matrix calculation may be used as they are, or the first $n+1$ of them may be used with the n complex conjugates to produce an array with an odd number of elements formed along Fourier lines. Rapid matrix methods may be used in either case.

Almost any desired antenna pattern shape can be realized as a purely real pattern. In addition, the Fourier selection of array coefficients tends to make the synthesis more responsive to the shape of the pattern as a whole rather than merely match the pattern on a point-by-point basis. If, however, a prescribed variation of far field phase is desired, the coefficients should be used just as they come from multiplication by the inverse matrix.

An example of the results of a matrix calculation are the two synthesized shapes shown in Figs. 1 and 2 for 9- and 31-element arrays, respectively. Both plots are computed from the coefficients given in Table I, which was synthesized by the use of the conjugate transpose matrix in the manner derived. A 9-element waveguide array was constructed. The resulting pattern should be that of the array factor of Fig. 1 multiplied by the element factor $P_0(\theta, \Phi)$ of a waveguide slot. Fig. 3 is a comparison of the calculated and measured patterns of that array.

[5] A. Sommerfeld, "Partial Differential Equations of Physics," Academic Press, New York, N. Y.; 1949.

On the Radiation from Several Regions in Spiral Antennas*

M. S. WHEELER†, MEMBER, IRE

A FILAMENTARY conductor spiral is sometimes used as a radiating model to describe some aspects of performance of spiral antennas. Curtis has made such an analysis for Archimedes spirals by approximating the spiral with sections of semicircles.[1] A similar analysis of the equiangular spiral is possible without making the semicircle approximation, but using the exact geometric spiral form. By so doing, some interesting studies can be made on radiation from various regions of the spiral antennas. This work lends some quantitative weight to a discussion by Kaiser on radiation regions in spiral antennas.[2]

An equiangular spiral is normalized to a one-wavelength circumference circle

$$r = \frac{\lambda}{2\pi}\epsilon^{a\alpha}$$

where a is the spiral growth rate and r is the spiral radius at an angle α. The spiral is further defined as having N turns inside and M turns outside the one-wavelength circle. Thus, the minimum radius is

$$r_{\min} = \frac{\lambda}{2\pi}\epsilon^{-2\pi Na},$$

and the maximum radius is

$$r_{\max} = \frac{\lambda}{2\pi}\epsilon^{+2\pi Ma}.$$

The far-field pattern for such a two-arm spiral sustaining antiphased traveling waves may be found by

* Received by the PGAP, July 22, 1960.
† Air Arm Div., Westinghouse Elec. Corp., Baltimore, Md.
[1] W. L. Curtis, "Spiral antennas," IRE TRANS. ON ANTENNAS AND PROPAGATION, vol. AP-8, pp. 298–306; May, 1960.
[2] J. A. Kaiser, "The Archimedean two-wire spiral antenna," IRE TRANS. ON ANTENNAS AND PROPAGATION, vol. AP-8, pp. 313–323; May, 1960.

numerical integration.[3] We will first examine the pattern in the region of the one-wavelength circle for an unattenuated wave and for very slow growth rate of the spiral.

For example, if the growth rate is $a=0.01$ and $M=0.25$ and $N=0.25$, one is left with essentially a unit circle one wavelength in circumference [Fig. 1(a)]. The far-field pattern has been calculated and is shown in Fig. 1(c), where F_H^2 is relative power as measured in the H-plane of a linearly-polarized detector and F_E^2 is relative power as measured in the E-plane of a linearly-polarized detector. It is seen that this is a typical spiral pattern, and it is said that this represents the fundamental mode of spiral radiation.

From this unit circle, if additional fractional turns are added inside or outside the circle, no change in pattern is observed. To be specific, for $M=0.5$, $N=0.5$ [Fig. 1(b)], two complete turns exist side by side and the patterns are identical to 0.2 per cent for the given slow growth rate. This is in agreement with Kaiser's thesis that adjacent turns in the one-wavelength region reinforce one another.

To investigate the region of the spiral at two wavelengths circumference for the same slow growth rate, the outer turns are set at 11.282 and the inner turns at -10.782. Notice that the inner turns are negative in this unusual situation. Together, this represents [Fig. 1(d)] one complete turn at two-wavelength circumference. The resulting elliptically-polarized far-field pattern is shown in Fig. 1(f). It should be noted that, although this ring is elliptically-polarized, it is at least forward radiating. This situation is contrary to the statement that is sometimes made, that a single turn at two-wavelengths circumference is not forward radiating. The mistake that is made which leads to this incorrect conclusion is in comparing the spiral to a circular conductor of two-wavelengths circumference and sustaining an uninterrupted traveling wave. This model, however, does not have the antiphase symmetry of the spiral and such a comparison is not valid.

The final step in this examination is to extend the spiral turns at the two-wavelength circle to produce two complete adjacent turns [Fig. 1(e)] as was done for the one-wavelength circle. The far-field power is now depressed by four orders of magnitude at this slow growth rate. This, again, is in agreement with Kaiser's discussion concerning radiation from the two-wavelength region of the spiral where radiation from adjacent turns tends to cancel.

All of these approaches are interesting in that they apply generally to any spiral type with closely wound turns. The most direct approach to the problem, however, is to use an attenuated traveling wave on the spiral arms and to study the spiral as a whole.

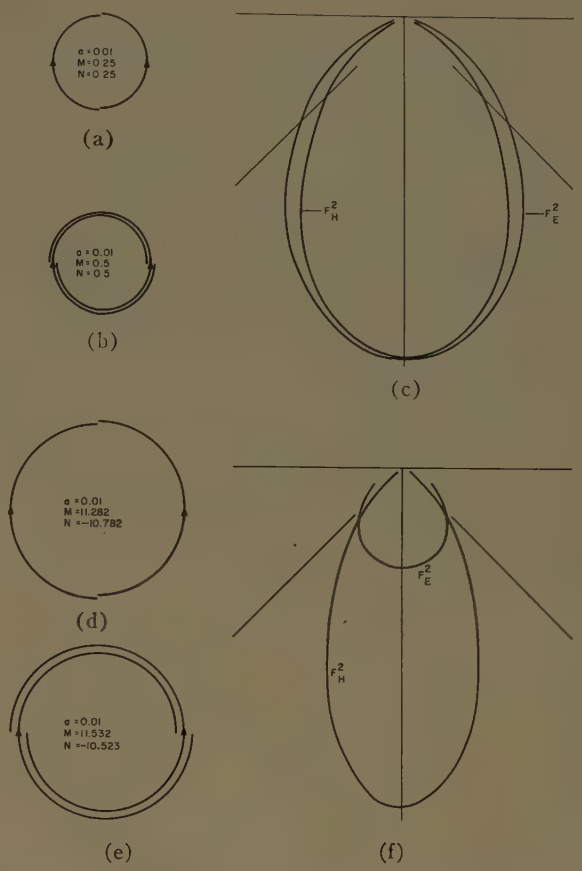

Fig. 1—Spiral configurations (a) and (b) give identical radiation patterns (c) to 0.2 per cent at the one-wavelength circle. Configuration (d) gives an elliptically-polarized pattern (f), but (e) gives almost perfect pattern cancellation. (a) ½-turn arms at 1 λ circle. (b) One-turn arms at 1 λ circle. (c) Relative power. (d) ½ turn arms at 2 λ circle. (e) One-turn arms at 2 λ circle. (f) Relative power.

The far-field pattern is given by an integral, the limits of which are the number of inner and outer spiral turns (N and M). This integral converges as M is increased by the attenuation factor on the traveling wave. Similarly the value of the integral converges as N is increased, by the vanishing of the spiral at the center.

It is found that, for a given spiral growth rate, if the outer turns are maintained sufficiently large so that they no longer affect the value of the integral, the results of changing the inner turns can be studied. Similarity as a function of outer turns and spiral growth outer turns can be investigated. To say this another way, by using a large excess of outer turns, the high-frequency limitation is found, and by using a large excess of inner turns, the low-frequency limitation is found.

In this manner, the on-axis circularity of two-arm spirals has been calculated and is shown in Figs. 2 and 3. Fig. 2 gives the circularity as a function of inner turns and spiral growth rate. Similarly, Fig. 3 gives the circu-

[3] M. S. Wheeler, "Design procedure for equiangular spiral antennas," *Seventh East Coast Conf. on Aeronautical and Navigational Electronics*, pp. 1.2.4-1—1.2.4-6; October, 1960.

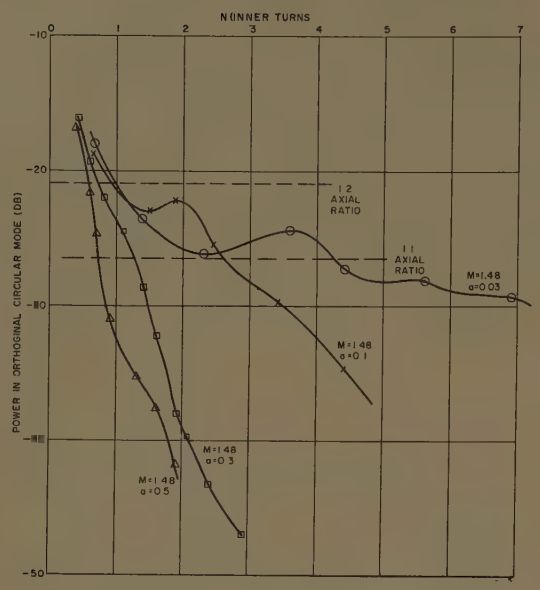

Fig. 2—On-axis circularity in two-arm spirals as a function of inner turns.

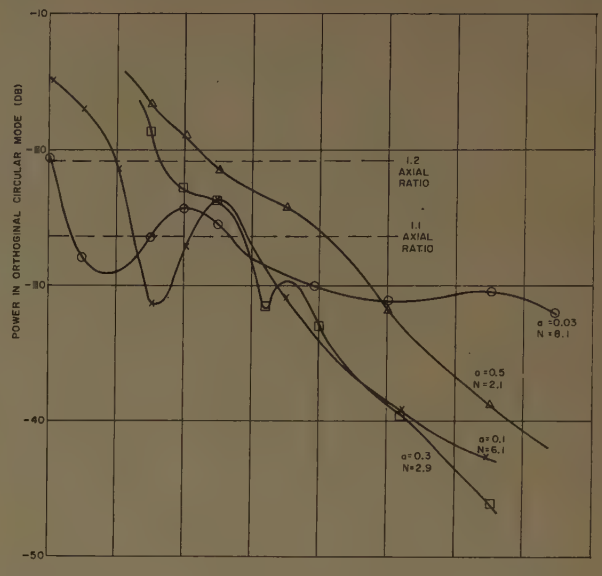

Fig. 3—On-axis circularity in two-arm spirals as a function of outer turns.

larity as a function of outer turns and spiral growth rate. It is interesting that the circularity continues to improve with the addition of turns. This is in contrast to the general pattern appearance which stabilizes at some number of inner and outer turns and remains essentially constant.

Other conclusions from Figs. 2 and 3 are that the spirals having slow growth rate require less outer diameter and allow a larger inner diameter for a given degree of circularity. For this reason and because this type of calculation shows that the radiation pattern is essentially independent of growth rate, the slow growth rate spiral is to be preferred.

For experimental verification, reference is made to the measurements by Dyson.[4] The above calculation uses the current attenuation function measurements from this report. If the inner and outer turns of Figs. 2 and 3 are converted to inner and outer radii, they agree generally with Dyson's measurements of on-axis circularity within 2 to 1. Physical differences which likely account for this error are the arm terminations which are either open or short circuited and are thereby reflecting, and the problem involving the width of arms. When the actual arms are wide (not filamentary), it is hard to specify the effective number of turns present.

[4] J. D. Dyson, "The Equiangular Spiral Antenna," Antenna Lab., Univ. of Illinois, Urbana, Rept. No. 21; September 15, 1957.

Rectangular-Ridge Waveguide Slot Array*

A. Y. HU†, MEMBER, IRE AND C. D. LUNDEN†

Summary—**A four-slot, linear broadside array on a rectangular-ridge waveguide is discussed. The slot conductances were adjusted to obtain a 20-db Dolph-Tchebycheff power distribution across the array. *H*-plane and *E*-plane patterns and gain were obtained; these agreed quite well with the theory.**

IN recent years, flush-mounted slot radiators have been developed for aircraft and missiles, where drag is of great importance. Linear waveguide-slot arrays[1–3] can be employed in two-dimensional antenna arrays. However, where large beam-scanning angles are required, the element spacing in the plane of scan must be reduced to about a half wavelength. This spacing is

* Received by the PGAP, July 29, 1960.
† Boeing Airplane Co., Transport Div., Renton, Wash.

[1] A. A. Oliner, "The impedance properties of narrow radiating slots in the broad face of rectangular waveguide," IRE TRANS. ON ANTENNAS AND PROPAGATION, vol. AP-5, pp. 4–20; January, 1957.
[2] A. F. Stevenson, "Theory of slots in rectangular waveguides," *J. Appl. Phys.*, vol. 19, pp. 24–38; January, 1948.
[3] S. Silver, "Microwave Antenna Theory and Design," M.I.T. Rad. Lab. Ser., vol. 12, McGraw-Hill Book Co., Inc., New York, N. Y., pp. 291–295; 1949.

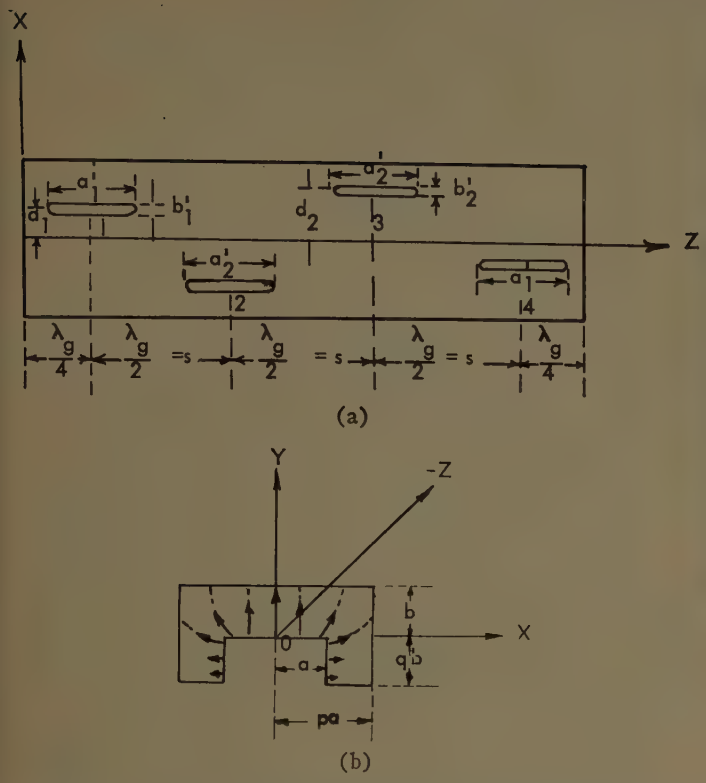

Fig. 1—(a) The slot array on broad face of ridge waveguide. (b) Cross section of ridge waveguide. $\lambda_g=7.1''$, $a=0.64''$, $b=0.5''$, $a'_1=2.68''$, $p=2.5$, $q=1$, $a'_2=2.76''$, $b_1'=0.06''$, $d_1=0.18''$, $b_2'=0.075''$, $d_2=0.6''$.

too small for ordinary rectangular waveguide, but can accommodate ridge waveguide structures. A four-slot, ridgeguide-fed linear array was designed as one element, or bay, for a two-dimensional array [Figs. 1(a), 1(b), and 2]. The slot conductances were adjusted to get a 20-db Dolph-Tchebycheff distribution.

The slot length is a half wavelength long, and its radiation pattern will be equivalent to the pattern produced by a half-wavelength dipole with different polarization, provided the current distribution on the dipole is equivalent to the electric field distribution across the aperture of the slot. The *H*-plane pattern of a half-wavelength slot on an infinite ground plane may be written as[4]

$$E_\phi(\theta)_{\phi=0^\circ} = \frac{\cos\left(\frac{\pi}{2}\cos\theta\right)}{\sin\theta}. \qquad (1)$$

The *E*-plane pattern of a half-wavelength slot on the infinite ground plane may be written as

$$E_\phi(\phi)_{\theta=90^\circ} = \text{constant}. \qquad (2)$$

The coordinate system of θ and ϕ is shown as Fig. 3.

The distance between the adjacent slots is equal to $\lambda_g/2$. The slots are transposed about the centerline of the guide (z axis) to form a broadside array. For a

[4] J. D. Kraus, "Antennas," McGraw-Hill Book Co., Inc., New York, N. Y., p. 358; 1950.

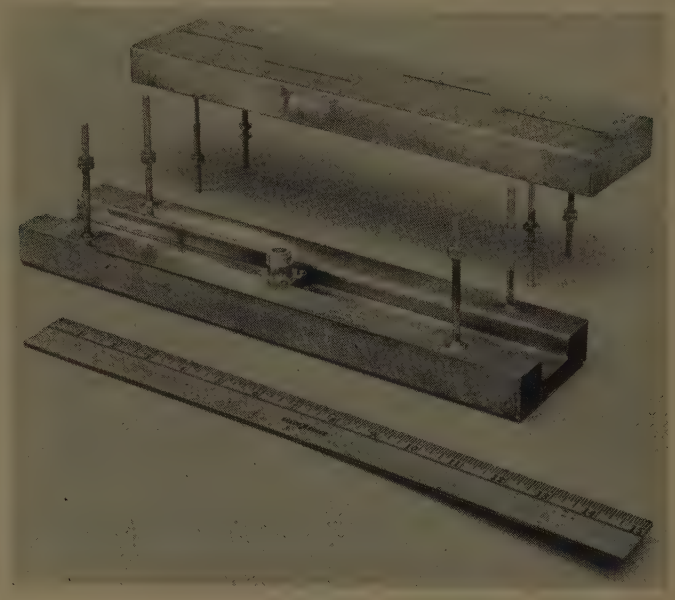

Fig. 2—Rectangular ridge waveguide slot array.

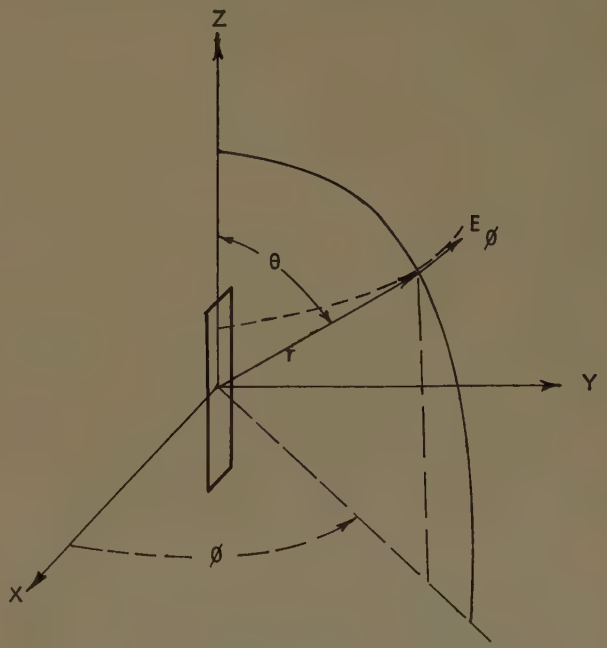

Fig. 3—The radiation coordinate system of one slot on an infinite ground plane.

Dolph-Tchebycheff distribution and for a sidelobe level of 20 db,[5] the mainlobe to sidelobe ratio, R, is

$$R = \frac{\text{Max. mainlobe of field}}{\text{Sidelobe level of field}} = 10. \qquad (3)$$

The Tchebycheff polynomial of degree $m=n-1=4-1=3$ is

$$T_3(x) = 4x^3 - 3x, \qquad (4)$$

where

x = the variable of Tchebycheff polynomial.

[5] *Ibid.*, p. 106.

Thus:

$$T_3(x_0) = R = 10, \tag{5}$$

and

$$\left.\begin{aligned} x_0 &= 1/2[(R+\sqrt{R^2-1})^{1/m} + (R-\sqrt{R^2-1})^{1/m}] \\ x_0 &= 1.54043 \end{aligned}\right\}. \tag{6}$$

The array factor is

$$\frac{E_4}{2} = A_0 \cos\frac{\psi}{2} + A_1 \cos\frac{3\psi}{2}, \tag{7}$$

where

E_4 = the total field of four slots

$$\psi = \frac{2\pi s \sin\theta'}{\lambda_g} = \pi \sin\theta'$$

$s = \dfrac{\lambda_g}{2}$ the distance between the adjacent slots.

$$\theta' = \frac{\pi}{2} - \theta.$$

Let

$$\cos\frac{\psi}{2} = \frac{x}{x_0}, \tag{8}$$

and equating (7) and (4)

$$4x^3 - 3x = A_0\left(\frac{x}{x_0}\right) + A_1\left[4\left(\frac{x}{x_0}\right)^3 - 3\left(\frac{x}{x_0}\right)\right]. \tag{9}$$

Since

$$\cos\frac{3\psi}{2} = 4\cos^3\left(\frac{\psi}{2}\right) - 3\cos\frac{\psi}{2} = 4\left(\frac{x}{x_0}\right)^3 - 3\left(\frac{x}{x_0}\right), \tag{10}$$

so

$$A_1 = 3.65532, \qquad A_0 = 6.34463. \tag{11}$$

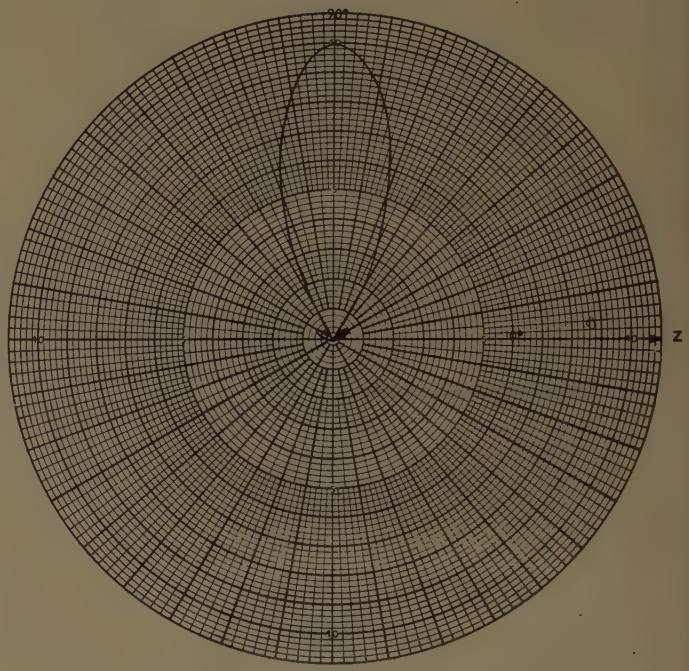

Fig. 4—Calculated four-slot array H-plane field pattern.

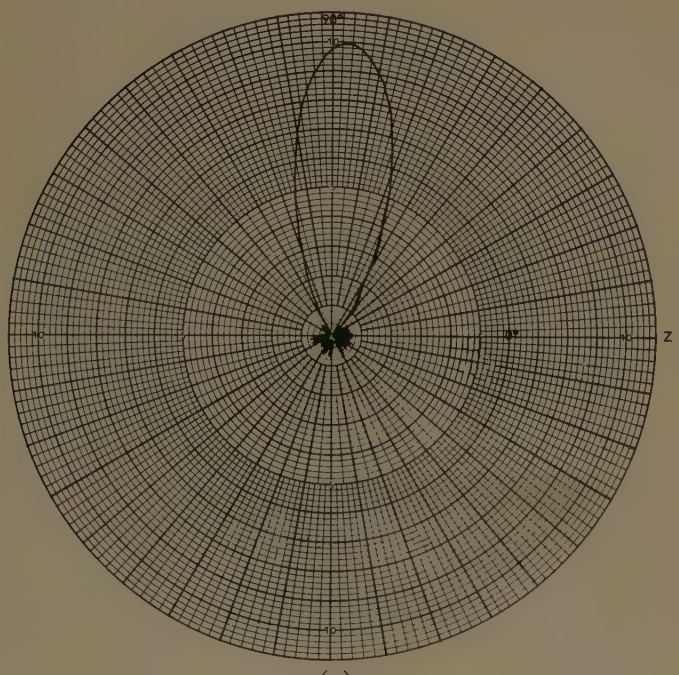

(a)

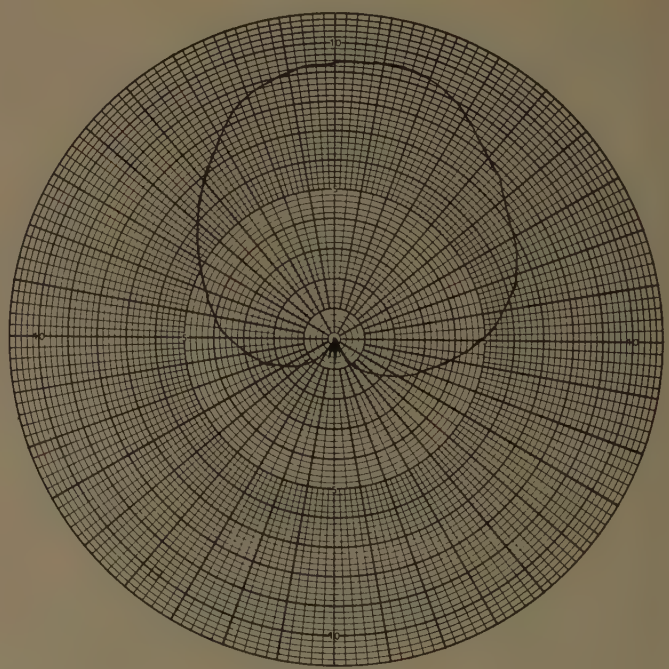

(b)

Fig. 5—(a) H-plane field pattern. $f=2100$ Mc. (b) E-plane field pattern. $f=2100$ Mc.

Thus, the array factor of the four isotropic, in-phase point sources is

$$E_\phi(\theta) = \frac{E_4(\theta)}{2} = 6.34463 \cos\left[\frac{\pi}{2}\sin\left(\frac{\pi}{2}-\theta\right)\right] + 3.65532 \cos\left[\frac{3\pi}{2}\sin\left(\frac{\pi}{2}-\theta\right)\right]. \quad (12)$$

Applying the principle of pattern multiplication, the total H-plane normalized field is obtained by multiplying (1) and (12) (Fig. 4). The amplitude of slot excitation is proportional to the square root of the slot conductance. The calculation of slot conductance on the ridgeguide will be considered in another note.

Experimental E- and H-plane patterns of the slot array are shown in Fig. 5. The mainlobe in the H plane is three degrees from the y direction, which may be attributed to the off-center position of the slots and to the asymmetrical excitation (TE_{10} mode). The half-power beamwidth and sidelobe level of the H-plane field are close to the field calculated for the 20-db Dolph-Tchebycheff distribution. The antenna gain with respect to an isotropic source, using the pattern-range integrator, is 12 db.

ACKNOWLEDGMENT

The authors wish to acknowledge the assistance of the various members of the Transport Division, Electrodynamics Staff, Boeing Airplane Co., Renton, Wash.

Measurements on the Asymmetrically-Excited Prolate Spheroidal Antenna*

HANS H. KUEHL†

THE prolate spheroidal antenna has been considered from an analytical point of view by numerous authors. Schelkunoff[1] has analyzed the asymmetrically-fed prolate spheroidal antenna and, more recently, Myers[2] has presented radiation patterns for such an antenna. As far as is known to the author, however, no experimental study has been performed on the asymmetrically-fed prolate spheroidal antenna. This is probably due to the fact that it is an inconvenient configuration to construct and any transmission line to the antenna disturbs the radiation enough to make an accurate comparison between experimental and theoretical radiation patterns difficult. Therefore, the measurements presented in this communication were made on a spheroidal antenna operated in the receiving state and the detecting equipment was contained within the antenna so that the usual RF transmission line was not necessary to carry the signal from the antenna. High-resistance leads (about 20,000 ohms per foot) were used to carry the detected signal from the antenna. These disturb the field very little since any impressed field causes negligible current to flow on the leads.

The test antenna which was used is shown in Fig. 1.

Fig. 1—Prolate spheroidal antenna.

The "gap" is a polystyrene ring through which the impinging radiation travels. Two circular metal plates on either side of the "gap" form a radial transmission line which guides the received energy to the detector within the antenna. The terminals for the high-resistance leads can be seen projecting from the spheroid

* Received by the PGAP, August 4, 1960. This research was supported by the U. S. Air Force under Contract No. AF 18(600)-1113.

† Elec. Engrg. Dept., University of Southern California, Los Angeles, Calif., Formerly at Calif. Inst. Tech., Pasadena, Calif.

[1] S. A. Schelkunoff, "Advanced Antenna Theory," John Wiley and Sons, Inc., New York, N. Y., pp. 102–127; 1952.

[2] H. A. Myers, "Radiation patterns of unsymmetrically fed prolate spheroidal antennas," IRE TRANS. ON ANTENNAS AND PROPAGATION, vol. AP-4, pp. 58–64; January, 1956.

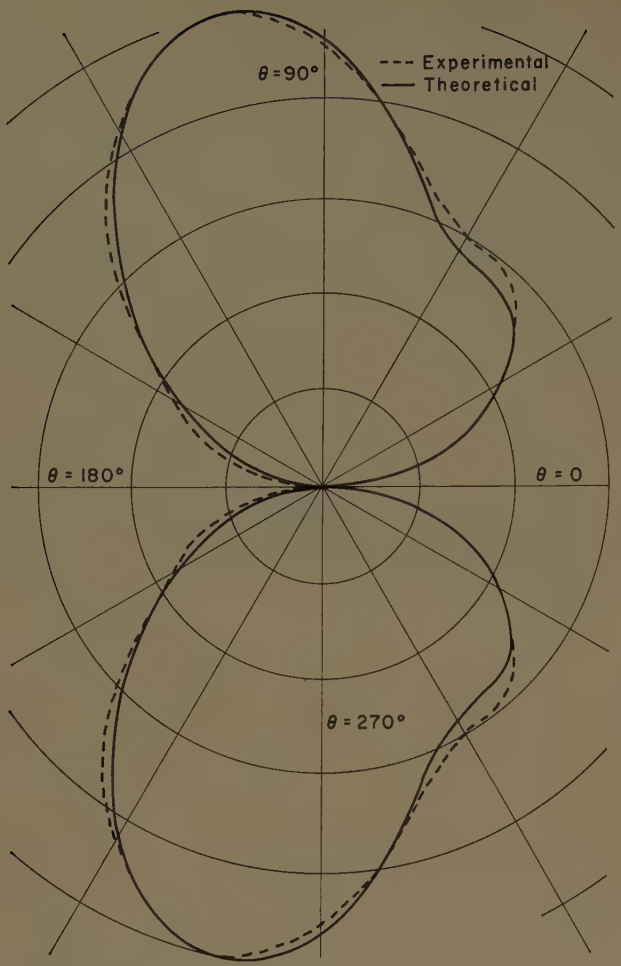

Fig. 2—Radiation patterns for $v_0=0.1$, $u_0=1.02$, $kL=3.0$.

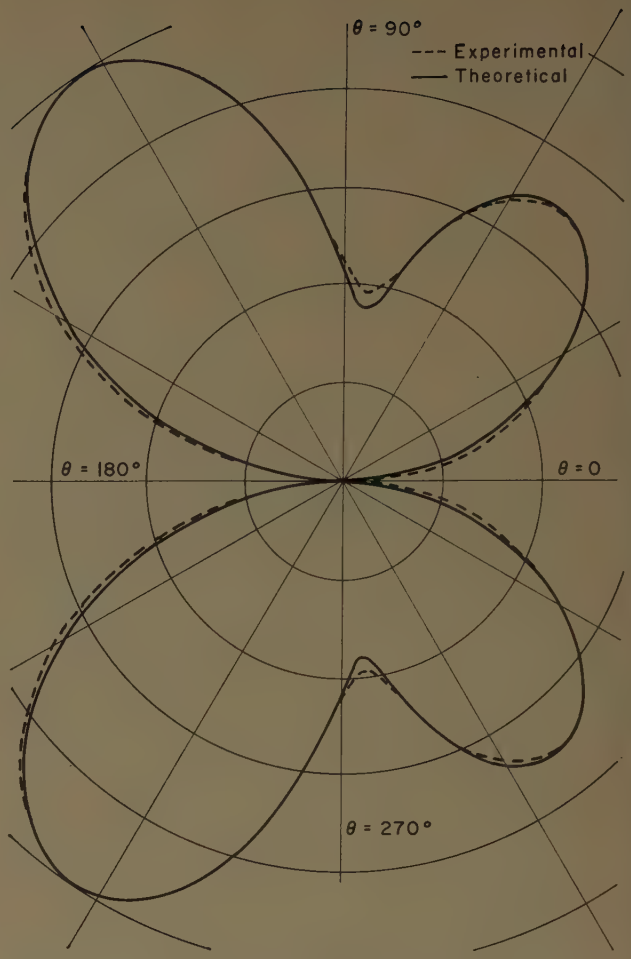

Fig. 3—Radiation patterns for $v_0=0.4$, $u_0=1\ 02$, $kL=3.0$.

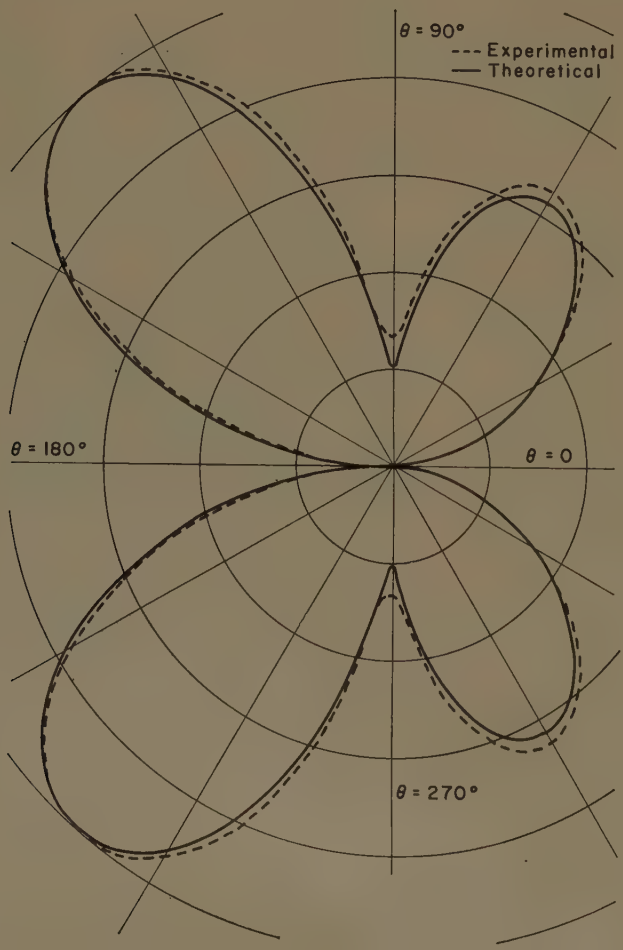

Fig. 4—Radiation patterns for $v_0=0.8$, $u_0=1.02$, $kL=3.0$.

The spheroid was constructed so that the "gap" could be placed in three alternative locations. While the "gap" is in one location the other two locations are filled by metal rings so that the spheroid is electrically continuous everywhere except at the "gap." The gap is $\frac{3}{4}$-inch wide or about $\lambda/30$ at 500 Mc, the frequency of measurement. The metal and polystyrene rings were threaded to make them easily removable.

The spheroid itself was constructed of wood with the outer surface sprayed with copper. The thickness of the copper greatly exceeds the skin depth at the frequency used so that electrically the spheroid body is solid copper.

The spheroid tested had $kL=3$, where $k=\omega\sqrt{\mu_0\epsilon_0}$ and $2L$ is the interfocal distance so that it is approximately a wavelength in length. Using the notation of Schelkunoff,[1] the "gaps" were centered at $v_0=0.1$, 0.4, 0.8 and the "radial" coordinate defining the spheroid was 1.02. The experimental together with theoretical patterns of the far zone electric field are shown in Figs. 2, 3 and 4 for the three positions of the "gap." In these figures the spheroid axis is along the direction of $\theta=0$ and the longer portion of the spheroid is always on the left. The experimental patterns were normalized equal to the theoretical patterns at the maxima. The patterns are plane sections of a figure of revolution around the spheroid axis. The theoretical field patterns were taken from results furnished by Dr. C. P. Wells.

It is seen that the agreement between theoretical and experimental patterns is quite good. As would be expected, the largest percentage differences occur near the relative minima of the patterns. The differences in minima are 7, 10 and 26 per cent, respectively, in Figs. 2, 3 and 4. It is estimated that the experimental error in the measurements is less than 2 per cent. The difference between the theoretical and experimental patterns is probably largely due to the difference in the "gap" width between the two cases since the theoretical analysis assumes an infinitesimal "gap" width. A narrow gap seems to cause deeper minima in the pattern. However, since the theoretical and experimental patterns agree very well except at the minima, the theoretical results can be used even for the case of the "gap" of nonzero width if the values near the minima are not important.

ACKNOWLEDGMENT

The author wishes to express his appreciation to Dr. C. H. Papas for encouragement throughout this work, to Dr. C. P. Wells of Michigan State University for the use of the computed theoretical radiation patterns, and to C. Yeh for assistance with the experimental work.

Electronically Steerable *S*-Band Array*

R. G. ROUSH†, SENIOR MEMBER, IRE, AND J. C. WILTSE†, SENIOR MEMBER, IRE

A NINE-ELEMENT *S*-band linear array phased by servo-controlled stripline ferrite phase shifters is described in this correspondence. This was a techniques demonstration model constructed under Air Force Contract which may be of general interest since the methods of control can be conveniently extended to large planar array applications.

The radiating elements are half-wave dipoles spaced one-half wavelength apart and mounted one-quarter wavelength in front of a ground plane. The dipole axes are parallel to each other and to the ground plane, but perpendicular to the line of the array. The dipoles are fed via the series arrangement of phase shifters and directional couplers shown in Fig. 1 on the next page. The advantages of this series-feed approach over a parallel scheme are:

1) All phase shifters used for steering in one coordinate have the same phase settings; thus, a series-fed planar array requires but two control signals to specify each beam position.

2) The maximum phase shifter excursion is substantially less than 2π radians; hence phase shifter dimensions and control power can be expected to be smaller in the series control mode.

3) Delay distortion across the array can be compensated with the series connections.

On the debit side is the cumulative phase shifter insertion loss. In large array applications this must occur at low levels; hence individual element amplifiers and antenna feed-line repeater amplifiers are required.

The antenna element isolation available with individual amplifiers is simulated in the linear model by 6-db pads in series with each element. The stripline directional couplers are the quarter-wave stub type, chosen

* Received by the PGAP, August 4, 1960. This work was sponsored by the Rome Air Dev. Center, Air Res. Dev. Command, under Contract AF 30(602)-1776.

† Res. Div., Electronic Communications, Inc., Timonium, Md.

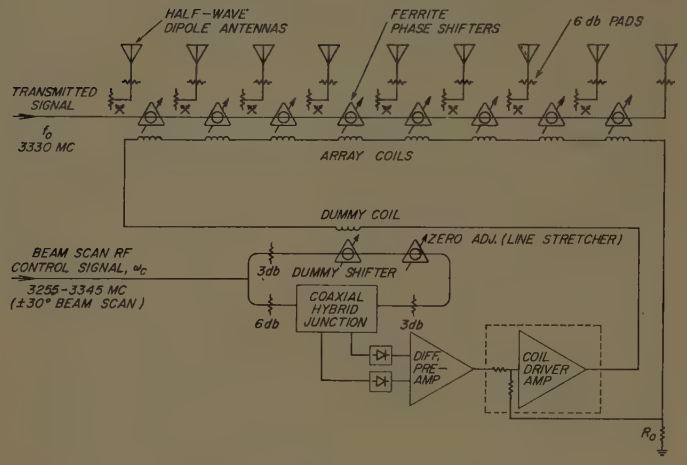

Fig. 1—Phase control system for the nine-element steerable array.

Fig. 2—Series feed network of phase shifters and couplers for the nine-element array.

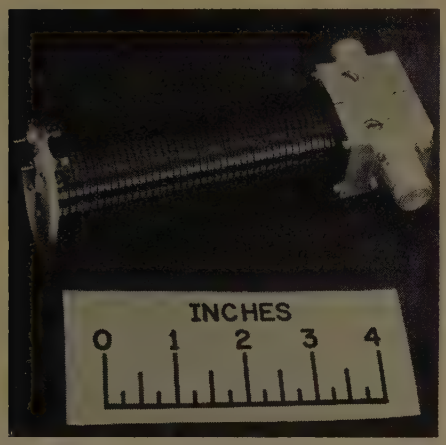

Fig. 3—*S*-band stripline ferrite phase shifter.

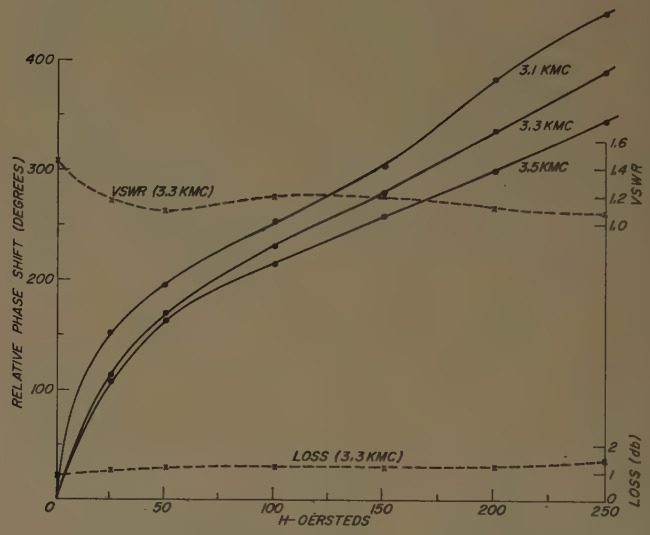

Fig. 4—Measured characteristics of the stripline ferrite phase shifters.

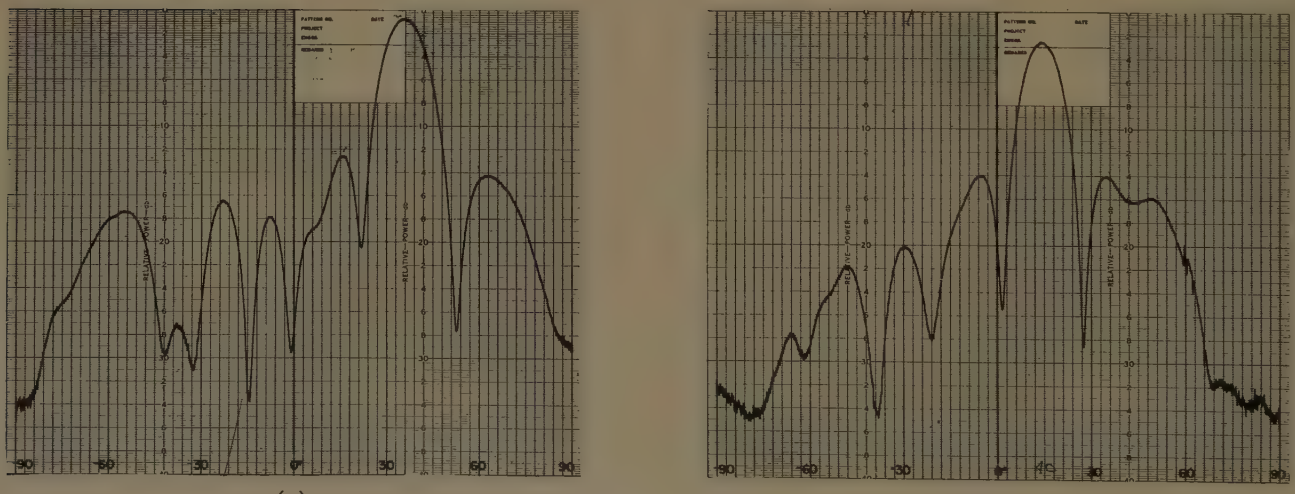

(a) (b)

Fig. 5—*H*-plane radiation pattern of nine-element array. (a) Scan angle +36°, coil current 0.7 amp, control frequency 3270 Mc, temperature=20°C. (b) Scan angle +14°, coil current 1.7 amp, control frequency 3300 Mc, temperature=20°C.

for their ability to provide the low coupling values (3 to 6 db) needed at the ports near the end of the array. The coupling coefficients of the couplers were individually adjusted to give approximately a uniform amplitude distribution across the array. In making this adjustment the reduction of power along the feed network due to both coupling loss and phase shifter attenuation was taken into consideration.

Since all phase shift values are to be equal in the series arrangement the coils of the eight inter-element phase shifters are connected in series with the coil of a ninth unit. By means of a simple phase comparison bridge and transistor servo loop arrangement[1] (also developed under this contract), the ninth phase shifter is forced to a phase shift value directly proportional to the frequency of an RF steering command signal. Thus, as long as the "dummy" servo-controlled shifter is subject to the same environmental conditions as are the array shifters, the beam steering angle is directly controlled by the RF command signal frequency. The effects of nonlinearities in the phase shift characteristic, hysteresis, stray fields, temperature, etc., are thus either eliminated or reduced to small values.

A photograph of the series feed network is shown in Fig. 2, which corresponds directly with the upper portion of Fig. 1. For transmitter use the signal input port is at the extreme left in the photograph. The nine evenly-spaced, unterminated coaxial connectors along the front of the structure are the directional coupler branch arms which connect to the antenna elements. The other coupler branch arms are terminated in short coaxial loads.

An original design was used for the reciprocal phase shifters. A shielded stripline geometry (equivalent to coaxial line of rectangular cross section) was filled with a ferrite possessing a $4\pi M_s$ of 600 gauss and a linewidth of 90 oersteds. The stripline was folded once in length so that two four-inch lengths of ferrite-filled line (in series) could be placed inside a coil about $4\frac{1}{2}$ inches long. A photograph of the resulting shifter (used as the "dummy") is shown in Fig. 3, and measured characteristics are given in Fig. 4. Over the linear phase-shift region the VSWR is less than 1.2. (Similarly the VSWR of the stripline directional couplers was also 1.2 or less. These low VSWR values may be conveniently achieved over about a 10 per cent bandwidth.) The phase shifters were constructed to be as nearly identical as was reasonable in the limited time available. The ferrite material was purchased at two separate times, but presumably from the same firing. After construction was completed, measurements of total electrical line length of each shifter showed differences amounting to as much as several tens of degrees. These differences are attributed to variations in the ferrite characteristics and to minor constructional differences. The ferrite supplier has since instituted more rigid manufacturing specifications and more accurate quality control. Nevertheless it would probably be desirable to provide future phase shifters with a mechanical line length trimmer so that all shifters could be matched accurately in length.

Some adjustment of phase shifter line lengths was made by shunting certain of the control coils, which provided slightly differing magnetic fields for the shifters. Although some phase errors were still present, the measured array patterns were satisfactory. Some typical curves are shown in Fig. 5 for scan angles of 36° and 14°. The theoretical sidelobe level for the array is −13 db, and the measured sidelobes are somewhat higher than this due to the phase errors. As the scan angle is decreased toward zero the power level in the main beam decreases slightly because the VSWR in the feed line is increasing. (The highest VSWR occurs at zero scan angle for half-wavelength spacing because reflections add in phase.)

Acknowledgment

Several persons at this laboratory made helpful contributions to the design and testing of this array. Particular credit is due S. N. Broady, C. W. Hicks and D. L. Mitchell.

[1] D. D. King, C. M. Barrack, and C. M. Johnson, "Precise control of ferrite phase shifters," IRE Trans. on Microwave Theory and Techniques, vol. MTT-7, pp. 229–233; April, 1959.

Concerning the Assumption of Random Distribution of Scatterers as a Model of an Aircraft for Tracking Radars*

L. PETERS, JR.†, SENIOR MEMBER, IRE, AND F. C. WEIMER†, SENIOR MEMBER, IRE

THE primary purpose of this communication is to discuss the model used to analyze the motion of the apparent radar center of radar targets and, in particular, to point out that certain assumptions which have been made to obtain this model are erroneous.

In a recent paper, Muchmore[1] uses a model of aircraft reflection developed by Delano[2] to determine the spectra of the "instantaneous radar center" or "apparent radar center." Delano's model consists of an infinite number of random scatterers with statistically independent amplitudes and phases. He states that independent phase criterion is adequate, provided that there are 5 or 6 scatterers whose amplitudes are approximately equal. This leads to an amplitude of the echo area which is Rayleigh distributed. It has been noted that a Rayleigh distribution has been obtained from many targets when a wide range of aspects (or long time of observation) is considered. However, this is not likely to be the case when the range of aspects is restricted or the time of observation held to the order of magnitude of one second, which is approximately the response time of tracking-radar servo system. Furthermore, even if the amplitude is Rayleigh distributed, it does not necessarily fit the conditions set forth by Delano of a statistically independent phase distribution. This may be demonstrated by a line scatterer with a uniform amplitude and a linear phase distribution. Such a distribution produces a far-field pattern of the form $\sin u/u$. This pattern yields a Rayleigh-distributed amplitude if a sufficient number of aspects is considered and provided $u > \pi$.[3] Therefore, it is concluded that the phase distribution need not be statistically independent to obtain a Rayleigh distribution of the amplitude of the echo. Indeed, it would be hard to picture a more coherent scatterer than the one discussed above.

However, both Delano and Muchmore have apparently decided that most targets do exhibit a Rayleigh distribution of echo and have concluded that the phase distribution is statistically independent. It has already been demonstrated that this reasoning is erroneous.

Another point that has prompted this communication is the fact that five or six scatterers of nearly equal magnitudes are generally a poor representation of a radar target such as an aircraft. Two such scatterers are a more reasonable representation over many aspects. Published level-flight S-band echo area patterns[4] of an AT-11 and a B-26 tend to verify this statement. A careful study[5] of such patterns shows that the depth of successive minima and the magnitude of successive maxima tend to repeat. Such a repetition would not exist if there were more than two scatterers.

In the remainder of this communication, a two-point scatterer and a linear scatterer are used to demonstrate the discrepancies that can arise when this model is used indiscriminately.

For the case in which "all scatterers are concentrated into two equal groups," Delano obtains an rms radar center fluctuation about the mean radar center

$$\eta_{\text{rms}} = \frac{L}{\sqrt{2\pi}\, R},$$

where L is the distance between two scatterers and R is the range. While it is not clear what is meant by "two equal groups," it is assumed that this corresponds to equal amplitudes and random phases. No other interpretation has significance in terms of actual radar targets. It should be noted that in the last line of his paper, Delano mentions the case of "an infinite number of sources all at the same location" which produce a Rayleigh distribution of scattered amplitudes. One cannot have an actual point scatterer that produces such an amplitude distribution.

If one considers the following equation [(17) of Delano's paper or (4) of Muchmore's paper], it is easy to show that the apparent radar center ϵ_0 always lies midway between the two scatteres for the practical case, regardless of their respective phases. It does not fluctuate. This may be done as follows. Delano obtains for the apparent radar center

$$\epsilon_0 = \frac{E_s \cos(\theta_r - \theta_s)}{b_0 E}, \tag{1}$$

* Received by the PGAP, September 11, 1960.

† Antenna Lab., Dept. of Elec. Engrg., Ohio State University, Columbus, Ohio.

[1] R. B. Muchmore, "Aircraft scintillation spectra," IRE TRANS. ON ANTENNAS AND PROPAGATION, vol. AP-8, pp. 201–212; March, 1960.

[2] R. H. Delano, "A theory of target glint or angular scintillation in radar tracking," PROC. IRE, vol. 41, pp. 1778–1784; December, 1953.

[3] This was pointed out by Dr. R. G. Kouyoumjian.

[4] L. N. Ridenour, "Radar System Engineering," M.I.T. Rad. Lab. Ser., McGraw-Hill Book Co., Inc., New York, N. Y., vol. 1, pp. 76–77; 1947.

[5] L. Peters, Jr., "Location of Scatterers of a Complex Target by Means of Tracking Radar Systems," Antenna Lab., Ohio State Univ. Res. Foundation, Columbus, Ohio, Rept. 777-1, March, 1958; prepared under Contract AF 33(616)-5341 with the Air Res. and Dev. Command, Wright-Patterson AFB, Ohio.

where

$$Ee^{j\theta_r} = \sum_{n=1}^{N} a_n e^{j\theta_n} \tag{2}$$

$$E_s e^{j\theta_s} = \sum_{n=1}^{N} \delta_n a_n b_0 e^{j\theta_n} = \frac{b_0}{R} \sum_{n=1}^{N} a_n x_n e^{j\theta_n}, \tag{3}$$

θ_n = phase of the nth scatterer,
a_n = amplitude of the nth scatterer,
N = number of scatterers,
$\delta_n = x_n/R$,
R = the range,
x_n = the distance of the nth scatterer from some arbitrary origin in a plane normal to the line of sight. Only one channel need be considered as there is no interaction between channels for most tracking radar systems, and
b_0 = a constant.

Let us now consider the two point scatterer with equal amplitudes but an arbitrary phase distribution, *i.e.*, $\theta_1 = f_1(t)$ and $\theta_2 = f_2(t)$. Then

$$Ee^{j\theta_r} = Ke^{j[f_1(t)+f_2(t)]/2} \cos\left(\frac{f_1(t) - f_2(t)}{2}\right),$$

and

$$E_s e^{j\theta_s} = Ke^{j([f_1(t)+f_2(t)]/2+\pi/2)} \sin\left(\frac{f_1(t) - f_2(t)}{2}\right),$$

and since θ_r and θ_s are separated by $\pi/2$ radians,

$$\epsilon_0 = \frac{E_s \cos \pi/2}{bE} = 0 \text{ except for } E = 0.$$

This exception is trivial since no reflected signal is received at this time. Yet Delano obtains a fluctuation of this apparent radar center. It must be concluded that this fluctuation obtained by Delano is due solely to the assumptions made in his derivation. At this point it should be noted that the apparent radar center does wander for most multipoint targets, and that the conclusion to be drawn is that the statistical theory set forth to describe this scintillation is not adequate. Indeed, measurements have been made on a static model range at Ohio State University of the position of this apparent radar center as a function of target aspect.[6]

Now let us examine the line scatterer or long thin target treated by Muchmore and Delano. It would appear that this does satisfy the condition of an infinite number of scatterers, each infinitesimally small. The next condition is that of a statistically independent phase distribution. We can think of no physical scatterer which is represented by a line source made up of randomly phased points. Even if we attempt to approximate this by causing our target to flex in some arbitrary manner, it is noticed that the dominant signal comes from a number of stationary points. If we examine the tolerable flexing associated with any practical aircraft frames, it is seen that the number of stationary points is too few to justify this model.

In this case then, one has either a finite number of scatterers or a scatterer with a linear-phase distribution. Therefore, the model considered by Muchmore is not only rough, as he points out, but is highly impractical.

It has already been noted that this last case yields a Rayleigh distribution, provided $u > \pi$. It would, therefore, appear necessary to show that this case does not yield the spectra predicted by Muchmore to complete this line of reasoning. This will also demonstrate that the conditions which must be met are those of statistically independent amplitudes and phases, in addition to the requirement that the amplitude of the received echo be Rayleigh distributed.

For the case of the long thin target of length L with a uniform amplitude and linear phase distribution and the origin taken at the center of the target, (2) takes the form

$$Ee^{j\theta_r} = K_1 \int_{-L/2}^{L/2} e^{jK_2 x} dx = \frac{K_1}{K_2} \sin \frac{K_1 L}{2} e^{j0},$$

and (3) takes the form

$$E_s e^{j\theta_s} = K_3 \int_{-L/2}^{L/2} X e^{jK_1 x} dx = K_3 \left[2 \sin \frac{K_1 L}{2} - K_1 L \cos \frac{K_1 L}{2}\right] e^{j\pi/2}.$$

Again, θ_r and θ_s are separated by $\pi/2$ radians, and the apparent radar center lies at the center of this particular target. It may, therefore, be concluded that Figs. 6 and 7 of Muchmore's paper do not apply to this case.[1]

Conclusions

It is suggested that signals reflected from an aircraft and detected are not necessarily Rayleigh distributed, particularly for small-time intervals. It is further concluded that a Rayleigh-distributed reflection does not show that the target may be considered to be an ensemble of random point sources. Such assumptions when applied to radar targets can result in significant errors, as has been demonstrated by example for certain practical cases.

In particular, the above remarks are not intended as a criticism of the method of solution, but rather as a criticism of the universal application of this model.

Acknowledgment

The authors are indebted to Dr. E. M. Kennaugh and Dr. R. G. Kouyoumjian for their suggestions.

[6] L. Peters, Jr., "Accuracy of Radar Tracking Systems," Antenna Lab., Ohio State Univ. Res. Foundation, Columbus, Rept. No. 601–29, December, 1957; prepared under Contract AF 33(616)-7546, Air Res. and Dev. Command, Wright Air Dev. Div., Wright-Patterson AFB, Ohio.

Reply to Comments by Leon Peters, Jr., and F. C. Weimer*

R. B. MUCHMORE†, SENIOR MEMBER, IRE

PETERS and Weimer have objected to the use of the model for aircraft reflection used in papers by myself and Delano[1,2] to calculate certain characteristics of the signals reflected from complex radar targets. It is true that the model used cannot be regarded as completely realistic under all conditions. However, I believe the assumptions made in the analyses are reasonable.

The work of Kouyoumjian is not available to me, and so I cannot comment upon its relevance to the problem; however, I believe that it is not pertinent as the following discussion will show. The fact that there may be very special cases which will produce a Raleigh amplitude distribution other than the random one is, I think, beside the point. A model with several random reflection points would seem to be far more reasonable than one in which amplitudes and phases must be carefully and exactly specified.

In certain instances, two more or less equal scatterers form a good representation of an aircraft target. However, I submit that it is unreasonable to expect that such a complex object as an aircraft will produce exactly two scattering points with exactly equal, unchanging amplitudes and fixed phase. Two randomly phased scatterers with variable amplitudes would seem to be a far more reasonable approximation. Even for the singular case of two exactly equal scatterers with fixed phases, it is not true that there is no fluctuation. The derivation of Peters and Weimer is correct in every detail. Their interpretation, however, seems to miss the significant point. In regard to their last equation for the two point case, which is

$$\epsilon_0 = \frac{E_s \cos \pi/2}{bE} = 0 \text{ except for } E = 0,$$

they state that the exception is trivial. It is *not* trivial since this is, of course, exactly the crux of the matter. Perhaps it is easier to see this situation by having recourse to a simple wave picture rather than using the summation form of Delano. Two equal scatterers, a distance L apart, form an array whose scattering pattern in a plane containing the line of the array is a series of equal amplitude lobes with nulls between them. Now, as will be recalled, in any such array, phases differ by π in adjacent lobes. Thus, a series of equiphase surfaces could be drawn in each lobe, but to connect them across the null there must be a sudden jump of π radians in phase or one-half wavelength in space. If we consider the half-wavelength-in-space-jump at the null, then the phase surfaces consist of portions of concentric spheres in the lobes, but there is a half-wavelength-jump just across the null. Now, a direction finding system points normal to the phase-fronts. Thus, at every point, except exactly on the null, the normal to the phase-front points to the midpoint of the two element array as Peters and Weimer correctly deduce. However, on the null one might consider that the normal to the phase-front points 90° away from the direction, towards the center of the array.

Actually, the case just discussed and the one Peters and Weimer have chosen have this singularity at the null, which tends to obscure the true situation. One can remove the singularity by letting the two scatterers have almost but not quite equal amplitudes. Now the space pattern is very nearly that described above, but with the significant exceptions that the nulls do not go completely to zero, and that the phase fronts do not jump discontinuously by half wavelengths. There is, instead, a continuous smooth transition such that the normal to the phase-front, in passing from one lobe to another, goes from a direction pointing directly at the midpoint of the array to a direction not quite 90° away, at the center point of the null, and then back again towards the center of the array. Thus, Delano's result is correct, and the apparent radar center does wander.

It might be argued that the rather special distribution of angular fluctuation involved for two equal scatterers (*i.e.*, all points but one at the center and one point 90° off) is physically unreasonable—and it is. But the unreasonableness arises only from the unreasonable assumption that the scatterers are precisely equal in amplitude. The probability distribution of angles derived by assuming two equal scatterers contains a point (the point 90° away from the target center) of measure zero; *i.e.*, the probability of obtaining this point is zero. But the reason one obtains this singular result is that one has made singular assumptions to begin with. If one assumes that the two scatterers have some distribution of relative amplitudes, then choosing exactly the one point where the two amplitudes are equal is a choice of probability zero. If one makes what would appear to be a more reasonable choice, physically, and assumes that there is some distribution of relative amplitudes, then

* Received by the PGAP, October 14, 1960.
† Space Technology Labs., Inc., Los Angeles, Calif.
[1] R. B. Muchmore, "Aircraft scintillation spectra," IRE TRANS. ON ANTENNAS AND PROPAGATION, vol. 8, pp. 201–212; March, 1960.
[2] R. H. Delano, "A theory of target glint or angular scintillation in radar tracking," PROC. IRE, vol. 41, pp. 1778–1784; December, 1953.

one will not obtain a singular result, and an observable distribution of angular deviations results from the mathematics.

In relation to the line scatterer, it still seems to me that this is a reasonable model for an aircraft target viewed from exactly the same altitude. If one were to pass a plane normal to the line connecting the radar with the mean target center and consider that plane insofar as the radar is concerned, then all scatterers could be considered to lie within this plane after accounting for the appropriate round-trip phase delay from the plane to the scatterer and back. If one considers that the average aircraft dimension is tens and hundreds of feet, while the wavelength in the centimeter region is fractions of a foot, then it seems to be reasonable that this round-trip phase delay to various reflecting points on the target could be considered a random quantity and, in view of the fact that it is many, many wavelengths, the distribution must—if random—surely be uniform from zero to 2π. To me, this assumption seems to mean no more than that aircraft design dimensions are uncorrelated with radar wavelengths. Consider several reflection points on an aircraft target such as, for instance, a light spot on the vertical stabilizer and reflections from four motor nacelles. It seems almost obvious, after riding in a plane and watching the flexure of the wings in actual cases, that these points move many wavelengths relative to one another if one is thinking of microwave wavelength scales.

The discussion of long thin targets with uniform phase contains the same singularity as the discussion of the two point case. The results as presented are correct, but as is often the case, singular solutions fail to give any true insight into the problem.

One last point concerns Delano's example of many random scatterers with the same location. I agree that one cannot have an actual point scatterer that produces this result. But then, neither can one have a true point scatterer of any kind. All that this example purports to illustrate is the case of a complex target at a very great distance from the observing radar. The angular extent of the target can become negligibly small, but the resulting signal still behaves as though it were constructed from a large number of scatterers. It seems obvious that a target whose amplitude reflection scintillates will continue to do so no matter how distantly it recedes, and yet, at great distances, it might be thought of as many random sources at the same location.

Polyconic Approximation to a Parabolic Surface*

F. W. BROWN†, MEMBER, IRE

A PARABOLIC reflector, being a doubly-curved surface, presents some fabrication difficulties. If made from flat sheet metal, part of the material must be stretched, and/or part compressed to conform to a parabola of revolution. It would be attractive from a constructional standpoint to obtain a quasi-parabolic surface with a minimal number of singly-curved surfaces. The deviation from a true parabola should not exceed $\pm\lambda/16$ at the highest operating frequency if gain and pattern are not to suffer. One simple approximation is to employ a number of coaxial conical surfaces. Shallow cones can be very easily formed from sheet metal simply by removing a sector from a disc and joining the two edges. The optimum solution for two cones is given in this note. The method can easily be extended to any greater number.

Referring to Fig. 1, the paraboloid is represented in cross section by its generating function, $x^2=4fy$. The conical surfaces are seen as straight line generating functions $y=ax+b$ and $y=cx+d$; intersecting at some point (x_1, y_1). The error between the inner cone and the parabola will have the value

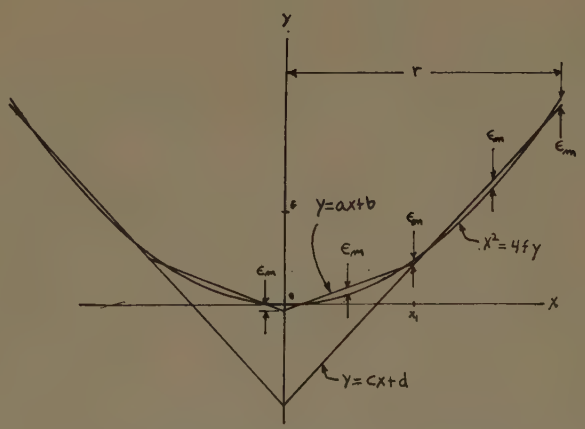

Fig. 1—Cross section of the paraboloid $x^2=4fy$, approximated by the two conical surfaces $y=ax+b$ and $y=cx+d$.

$$\epsilon = ax + b - \frac{x^2}{4f}, \tag{1}$$

* Received by the PGAP, August 24, 1960.
† Box 78, Star Route, Idyllwild, Calif.

being a maximum ϵ_m at $x=0$, $x=x_1$, and at some point x' in between. Equating $d\epsilon/dx$ to zero, we find $x'=2fa$, and substituting in (1):

$$\epsilon_m = fa^2 + b. \tag{2}$$

Since the same error occurs at $x=0$ and at $x=x_1$, the slope of the inner cone must be

$$a = \frac{x_1}{4f}. \tag{3}$$

By the same reasoning, the slope of the larger cone will be

$$c = \frac{r + x_1}{4f}. \tag{4}$$

The condition that the two cones intersect at $x=x_1$ yields

$$cx_1 + d = ax_1 + b. \tag{5}$$

At $x=r$, we again have the maximum error ϵ_m so that

$$cr + d + \epsilon_m = \frac{r^2}{4f}. \tag{6}$$

ϵ_m is found as in the case of the smaller cone to satisfy

$$\epsilon_m = fc^2 + d. \tag{7}$$

Substituting in (6),

$$cr + 2d + fc^2 = \frac{r^2}{4f}. \tag{8}$$

(1), (3), (4), (5), and (8) may be solved simultaneously for a, b, c, d, and x_1, yielding

$$a = \frac{r}{8f} \tag{9}$$

$$b = -\frac{r^2}{128f} \tag{10}$$

$$c = \frac{3r}{8f} \tag{11}$$

$$d = -\frac{17r^2}{128f} \tag{12}$$

$$x_1 = \frac{r}{2}. \tag{13}$$

By substituting (9) and (10) in (2), we see that

$$|\epsilon_m| = \frac{r^2}{128f}. \tag{14}$$

Most parabolic reflectors utilize an illuminator with a beamwidth of about 120°.[1] This requires the ratio of r to f to be about 1.155, meaning that $|\epsilon_m| = 0.00903r$. For $|\epsilon_m|$ not to exceed $\lambda/16$ then, the largest dish constructed by this method must not exceed a diameter of about 13.86 λ. To accommodate larger diameters it would be necessary to either use more than two cones, or to increase the ratio of f to r.

[1] C. C. Cutler, "Parabolic antenna design for microwaves," PROC IRE, vol. 37, pp. 1284–1294; November, 1947.

Comment on "Reciprocity Theorems for Electromagnetic Fields Whose Time Dependence Is Arbitrary"*

W. J. WELCH†

THEOREM II of a previous paper[1] presents a reciprocity relation between two sources of electromagnetic fields, a and b:

$$\iint [\boldsymbol{E}_a \cdot \boldsymbol{J}_b + \boldsymbol{H}_a \cdot \boldsymbol{K}_b] dv dt = -\iint [\tilde{\boldsymbol{E}}_b \cdot \boldsymbol{J}_a + \tilde{\boldsymbol{H}}_b \cdot \boldsymbol{K}_a] dv dt. \tag{1}$$

Both fields a and b satisfy Maxwell's equations:

$$\nabla \times \boldsymbol{E} + \frac{\partial \boldsymbol{B}}{\partial t} = -\boldsymbol{k}; \qquad \nabla \times \boldsymbol{H} - \frac{\partial \boldsymbol{D}}{\partial t} = \boldsymbol{J}. \tag{2}$$

The tildes over the b fields indicate that they are advanced wave solutions to Maxwell's equations, whereas the a fields are the usual retarded wave solutions. Since both sets have the same differential operator, we can say that Maxwell's equations are "formally self-adjoint" in a lossless medium. As pointed out by the author in the previous paper, this relation is not valid if the medium has finite conductivity.

* Received by the PGAP, September 29, 1960.
† Dept. of Elec. Engrg., University of California, Berkeley, Calif.
[1] W. J. Welch, "Reciprocity theorems for electromagnetic fields whose time dependence is arbitrary," IRE TRANS. ON ANTENNAS AND PROPAGATION, vol. AP-8, pp. 68–73; January, 1960.

One can include the case of finite conductivity by using for the adjoint operator Maxwell's equations with $\partial/\partial t$ replaced by $-\partial/\partial t$. This operator has both retarded and advanced wave solutions, and if there is no conductivity in the medium, it is equivalent to (2). However, with the addition of conductivity, it differs distinctly from (2) in that its solutions grow exponentially with time because of the conductivity, whereas those of (2) decay with time. The proper reciprocity relation can be found in much the same manner as was (1) in the previous article. Let there be two sources of electromagnetic fields, (J_a, K_a) and (J_b, K_b). We will consider the retarded field caused by (J_a, K_a) and the adjoint field caused by (J_b, K_b). The differential equations which must be solved are

$$\nabla \times E_a + \frac{\partial B_a}{\partial t} = -k_a,$$
$$\nabla \times H_a - \frac{\partial D_a}{\partial t} = J_a + \sigma E_a. \tag{3a}$$

$$\nabla \times \tilde{E}_b - \frac{\partial \tilde{B}_b}{\partial t} = -k_b,$$
$$\nabla \times \tilde{H}_b + \frac{\partial \tilde{D}_b}{\partial t} = J_b + \sigma \tilde{E}_b. \tag{3b}$$

The advanced wave solution to (3b) must be used. It should be clear that the adjoint field defined in this way is obtained from the usual retarded solution by replacing t by $-t$. Expanding the divergence of $(E_a \times \tilde{H}_b - \tilde{E}_b \times H_a)$ and substituting from (3), we obtain

$$\begin{aligned}
&\nabla \cdot (E_a \times \tilde{H}_b - \tilde{E}_b \times H_a) \\
&= \tilde{H}_b \cdot \left(-\frac{\partial B_a}{\partial t} - K_a \right) - E_a \cdot \left(-\frac{\partial \tilde{D}_b}{\partial t} + J_b + \sigma \tilde{E}_b \right) \\
&\quad - H_a \cdot \left(\frac{\partial \tilde{B}_b}{\partial t} - K_b \cdot \right) + \tilde{E}_b \cdot \left(\frac{\partial D_a}{\partial t} + J_a + \sigma E_a \right) \\
&= -\mu \frac{\partial}{\partial t} [\tilde{H}_b \cdot H_a] + \epsilon \frac{\partial}{\partial t} [\tilde{E}_b \cdot E_a] - (E_a \cdot J_b - H_a \cdot K_b) \\
&\quad + (\tilde{E}_b \cdot J_a - \tilde{H}_b \cdot K_a).
\end{aligned} \tag{4}$$

Next, we integrate (4) over a volume and a time interval which contain both sources. Then, with the application of the divergence theorem, it follows that

$$\begin{aligned}
&\int_{T_1}^{T_2} \int_S (E_a \times \tilde{H}_b - \tilde{E}_b \times H_a) \cdot n ds dt \\
&= -\mu \int_v \tilde{H}_b \cdot H_a dv \Big|_{T_1}^{T_2} + \epsilon \int_{T_1} \tilde{E}_b \cdot E_a dv \Big|_{T_1}^{T_2} \\
&\quad + \int_{T_1}^{T_2} \int_v ([\tilde{E}_b \cdot J_a - \tilde{H}_b \cdot K_a] \\
&\quad - [E_a \cdot J_b - H_a \cdot K_b]) dv dt.
\end{aligned} \tag{5}$$

Because the retarded fields are zero at time T_1 and the adjoint fields are zero at time T_2, the first two volume integrals on the right-hand side of (5) vanish identically. The remaining integral on the right contains the sources explicitly, so that the value of the surface integral on the left is independent of the size or shape of the surface. Then, if T_1 and T_2 are finite (however large), the surface can always be made large enough so that the retarded fields will not reach it during the interval $T_1 < t < T_2$, and the surface integral then is identically zero. In fact, with finite conductivity, the time interval may be infinite and the contribution from the surface integral at infinity will be zero, as long as the sources are of finite spatial extent. It follows then that, if the integrations over space and time completely enclose the sources,

$$\int\int (E_a \cdot J_b - H_a \cdot K_b) dv dt = \int\int (\tilde{E}_b \cdot J_a - \tilde{H}_b \cdot K_a) dv dt. \tag{6}$$

This form is more symmetrical than (1) and, except for the tildes and the time integrations, looks like the more familiar Lorentz reciprocity theorem. In the notation of the "reaction concept"[2] (6) becomes $\langle a, b \rangle = \langle \tilde{b}, a \rangle$, where

$$\langle a, b \rangle = \int\int (E_a \cdot J_b - H_a \cdot K_b) dv dt,$$
$$\langle \tilde{b}, a \rangle = \int\int (\tilde{E}_b \cdot J_a - \tilde{H}_b \cdot K_a) dv dt.$$

It was pointed out in the previous article that the self-reaction defined in terms of (1) was negative definite because

$$\int\int (E_a \cdot J_a + H_a \cdot K_a) dv dt \leq 0.$$

It is clear that the self-reaction defined in terms of (6) has a definite sign only if we are dealing with either electric current or magnetic current alone.

The variational principle for scattering which was derived in the previous paper may be demonstrated with (6) just as well. The only differences are a few minor sign changes.

Acknowledgment

The author is pleased to acknowledge the contribution of B. R. Cheo.

[2] V. H. Rumsey, "Reaction concept in electromagnetic theory," *Phys. Rev.*, vol. 94, pp. 1483–1491; June, 1954.

Coaxial Transmission Lines of Elliptical Cross Section*

M. J. KING† AND J. C. WILTSE†, SENIOR MEMBER, IRE

STRIPLINES have now found wide use in many applications. The stripline geometry is often shown as a degenerate form of a coaxial line which has been deformed from a circular to an elliptical cross section. In spite of this common manner of evolving striplines and the representation of magnetic field lines of the lowest (TEM) mode as ellipses in striplines, the correct analysis of this boundary-value problem does not appear to have been published. A formal solution for the case of an elliptic coax filled with isotropic dielectric material is given below.

The cross section of a straight elliptic coaxial line of infinite length is shown in Fig. 1 where the surfaces are

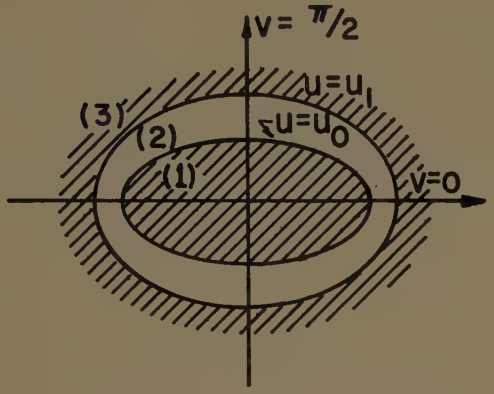

Fig. 1—Cross section of elliptical coaxial line.

confocal ellipses. In order to simplify the problem, it is assumed that Regions 1 and 3 are occupied by metals with infinite conductivity and Region 2 by an isotropic, lossless dielectric material. For convenience, the usual elliptic coordinate system is used where u and v are the radial and angular variables, respectively. The elliptic coordinates (u, v, z) are related to the rectangular coordinates (x, y, z) as follows:

$$x = d_0 \cosh u \cos v$$

$$y = d_0 \sinh u \sin v$$

$$z = z,$$

where d_0 is the semi-focal distance of the ellipse and is constant for the confocal elliptical coordinate system. For Region 2, the tangential components of the electric and magnetic fields E_{z_2} and H_{z_2} may be written (omitting the phase factor $e^{i(\omega t-\beta z)}$) as follows:

$$E_{z_2} = \sum_{n=0}^{\infty} (ae,o_n\, Je,o_n + ce,o_n\, Ne,o_n) Se,o_n \qquad (1)$$

$$H_{z_2} = \sum_{n=0}^{\infty} (be,o_n\, Je,o_n + de,o_n\, Ne,o_n) Se,o_n, \qquad (2)$$

where $Se_n = Se_n(s, v)$ and $So_n = So_n(s, v)$ are the even and odd periodic Mathieu functions; $Je_n = Je_n(s, u)$ and $Jo_n = Jo_n(s, u)$ are the radial Mathieu functions of the first kind; and $Ne_n = Ne_n(s, u)$ and $No_n = No_n(s, u)$ are the radial Mathieu functions of the second kind. The arbitrary constants ae,o_n, ce,o_n, be,o_n, and de,o_n are associated with even or odd solutions, respectively. The parameter $s = k^2 d_0^2$, where $k^2 = \omega^2\mu\epsilon - \beta^2$, ω = angular frequency, μ = permeability, ϵ = dielectric constant, and β = propagation constant.

The expressions for the remaining components, derived from the Maxwell curl equations, are

$$E_u = \frac{-i}{Lk^2}\left[\beta \frac{\partial E_z}{\partial u} + \omega\mu \frac{\partial H_z}{\partial v}\right] \qquad (3)$$

$$E_v = \frac{i}{Lk^2}\left[\omega\mu \frac{\partial H_z}{\partial u} - \beta \frac{\partial E_z}{\partial v}\right] \qquad (4)$$

$$H_u = \frac{i}{Lk^2}\left[\omega\epsilon \frac{\partial E_z}{\partial v} - \beta \frac{\partial H_z}{\partial u}\right] \qquad (5)$$

$$H_v = \frac{-i}{Lk^2}\left[\beta \frac{\partial H_z}{\partial v} + \omega\epsilon \frac{\partial E_z}{\partial u}\right] \qquad (6)$$

where

$$L = d_0\sqrt{\cosh^2 u - \cos^2 v}.$$

Let us now examine the boundary conditions to see if they can be satisfied for various possible modal solutions by expressing the components as single order Mathieu function products. Since infinite conductivity is assumed in Regions 1 and 3, the components E_{z_2}, E_{v_2}, and H_{u_2} must be zero at the boundaries.

By setting all the arbitrary constants, except be_n and de_n, equal to zero, even TE modes are described whose field components are given below (the primes indicate partial differentiation with respect to the appropriate variable, u or v):

$$E_{z_2} = 0 \qquad (7)$$

$$E_{u_2} = \frac{-i\omega\mu_2}{Lk_2^2}(be_n Je_n + de_n Ne_n) Se_n' \qquad (8)$$

* Received by the PGAP, September 16, 1960.
† Electronic Communications, Inc., Res. Div., Timonium, Md.

$$E_{v_2} = \frac{i\omega u_2}{Lk_2^2}(be_nJe_n' + de_nNe_n')Se_n \tag{9}$$

$$H_{z_2} = (be_nJe_n + de_nNe_n)Se_n \tag{10}$$

$$H_{u_2} = \frac{-i\beta}{Lk_2^2}(be_nJe_n' + de_nNe_n')Se_n \tag{11}$$

$$H_{v_2} = \frac{-i\beta}{Lk_2^2}(be_nJe_n + de_nNe_n)Se_n'. \tag{12}$$

Application of the boundary conditions gives the following equation:

$$\frac{Ne_n'(s_2, u_0)}{Je_n'(s_2, u_0)} = \frac{Ne_n'(s_2, u_1)}{Je_n'(s_2, u_1)}, \tag{13}$$

where u_0 and u_1 describe the contours of the inner and outer surfaces, respectively, and $s_2 = k_2^2 d_0^2$. Odd TE modes may also be obtained having an analogous boundary equation.

Similarly, by setting all the arbitrary constants equal to zero, except ae_n and ce_n, even TM modes are obtained whose components may be expressed as follows:

$$E_{z_2} = (ae_nJe_n + ce_nNe_n)Se_n \tag{14}$$

$$E_{u_2} = \frac{-i\beta}{Lk_2^2}(ae_nJe_n' + ce_nNe_n')Se_n \tag{15}$$

$$E_{v_2} = \frac{-i\beta}{Lk_2^2}(ae_nJe_n + ce_nNe_n)Se_n' \tag{16}$$

$$H_{z_2} = 0 \tag{17}$$

$$H_{u_2} = \frac{i\omega\epsilon_2}{Lk_2^2}(ae_nJe_n + ce_nNe_n)Se_n' \tag{18}$$

$$H_{v_2} = \frac{-i\omega\epsilon_2}{Lk_2^2}(ae_nJe_n' + ce_nNe_n')Se_n. \tag{19}$$

From the boundary conditions we obtain the equation:

$$\frac{Ne_n(s_2, u_0)}{Je_n(s_2, u_0)} = \frac{Ne_n(s_2, u_1)}{Je_n(s_2, u_1)}. \tag{20}$$

Again odd TM modes exist for an analogous boundary equation. The boundary equations can be considered determining or characteristic equations for k_2 and hence for cutoff frequencies of the different modes.

A principal wave in the form of a TEM mode can be derived from the even TM mode for $n=0$ (the odd Mathieu functions do not exist for $n=0$). The determining equation for k_2 becomes

$$\frac{Ne_0(s_2, u_0)}{Je_0(s_2, u_0)} = \frac{Ne_0(s_2, u_1)}{Je_0(s_2, u_1)}, \tag{21}$$

where $s_2 = k_2^2 d_0^2$ and the Mathieu functions Ne_0 and Je_0 may be defined as follows:

$$\left.\begin{aligned} Je_0(s_2, u) &= \sqrt{\frac{\pi}{2}}\sum_{k=0}^{\infty}(-1)^k De_{2k}J_{2k}(\sqrt{s_2}\cosh u) \\ Ne_0(s_2, u) &= \sqrt{\frac{\pi}{2}}\sum_{k=0}^{\infty}(-1)^k\frac{De_{2k}}{De_0} \\ &\quad\cdot\left[Y_k\left(\frac{\sqrt{s_2}}{2}e^u\right)J_k\left(\frac{\sqrt{s_2}}{2}e^{-u}\right)\right] \end{aligned}\right\}. \tag{22}$$

The coefficient De_{2k} is a function of the parameter s_2; J and Y are the usual Bessel functions.

If we let $k_2 \to 0$, and therefore $s_2 \to 0$, in such a way that $\sqrt{s_2}\cosh u \ll 1$, the following approximations are permitted:

$$J_n(\sqrt{s_2}\cosh u) \to \frac{(\sqrt{s_2}\cosh u)^n}{2^n n!}$$

$$J_n\left(\frac{\sqrt{s_2}}{2}e^{-u}\right) \to \frac{\left(\frac{\sqrt{s_2}}{2}e^{-u}\right)^n}{2^n n!}$$

$$Y_n\left(\frac{\sqrt{s_2}}{2}e^{u}\right) \to -\frac{2^n(n-1)!}{\pi}\left(\frac{\sqrt{s_2}}{2}e^{u}\right)^{-n},\ n \neq 0$$

$$Y_0\left(\frac{\sqrt{s_2}}{2}e^{u}\right) \to \frac{2}{\pi}\ln\left(\frac{\sqrt{s_2}}{2}e^{u}\right).$$

Also, as $s_2 \to 0$, all the coefficients De_{2k} approach zero except De_0 which approaches unity. Hence, $Je_0(s_2, u) \to \sqrt{\pi/2}$ and $Ne_0(s_2, u) \to \sqrt{2/\pi}\ln[(\sqrt{s_2}/2)e^u] \to -\infty$ as $k_2 \to 0$. The principal solution of (21) is then $k_2 = 0$, or $s_2 = 0$, and corresponds to

$$\beta = \omega\sqrt{\epsilon_2\mu_2}. \tag{23}$$

At the boundary $u = u_0$ the longitudinal current may be obtained from Ampere's law:

$$I = \oint H_{v_2}(u_0, v)dl, \tag{24}$$

where the path of integration is around the ellipse u_0. The element of path length dl is

$$dl = \sqrt{dx^2 + dy^2} = L(u_0)dv,$$

or (24) becomes

$$I = \oint H_{v_2}(u_0, v)L(u_0)dv \tag{25}$$

where

$$L(u_0) = d_0\sqrt{\cosh^2 u_0 - \cos^2 v}.$$

Consider the expression for the field component H_{v_2} when $k_2 \to 0$ or $s_2 \to 0$. Examining the functions Ne_0' and Se_0 as $s_2 \to 0$ for finite u, we find

$$\frac{\partial}{\partial u}[Ne_0(s_2, u)] \cong \sqrt{\frac{2}{\pi}}$$

$$Se_0(s_2, v) \cong 1.0.$$

If ae_0 is set equal to zero, the component H_{v_2} can be written (for small s_2) as follows:

$$H_{v_2} \cong -\sqrt{\frac{2}{\pi}} \frac{i\omega\epsilon_2}{Lk_2^2} ce_0 e^{i(\omega t - \beta z)}. \tag{26}$$

From (25) and (26), and using $I = I_0 e^{i(\omega t - \beta z)}$ we are able to solve for the constant ce_0:

$$ce_0 = \frac{ik_2^2 I_0}{2\sqrt{2\pi}\,\omega\epsilon_2}. \tag{27}$$

In considering the field components for the principal wave we will make use of the approximations given previously and also the fact that $Se_0' \to 0$ as $k_2 \to 0$. Substituting the expression given above for ce_0 into (14)–(19) for $n = 0$ and $ae_0 = 0$, it can be shown that all the components, except E_{u_2} and H_{v_2}, go to zero as $k_2 \to 0$. E_{u_2} and H_{v_2} become

$$E_{u_2} = \sqrt{\frac{\mu_2}{\epsilon_2}} \frac{I}{2\pi L} \tag{28}$$

$$H_{v_2} = \frac{I}{2\pi L}. \tag{29}$$

As d_0 approaches zero, the ellipse tends toward a circle; $L \to r$, where r is the cylindrical coordinate; and the TEM elliptic mode reduces to the circular coaxial TEM mode described by Stratton.[1]

The characteristic impedance, Z_0, is defined as the ratio of the maximum tranverse voltage to the total axial current.[2] The tranverse voltage, V, is found by integrating the radial component of the electric field from u_0 to u_1. For the TEM wave,

$$V = \int_{u_0}^{u_1} E_{u_2} L\,du = \sqrt{\frac{\mu_2}{\epsilon_2}} \frac{I}{2\pi}(u_1 - u_0) \tag{30}$$

and the characteristic impedance becomes

$$Z_0 = \frac{\sqrt{\frac{\mu_2}{\epsilon_2}}}{2\pi}(u_1 - u_0). \tag{31}$$

The power flow in the axial or z direction in Region 2 may be obtained from the z component of the Poynting vector, or, since our expressions are real,

$$S_z = \tfrac{1}{2}[E_{u_2} H_{v_2} - E_{v_2} H_{u_2}]. \tag{32}$$

The total power flow for the TEM wave is given by the following integral:

$$N = \int_0^{2\pi} \int_{u_0}^{u_1} S_z L^2\,du\,dv$$

$$= \frac{1}{2}\sqrt{\frac{\mu_2}{\epsilon_2}} \frac{I^2}{2\pi}(u_1 - u_0). \tag{33}$$

For the case of imperfectly conducting metal walls, if we assume the field in the dielectric is distorted very little when the metal has very high conductivity, it appears the calculation of the attenuation constants can be done by methods similar to those used by Chu.[3] An outline of this method, however, is too lengthy to go into here.

The solutions presented above are not entirely in agreement with results presented by Wong.[4] The method of solution used in the earlier article has, however, been questioned recently by other workers.[5]

[1] J. A. Stratton, "Electromagnetic Theory," McGraw-Hill Book Co., Inc., New York, N. Y.; 1941.

[2] G. R. Valenzuela, "Impedances of an elliptic waveguide," IRE TRANS. ON MICROWAVE THEORY AND TECHNIQUES, vol. MTT-8, pp. 431–435; July, 1960.

[3] L. J. Chu, "Electromagnetic waves in elliptic hollow pipes of metal," *J. Appl. Phys.*, vol. 9, pp. 583–591; September, 1938.

[4] J. Y. Wong, "On the theory of a coaxial transmission line consisting of elliptic conductors," *Canad. J. Phys.*, vol. 34, pp. 354–361; 1956.

[5] Private communications from Drs. J. R. Wait and A. E. Karbowiak to one of the authors (Wiltse).

Cassegrain Systems*

E. J. WILKINSON† AND A. J. APPELBAUM†

Summary—**The effective F/D ratio for a parabolic-hyperbolic (Cassegrain) antenna system is shown under practical considerations to be only slightly larger than that of the parabola alone. Furthermore, when advantage is being taken of this increase in effective F/D ratio for the purpose of providing wider angle multiple beam antenna systems, it is shown that the size of the feed horn structure may become prohibitive.**

THE Cassegrain antenna system is often mentioned as a possible means of realizing a large increase in effective F/D ratio for the purpose of permitting wider angle scanning or beam positioning. It is the purpose of this note to show that while an increase in F/D ratio can be realized, it is not, under practical considerations, very great.

Consider the two-reflector system of Fig. 1, which consists of a parabola at $x=b$ and a hyperbola at $x=a$,

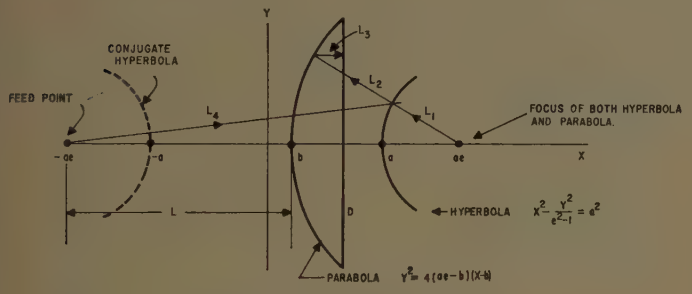

Fig. 1—Cassegrain system.

each having its focus at $x=a\epsilon$, where ϵ is the eccentricity of the hyperbola. By definition the parabola is a curve such that

$$L_1 + L_2 + L_3 = c_1$$

for all rays, and the hyperbola is a curve defined by

$$L_4 - L_1 = c_2$$

for all rays. Therefore,

$$L_4 + L_2 + L_3 = c_1 + c_2,$$

or, all rays from a feed point located at $x=-a\epsilon$, the conjugate focus of the hyperbola, will traverse an equi-length path to the aperture of the parabola. The focal length of the parabola alone (defined as the distance from focus to vertex) is from Fig. 1.

$$F = a\epsilon - b,$$

and for the Cassegrain system with feed at $x=-a\epsilon$,

$$F' = a\epsilon + a + (a - b).$$

Thus, the effective focal length to diameter ratio for the Cassegrain system is given by

$$\frac{F'}{D} = \frac{F}{D} \cdot \frac{\epsilon + 2 - \frac{b}{a}}{\epsilon - \frac{b}{a}}. \tag{1}$$

Consider first the situation where the feed point is located at the vertex of the parabola. For this case $b=-a\epsilon$ and (1) becomes

$$\frac{F'}{D} = \frac{F}{D} \cdot \frac{\epsilon + 1}{\epsilon}. \tag{2}$$

Since the eccentricity ranges from $1<\epsilon\leq\infty$, for which the hyperbola goes from a line parallel to the x axis to a line parallel to the y axis (plane reflector), the effective F'/D ratio for the Cassegrain system with the feed at the vertex of the parabola can never exceed that of the parabola alone by more than a factor of 2.

Consider next the situation where the feed point is located between the parabola and the hyperbola. For this case $b<-a\epsilon$, which from (1) results in the F/D of the parabola being magnified by a factor always less than 2.

Finally, if the feed is placed behind the parabola, $b>-a\epsilon$, it is possible to get F'/D greater than F/D by more than a factor of 2. In fact, it will be observed that when $b/a\rightarrow 1$, (1) approaches

$$\frac{F'}{D} = \frac{F}{D} \cdot \frac{\epsilon + 1}{\epsilon - 1}, \tag{3}$$

which appears to predict very large effective F'/D ratios for the Cassegrain system, relative to the parabola alone as $\epsilon\rightarrow 1$. It should be noted, however, that the F/D of the parabola is approaching zero under these conditions, and the practical increase in F'/D that is possible with the Cassegrain system is not clear from this form of the expression. If we define L to be the distance of the feed behind the parabola, which from Fig. 1 is seen to be $L=a\epsilon+b$, then F' may be written as

$$\frac{F'}{D} = \frac{L}{D} \cdot \frac{\epsilon + 2 - \frac{b}{a}}{\epsilon + \frac{b}{a}}. \tag{4}$$

* Received by the PGAP, September 16, 1960.
† Sylvania Electronic Systems, Waltham Labs., Mass.

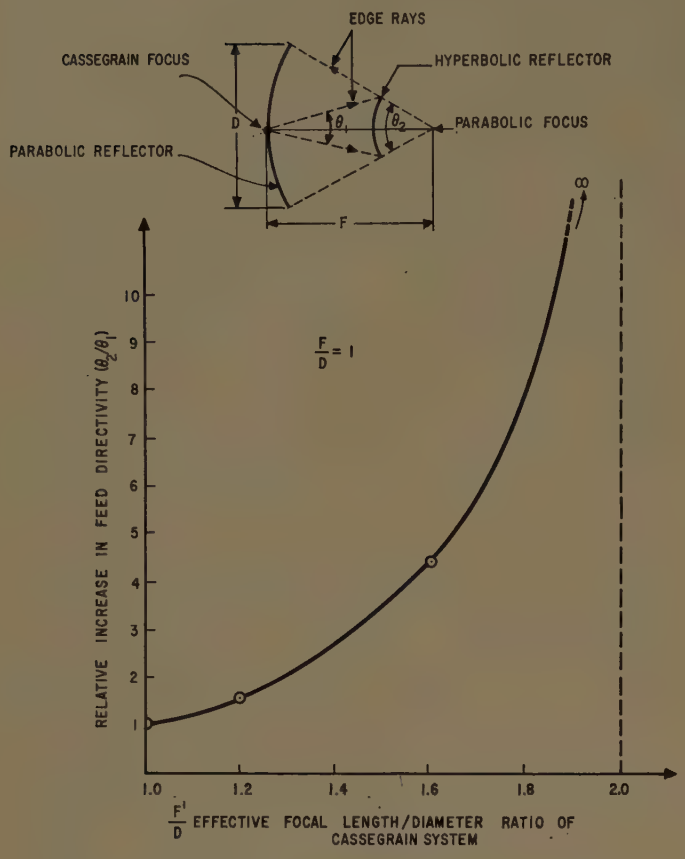

Fig. 2—Increased feed directivity for Cassegrain system.

It can now be seen that as $b/a \rightarrow 1$, the F'/D ratio possible with the Cassegrain system approaches the spacing of the feed behind the parabola as measured in terms of the aperture width D.

Since it is questionable whether one would ever consider an antenna design in which the feed was located very much more than an aperture diameter or two behind the reflector, it would appear that very large effective F'/D ratios for the Cassegrain system, even when the feed is behind the parabola, cannot be realized.

Finally, if we return to the case where the feed is at the vertex of the parabola, it is found that increasing the effective F'/D ratio by increasing the curvature of the hyperbola ($\epsilon \rightarrow 1$) results in an increase in the required directivity of the feed relative to the feed directivity required for the parabola alone. This can be seen from the sketch in Fig. 2 where the angle that the edge rays subtend at the Cassegrain focus is smaller than that subtended at the focus of the parabola, *i.e.*, $\theta_1 < \theta_2$. The increase in feed directivity θ_2/θ_1, is plotted in Fig. 2 for $F/D=1$. If the interest in obtaining an increase in effective F/D ratio is for the purpose of allowing multiple beam formation by placement of a cluster of feed horns about the focal point, then it would appear that one must settle for much less than a factor of two increase in effective F/D ratio, or the size of the feed horn cluster will become prohibitive.

Contributors

Charles B. Arnold was born in Detroit, Mich., on July 17, 1937. He received the B.S. degree in engineering from the University of Michigan, Ann Arbor, in 1959.

C. B. Arnold

He then joined the Radio Observatory staff of the University of Michigan, where he was engaged in radiometer development. In 1960, he joined the Solid State Physics Laboratory of Willow Run Laboratories, the University of Michigan, as an assistant in research, engaged in maser research and development.

❖

Max E. Bair (M'61) was born in Morenci, Mich., on March 12, 1932. He received the B.S. degree in electrical engineering from the University of Michigan, Ann Arbor, in 1960.

From 1951 to 1955 he served with the United States Air Force as an electronics and radar instructor. In 1955 he was employed by the RCA Service Company as a contract instructor. He joined Willow Run Laboratories, the University of Michigan, as an electronics technician in 1956. He is currently a research assistant at Willow Run Laboratories with the Solid State Physics Group, and is actively engaged in the basic and applied research of maser devices.

M. E. Bair

❖

R. N. Bracewell (SM'56–F'61) was born in Sydney, Australia, in 1921. He received the B.Sc. degree in mathematics and physics from the University of Sydney in 1941, the B.E. degree in 1943, and the M.E. degree in 1948, in communications with first class honors. He received the Ph.D. degree from the University of Cambridge, Cambridge, England, in 1949.

R. N. Bracewell

He worked on electromagnetic theory and microwave radar development in the Radiophysics Division of the CSIRO during the war. From 1946 to 1949, he made experimental studies of solar ionospheric phenomena using very long waves in the Cavendish Laboratory, Cambridge. A developing interest in the astronomical aspects of radio science led to his spending 1954–1955 as a visiting professor at the Berkeley Astronomical Department, University of California, Berkeley, on leave from CSIRO with a Fulbright grant. He is now professor of electrical engineer-

ing in the Radioscience Laboratory at Stanford University, and directs the research of the Stanford Radio Astronomy Institute.

Dr. Bracewell is an associate member of the IEE, Fellow of the Royal Astronomical Society, life member of the Astronomical Society of the Pacific, member of the American Astronomical Society, IAU, URSI, and has been appointed to astronomical panels advisory to the National Radio Astronomy Observatory, Naval Radio Research Station, and Office of Naval Research.

❖

Dimitri S. Bugnolo (S'52–A'53–M'59) was born on February 3, 1929, in Atlantic City, N. J. He received the B.S. degree in electrical engineering from the University of Pennsylvania, Philadelphia, in 1952, the M.E. degree from Yale University, New Haven, Conn., in 1955, and the D.Eng.Sc. degree from Columbia University, New York, N. Y., in 1960.

D. S. Bugnolo

From 1952 to 1954, he was a research engineer with the Burroughs Corp., Paoli, Pa. While working for the M.E. degree, he was a member of the staff of Yale University. From 1956 to 1960, he was an instructor in the Department of Electrical Engineering at Columbia University. He was also project director and chief investigator of a research contract sponsored by the Air Force Office of Scientific Research. He is currently a staff engineer with the Bell Telephone Labs., Inc., Holmdel, N. J.

Dr. Bugnolo is a member of Sigma Xi, and the American Physical Society.

❖

Dwight W. Casey II was born in Indianapolis, Ind., on June 5, 1930. He received the B.S. degree in electrical engineering in 1952, and the M.S. degree in 1953, both from Purdue University, Lafayette, Ind.

D. W. Casey

From 1953 to 1955, he was an associate engineer with Douglas Aircraft Company, Santa Monica, Calif, where he was engaged in the design and analysis of auto-pilot systems. In 1955 he joined the Farnsworth Electronics Company, Fort Wayne, Ind., which became the Space Communications Laboratory of ITT-Kellogg in June, 1960. He is presently a senior engineer with this laboratory, and is primarily concerned with low-noise microwave receiver techniques and their application to radiometric equipment.

❖

Jerald J. Cook was born in West Frankfort, Ill., on August 9, 1933. He received the B.S. degree in physics from Western Michigan University, Kalamazoo, in 1956, and the B.S. degree in electrical engineering from the University of Michigan, Ann Arbor, in 1957.

J. J. Cook

From 1957 to 1958 he was a research assistant with the Upjohn Company, Kalamazoo, working in instrumentation. In 1958 he returned to the University of Michigan to pursue a graduate curriculum in engineering mechanics, working in the fields of solid state physics and radio astronomy at Willow Run Laboratories. He is presently a research associate at Willow Run, and a member of the teaching staff of the University of Michigan, Department of Engineering Mechanics.

Mr. Cook is a member of Tau Beta Pi Eta Kappa Nu, and Sigma Xi.

❖

Lloyd G. Cross was born in Flint, Mich., on October 7, 1934. He received the B.S. degree in physics in 1957 and the M.S. degree in 1960, both from the University of Michigan, Ann Arbor. He is doing work toward the Ph.D. degree in physics at the University of Michigan.

L. G. Cross

From 1956 to 1958 he was an assistant in research at Willow Run Laboratories, the University of Michigan, working in the field of infrared physics. In 1958 he transferred to the Solid State Physics Group of the same laboratory, and began work on masers. He is presently a research associate at Willow Run Laboratories.

❖

William E. Gordon (A'46–M'49–SM'58) was born in Paterson, N. J., on January 8, 1918. He received the B.A. degree in mathematics from Montclair State Teachers College, Montclair, N. J., in 1939, the M.S. degree in meteorology from New York University, New York, in 1946, and the Ph.D. degree from Cornell University, Ithaca, N. Y., in 1953.

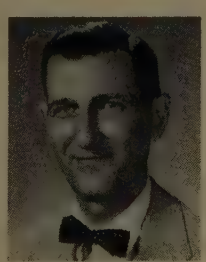

W. E. Gordon

He was in the Air Force during World War II, engaged in radio-meteorological studies in association with the Committee on Propagation of NDRC. At the close of the war, he became associate director of the Electrical Engineering Research Laboratory, University of Texas, Austin. In 1948, he joined the staff of the School of Electrical Engineering, Cornell University, as research associate, becoming associate professor in 1953 and professor in 1959.

Dr. Gordon is Chairman of the U. S. National Committee of URSI, and a member of Eta Kappa Nu, Tau Beta Pi, Sigma Xi, and the American Meteorological Society.

❖

Fred T. Haddock (A'42–M'55) was born on May 31, 1919, in Independence, Mo. He received the B.S. degree in physics from the Massachusetts Institute of Technology in 1941, and was awarded the M.S. degree in physics by Maryland University, College Park, in 1950.

F. T. Haddock

In 1941 he joined the Naval Research Laboratory, Washington, D. C., where he did research in the field of microwave components and antennas. After 1946, he was engaged in radio astronomy research at NRL. He is associate professor in the Departments of Electrical Engineering and Astronomy at the University of Michigan, Ann Arbor, where he is in charge of the radio astronomy project.

Mr. Haddock was U. S. Chairman of the URSI Commission on radio astronomy. He is a member of the American Physical Society, the American Astronomical Society, the International Astronomical Union, and Sigma Xi, and is a Fellow of the Royal Astronomical Society.

❖

Hsien Ching Ko (S'53–M'56–SM'60) was born in Formosa, China, on April 28, 1928. He received the B.S. degree in 1951 from the National Taiwan University in China, and the M.S. and the Ph.D. degrees in electrical engineering from The Ohio State University, Columbus, in 1953 and 1955, respectively.

H. C. Ko

From 1951 to 1952 he worked on ionospheric physics and propagation at the Radio Wave Research Laboratories in Taipei, China. Since 1952 he has been associated with the Radio Observatory, Department of Electrical Engineering, The Ohio State University. He has worked on the problems of cosmic radio noise, radio star scintillation, and development of antennas and receivers for radio astronomy. He is now associate professor of electrical engineering and assistant director of the Radio Observatory.

Dr. Ko is a member of Sigma Xi, Pi Mu Epsilon, Eta Kappa Nu, the American Astronomical Society, and Commission V of the U.S. National Committee of URSI.

❖

John D. Kraus (A'32–M'43–SM'43–F'54) was born in Ann Arbor, Mich., on June 28, 1910. He received the B.S. degree

in 1930, the M.S. degree in 1931, and the Ph.D. degree in 1933, all from the University of Michigan, Ann Arbor.

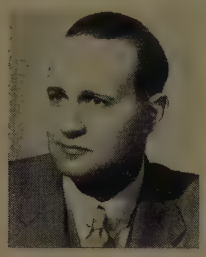

J. D. KRAUS

From 1934 to 1935, he did research on industrial noise-reduction problems, and from 1936 to 1937 was engaged in nuclear research with the newly completed University of Michigan cyclotron. From 1938 to 1940, he was an antenna consultant. He joined the Naval Ordnance Laboratory, Washington, D. C., in 1940, working on the degaussing of ships, and and in 1943, he became a member of the Radio Research Laboratory, Harvard University, Cambridge, Mass. He joined the faculty of the Ohio State University, Columbus, in 1946, where he is now professor of electrical engineering, professor of physics and astronomy, and director of the Radio Observatory. He is the inventor of the helical beam antenna, the corner-reflector antenna, and other antenna types.

Dr. Kraus is a member of the American Astronomical Society and the American Physical Society.

❖

James W. Kuiper (S'56–M'59) was born in Grand Rapids, Mich., on January 11, 1934. He received the B.S. and M.S. degrees in electrical engineering from the University of Michigan, Ann Arbor, in 1957 and 1958, respectively.

J. W. KUIPER

He has been with the Radio Astronomy Project of the University of Michigan since 1956, first as research assistant, and then as research associate, working with the various sweep-frequency receivers used to receive solar radio emission. Recently, he has been concerned with the development of the 2–4 kMc sweep-frequency receiver.

Mr. Kuiper is a member of the American Astronomical Society.

❖

Mukul R. Kundu (SM'60) was born in Calcutta, India, on February 10, 1930. He received the B.S. degree with honors in physics in 1949, and the M.S. degree in radio physics and electronics in 1951, both from the University of Calcutta. In 1957, he received the Docteur dès Sciences degree from the University of Paris.

From 1952 to 1954, he was a research assistant with the Council of Scientific and Industrial Research, Calcutta, India, and worked on ionospheric problems at the University of Calcutta. In 1954, he went to France with a scholarship from the French government, and joined the French group in radioastronomy at the observatories of Meudon and Nançay. From 1956 to 1958 he was a research assistant under Centre Nationale de la Recherche Scientifique of France. In France, he was engaged in studies on microwave techniques applied to radioastronomy and, in particular, was interested in problems related to solar radio emission on centimeter waves. From 1958 to 1959, as a senior research fellow, he worked on solar radioastronomy at the National Physical Laboratory of India. Since August, 1959, he has been associated with the Navy Radioastronomy Project of the University of Michigan, Ann Arbor, and has been working on various problems related to Solar Radioastronomy.

M. R. KUNDU

❖

L. Merle LaLonde was born in Clayton, N. Y., on July 20, 1931. He attended Cortland State Teachers College, Cortland, N. Y., from 1948 until the outbreak of the Korean War, when he enlisted in the U. S. Navy. From 1951 to 1954, his naval service was spent completing the Electronics Technician School and aboard a radar picket destroyer. He was discharged as ET I.

L. M. LALONDE

He was employed for one year by Stromberg-Carlson Company in the Sound Division before entering Cornell University, Ithaca, N. Y., where he received the B.E.E. degree in 1959. While at Cornell, he worked for the Research Department where he was primarily concerned with instrumentation of interferometer systems for ionospheric refraction measurements. He has been employed since 1959 by the Cornell Center for Radiophysics and Space Research, working full-time on the Arecibo radar project.

❖

Yuen-Tze Lo (S'49–A'53–M'58) was born on January 31, 1920, in Hankow, China. He received the B.S. degree in electrical engineering from the National Southwest Associated University, Kunming, China, in 1942, and the M.S. and Ph.D. degrees from the University of Illinois, Urbana, in 1949 and 1952, respectively.

From 1946 to 1948 he was an instructor in the Department of Electrical Engineering of the National Tsing Hua University, Kunming, China. From 1949 to 1952, he was a Fellow of the Department of Electrical Engineering, University of Illinois. He was a project engineer of the Channel Master Corp., Ellenville, N. Y., during the period from 1952 to 1956. Since then Dr. Lo has been with the Antenna Laboratory, University of Illinois, as a research assistant professor of electrical engineering.

Y.-T. LO

❖

Robert T. Nash (S'54–A'56) was born on September 20, 1929, in Columbus, Ohio. He received the B.S. degree in physics in 1952, and the M.S. degree in electrical engineering in 1955, both from The Ohio State University, Columbus.

R. T. NASH

At present, he is instructor in electrical engineering at The Ohio State University, and has been connected with the design and contruction of the 360-foot radio telescope.

Mr. Nash is a member of Sigma Xi.

❖

Richard B. Read was born in Long Beach, Calif., on September 25, 1933. He received the B.S. degree in physics from the California Institute of Technology, Pasadena, in 1955. After serving two years as a lieutenant in the United States Air Force, assigned to the Electronics Research Directorate of the Air Force Cambridge Research Center, Bedford, Mass., he returned to the California Institute of Technology, where he is currently pursuing studies toward the Ph.D. degree in the field of radio astronomy.

R. B. READ

Mr. Read is a member of the American Physical Society and the American Association for the Advancement of Science.

❖

Laura Ronchi was born in Florence, Italy, on May 7, 1929. She was graduated with a major in physics from the University

of Florence in 1950. In 1959 she received the Ph.D. degree in electromagnetic waves from the same institution.

L. RONCHI

From 1951 to 1953, she was an assistant at the Institute of Physics at the University of Florence. Since 1953, Miss Ronchi has been employed as a research assistant at the Centro Microonde del Consiglio Nazionale delle Richerche in Florence.

❖

Vera Russo was born in Pisa, Italy, on November 11, 1928. She attended the University of Pisa and was graduated with a major in mathematics in 1953.

V. RUSSO

Since that time she has been a research assistant at the Centro Microonde of Consiglio Nationale delle Ricerche in Florence, where her work has been primarily concerned with microwave optics.

❖

Govinda Swarup was born on March 23, 1929, in Thakurdwara, U. P., India. He received the B.Sc. and M.Sc. degrees in physics from Allahabad University, India, in 1948 and 1950, respectively.

G. SWARUP

From 1951 to 1953, he worked as Secretary to the Radio Research Committee, CSIR, India. Since 1953, he has been engaged in research in radio astronomy and has been particularly concerned with high-resolution studies of radio emission from the sun. From 1953 to 1955, he worked with the CSIRO Radiophysics Laboratory, Sydney, Australia, under a Colombo Plan fellowship. He worked at the National Physical Laboratory, New Delhi, from 1955 to 1956. He was then a research associate at the Harvard College Observatory, Cambridge, Mass., for one year. Since 1957, Mr. Swarup has been a research assistant in electrical engineering at Stanford University, Stanford, Calif., and is working with the Stanford radio astronomy group.

❖

George W. Swenson, Jr. (A'46–SM'52) was born on September 22, 1922, in Minneapolis, Minn. He received the B.S. degree in electrical engineering from Michigan College of Mining and Technology, Houghton, in 1944, the M.S. degree in electrical engineering from Massachusetts Institute of Technology, Cambridge, in 1948, and the Ph.D. degree in electrical engineering from the University of Wisconsin, Madison, in 1951.

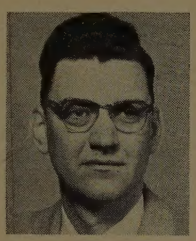

G. W. SWENSON, JR.

His professional affiliations have included faculty positions at Washington University, St. Louis, Mo., the University of Alaska, College, Alaska, and Michigan State University, East Lansing. He has also been engaged in research or consulting assignments with Boeing Airplane Company, Seattle, Wash., the Geophysical Institute of the University of Alaska, and the Army Ballistic Missile Agency. He is currently professor of electrical engineering and research professor of astronomy at the University of Illinois, Urbana, conducting research programs in radio astronomy and ionospheric physics.

Dr. Swenson is a member of Tau Beta Pi, Eta Kappa Nu, Sigma Xi, the American Astronomical Society, and Commission V of the U. S. National Committee of URSI.

Giuliano Toraldo di Francia was born in Florence, Italy, on September 17, 1916. He was graduated with a major in physics from the University of Florence in 1939, and after World War II, he received the Ph.D. degree in mathematical physics and optics from that University.

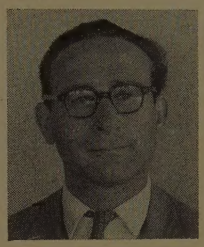

G. TORALDO DI FRANCIA

For some years, he was professor of electromagnetic waves at the University of Florence. In 1952–1953, he was a visiting professor at the Institute of Optics of the University of Rochester. At present, he is Director of the Institute for the Physics of Radiation at the University of Florence.

Dr. Toraldo di Francia is vice-president of the International Commission of Optics of the International Union of Pure and Applied Physics and a member of the Italian Committee of URSI.

❖

Kwang-Shi Yang was born in Shanghai, China, on July 11, 1931. He received the B.S. degree in electrical engineering from St. Louis University, St. Louis, Mo., in June, 1956, and the M.S. degree in electrical engineering from Stanford University, Stanford, Calif., in April, 1958.

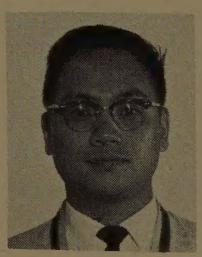

K. S. YANG

He has been a research assistant at Stanford University since September, 1956, and has been working on the transmission line system of the Stanford cross antenna.

Mr. Yang is a member of Pi Mu Epsilon and an associate member of Sigma Xi.

INSTITUTIONAL LISTINGS

The IRE Professional Group on Antennas and Propagation is grateful for the assistance given by the firms listed below, and invites application for Institutional Listing from other firms interested in the field of Antennas and Propagation.

AERO GEO ASTRO CORP., 1200 Duke St., Alexandria, Va.
Research and Development; Antennas; Transponders; Command Receivers; Augmenters; Telemetry-Radar.

ANDREW CORPORATION, P.O. Box 807, Chicago 42, Ill.
Antennas, Antenna Systems, Transmission Lines, Development and Production.

ANTLAB, INC., 6330 Proprietors Rd., Worthington, Ohio
Antenna Pattern Range Systems—Recorders & Mounts, & Telemetry Servo Pedestals.

BLAINE ELECTRONETICS, INC., 14757 Keswick St., Van Nuys, Calif.
Antennas, Paraboloids, Scale Models, Antenna Radiation Pattern Measurement Towers.

DEVELOPMENTAL ENGINEERING CORP., Leesburg, Va.; Boston, Mass.; Boulder, Colo.; Washington, D.C
Antenna Research, Design & Evaluation-Propagation Studies & Communications Systems Engineering

DORNE & MARGOLIN, INC., 29 New York Ave., Westbury, L. I., N. Y.
Research, Development and Manufacture—Antenna and Microwave Technology

FXR, Inc., 25–26 50th St., Woodside 77, N. Y.
Precision Microwave Test Equipment, High Power Microwave Electronics,
Microwave Components & Instrumentation

GABRIEL ELECTRONICS, Division of The Gabriel Company, Main & Pleasant Sts., Millis, Mass.
Research, Engineering and Manufacture of Antenna Equipment for Government and Industry.

HUGHES AIRCRAFT COMPANY, Florence and Teale Sts., Culver City, Calif.
Res., Dev., Mfg.: Radar Systems & Components; Antennas, Tubes, Radomes, Solid-State Devices.

I-T-E CIRCUIT BREAKER CO., Special Products Div., 601 E. Erie Ave., Philadelphia 34, Pa.
Design, Development and Manufacture of Antennas, and Related Equipment.

JANSKY & BAILEY, INC., An Affiliate of Atlantic Research Corp.,
1339 Wisconsin Ave., N.W., Washington, D. C.
Complete Engineering Services for Antennas and Propagation Programs.

MARK PRODUCTS CO., 5439 W. Fargo Ave., Skokie, Ill.
Antennas for Two-Way Communications, Grid Parabolas, Research & Development.

TECHNICAL APPLIANCE CORP., 1 Taco St., Sherburne, N. Y.
Des., Dev., & Mfg.: Antennas & Antenna Systems for Communications, Telemetry, & Tracking.

WEINSCHEL ENGINEERING COMPANY, INC., Kensington, Md.
Antenna Pattern Receivers; Bolometer Amplifiers; Modulated Microwave Sources;
Insertion Loss Measuring Systems.

WHEELER LABORATORIES, INC., Great Neck, N. Y.; Antenna Lab., Smithtown, N. Y.
Consulting Services, Research and Development, Microwave Antennas and Waveguide Components.

The charge for Institutional Listing is $50 for one issue or $200 for six consecutive issues (one year). Application may be made to the Technical Secretary, The Institute of Radio Engineers, Inc., 1 East 79th Street, New York 21, N. Y.